FACULTY OF ENGINEERING
AND ARCHITECTURE

Investigating the Effect of Curvature and Composition on Lipid Membrane Permeability Using Molecular Dynamics Simulations

Samaneh Davoudi

Doctoral dissertation submitted to obtain the academic degree of
Doctor of Biomedical Engineering

Supervisor
Prof. An Ghysels, PhD
Department of Electronics and Information Systems
Faculty of Engineering and Architecture, Ghent University

June 2024

GHENT
UNIVERSITY

ISBN 978-94-6355-846-4
NUR 928, 927
Wettelijk depot: D/2024/10.500/51

Members of the Examination Board

Chair

Prof. Hennie De Schepper, PhD, Ghent University

Other members entitled to vote

Prof. Charlotte Debbaut, PhD, Ghent University
Prof. Siewert-Jan Marrink, PhD, Rijksuniversiteit Groningen, the Netherlands
Prof. Ahmadreza Mehdipour, PhD, Ghent University
Prof. Kenno Vanommeslaeghe, PhD, Vrije Universiteit Brussel

Supervisor

Prof. An Ghysels, PhD, Ghent University

ACKNOWLEDGMENTS

I would like to express my deepest gratitude to my supervisor, Prof. An Ghysels, for her continuous support, guidance, and encouragement throughout my PhD journey. Her insightful feedback into my work have been truely invaluable.

I am also profoundly grateful to the members of my dissertation committee, Prof. Charlotte Debbaut, Prof.AhmadReza Mehdipour, Prof. Siewert-Jan Marrink and Prof. Kenno Vanommeslaegh for their constructive critiques and helpful suggestions, which significantly improved the quality of my research. A heartfelt appreciation goes to Prof. Siewert-Jan Marrink for his continuous support over the past few months throughout my efforts to secure employment. I would like to express my sincere gratitude to Prof. Hennie De Schepper, the Chair of my PhD defense, for expertly overseeing this process and providing invaluable guidance and support.

I would like to express my sincere appreciation to my colleagues in Molecular Modeling group, whose support assisted in the success of this thesis. A special note of gratitude is extended to Wouter, whose expertise and assistance have significantly helped me during my PhD.

I am deeply grateful to my friends, whose support and encouragement have been my rock through every twist and turn of this journey. Additionally, I extend my heartfelt appreciation to my colleagues and friends in the BioMMedA and Medisip groups for a nurturing and stimulating environment. Your emotional support has been invaluable, and I am truly thankful for the memories we share.

On a personal note, I extend my heartfelt appreciation to my family, Elmira, Fatemeh, Masoumeh, Reza, Hosein, Zahra, Mojtaba and Leila for their support and encouragement. To my mother, Leili, for her sacrifices, unconditional love, patience, understanding and endless support, especially during the most challenging times of this journey.

Lastly, I dedicate this thesis to the memory of my late father, SafarAli, who always believed in me and inspired me to strive for excellence. His memory continues to be a source of my strength and motivation.

Ghent, June 2024
Samaneh

TABLE OF CONTENTS

Papers 127

List of Figures

LIST OF TABLES

ABBREVIATIONS AND SYMBOLS

The following list summarizes the abbreviations and symbols in this dissertation.

Abbreviations

AA	all-atom
APL	area per lipid
BA	Bayesian analysis
CG	coarse-grained
Chol	cholesterol
CHOL	cholesterol
D	diffusion constant
DPPC	dipalmitoyl-phosphatidylcholine
DOPC	dioleoyl-phosphatidylcholine
FA	fatty acid
ISD	inhomogeneous solubility-diffusion
MD	molecular dynamics
P	permeability
POPC	1-palmitoyl-2-oleoyl-phosphatidylcholine
RETIS	replica exchange transition interface sampling
MSD	mean square displacement
SI	supporting information
T	temperature

Symbols

J	flux
$\Delta \mathrm{c}$	concentration gradient
h_m	membrane thickness
ΔF	free energy difference
F	free energy

N0	Martini 3 bead
Na	Martini 3 bead
F	flat membrane
L	liposome
L_{50}	50 Å-radius liposome
L_{100}	100 Å-radius liposome
L_{130}	130 Å-radius liposome
r	radius
hist	histogram
TC2	Martini 3 bead
TC3	Martini 3 bead
TX1	Martini 3 bead
TX2	Martini 3 bead
k_B	Boltzman constant
L	box length
c_ref	reference concentration
σ	Crossing area
n_cross	number of crossings
T_sim	simulation time
c_w	permeant concentration in water
c_m	permeant concentration in membrane
P_entr	permeability of entrance
P_esc	permeability of escape
P^*	liposome permeability
P_flat	flat membrane permeability
A	area per lipid
A_in	Area per lipid of liposome's inner layer
A_out	Area per lipid of liposome's outer layer
$\Delta G_\mathrm{transfer}$	free energy of transfer
$\Delta G_\mathrm{hydration}$	free energy of hydration
$\Delta G_\mathrm{solvation}$	free energy of solvation
R	ideal gas constant

SUMMARY

Permeability is an important property across various fields, notably in the transport of substances through cellular membranes. Membrane permeability might be affected by curvature in highly curved membranes. In the cell, numerous lipid membranes exhibit high curvature, exemplified by structures such as caveolae, mitochondrial cristae, nanotubes, membrane pearls, small liposomes, and exosomes.

Among these curved membranes, liposomes represent advanced drug delivery systems, particularly in cancer treatment. The development of pH-sensitive liposomes, employing fatty acids (FAs) as triggers for drug release in tumor tissues, is underway. However, FAs are also recognized for enhancing permeability, raising concerns regarding potential drug leakage or premature release from liposomal structures. *Thus, understanding the passive permeability of drugs through liposomal membranes becomes imperative for ensuring timely and controlled drug delivery.*

Another example of a curved membrane structure is caveolae, small invaginated membrane structures enriched with cholesterol. Previous studies have proposed that caveolae play a role in regulating cellular oxygen (O_2) levels. O_2 is vital for aerobic metabolism, powering oxidative phosphorylation in mitochondria. However, excessive O_2 can lead to the generation of reactive species, posing a threat to cellular integrity. Therefore, maintaining optimal O_2 balance entails balancing its benefits while minimizing potential harm. The precise role of caveolae in absorbing and modulating O_2 release to mitochondria remains elusive. *To address this knowledge gap, our objective is to investigate how structural features of caveolae, particularly membrane curvature, impact local O_2 levels.*

The aim of this PhD thesis is to assess how the membrane curvature and composition can affect the permeability in pH-sensitive liposomes and caveolae.

Unfortunately, the geometry of highly curved membranes creates ambiguity in the permeability value, even with an arbitrarily large factor purely based on geometry, caused by the radial flux not being a constant value in steady-state. To avoid the ambiguity in permeability for curved membranes, a new permeability definition should be provided.

Molecular dynamics (MD) simulations are a computational tool to gain insight in the transport behavior at the atomic scale. At the molecular scale, the counting method uses the number of membrane crossings in a conventional unbiased MD simulation to predict the permeability. In the case of rare events, there might be an insufficient number of crossings, and the statistics can be poor. This thesis will also investigate under which conditions the counting method has insufficient statistics.

In the introductory **Chapter 1**, an overview of key concepts such as permeability, pH-sensitive liposomes, and molecular modeling is presented. The subsequent discussion will focus on the importance of passive permeability of pH-sensitive liposomes and caveolae, showing the necessity to investigate the influence of curvature and composition on passive permeability of these systems.

Chapter 2 serves as a comprehensive guide to the simulation settings and parameters utilized in this thesis, aimed at facilitating reproducibility for fellow researchers. Additionally, this chapter provides detailed descriptions of the simulated systems and methods employed throughout our research.

In **Chapter 3**, the ambiguity in permeability for liposomes is resolved by providing a new permeability definition. The liposome permeability is defined guided by the criterion that a flat and curved membrane should have equal permeability, in case these were to be carved out from an imaginary homogeneous medium. The definition is then transferred to the counting method, which is a practical computational approach to derive permeability by counting complete membrane crossings. Finally, the usability of the approach is illustrated with MD simulations. Our new liposome permeability definition allows comparing a spherically shaped membrane with its flat counterpart, thus showcasing how the curvature effect on membrane transport may be assessed.

In **Chapter 4**, to illustrate the limitations of the counting crossing method to calculate the permeability, coarse-grained (CG) MD simulations were run for membranes with different permeant types.

In conclusion, a high permeability in itself is not an effective indicator of the sampling efficiency of the counting method, and caution should be taken for permeants whose solubility varies greatly over the simulation box. A practical consequence relevant in e.g. drug design is that a drug with high membrane permeability might get trapped by membranes, thus reducing its efficacy.

In **Chapter 5**, to investigate how curvature and lipid composition of pH-sensitive liposomes affect their passive permeability, CG MD simulations were performed. The permeability was determined with the counting method. Flat bilayers and liposomes with varying diameters and compositions were studied. The investigated permeants have different free energy profiles (solubility) across the membrane.

First, for the curvature effect, our results showed that curvature increases water permeability. However, a high curvature decreases permeability for permeants with free energy profiles that are a mix of wells and barriers in the head group region of the membrane. Importantly, the type of experimental setup is expected to play a dominant role in the permeability value, i.e. whether permeants are escaping or entering the liposomes. Second, for the composition effect, FAs increased permeability up to 55%. Cholesterol has the opposite impact on membrane permeability. Therefore, FAs and cholesterol have opposing effects on permeability, with cholesterol's effect being slightly stronger in our simulated bilayers. It can be concluded that the passive drug release from a pH-sensitive liposome does not seem to be significantly affected by the presence of FAs.

In **Chapter 6**, our focus lies on assessing how the structural characteristics of caveolae, particularly the curvature of the membrane, influence local O_2 abundance and membrane partitioning. To achieve this, we employed MD simulations to model both a flat bilayer and a liposome. Our investigation includes examining associated changes in membrane-level O_2 partition coefficients and free energy profiles. Given the inherent challenges in accurately simulating caveolae at their true size (60 to 80 nm diameter) using all-atom (AA) MD, we sought an alternative approach. Consequently, we selected a coarse-grained (CG) model for the O_2 among the Martini 3 CG beads. This choice was made after detailed assessment based on various criteria, including the bead's partitioning in oil-water and lipid membrane and diffusivity.

Conducting CG MD simulations with this new model, we simulated a curved membrane and selected CG model for O_2. A comparative analysis involving a flat bilayer and a liposome enables us to explore alterations in the O_2 free energy profile. It is noteworthy that our simulation did not include caveolae in their true size, because our primary aim is to utilize the CG model O_2 for the same system as our AA simulation of O_2, enabling us to compare the results effectively.

Finally, **Chapter 7** gives some concluding remarks on the passive permeability in pH-sensitive liposomes and the effect of curvature on O_2 partitioning in a membrane. Following the conclusion of this thesis, recommendations for future improvements in the research are provided, emphasizing the necessity for ongoing exploration in the field.

This PhD work has resulted in seven papers, six related to the thesis – published, in review, or to be submitted – and one published paper not directly related to the thesis. All publications are listed in the Appendix.

SAMENVATTING

Permeabiliteit is een belangrijke eigenschap op verschillende vlakken, vooral bij het transport van stoffen door celmembranen. De membraanpermeabiliteit kan worden beïnvloed door kromming in sterk gebogen membranen. In de cel vertonen talrijke lipidemembranen een hoge kromming, zoals bijvoorbeeld structuren zoals caveolae, mitochondriale cristae, nanobuizen, membraanparels, kleine liposomen en exosomen.

Onder deze gebogen membraanstructuren vertegenwoordigen liposomen geavanceerde medicijnafgiftesystemen, vooral bij de behandeling van kanker. De ontwikkeling van pH-gevoelige liposomen, waarbij vetzuren (FA's) worden gebruikt als triggers voor de afgifte van geneesmiddelen in tumorweefsels, is in volle gang. Er wordt echter ook erkend dat FA's de permeabiliteit vergroten, wat aanleiding geeft tot bezorgdheid over mogelijke medicijnlekkage of voortijdige afgifte in liposomale structuren. *Dus wordt het begrijpen van de passieve permeabiliteit van medicijnen door liposomale membranen absoluut noodzakelijk voor het garanderen van een tijdige en gecontroleerde medicijnafgifte.*

Een ander voorbeeld van een gebogen membraanstructuur zijn caveolae, kleine instulpingen in het membraan verrijkt met cholesterol. Eerdere studies hebben voorgesteld dat caveolae een rol spelen bij het reguleren van cellulaire zuurstofniveaus (O_2). O_2 is van vitaal belang voor het aerobe metabolisme en stimuleert oxidatieve fosforylatie in de mitochondriën. Overmatige O_2 kan echter leiden tot het ontstaan van reactieve soorten, wat een bedreiging vormt voor de cellulaire integriteit. Daarom wordt een optimaal O_2-evenwicht behouden, waarbij de voordelen in evenwicht worden gebracht en de potentiële schade wordt geminimaliseerd. De precieze rol van caveolae bij het absorberen en moduleren van de afgifte van O_2 aan de mitochondriën blijft ongrijpbaar. *Om deze kloof te dichten, is het ons doel om te onderzoeken hoe structurele kenmerken van caveolae,* *met name de membraankromming, de lokale O_2-niveaus beïnvloeden.*

Het doel van dit proefschrift is om te beoordelen hoe membraan-kromming en compositie de permeabiliteit van pH-gevoelige liposomen en caveolae kunnen beïnvloeden.

Helaas creëert de geometrie van sterk gekromde membranen dubbelzinnigheid in de permeabiliteitswaarde, zelfs met een willekeurig grote factor die puur gebaseerd is op geometrie. Dit wordt veroorzaakt doordat de radiale flux in stabiele toestand niet constante is, maar afhangt van de lokale kromming. In dit proefschrift zal dus ook de dubbelzinnigheid in de permeabiliteit voor gebogen membranen worden tegengegaan door een nieuwe permeabiliteitsdefinitie te geven.

Moleculaire-dynamica-simulaties (MD-simulaties) zijn een computationeel hulpmiddel om inzicht te krijgen in het transportgedrag op atomaire schaal. Op moleculaire schaal gebruikt de telmethode het aantal membraanovergangen in een conventionele MD-simulatie om de permeabiliteit te voorspellen. In het geval van zeldzame gebeurtenissen kan er sprake zijn van een onvoldoende aantal membraantransities en kunnen de statistieken slecht zijn. In dit proefschrift wordt ook onderzocht onder welke omstandigheden de telmethode onvoldoende statistisch is.

In het inleidende **Hoofdstuk 1** wordt een overzicht gegeven van sleutelconcepten zoals permeabiliteit, pH-gevoelige liposomen en moleculaire modellering. De daaropvolgende discussie zal zich richten op het belang van passieve permeabiliteit van pH-gevoelige liposomen en caveolae, waaruit de noodzaak voor onderzoek naar de invloed van kromming en samenstelling op passieve permeabiliteit binnen deze systemen zal blijken.

Hoofdstuk 2 dient als een uitgebreide gids voor de simulatie-instellingen en parameters die in ons onderzoek zijn gebruikt, gericht op het vergemakkelijken van de reproduceerbaarheid voor collega-onderzoekers. Daarnaast biedt dit hoofdstuk gedetailleerde beschrijvingen van de gesimuleerde systemen en methoden die in ons onderzoek zijn gebruikt.

In **Hoofdstuk 3** wordt de dubbelzinnigheid in de permeabiliteit voor liposomen opgelost door een nieuwe permeabiliteitsdefinitie te geven. Vervolgens wordt de liposoompermeabiliteit gedefinieerd op basis van het criterium dat een plat en gebogen membraan een gelijke permeabiliteit moeten hebben, voor het geval deze uit een denkbeeldig homogeen medium zouden worden gesneden. De definitie wordt vervolgens overgebracht naar de telmethode, wat een praktische computationele benadering is om de permeabiliteit af te leiden door volledige membraantransities te tellen. Tenslotte wordt de bruikbaarheid van de aanpak geïllustreerd met MD-simulaties. Onze nieuwe definitie van liposoompermeabiliteit maakt het mogelijk een bolvormig membraan te vergelijken met zijn vlakke tegenhanger, en laat daarmee zien hoe het krommingseffect op membraantransport kan worden beoordeeld.

In **Hoofdstuk 4** werd, om de beperking van het tellen van membraantransities bij de berekening van de permeabiliteit te illustreren, grofkorrelige (coarse-grained, CG) MD uitgevoerd voor membranen met verschillende soorten permeatie. De conclusie is dat een hoge permeabiliteit op zichzelf geen effectieve indicator is voor de statistische efficiëntie van de telmethode. Voorzichtigheid is vereist bij stoffen waarvan de oplosbaarheid sterk varieert in de simulatiebox. Een praktisch gevolg is bijvoorbeeld dat een geneesmiddel met een hoge membraanpermeabiliteit vast kan komen te zitten in membranen, waardoor de werkzaamheid ervan wordt verminderd.

In **Hoofdstuk 5** werden CG MD-simulaties uitgevoerd om te onderzoeken hoe de kromming en lipidensamenstelling van pH-gevoelige liposomen hun passieve permeabiliteit beïnvloeden. De permeabiliteit werd bepaald met de telmethode. Platte membranen en liposomen met verschillende diameters en samenstellingen werden bestudeerd. De onderzochte permeanten hebben verschillende vrije energieprofielen (oplosbaarheid) over het membraan.

Ten eerste lieten onze resultaten voor het krommingseffect zien dat kromming de waterpermeabiliteit verhoogt. Een hoge kromming vermindert echter de permeabiliteit voor permeanten met vrije energieprofielen die een mix zijn van putten en barrières in de hydrofiele kopgroep-regio van het membraan. Belangrijk is dat het type experimentele opstelling naar verwachting een dominante rol zal spelen in de permeabiliteitswaarde, d.w.z. of er permeanten ontsnappen of de liposomen binnendringen. Ten tweede verhoogden FA's door het samenstellingseffect de permeabiliteit tot 55%.

Cholesterol heeft het tegenovergestelde effect op de membraanpermeabiliteit. Daarom hebben FA's en cholesterol tegengestelde effecten op de permeabiliteit, waarbij het effect van cholesterol iets sterker is in onze gesimuleerde membranen. Er kan worden geconcludeerd dat de passieve geneesmiddelafgifte uit een pH-gevoelig liposoom niet significant lijkt te worden beïnvloed door de aanwezigheid van FA's.

In **Hoofdstuk 6** ligt onze focus op het beoordelen hoe de structurele kenmerken van caveolae, met name de kromming van het membraan, de lokale O_2-abundantie en -partitie binnen in het membraan beïnvloeden. Om dit te bereiken hebben we MD-simulaties gebruikt om zowel een vlak membraan als een liposoom te modelleren. Ons onderzoek omvat het onderzoeken van de geassocieerde veranderingen in O_2 verdelingscoëfficiënten en vrije energieprofielen op membraanniveau. Gezien de inherente uitdagingen bij het nauwkeurig simuleren van caveolae op hun ware grootte (60 tot 80 nm diameter) met behulp van all-atom (AA) MD, zochten we naar een alternatieve aanpak. Daarom hebben we een CG-model geselecteerd voor de O_2-molecule onder de Martini 3 CG-modellen. Deze keuze werd gemaakt na een gedetailleerde beoordeling op basis van verschillende criteria, waaronder enerzijds de verdeling van O_2 in olie-water of in een lipidemembraan en anderzijds de diffusiviteit.

Met CG MD-simulaties gebaseerd op dit nieuwe model hebben we een gebogen membraan gesimuleerd en een CG-model voor O_2 geselecteerd. Een vergelijkende analyse met een plat membraan en een liposoom stelt ons in staat veranderingen in het O_2 vrije energieprofiel te onderzoeken. Het moet opgemerkt worden dat onze simulatie geen caveolae in hun ware grootte omvatte omdat ons primaire doel is om het CG-model voor O_2 te gebruiken in hetzelfde systeem als onze referentie-AA-simulatie van O_2, zodat we de resultaten effectief kunnen vergelijken.

Tenslotte geeft **Hoofdstuk 7** enkele slotopmerkingen over de passieve permeabiliteit in pH-gevoelige liposomen en het effect van kromming op de O_2-verdeling in een membraan. Na de conclusie van dit proefschrift zullen aanbevelingen worden gedaan voor toekomstige verbeteringen in het onderzoek, waarbij de noodzaak van verdere exploratie in dit onderzoeksdomein wordt benadrukt.

Dit promotiewerk heeft geresulteerd in zeven artikelen, waarvan zes gerelateerd aan het proefschrift (gepubliceerd, in review of in te dienen) en één artikel dat niet direct verband houdt met het proefschrift. Alle publicaties zijn opgelijst in de bijlage.

I

Research overview

Chapter 1

Introduction

This introduction on lipid membrane permeability gives a thorough examination of existing research on the topic. Furthermore, this chapter will elaborate on the motivation behind selecting this topic and the specific methodology employed to calculate permeability. Finally, an overview of the thesis structure will be provided.

1.1 Background and context

1.1.1 Lipids

This section introduces three key lipids employed in the composition of the membranes discussed in this thesis, along with their respective molecular structures illustrated in Fig. 1.1.

Phospholipids

Phospholipids are a crucial component of biological membranes and play a fundamental role in cell structure and function. Structurally, they consist of a hydrophilic head group and two hydrophobic fatty acid tails, creating an amphipathic molecule [1]. This unique structure enables phospholipids to form bilayers that serve as the basic framework of cell membranes. Additionally, phospholipids are dynamic molecules, allowing for fluidity within the membrane, facilitating various cellular processes such as membrane trafficking and signaling [2]. Furthermore, phospholipids serve as a platform for the integration of membrane proteins, contributing to cell-cell communication and the regulation of cellular activities [3]. In general, phospholipids are indispensable for the structure, function, and regulation of cellular membranes and play a crucial role in maintaining cellular homeostasis.

Fatty acids

Fatty acids (FAs) are fundamental molecules in biological systems, serving as essential building blocks for various cellular components and playing crucial roles in metabolic processes [4]. Structurally, they consist of a hydrocarbon chain with a carboxyl group at one end. These hydrocarbon chains can vary in length and saturation, influencing the physical properties and biological functions of the FA. Saturated FAs lack double bonds in their hydrocarbon chains, while unsaturated FAs contain one or more double bonds, which introduce kinks and flexibility into the molecule. FAs are key components of cell membranes, where they contribute to membrane fluidity and stability [5].

Cholesterol

Cholesterol (abbreviated as Chol or CHOL) is a crucial lipid molecule found in the cell membranes of all animal tissues, playing an indispensable role in various physiological processes [6]. Structurally, cholesterol consists of a sterol nucleus composed of four fused rings, with a hydrocarbon tail and a hydroxyl group attached. While it's often associated with negative connotations due to its role in cardiovascular diseases, cholesterol is essential for the proper functioning of cells. It helps regulate membrane fluidity and permeability, ensuring structural integrity and stability [7]

1.1.2 Liposomes

Liposomes are spherical lipid-based carriers which may encapsulate drugs and reduce the drugs' unwanted side effects [8–11] (Fig. 1.2). These vesicles possess a hydrophilic exterior and an internal hydrophobic core, mimicking the basic structure of cell membranes. This unique architecture allows liposomes to encapsulate hydrophilic molecules within their aqueous core and hydrophobic compounds within their lipid bilayers, making them versatile carriers for drug delivery, gene therapy, and cosmetic applications [12]. Their biocompatibility, tunable size, and ability to protect encapsulated payloads from degradation make liposomes a promising tool in pharmaceutical research

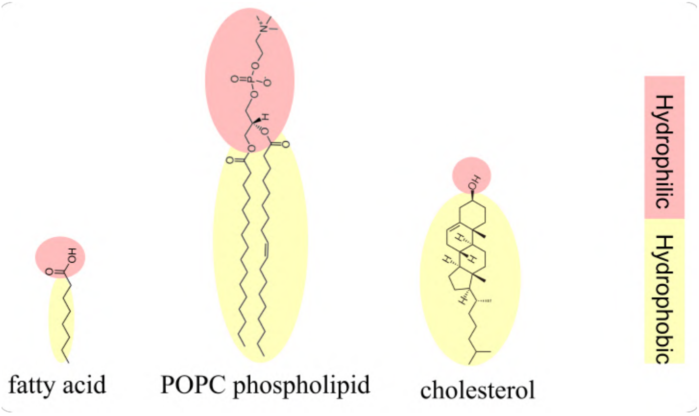

Figure 1.1: Molecular structure of a fatty acid, POPC phospholipid and cholesterol.

and development [8]. Additionally, their surface can be modified with targeting ligands to enhance specificity, enabling precise delivery to target tissues or cells [13]. With ongoing advancements in liposome engineering and formulation techniques, these nanostructures have great potential to revolutionize personalized medicine and therapeutics.

pH-sensitive liposomes

pH-sensitive liposomes are one type of liposomes with specific composition, and they are currently investigated as potential drug delivery carriers *in vitro* and *in vivo*, but not yet clinically [14]. pH-sensitive liposomes typically contain a phosphatidylethanolamine derivative and a weakly acidic amphiphile such as a FA. These carriers

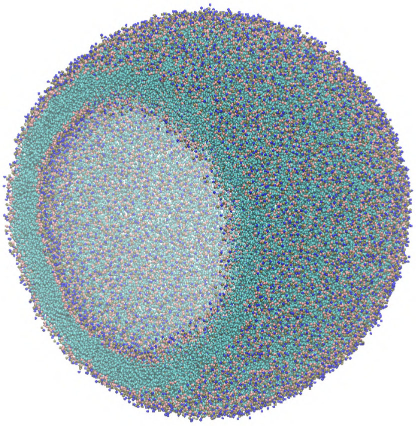

Figure 1.2: A depiction of a partially sliced liposome structure.

are designed to respond to the acidic environment of cancerous tissue by utilizing the destabilization of negatively charged groups of FAs (protonation of FAs), triggering the release of their payload [15–19].

1.1.3 Permeability

Permeability is a key property to describe the kinetics of mass transport of a substance through a membrane. It is highly relevant in various research and application fields, such as membrane technology for chemical separation, and passive permeation of substances through the cell membrane [20–25]. In biology, permeation through the cell membrane is a vital process that is relevant for drug delivery [24, 25] and the regulation of cell death and proliferation [26]. The membrane permeability affects the transport of oxygen or nutrients, while it dictates the retention time of drug molecules when liposomes are used as nanocarriers for drug delivery. Permeability is defined as the ratio of the steady-state net permeant flux J through the membrane, per time per area, and the concentration gradient Δc that is set over the membrane,

$$P = \frac{J}{\Delta c} \tag{1.1}$$

Counting crossings method

To calculate the permeability in our simulations, we will utilize the counting crossings method [27, 28]. This method determines permeability by quantifying the number of crossings through the membrane. In the case of rare events, there might be an insufficient number of crossings and statistics can be poor. To set the mind, imagine aiming for a 10% error on the number of crossings. When crossings occur independently according to a waiting time distribution of a Poisson process, at least 100 events would be needed to achieve the standard error of 10% [29]. An example of using the counting method is the diffusion of oxygen and water through phospholipid membranes [29–33].

1.1.4 Molecular Modeling

Molecular modeling is a computational technique that is used to study the structure, dynamics, and properties of molecules at the atomic level. It involves mathematical and computational algorithms to simulate the behavior of molecules based on fundamental principles of physics and chemistry. By representing molecules as collections of atoms and applying forcefields to describe their interactions, molecular modeling enables scientists to predict various molecular properties such as conformational changes, binding affinities, and reaction pathways [34]. This powerful tool finds widespread applications in drug discovery, material science, and biochemistry, allowing researchers to design novel compounds, understand molecular mechanisms, and optimize molecular structures for desired properties [35]. Molecular modeling techniques, such as molecular dynamics (MD) simulations, offer unique insights into molecular behavior, thereby facilitating the rational design of molecules with tailored functionalities [36]. A detailed description of the modeling method in this thesis will be presented in Chapter 2.

1.2 Motivation & goals of the thesis

The pH-sensitive liposomes have the potential to act as effective vehicles for drug delivery. Additionally, caveolae are another type of curved membranes of high interest: a caveola is a cholesterol-enriched invagination of the plasma membrane with the intriguing opportunity to target them for disease treatment. This led us to investigate the details of permeability mechanisms in these curved membranes in this thesis. This section gives a detailed rationale for why these two systems were chosen for exploration (see Fig. 1.3 for a general description of the research questions).

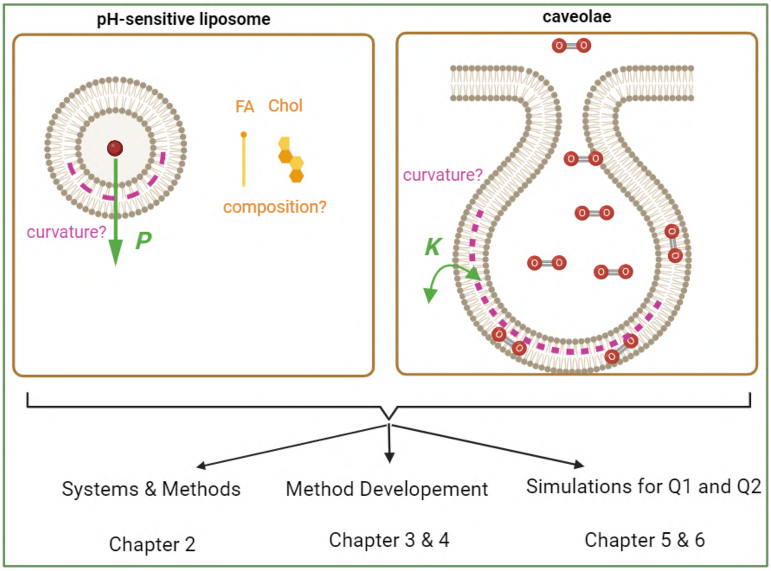

Figure 1.3: left: gray lipids represent DPPC. Right: gray lipids represent POPC. FA, Chol, *P* and *K* refer to fatty acid, cholesterol, permeability and partition coefficient, respectively.

1.2.1 Passive permeability in pH-sensitive liposomes

Liposomes have been used to facilitate the delivery of drugs to therapeutic targets in the body and to improve their therapeutic efficiency [37]. Physical parameters such as bilayer composition and membrane curvature can significantly affect liposome stability [38–41]. Among liposomes, pH-sensitive liposomes release the drug within the cancerous environment through a mechanism involving the protonation of FAs, leading to the disruption of the liposomal structure. However, FAs are also known as so-called permeability enhancers, as they increase the permeability by disrupting the membrane structure [42–44]. An important question is whether FAs can cause drug leakage and premature drug release from these FA containing liposomes. Such an untimely drug delivery would make the pH-sensitive liposomes less efficient. Therefore, the rate at which drugs permeate through the curved bilayers is a crucial parameter in the design of pH-sensitive liposomes as targeted drug delivery systems. Hence, the central question (Q1) that arises is: *what is the relationship between lipid composition, curvature, and passive permeability in pH-sensitive liposomes*?

1.2.2 The role of caveolae on oxygen buffering

Caveolae have captured our attention, motivating us to focus on understanding how membrane curvature and composition impact their permeability. Caveolae have been proposed to function as "oxygen (O_2) capacitors" or storage sites, helping to regulate and buffer oxygen levels, to optimize cellular metabolic function and promote stress adaptation [45]. Buffering O_2 levels inside the cell is crucial due to the toxic effect of it in high concentration[46, 47]. This molecule is necessary for the metabolic machinery of a living cell by fueling oxidative phosphorylation in the cellular energy generation process [46, 47]. However, at high concentrations, it can generate reactive species that cause cellular damage [48]. It is suggested that during evolution, the response to this paradox was to create cholesterol inside the membrane to control the concentration of O_2 that is inside the cell and minimize its toxicity [49]. Caveolin, a scaffold protein, plays an important role in controlling O_2 concentration by regulating caveolae [50, 51]. With aging, the expression of the caveolin protein decreases in some organs and may be associated with increased O_2 toxicity and related disease [52]. Manipulation of caveolin protein levels within cells has therapeutic potential for the treatment of O_2 related disorders such as cardiovascular diseases, cancer, and aging. However, the role of caveolin in the plasma membrane and the mechanism by which it regulates O_2 levels in cells are not yet clear. Once more, the question (Q2) that emerges is: *what precisely is the correlation between caveolae's structural attributes, including lipid composition and curvature, and the partitioning of O_2 in the cell membrane?*

In both pH-sensitive liposomes and caveolae, the impact of membrane composition and curvature on their permeability remains unclear, necessitating further detailed investigations at the molecular levels.

1.3 RATIONALE FOR THE METHODOLOGY

Numerous experimental studies have been carried out to provide the information on the permeation through the cell membrane during the past decade [53–59]. However, these methods are either expensive or not informative enough, as they are usually unable to provide data on a molecular level. For instance, measuring O_2 distributions across the cell remains a major challenge for experiments, where the spatial resolution is not on par with the sub-nanometer size of the O_2 molecule itself. On the other hand, computational simulations have been shown to give more insight into permeation at the atomic scale [28, 60, 61].

Different simulation methods have been applied to calculate permeability, many of which rely on enhanced sampling methods [62–64] and the inhomogeneous solubility diffusion (ISD) model based on the Smoluchowski equation [29, 30, 65–70]. In the ISD model, the permeability P is expressed in terms of a local diffusivity and free energy gradients [65]. However, a limitation of this approach is that it is generally not clear *a priori* to what degree and in which situation the diffusive hypothesis is valid for the system under study. Moreover, accessing permeability in this model can be challenging with respect to simulation setup and Bayesian analysis (BA) [71]. As an example, theoretically, high accuracy in calculating O2 permeability is possible through quantum mechanical calculations. However, in practice, the computational costs associated with such calculations are prohibitively expensive. Instead, a much cheaper classical AA model has been successfully used to investigate O_2 transport through membranes.

Among classical simulation methods, MD can lay open more details on the kinetics of the process, the property that experiments often cannot provide directly, under the condition that a proper force-field for the molecular interactions is available [64]. As an example, MD made it more feasible to examine O_2 transport at the molecular scale, such as the permeation through the phospholipid bilayers [30, 72–76]. Furthermore, various studies have explored the impact of cholesterol on O_2 permeability through MD simulations of AA, with notable contributions from Pias et al. [77–80]. Using AA MD, Pias et al. have analyzed the pathway by which O_2 travels through cells and tissues [81, 82]. Furthermore, their investigations have been extended to the examination of how protein integration into membranes influences O_2 permeability [83]. Moreover, to shed light on the effect of caveolae's role on O_2 buffering, Davoudi et al. has explored the effect of membrane curvature on O_2 partitioning through lipid membranes, employing AA MD [84, 85]. Other researchers have also examined the diffusion of O_2 in a lipid membrane using AA MD simulations [73, 86, 87]. Their investigations have focused on elucidating the impact of lipid chain saturation and temperature on O_2 diffusion through the lipid membrane, its diffusion pathways, and the time and length of its diffusion.

1.4 Content of the thesis

In this thesis, our primary aim is to evaluate permeability in curved membranes of pH-sensitive liposomes and caveolae and explore the influence of membrane curvature and composition on this property. Initially, in Chapter 3, we derived the permeability equation for curved membranes in the radial direction, drawing from Smoluchowski's equation. Given our objective to also employ the counting crossings method to calculate curved membranes permeability, we adapted the derived equation in the radial direction for this specific method in this chapter.

Subsequently, we assessed the efficiency of the counting crossings method for different types of permeants [27, 28]. To achieve this, we utilized the coarse-grained MD (CG MD) method, conducting simulations to analyze the permeation of few distinct permeants with different free energy profiles through a flat bilayer in Chapter 4. Notably, we applied the counting method tailored for flat membranes in this chapter.

Finally, we conducted a comprehensive examination of the derived equation for curved membranes within two systems of pH-sensitive liposomes and caveolae in Chapter 5 and Chapter 6, presenting a detailed array of results. Additionally, we have introduced a new model for O_2 to enable more precise simulations of caveolae at their exact size in the upcoming research. Chapter 7 will offer a comprehensive summary of the results obtained.

In the following sections, an extensive review of previous research works pertaining to different parts of this study will be conducted. This thorough review aims to help us understand the history and progress in the field, which will build a strong basis for our current research. Each section will also outline the steps taken to achieve the main aim of this thesis, which is evaluating permeability in curved membranes.

1.4.1 Curved membrane permeability

As the primary objective of this research is to explore the impact of membrane curvature on the permeability, it is essential to establish a clear definition of permeability for curved membranes. In the past decade, the role of curved membranes has received increased attention, given their fascinating presence in the cell. Biologically, membranes occur in highly curved shapes, for instance in the crystae of the inner mitochondrial membrane, or the caveolae, which are membrane invaginations in healthy, young cells [50, 88]. Other membrane structures with high curvature are the rod-like shaped membrane nanotubes (radius 10-100 nm) [89, 90], and the spherically shaped membrane pearls [91], exosomes (radius 15-50 nm), or small liposomes.

Traditionally, flat membranes have been simulated, as they present a decent approximation of membranes with low curvature. Consider for instance a larger liposome or extracellular particle with diameter 1 μm. When the simulation box encompasses a patch of membrane of about 5 nm by 5 nm in area while the membrane thickness is roughly ±5 nm, then the membrane curvature would be barely noticeable. Simulating flat membranes is moreover straightforward to implement with standard periodic boundary conditions, allowing to limit the unit cell dimensions to reasonably small values. In contrast, the cell dimensions and hence the computational load are challenged for curved membranes, as the unit cell has to encompass the whole curved structure. Nevertheless, in recent years, a lot of progress was made in computational tools. Yesylevskyy et al. designed simulations of curved membrane patches [92, 93]. Boyd et al. created the BumPy code to generate curved membrane simulation boxes of various shape, such as cylinders and half-spheres [94]. Code implementations, computational resources, and CG approaches have evolved to the point of studying systems with tens of thousands to even millions of particles for multiple microseconds, for instance whole spherical virus particles [95, 96]. Marrink and coworkers have gradually worked on computational tools to simulate realistic membrane compositions in realistic geometries [97–99]. With all of these developments, studying curved membranes has nowadays become feasible.

However, defining permeability in curved membrane is still a challenge. At the atomic scale, permeability can be measured with several methodologies using MD simulations. In the counting method, the number of membrane crossings observed in an equilibrium simulation is converted to the permeability [27, 28, 32, 100]. In the ISD methodology [66], free energy and diffusion profiles in the Smoluchowski equation are fit on short MD trajectories, using Bayesian analysis or a minimum likelihood estimate [28–31, 71, 101]. In the path sampling methodology, rare events are sampled by sampling path ensembles that focus on the more successful permeating trajectories. The permeability calculation was first derived for milestoning [63, 102] with some diffusive approximations, and more recently, it was included in an exact way in the replica exchange transition interface sampling (RETIS) method [103–105]. These methods have been developed and are used for flat membranes. However, for a curved membrane simulation of e.g. a liposome, the permeability definition needs to be revisited. The flux J is a quantity that is expressed *per area*, and for a spherical liposome, this area $4\pi r^2$ clearly depends on the radial distance r from the liposome center. As we will show in Chapter 3, this makes the radial flux J inherently r-dependent, and the permeability is ill-defined. This part of the research will therefore provide a definition of the permeability of spherically curved membranes. The criterion for our definition is that it should be possible to compare permeability between flat and curved membranes. Hence, the definition allows us to assess the curvature effect on permeability.

Chapter 3 includes the revision of the Smoluchowski equation, which assumes that transport is fully diffusive (without memory), and which can be solved analytically. Based on the analytical derivations, the new permeability definition for curved membranes is presented, which is no longer r-dependent. Using this definition, the counting method is also revised for curved membranes. In this chapter, a flat and spherically shaped dipalmitoylphosphatidylcholine (DPPC) membrane with or without cholesterol are simulated with CG MD, and their water permeability is effectively compared using the new permeability definition.

1.4.2 Counting crossings limitations

As the counting crossings method will be employed to calculate permeability, identifying its limitations will be instrumental in enhancing our understanding of the obtained results. To do this, the number of crossings expected in a simulation will be investigated as a function of the simulation properties. Several properties are dictated by the simulation setup, such as the number of permeants and box dimensions. A straightforward way to improve the sampling of the unit cell is to increase the system size. When the cross-section doubles and the total number of permeants doubles, then the concentration in the solvent phase will remain unaltered, while the number of crossings would double. There are unfortunately limits to this approach because the computational cost increases faster than linearly with the box size, and in comparison, it would be more efficient to double the simulation time T_{sim}. Another approach could be to insert more permeants without altering the simulation box size, meaning that all concentrations – both solvent and membrane – increase. One should be wary of clustering of the permeants, however, and the permeability might become concentration dependent. For instance, O_2 showed no clustering for O_2 concentrations about 10-fold higher than the O_2 solubility in water, while ethanol permeation through POPC membranes differs substantially between low and high concentrations [30, 71, 106].

Other properties are inherent to the chosen membrane, solvent, and permeants. This research considers the permeant's solubility (or equivalently, partitioning coefficient K) and the membrane thickness h_m. It is well known that the membrane forms a high free energy barrier when a permeant is nearly insoluble in the membrane, and the associated low permeability prevents good sampling of the unit cell. It will be shown in Chapter 4 that a high permeability, for permeants that are highly soluble in the membrane, is another cause for poor sampling. In contrast to low permeability, a high permeability membrane is often regarded as a membrane where the flux is not rate-limiting, but we will show that high permeability cannot guarantee good sampling of the simulation box either.

The membrane thickness follows from the self-aggregation of the phospholipid molecules in the bilayer. It is less discussed in permeability literature than the partitioning coefficient. Still, using the simplified Overton's model $P = KD/h_m$, where D is the diffusion constant, it is clearly of equal importance as the partitioning coefficient [107]. The membrane thickness is however ill-defined, since there is no unique answer as to where an atom ends and another atom begins, and moreover membranes exhibit thermal undulations with lipid protrusions. In experimental work, a roughly estimated membrane thickness is used to estimate the permeability [55, 108]. In simulation work, it is often derived in relation to the plane of the phosphate groups [71]. Hence, another aim of this research is to showcase the sensitivity of the permeability to the considered thickness. Therefore, in addition to the membrane thickness, the thickness of 2 additional water layers will be treated as an extra parameter in the discussion. Moreover, this parameter allows us to discuss the overall sampling efficiency. When the limit of the water layer thickness is taken to cover the whole simulation box, then the associated number of crossings represents crossings through the whole simulation box.

Chapter 4 will use the ISD model to derive a theoretical expression of how the counting method is affected by the solubility of permeants in the membrane. It will also discuss the dependencies and limiting cases for the derived equation. It is shown, under which conditions, membrane crossings can be considered as a rare event. A composition rule for the flux is derived as well. The number of crossings of 16 different permeants through a DPPC bilayer, as well as the effect of permeant type on the efficiency of counting crossings, will be shown in this chapter.

1.4.3 Membrane permeability: curvature and composition effect

Upon deriving the permeability equation for curved membranes, we will apply this equation to investigate the membrane permeability in two systems: pH-sensitive liposomes and caveolae. This investigation aims to discern the influence of membrane curvature and composition on permeability in these systems.

Investigating pH-sensitive liposome

Several groups have applied different methods and models to calculate drug permeability through liposomes [109–112]. For instance, Winter et al. simulated arsenic trioxide permeation in a thermosensitive liposome using CG MD simulations and calculated the permeability of a DPPC membrane containing a permeation enhancing lysolipid [111]. Here, we will use MD simulations to estimate the permeability rate through liposome membranes containing FAs, as these are relevant for the pH sensitive liposomes. The membranes will have a varying composition and curvature, where the possible dissociation of the FAs will also be taken into account.

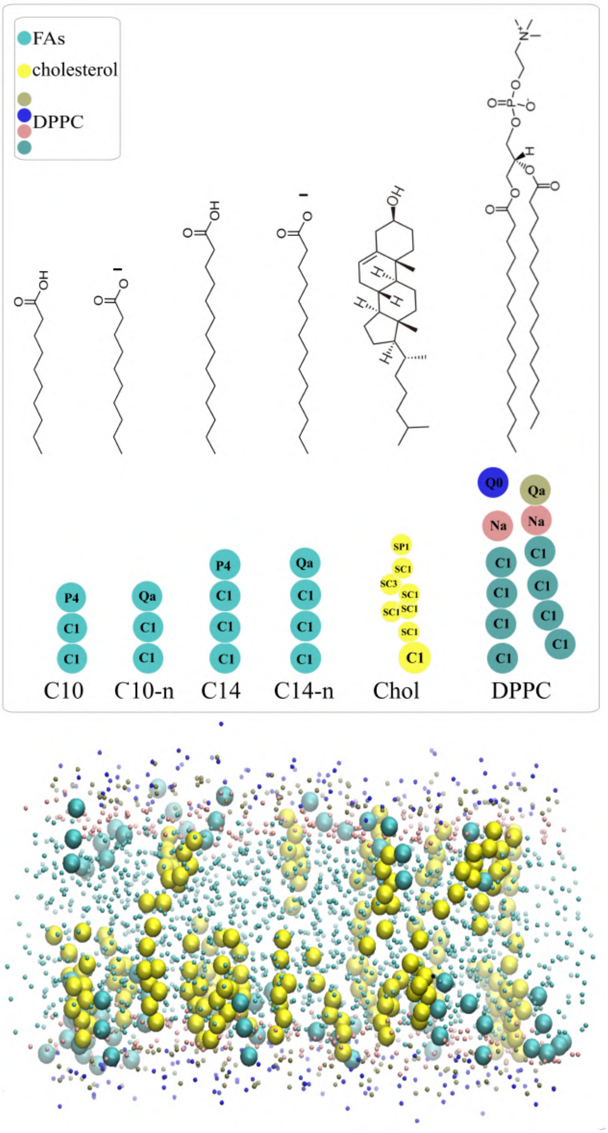

Figure 1.4: Top: Structural formula and corresponding CG structure of the various lipid types (FAs, cholesterol, phospholipids) in the simulations. Suffix -n refers to deprotonated FAs. Bottom: Example of a flat membrane containing DPPC, FAs, and cholesterol. Light green beads are FAs; yellow beads are cholesterol. DPPC is presented by points, colored by bead type: green for hydrocarbons, pink for glycerol, brown for phosphate, and blue for choline bead type. Water and ions not shown.

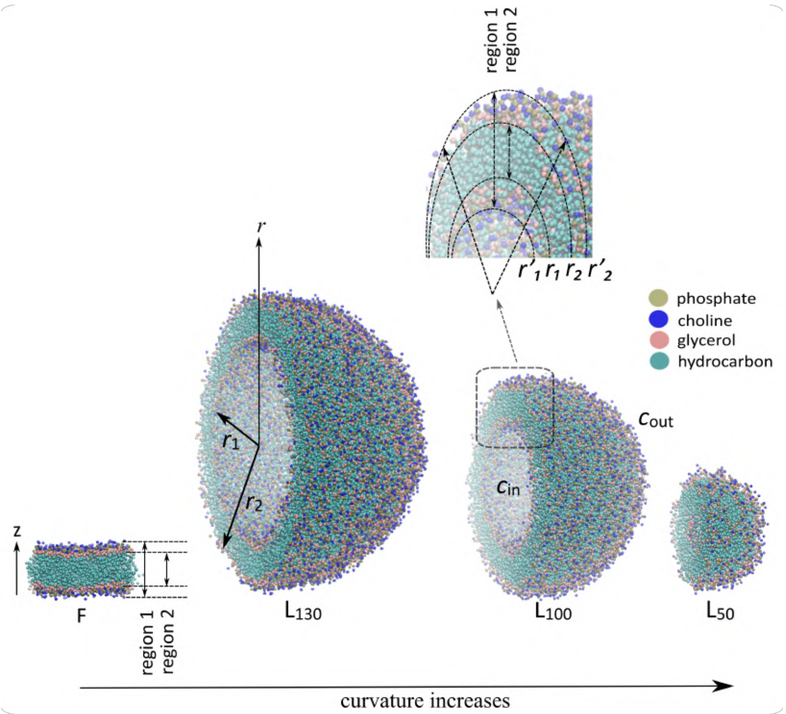

Figure 1.5: Systems with pure DPPC. From left to right, the curvature of the membrane increases. DPPC is presented by points, colored by bead type: green for hydrocarbons, pink for glycerol, brown for phosphate, and blue for choline bead type. Water and ions not shown. Region 1 and region 2 are depicted in both a flat bilayer and a liposome. To enhance the clarity of the distinct radius definitions, a segment of the central liposome has been excised and magnified, positioned at the upper portion of the figure. L_{50}, L_{100} and L_{130} refer the liposomes with the radius of 50 Å , 100Å and 130Å. F refers to flat bilayer.

Effect of membrane lipid composition on the membrane permeability. To assess the effect of membrane composition on the permeation rate, a wide range of studies has been done [113–120]. Among them, cholesterol has been proven to decrease the permeability of the permeants by decreasing the membrane fluidity caused by an unsaturated tail [120]. Using MD simulations, other groups have concluded that the alteration in the permeability in the presence of cholesterol is due to the gradual reduction in the permeant's solubility in the lipid section of the membrane and enhancement in its center [77, 121]. Falck et al. also found that the reduction in the membrane permeability by the presence of cholesterol is due to the decrease in the membrane's free volume [122].

The effect of FAs in lipid mix has also been investigated. In contrast to cholesterol, saturated FAs like capric acid (C10) have been shown experimentally to increase the permeability of 1-palmitoyl-2-oleoyl-phosphatidylcholine (POPC) membrane by measuring the liposome leakage of a fluorescent dye upon exposure to C10 or the permeability of [^{14}C]-mannitol through Caco-2 monolayers [43, 44]. Another study, using experimental methods, found that the FA-induced calcein leakage through DPPC liposomes increases with the length of incorporated saturated FAs, C8 to C20, except for C8 [42]. They also reported that the effect of C10 on calcein's release rate from liposomes is almost negligible compared to myristic acid (C14). Moreover, liposomes containing oleic acid (C18) were evaluated for drug delivery and their ability to encapsulate and release the model drugs [123], and the permeability increase of the FA was attributed to the presence of the relatively highly soluble single-chain amphiphiles (FAs) rather than the two chains of the POPC phospholipids. In other studies, FAs were confirmed for their effect as permeability enhancers in the intestine [43, 44, 124, 125], where it is also seen that C10 acts differently *in vivo* on the intestine permeability at low and high concentration [124]. The most reported mechanism by different groups is that these FAs fluidize and perturb the membrane and as a result, intracellular signaling changes and leads to the alteration in intestinal tight junction expression [124, 126].

Effect of fatty acid's dissociation constant on the membrane permeability. A particular aspect of a fatty acid is its possible dissociation. A FA molecule can dissociate from its protonated (neutral) state into its deprotonated (negatively charged) state, depending on the FA's dissociation constant, which differs between the membrane and the water phase. Consequently, when the pH changes, the partitioning of the FA between water phase, membrane phase, and its neutral or deprotonated form can shift [127]. Different research groups estimated FA dissociation constants in different lipid membranes using MD simulations [127–129], and a detailed MD study showed the change in FA mobility depending on the charge and chain length [130]. However, previous simulation studies do not explicitly evaluate the permeability at the molecular level for both neutral and deprotonated FAs, thus disregarding the effect of pH and the dissociation constants altogether. Therefore, here, we will measure the effect on the permeability for both neutral and deprotonated FAs in liposomes.

Effect of membrane curvature on the membrane permeability. Curvature is another parameter that can affect the membrane's permeability [131]. Risselada and Marrink measured the structural properties such as the lipid packing and the lipid order parameter, and their findings suggest that curvature causes the membrane to become thinner and disrupts the packing of the leaflets [132]. Yesylevskyy et al. simulated a series of curved membrane patches and showed that the curvature decreases the order parameter and increases the APL, as computed with a Voronoi technique [92]. As for the permeability of curved membranes, Winter et al. simulated a whole liposome, consisting of a phospholipid bilayer containing a lysolipid, as mentioned above. The permeability was calculated to assess the effect of temperature on the dynamical properties, and they found that the permeability is the highest when the membrane goes through a phase transition from gel to liquid in the presence of lysolipid [133]. Yesylevskyy et al. also measured the permeability in the curved membrane patches and studied the liposome's interaction with a loaded drug, where the curvature was found to increase the permeability for small solute like ions, water and also bigger ones such as anti-cancer drugs [93]. However, the mixed effect of the curvature and the FAs on the membrane's permeation rate is still unknown at the molecular scale, despite its importance for the understanding and design of drug delivery systems.

In Chapter 5, we will use CG MD to simulate different systems consisting of liposomes and flat bilayers. To assess the effect of composition and the curvature, permeability through liposomes with different lipid types (Fig. 1.4) and sizes (Fig. 1.5) will be compared to the permeability of flat bilayers with similar composition. Both neutral and deprotonated FAs will be simulated to have a comprehensive view of their effect. To quantify the permeability, the counting crossings method will be applied, which involves tallying the number of crossings that the permeants make through the membrane. Besides the permeability, structural properties of the flat bilayers and liposomes will also be measured, such as APL and membrane thickness. The simulation analysis for this section will be presented in Chapter 5.

Investigating caveolae

AA O_2 partitioning through a curved membrane. We used AA MD simulations to investigate how a key structural aspect of caveolae, i.e. membrane curvature, may affect oxygen partitioning into the membrane. Two DPPC bilayers with different curvature are simulated at the atomic scale: a flat bilayer with zero curvature and a curved bilayer forming a spherical particle (liposome) with very high curvature. The simulations results will be presented in Chapter 6.

The results feature partition coefficient and free energy profiles for O_2, spanning the membrane. However, it is worth noting that in this context, the membrane size doesn't align with the dimensions of caveolae (60 to 80 nm in diameter). When dealing with larger simulations comprising millions of atoms, like a caveolae in true size, the computational burden and time required for AA simulations can become prohibitive.

CG O_2 model. To address the challenge with AA simulation of caveolae, employing lower-resolution forcefields such as the CG Martini offers a practical solution. In the Martini model, atoms are grouped together into beads, thereby reducing the computational complexity. The Martini model is a widely used CG general purpose forcefield, employed in a range of applications, including assessments of oil/water distribution, gas model for nanobubble and the examination of complex interactions among proteins, lipids, and diverse materials like ionic liquids and aedamers [134]. For instance, a newly parameterized CG Martini gas model for nitrogen (N_2) molecule enables simulations of larger systems containing N_2 [135].

A CG O_2 model was, however, still lacking. Therefore, in this part, we aim to develop a CG O_2 model, where the two atoms of molecular O_2 are lumped together into a single bead. The interactions of this bead with the other lipid molecules and with water are responsible for the partitioning, and potential buffering, of O_2. Moreover, this bead's interaction with amino acids leads to its binding preference to hydrophobic cavities of proteins instead of hydrophilic ones. In Chapter 6, the proposed CG bead with its interactions will therefore be evaluated by testing a set of criteria, such as the partitioning in oil-water and in membranes and the diffusivity. The CG Martini model for O_2 facilitates diverse simulations of biosystems and O_2 at the CG level, significantly reducing computational expenses for larger systems. It will enable us to go beyond the modeling of flat membranes, and the simulation box may even encompass curved membrane and liposomes [136]. This will be extremely valuable for gaining insight in the dynamics of O_2 buffering in caveolae, requiring a large simulation box to capture the complex membrane structure.

CG O_2 partitioning through a curved membrane. Subsequently, this new O_2 model will be used to test the effect of membrane curvature on O_2 partitioning, and the results are presented in Section 6.3. It is worth noting that the curved membrane in this simulation still does not match the size of caveolae. This simulation serves as an

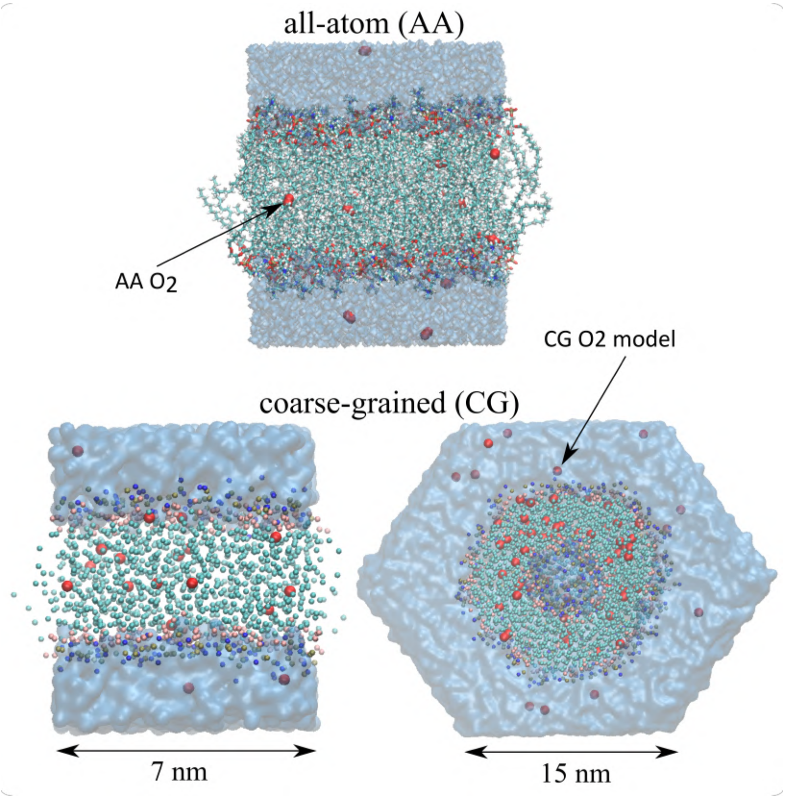

Figure 1.6: AA description of a flat membrane and CG description of flat membrane (left) and liposome (right). Notice the difference in scale for the liposome. O_2 (red) is indicated with an arrow in both descriptions. For CG systems: POPC is presented by points, color-coded by bead type: green for hydrocarbons, pink for glycerol, brown for phosphate, and blue for choline beads. For AA system: the same color scheme is applied, except the glycerol group is red. Water is depicted as transparent light blue. To maintain clarity, ions are not displayed in the visualization.

illustration of the system utilizing CG O_2, allowing for a comparison with the previous simulation employing AA O_2. In this section, a box containing a flat membrane composed of POPC and a number of O_2 molecules is simulated as shown in Fig. 1.6. This membrane with zero curvature serves as the benchmark. In addition, a liposome with non-zero membrane curvature is modelled to observe the effect of curvature. This approach allows us to examine associated changes in the O_2 concentration across the membrane. With this comparison, we aim to deepen our understanding of the underlying mechanisms governing O_2 homeostasis. Future steps will focus on simulating caveolae at their true size, ranging between 60-80 nm in diameter. Additionally, the caveolin protein will be incorporated into the membrane to bring the simulations closer to realistic caveolae. This deeper understanding has the potential to unlock insights into O_2-related disorders, potentially catalyzing new avenues of research aimed at treating these conditions.

CHAPTER 2

SIMULATIONS SETTINGS

This chapter provides a comprehensive overview of the methods utilized for our simulations, along with the simulation parameters applied to all systems analyzed in this study, enabling the reproducibility of the data. It starts by outlining the simulation setting used to illustrate the counting crossings method limitations. Subsequently, it provides the simulation settings for both pH-sensitive liposome and caveolae simulations.

2.1 COARSE-GRAINED (CG) MARTINI FORCEFIELD

In this thesis, we will utilize coarse-grained (CG) Martini to simulate the majority of the systems. An example of the CG representation of phospholipids, fatty acids, and cholesterol is shown in Fig. 1.4. The CG Martini represents a significant advancement in MD simulations, particularly in the study of complex biological systems and soft matter [134]. Developed by Marrink and co-workers, this innovative approach simplifies atomistic models into larger particles, thereby reducing computational costs while retaining essential structural and dynamic properties. By grouping atoms into CG beads, Martini captures the overall behavior of biomolecules and lipid bilayers with remarkable accuracy. Its versatility extends to diverse biological processes, including protein folding, membrane dynamics, and protein-lipid interactions. Martini's CG representation facilitates longer simulation timescales, enabling researchers to explore phenomena such as self-assembly and phase transitions inaccessible to traditional atomistic simulations. This forcefield continues to evolve, providing a powerful tool for understanding complex biological systems at the mesoscale.

2.2 Counting crossings limitations

To illustrate the discussion of the counting methods limitations, a membrane of DPPC was simulated at the molecular scale using a CG model in Chapter 4. A range of different permeants was considered with both positive ΔF (barrier) and negative ΔF (well) (Fig. 4.1): the 16 bead types of the Martini CG model were used as the permeating molecule. These beads span a wide range of free energy profiles $F(z)$ across the membrane.

Simulation details

Using Gromacs-2019.3 package, simulations were performed on sixteen systems consisting of a phospholipid membrane, CG beads and water [137]. Each system contained twenty permeant beads of one specific CG type, and it was solvated in 2000 water molecules. The membrane consists of 128 DPPC lipid molecules in each simulation, and its initial coordinates were taken from the Martini website [138]. The topology file and initial coordinates of the permeant beads were created manually. The Martini forcefield was used in all systems, mapping atoms of each phospholipid molecule and water molecule into 12 and 1 bead, respectively [139].

Regular Martini Water beads were used to model water [140]. The reaction-field approach was used to calculate the Coulombic interactions [141]. Both the Coulombic and the van der Waals interactions were truncated at 1.1 nm, with the potentials shifted to zero at the cutoff using the potential modifiers. The neighbor list length is 1.4 nm, updated using the Verlet neighbor search algorithm. With a time step of 30 fs, the leapfrog integrator was used to integrate the equations of motion. A temperature of 320 K was considered for the simulated systems by coupling of velocity rescale thermostats, with coupling constant set to 1.0 ps. At every time step, the center of mass motion of the system was removed, and periodic boundary conditions were applied in all directions (x, y, z). A Parrinello-Rahman barostat was employed to subject the box vectors to semi-isotropic pressure, using a reference pressure of 1 bar, a coupling parameter of 12 ps and an isothermal compressibility of 3×10^{-4} bar^{-1}. After adding the permeants, an energy minimization was performed. Next, two equilibrations were performed: NVT simulation of 30 ns and NPT simulation of 30 ns. The production run was 270 ns of NPT simulation for each system. Coordinates were stored every 3 ps resulting in 90 000 snapshots in total for each system.

The number of membrane crossings was determined with the Rickflow package code using dividing surfaces at $|z| = h_m/2 = 2.3\,\mathrm{nm}$ [71]. The diffusion tensor with diagonal elements D_{xx}, D_{yy}, D_{zz} was computed with Gromacs.

2.3 INVESTIGATING PH-SENSITIVE LIPOSOMES

In Chapter 5, the effect of membrane curvature and composition was investigated in the system of pH-sensitive liposomes using the defined equation for liposome permeability from the counting methods in Chapter 3. In this section, the simulation systems and settings are presented.

2.3.1 Selection of systems

MD simulations were run for 34 systems containing a flat bilayer (label F in name) and 28 systems containing a liposome (label L in name) with various lipid compositions. The sizes of the liposomes (Fig. 1.5) were chosen to be approximately 50 Å, 100 Å, and 130 Å to be able to assess the curvature effect on the permeability while avoiding a very large system with a limit for the simulation time. Liposomes in drug delivery experiments are often larger and will exhibit hence less curvature effects. We chose to investigate highly curved membranes to make the curvature effect as prominent as possible. Coarse-graining was applied to reduce the computational cost of the simulations by mapping every few atoms of every molecule to one bead [142, 143]. All simulated systems were composed of a membrane, 20 CG beads as permeants, water, and 0.15 M sodium chloride. Various compositions of six lipid types (Fig. 1.4) were included to examine their effect on the permeability: DPPC, cholesterol (Ch, Chol), capric acid (C10), myristic acid (C14), deprotonated capric acid (C10-n), and deprotonated myristic acid (C14-n). DPPC was chosen as phosphatidylcholines are the most frequently used phospholipid in liposome preparation [144]. The deprotonated FAs (suffix ‘-n’ refers to negative charge) were simulated to investigate the effect of the FAs’ dissociation. While recently a titratable Martini forcefield was developed, which would allow the simulation to run at constant pH, the accuracy of the pKa for the FAs is still uncertain for these coarse-grained beads [145]. Therefore, the FAs in a system are either all neutral or all deprotonated.

Based on a study of the sampling efficiency of the counting crossings method, we selected two CG beads: N0 with more outspoken free energy wells in the head group region, and Na with a higher barrier at the membrane center (Fig. 2.1) [100]. They were chosen to assess the effect of different free energy profiles on the permeability. N0 and Na are CG beads of the Martini forcefield, with intermediate polar character, a radius of 0.23 nm, zero charge, and a mass of 72 amu. The beads do not correspond to a specific molecular structure, but they can match several chemical compounds. Na is more polar and a hydrogen acceptor, and in combination with the free energy well and higher barrier, it bears resemblance to molecules such as ester, ether, and ethyl methyl ether. N is less polar and not a strong hydrogen acceptor nor hydrogen donor, and it shares similarities with e.g. trimethylamine. The first series of simulations were 12 flat bilayers (Table 2.1) with the 20 N0 permeants and neutral FAs. Similarly, the second series of 12 flat bilayers was done with the 20 Na permeants. The third series of 10 flat bilayers was again done with the N0 permeants, but all FAs were deprotonated. The detailed description of the last two series is provided in the Supporting Information (SI).

For the liposomes, a first series of 11 systems (Table 2.2) contained N0 permeants and neutral FAs. All liposomes have a radius of approximately 50 Å, except for the L_{100} system and L_{130} system. The second series of 11 systems contained Na permeants. The third series of 6 liposomes contained the N0 permeants, but all FAs were deprotonated. The detailed description of the last two series is outlined in the SI of Paper 4 (pages: 2-4) in Part 7.2. The lipid composition varied from 100% DPPC down to 60% DPPC. Composition and membrane thickness h of all 62 systems can be found in Table 2.1, Table 2.2, and SI of Paper 4 (pages: 2-4) in Part 7.2.

An important aspect is whether the membrane is in the liquid disordered (L_α, L_d) phase or in a gel (L_β) or liquid ordered phase (L_o). A phase transition can drastically change the area per lipid and other structural and dynamical properties of the membrane, thus likely affecting the permeability as well. This will be discussed when assessing the structural parameters in the Results section in Chapter 4.

2.3.2 Computational details

The same protocol as our recent paper was followed in this work [136]. The systems were simulated using Gromacs-2021.4 [146].

	system name	lipid types	lipid composition (%)	# of lipids	# of water CG beads	# of ions	h (Å)
1	F	DPPC	100	256	2504	29	40.2
2	F-5C10	DPPC:C10	95:5	280	2753	32	40.1
3	F-10C10		90:10	260	2575	30	39.9
4	F-20C10		80:20	250	2491	30	39.3
5	F-30C10		70:30	260	2640	32	38.7
6	F-5C14	DPPC:C14	95:5	280	2753	32	40.1
7	F-10C14		90:10	260	2575	30	40.1
8	F-20C14		80:20	250	2491	30	39.8
9	F-30C14		70:30	260	2640	32	39.3
10	F-10Ch	DPPC:Chol	90:10	260	2452	28	41.2
11	F-10Ch-10C10	DPPC:Chol:C10	80:10:10	260	2498	29	41.0
12	F-10Ch-10C14	DPPC:Chol:C14	80:10:10	260	2498	29	40.9

Table 2.1: Detailed description of simulated systems containing a flat bilayer (F). Each system contained 20 N0 permeants. FAs (C10 and C14) are neutral. h is the membrane thickness between PO4 beads (region 2, see Section 2.3.3). The number of ions column refers to both the number of Na^+ ions and the number of Cl^- ions. Details of other flat bilayer systems can be found in the SI of Paper 4 in Part 7.2

	system name	lipid types	lipid comp. (%)	# of lipids		# of water CG beads	# of ions	r_1 (Å)	r_2 (Å)	h (Å)	A^* (Å^2)
				in	out						
1	L_{50}	DPPC	100	124	394	54507	603	20.7	56.3	35.6	66.3
2	L_{100}	DPPC	100	1097	1784	185289	2064	67.7	106.4	38.7	64.6
3	L_{130}	DPPC	100	2092	2992	317684	3555	96.1	135.0	38.9	65.0
4	L-10C10	DPPC:C10	90:10	113	398	76779	842	19.3	54.6	35.3	62.0
5	L-10C14	DPPC:C14	90:10	124	387	76779	842	19.6	54.8	35.2	62.2
6	L-10Ch	DPPC:Chol	90:10	145	400	76608	842	21.0	56.3	35.3	60.8
7	L-20Ch		80:20	123	451	76600	842	21.1	55.3	34.2	61.3
8	L-10Ch-10C10	DPPC:Chol:C10	80:10:10	142	396	76730	842	18.6	54.2	35.6	53.6
9	L-20Ch-20C10		60:20:20	144	418	78207	842	17.1	52.1	35.0	45.3
10	L-10Ch-10C14	DPPC:Chol:C14	80:10:10	147	391	76730	842	19.0	54.4	35.4	53.1
11	L-20Ch-20C14		60:20:20	148	414	78207	842	17.3	52.6	35.3	45.4

Table 2.2: Detailed description of simulated systems containing a liposome (L). L_{50}, L_{100}, and L_{130} are pure DPPC liposomes with a radius of 50 Å, 100 Å, and 130 Å, respectively. Other liposomes have a radius of 50 Å. FAs (C10 and C14) are neutral. The systems include 20 N0 permeants. h is the membrane thickness between PO4 beads (region 2, see Section 2.3.3). The number of ions column refers to both the number of Na^+ ions and the number of Cl^- ions. Details of other liposome systems can be found in the SI of Paper 4 in Part7.2

Using CHARMM-GUI, initial structures of the membranes were prepared [147–150]. Setting up the liposomes involved a step utilizing artificial pores to equilibrate lipids between the leaflets and balance the water pressure differences between the inside and outside of the liposomes. The Martini 2 forcefield was used [139]. The reaction-field approach was used to calculate the Coulombic interactions [141]. With the potential-shift-Verlet modifiers, the Coulombic and the van der Waals potentials were shifted to zero at the cutoff of 1.1 nm. The neighbor list was updated using the Verlet neighbor search algorithm with the buffer tolerance set to 0.005 kJmol^{-1}ps^{-1}, which leads to neighbor list cutoffs of about 1.2 nm for various systems. The equation of motion was integrated using the leap-frog integrator with a time step of 20 fs. A temperature of 323 K and a pressure of 1 bar were set for all the systems. A velocity rescale thermostat coupling was implemented for the entire system as a whole, utilizing a coupling constant of 1.0 ps [151]. The Parrinello-Rahman barostat was used with a coupling constant of 12 ps. For systems with a flat bilayer and a liposome, semi-isotropic and isotropic isothermal compressibility of 3×10^{-4} and 4.5×10^{-5} bar^{-1} was employed, respectively. At every 100 time steps, the center of mass motion of the system was removed, and periodic boundary conditions were applied in all directions (x, y, z). Systems were first energy minimized and next, they were equilibrated applying NPT ensemble for 100 ns. Some of the liposome systems required a longer equilibration run to let the water density inside and outside the liposome equilibrate through water membrane crossings. The equilibration times are reported in the SI of Paper 4 in Part7.2. The production run was 1 μs of NPT simulation and coordinates were stored every 20 ps. For the smallest pure DPPC liposome with N0 or Na beads (L_{50}), as the crossing statistics were not good enough (small water phase inside the liposome), the simulation was extended to 5 μs.

2.3.3 Analysis of MD trajectories

For flat membranes, the center of the membrane is first computed by averaging the z-coordinate of the DPPC beads, and the trajectories are shifted as a whole along the z-axis to let the center of mass of the membrane coincide with the $z = 0$ plane. Next, periodic boundary conditions are applied to let all coordinates fall in the range $-L(t)/2$ to $L(t)/2$, where $L(t)$ is the instantaneous box dimension in the z-direction. For liposomes, the center of mass of the DPPC beads is computed as well, and the whole box is shifted to let it coincide with the origin. Periodic boundary conditions are applied in all 3

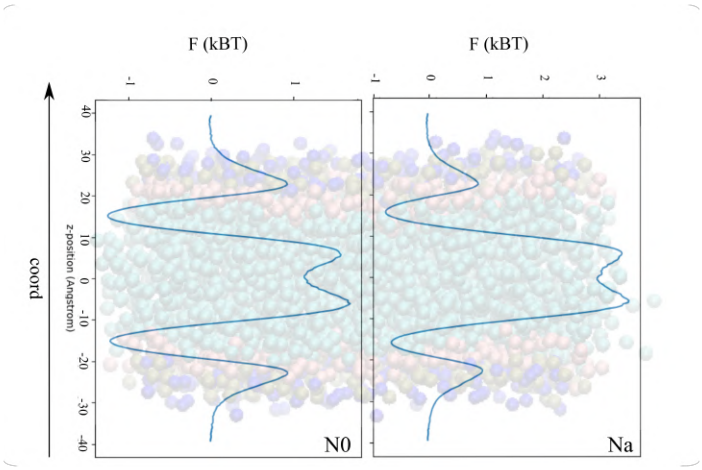

Figure 2.1: Free energy of permeants N0 and Na through a flat membrane in the z-direction. Na and N0 are CG beads with intermediate polar character. DPPC is presented by beads, colored by bead type: green for hydrocarbons, pink for glycerol, brown for phosphate, and blue for choline bead type. Water and ions not shown.

dimensions, such that all coordinates fall in the range $-L_\mu(t)/2$ to $L_\mu(t)/2$, $\mu = x, y, z$.

The membrane thickness of flat membranes is computed as the distance between the average z-position of the PO4 beads in the upper leaflet and the average z-position of the PO4 beads in the lower leaflet, averaged over the trajectory. To compute the properties of systems with liposomes, a few additional settings need to be specified. We considered two radii, the inner radius r_1 and outer radius r_2 ($r_1 < r_2$, shown in Fig. 1.5). For a liposome, the membrane is centered around $r = 0$ and the two average radial distances of the PO4 beads in the inner and outer layer are used as the two radii r_1 and r_2, which determine the thickness $h = r_2 - r_1$. This is in line with the approach followed by Risselada and Marrink for pure DPPC CG liposomes [132].

To determine the APL of a liposome, the cross-section areas of the inside ($4\pi r_1^2$) or the outside ($4\pi r_2^2$) leaflets were divided by the number of molecules (DPPC, FAs, and cholesterol) in that leaflet, giving the values A_{in} and A_{out}, respectively. The number of molecules in the inner or outer leaflet of the liposome was determined by counting all molecules below or above the mid-radius value of r_1 and r_2, respectively. In order to be able to compare the flat and the liposome bilayers, $A^* = \sqrt{A_{\text{in}} A_{\text{out}}}$ was computed, similarly to Eq. 3.41 [136].

To be more precise in the calculation of the reference permeant concentration c_{ref} inside or outside the liposomes, the r_1 and r_2 radii were not used. Instead, based on the histogram of water bead positions in every system, the radius in which the water phase separated completely from the lipid phase was applied to compute c_{ref}. The number of permeant molecules in these regions were counted and divided by the volume of the relevant region, to derive the concentration. The SI of Paper 4 in Part 7.2 reports the specific cutoff values that define these regions.

For the N0 and Na permeants, the membrane thickness h covers the central membrane part where the highest free energy barrier (see further) for these two permeants is located. However, besides the free energy barrier at the membrane center, the N0 and Na permeants have additional free energy barriers and wells. A complete membrane crossing means that a permeant is first on one side of the membrane, and next it crosses the membrane and emerges on the other side of the membrane. The dividing surfaces to detect a membrane crossing are a choice in simulations [71]. The thickness h does not encompass the additional free energy barriers and wells at $|z| = 2.5$ nm, so $|z| = h/2$ is a non-ideal dividing surface for the N0 and Na permeants. Therefore, another dividing surface is introduced. This extended membrane thickness is defined for the N0 and Na permeants based on visual inspection, where the free energy curves of the permeants flatten out: we extend h by 0.8 nm on both sides. The extended membrane thickness is called *region 1* (see Fig. 1.5) and is relevant for full membrane crossings. For a flat membrane, region 1 ranges from $-h/2 - 0.8\,\mathrm{nm}$ to $h/2 + 0.8\,\mathrm{nm}$. For a liposome, region 1 is defined by two new radii, $r_1' = r_1 - 0.8\,\mathrm{nm}$ and $r_2' = r_2 + 0.8\,\mathrm{nm}$. These radii have also been utilized to calculate the crossing areas σ_1' and σ_2' to be used in Eqs. 3.52-3.53 when computing the N0 or Na permeability in the liposome systems.

For water as a permeant, the membrane thickness h was used to determine the number of full membrane crossings n_{cross} of water molecules. Given the very high free energy barrier for water permeation through the hydrophobic phase, the water permeability is insensitive to the exact location of the dividing surfaces [29, 71]. We refer to this as *region 2* (see Fig. 1.5), the region extending over the membrane thickness h. For a flat membrane, the dividing surfaces for water crossings are located at $z = -h/2$ and $z = h/2$, while for a liposome the dividing surfaces are located at the $r = r_1$ and $r = r_2$ radii. (Note that membrane thickness h in earlier papers by the authors refers to region 1 [29, 30].)

In summary, water permeability is based on region 2, N0 permeability on region 1, and Na permeability on region 1, unless specified differently. The error bars or shaded gray areas in the figures of the main document and SI of Paper 4 in Part 7.2 are computed as two standard errors, assuming the observed crossings follow a Poisson process [32, 71].

Histograms of the permeants (water, N0, and Na beads) and of the DPPC CG beads are generated as follows. For flat membranes, the z-coordinates were normalized with the instantaneous box $L(t)$ dimension in the z-direction, giving values in the -0.5 to 0.5 interval. A histogram of these normalized z-coordinates is computed using 200 bins. The histogram is then scaled back with the average box length $\langle L \rangle$ in the z-direction, giving values $-\langle L \rangle/2$ to $\langle L \rangle/2$. Free energy profiles of the permeants are computed from this histogram ($hist(z)$) using $F(z) = -k_B T \ln\bigl(hist(z)\bigr)$, and the profiles are shifted as a whole to make $F(z) = 0$ in the water phase. For liposomes, the distance of the relevant beads to the liposome center, which coincides with the origin, is computed at every snapshot. A histogram $hist(r)$ is constructed from these r-distances using 200 bins, and the free energy is constructed using $F(r) = -k_B T \left(\ln\bigl(hist(r)\bigr) - 2r\right)$ and shifting to make $F(r) = 0$ in the water phase. The additional term $-2r$ comes from the Jacobian factor $4\pi r^2$, which lets us interpret $F(r)$ as a measure for solubility. For both flat membranes and liposomes, a density distribution of DPPC beads along z or r is obtained by normalizing a histogram of DPPC bead positions $hist(z)$ or $hist(r)/r^2$ by the total count in the histogram.

2.4 INVESTIGATING CAVEOLAE

Chapter 6 will explore the impact of curvature on O_2 partitioning between the lipid membrane and the water phase. The simulation setting for this investigation is detailed in this section.

2.4.1 AA O_2 partitioning

Two systems with DPPC lipids were simulated using the Gromacs-2021.4 [137]: a flat bilayer consisting of 128 lipids Fig. 2.2 right and a 50Å-radius liposome consisting of 518 lipids Fig. 2.2 middle. A detailed description of the systems can be found in Table 2.3. Both systems were simulated using AA MD. For the system with a liposome, we first generated the model as a CG structure with CHARMM-GUI [150]. Then, the Martini backmapping tool was used to convert the

CG model to an AA one [99]. The two systems were simulated at 323 K, coupled to velocity rescale thermostats with a coupling constant of 1.0 ps [151]. The Parrinello–Rahman barostat was employed to couple the pressure in the system with the flat bilayer, while the system with the liposome was coupled with the Berendsen barostat. Periodic boundary conditions were applied in all three dimensions and the box vectors were subjected to semi-isotropic pressure coupling (flat bilayer) or isotropic pressure coupling (liposome), using a reference pressure of 1 bar, a coupling parameter of 5 ps, and an isothermal compressibility of 3×10^{-4} bar^{-1} and 4.5×10^{-4} bar^{-1}. The coordinates were saved every 2 ps. The particle mesh Ewald approach was employed to calculate the Coulombic interactions. At the cutoff of 1.2 nm, the Coulombic and the van der Waals potentials were shifted to zero using force-switch modifiers. CHARMM36 forcefield was implemented to model the lipid and oxygen molecules [152]. Water was modeled by applying the TIP3P model [153]. Using the Verlet neighbor search algorithm, the neighbor list length was updated at 1.2 nm. The equation of motion was integrated with a time step of 2 fs, using the leapfrog integrator. At every time step, the center of mass motion of the system was removed. After adding oxygen molecules at a concentration of 86 μM, an energy minimization was performed, followed by a 50 ns equilibration and 200 ns production run with constant pressure and constant temperature (NPT ensemble).

2.4.2 CG O_2 model

To enable simulations of larger systems like caveolae, including O_2, we've chosen the CG O_2 model from the Martini 3 CG beads, and its

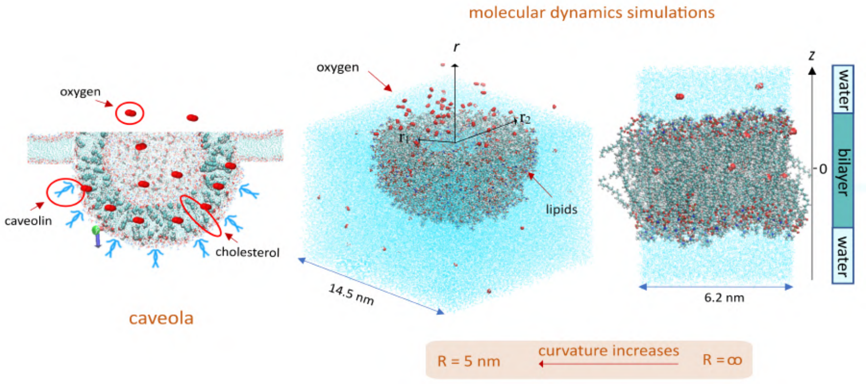

Figure 2.2: Left: the schematic picture of caveolae. Middle: the system with a liposome, only the lower part is shown. Right: the system with the flat bilayer.

systems	# lipid	# water	# O_2
flat bilayer	128	6341	18
liposome	518	78804	164

Table 2.3: The detailed description of the two systems: flat bilayer and liposome.

suitability as a representation for O_2 is examined. In the subsequent section, we present the simulation systems and settings designed to evaluate the efficacy of this CG model.

Computational details

The selection and the validation of the CG bead for O_2 is based on comparing experimental data, AA simulation data, and CG simulation data. Part of the simulations have been reported elsewhere, e.g. the CG simulations of the Martini 3 forcefield, which were complemented by several new simulations. For clarity, this section reviews the simulation details of the new simulations.

Permeant	POPC	CHOL	W	HD	Na^+/ Cl^-	# permeants	T (K)
			Hydration				
CG TC3	0	0	17474	0	0	100	310
			Free energy and permeability				
CG TC2	128	0	1395	0	14	18	310
CG TC3	128	0	1395	0	14	18	310
	96	32	1395	0	14	18	310
CG TX1	128	0	1395	0	14	18	310
CG TX2	128	0	1395	0	14	18	310
AA O_2	128	0	5580		14	18	310
	96	32	5580		14	18	310
			Diffusion				
CG TC3	0	0	68400	0	0	10	310
CG TC3	0	0	0	18256	0	10	310

Table 2.4: Detailed description of the systems. 'HD', 'W' and 'CHOL' refer to hexadecane, water and cholesterol, respectively.

AA O_2 permeation through lipid membrane

Table 2.4 presents a detailed description of two AA simulated systems, each composed of 1-palmitoyl-2-oleoyl-sn-glycero-3-phosphocholine (POPC) and cholesterol (CHOL) lipids (See Fig. 1.1 for molecular structures). One box contains a homogeneous

POPC membrane, while the other box contains a heterogeneous POPC:CHOL membrane. The systems include 0.15 M sodium chloride.

Utilizing Gromacs-2021.4 [146], both systems underwent extensive AA MD simulations at 310 K. The simulations were conducted with the velocity rescale thermostat with a 1.0 ps coupling constant [151]. Periodic boundary conditions were applied in all three dimensions. To maintain pressure, the Parrinello–Rahman barostat was used, semi-isotropic pressure coupling was implemented with a reference pressure of 1 bar, a coupling constant of 5 ps, and an isothermal compressibility of 3e-4 bar^{-1}. Coulombic interactions were computed using the particle mesh Ewald approach. At a 1.2 nm cutoff, both Coulombic and van der Waals potentials were smoothly shifted to zero using force-switch modifiers. The lipid molecules were modeled using the CHARMM36 forcefield [152], and the oxygen molecules were modeled as a neutral molecule without quadropolar moment [30]. Water was represented by the TIP3P model [153]. The Verlet neighbor list algorithm with cutoff 1.2 nm was used. Integrating the equation of motion involved a time step of 2 fs with the leapfrog integrator. Center of mass motion was removed at each time step. Following the addition of oxygen molecules at a concentration of 86 μM, an energy minimization was executed. This concentration is selected to prevent the aggregation of O_2 model beads [73]. Subsequently, a 100 ns equilibration and a 1000 ns production run were conducted under constant pressure and temperature conditions (NPT ensemble). Snapshots of coordinates were saved at 1 ps intervals.

New CG simulations

A series of additional MD simulations with CG was performed to further validate the Martini 3 beads as models for molecular oxygen.

In these simulations, the Martini 3 forcefield was again used [134]. The systems were simulated using Gromacs-2021.4 [146]. The reaction-field approach was used to calculate the Coulombic interactions [141]. With the potential-shift-Verlet modifiers, the Coulombic and the van der Waals potentials were shifted to zero at the cutoff of 1.1 nm. The neighbor list was updated using the Verlet neighbor search algorithm with cutoff length 1.1 nm. The equation of motion was integrated using the leap-frog integrator with a time step of 20 fs. A temperature of 310 K and a pressure of 1 bar were set for all the systems. The velocity rescale thermostat was used with coupling constant 1.0 ps [151]. The Parrinello-Rahman barostat was used with a coupling constant of 12 ps. For systems with a membrane, semi-isotropic isothermal compressibility of 3e-4 bar^{-1} was used. At every 100 time steps, the center of mass motion of the system was removed, and periodic boundary conditions were applied in all directions (x, y, z).

The next subsections specify the simulation boxes in the different types of simulations, as summarized in Table 2.4.

CG O_2 permeation through lipid membrane. Using CHARMM-GUI, initial structures of the membranes were prepared [147–150]. The exact same box compositions were used as in the AA membrane simulations of section 2.4.2 for a homogeneous POPC and heterogeneous POPC:CHOL membrane. As one CG water bead represents 4 water molecules, the CG simulation box contains 1395 CG water beads whereas the AA simulation boxes contained 5580 water molecules (Table 2.4).

Systems were first energy minimized and next equilibrated in the NPT ensemble. The production run was 1000 ns of NPT simulation, and coordinates were stored every 1 ps for analysis.

CG O_2 diffusion in solvent. We conducted simulations with the CG models for O_2 in a water box measuring 20.3x20.3x20.3 nm^3 ($\sim$ 68,400 water beads or $\sim$ 273,600 water molecules). The experimental solubility of O_2 in water at 310 K and 1 bar is 1.3e-3 mol/lit.atm as reported by Battino et al. [154], indicating that approximately 42,000 water molecules can dissolve a single O_2 molecule. In our CG simulation, however, each CG water bead accounts for 4 water molecules. Hence, our simulation box accommodated 10 solvated TC3 beads. The same simulation is done with the CG O_2 models immersed in a hexadecane box measuring 20.5x20.5x20.5 nm^3 ($\sim$ 18,256 hexadecane molecules) using the same computational settings.

For both systems, an energy minimization, a 50 ns equilibration run, and a subsequent 200 ns production run were performed. The diffusion coefficient was determined by analyzing the mean square displacement (MSD) of O_2 versus time plot. The diffusion coefficient is obtained from the slope of the linear regression applied to the MSD(t) plot from 1 ns to 50 ns.

2.4.3 CG O_2 partitioning

In this section, we utilize the CG O_2 model within a curved membrane configuration to explore the influence of membrane curvature on the partition coefficient of the O_2 model. The subsequent sections will provide a comprehensive overview of the simulation systems and their settings.

Simulated systems

To study the effect of curvature, two model systems were simulated in a CG description, i.e. a flat membrane and a liposome with radius of about 50 Å(Fig. 1.6). Table 2.5 gives an overview of the components, which shows that ion pairs were added to represent physiological conditions. Each O_2 molecule is represented by one TC3 Martini bead, which was selected based on its size (tiny, "T"), polarity, and charge (non-polar and neutral, "C"), and interaction with phospholipids ("3") in earlier work. Note that one water CG beads represents four water molecules in the Martini forcefield [134]. The simulations were carried out at a temperature of 310 K (body temperature) and pressure of 1 bar.

Systems	#POPC	#W	#Na^+/Cl^{-1}	#O_2
POPC-flat	128	1395	14	18
POPC-liposome-50 Å	394	16618	192	11

Table 2.5: Detailed description of the two simulated systems: a flat membrane and a liposome with radius of about 50 Å. The number of phospholipid molecules (#POPC), water CG beads (#W), ion pairs (#Na+/Cl-), and oxygen CG beads (#O_2) is indicated.

Computational details

The systems were simulated using Gromacs-2021.4 [146]. Using CHARMM-GUI, initial structures of the membranes were prepared [147–150]. The Martini 3 forcefield was used [134]. The reaction-field approach was used to calculate the Coulombic interactions [141]. With the potential-shift-Verlet modifiers, the Coulombic and the van der Waals potentials were shifted to zero at the cut-off of 1.1 nm. The neighbor list was updated using the Verlet neighbor search algorithm with cutoff length 1.1 nm. The equation of motion was integrated using the leap-frog integrator with a time step of 20 fs. A temperature of 310 K and a pressure of 1 bar were set for all the systems. The velocity rescale thermostats coupling constant was set at 1.0 ps [151]. The Parrinello-Rahman barostat was used with a coupling constant of 12 ps. For systems with a flat membrane and a liposome, semi-isotropic and isotropic isothermal compressibility of 3×10^{-4} and 4.5×10^{-4} bar^{-1} was employed, respectively. A dodecahedron box was used to simulate the liposomes. At every 100 time steps, the center of mass motion of the system was removed. Systems were first energy minimized and next they were equilibrated applying NPT (Isothermal-Isobaric) ensemble for 100 ns. The production run was 500 ns of NPT simulation.

Analysis of results

A histogram was made of the position of the O_2 molecules with respect to the center of the membrane. In the case of a flat membrane, position is measured along the membrane's normal axis (z-direction). However, for a liposome, position is determined by measuring the radial distance from the center of the liposome. This center is defined by the average position of the phosphor CG beads (PO4) located in the head group of the POPC molecules. The logarithm of the histogram of the position q along the membrane normal leads to the free energy profile, $F(q) = -k_B T \ln\big(\text{hist}(q)\big)$ where k_B is Boltzmann's constant and T is the temperature. At 310 K, 1 $k_B T$ is approximately equivalent to 4.28×10^{-21} Joules.

CHAPTER 3

MEMBRANE PERMEABILITY DEFINITION

In this chapter, we will introduce permeability equations for flat membranes and derive an equation specifically for permeability in the radial direction. This derived equation will undergo further customization to facilitate its application in the counting crossings method, thereby enabling us to accurately calculate the permeability of liposomes across diverse systems. Following that, we will employ CG MD simulation to illustrate this equation by computing permeability of water molecules through both flat and curved membranes.

3.1 FLAT MEMBRANE PERMEABILITY

The Smoluchowski equation describes the transport of permeants through an inhomogeneous medium on a free energy profile $F(z)$ with a position-dependent diffusivity $D(z)$, where z is the coordinate along the membrane normal.[65] Assume F_{ref} is the free energy at the reference location, usually taken to be in the water phase on both sides of the membrane. The permeability P of a layer of thickness h follows from solving the Smoluchowski equation under steady-state conditions, [65]

$$\frac{1}{P} = e^{-\beta F_{\text{ref}}} \int_h \frac{e^{\beta F(z)}}{D(z)} dz \tag{3.1}$$

where the integration runs over a certain thickness h and $\beta = 1/(k_B T)$ is the inverse temperature with T the temperature. In a compartmental model, as illustrated earlier for oxygen transport[30], F and D are piecewise constant functions, and the integral becomes a sum over the several compartments,

$$\frac{1}{P} = \sum_i \frac{1}{P_i} = \sum_i \frac{h_i}{K_i\, D_i} \tag{3.2}$$

where each layer i is characterized by its thickness h_i, diffusivity D_i, and free energy F_i. The factor $K_i = \exp\bigl(-\beta(F_i - F_{\text{ref}})\bigr)$ is the partitioning constant in layer i compared to the water phase, and it is equal to the concentration ratio between layer i and the water phase, i.e. $K_i = c_i/c_{\text{ref}}$. The composition rule in Eq. 3.2 shows that the permeation through a series of layers can be seen as a series of local resistances $1/P_i$, if the same reference F_{ref} is used for each layer.

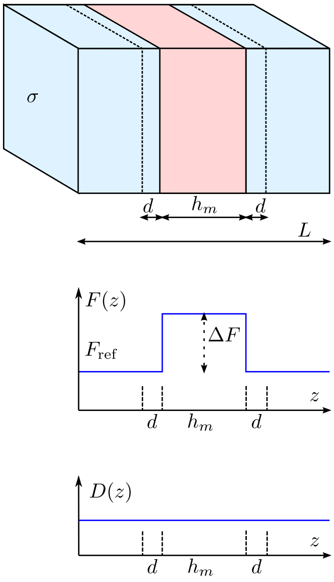

Figure 3.1: Simulation box with length L and cross area σ containing membrane (red) and water (blue). The compartmental model considers the membrane (thickness h_m) and a water layer on both sides (thickness d each). Diffusivity is assumed to be constant and free energy profile is piecewise constant.

Let us start with a one-compartmental model for a uniform membrane of thickness h_m, for which the integral in Eq. 3.1 simplifies to

$$P = \frac{KD}{h_m}\,. \tag{3.3}$$

The partitioning coefficient K relates to the free energy difference ΔF between the membrane and the water phase, where ΔF is also referred to as the free energy of transfer to bring a permeant from the water phase into the membrane.

This model is extended to the three-compartmental model depicted in Fig. 3.1, where a water layer of thickness d is added on both sides around the membrane. For simplicity, the diffusivity is assumed to be constant over the whole simulation box. This model allows for a more complete discussion of the behavior of the counting method. The permeability of this model is obtained by putting the previous permeation resistance $h_m/(KD)$ in series with the permeation resistance of the water phase $2d/D$, where the water phase's partitioning coefficient is simply 1.

This gives the permeability of the membrane plus water layers equal to

$$P = \frac{D}{2d + \dfrac{h_m}{K}} \,. \tag{3.4}$$

Filling in $d = 0$ in Eq. 3.4, results back in Eq. 3.3.

Two regimes exist for P, depending on the partitioning coefficient K of the membrane. In the limit of low K, the concentration in the membrane is much lower than in the water phase, and P reduces to the previous equation, $P \approx KD/h_m$, as if the water layer is unimportant. The permeability is then indeed dominated by the height of the barrier and is a linear function of K. This is expected from the integral form in Eq. 3.1 which is dominated by high F values. In the limit of large K, at least compared to $h_m/(2d)$, the membrane has a high concentration of permeants, and P becomes approximately a constant, $P \approx D/(2d)$, meaning that the permeability of the membrane is not the limiting factor, but rather the resistance coming from the water layer.

Flat membrane's permeability from the counting method

Given this compartmental model, we will now turn towards the practical situation of a simulation setup. In a simulation, P can be computed using the counting method, by determining the crossing rate J and the reference concentration c_{ref} in the water phase. The number n_{cross} of complete transitions through a membrane with cross-section area σ in either direction are counted during a long equilibrium MD simulation of length T_{sim}. Next, the (bidirectional) flux J per unit of time and unit of area in either direction is derived,

$$J = \frac{n_{\text{cross}}}{T_{\text{sim}}\sigma} = |J_{\leftarrow}| + |J_{\rightarrow}| \tag{3.5}$$

where $J_{\leftarrow}$ and $J_{\rightarrow}$ are the flux through the membrane in the negative or positive direction, respectively. The well-known formula [27, 28] for P from the counting method is

$$P = \frac{|J_{\leftarrow}|}{c_{\text{ref}}} = \frac{J_{\rightarrow}}{c_{\text{ref}}} = \frac{|J_{\leftarrow}| + J_{\rightarrow}}{2c_{\text{ref}}} = \frac{n_{\text{cross}}}{2\sigma\, T_{\text{sim}}\, c_{\text{ref}}} \tag{3.6}$$

The counting method for the permeability clearly relies on the number of crossings. The aim is to discuss the number of crossings as a function of the key properties of the membrane and the simulation setup: (1) the free energy of transfer ΔF, (2) considered layer thickness $h = h_m + 2d$, (3) the total number of permeants N_t that are present in the simulation box, and (4) the dimensions of the simulation box, i.e. the height L and cross area σ. For this reason, n_{cross} will be written as a function of these parameters in order to observe their role. Using the first equality in Eq. 3.5, it is clear that a discussion of J contains similar information as a discussion of n_{cross}, apart from the role of the simulation time T_{sim} and cross area σ, and therefore the discussion of n_{cross} will be largely based on the discussion of J.

From Eq. 3.6, it immediately follows

$$J = 2c_{\text{ref}}P \tag{3.7}$$

where P is given by Eq. 3.4. The task at hand is thus to express the reference concentration, located in the water phase, as a function of the key parameters K and N_t. The water concentration $c_{\text{ref}} = c_w$ is the average number of permeants $\langle N_w \rangle$ in the water phase divided by the volume of the water phase, which is $\sigma(L - h_m)$ according to Fig. 3.1. Similarly, the membrane concentration c_m is the average number of permeants $\langle N_m \rangle$ in the membrane divided by the membrane volume σh_m. Note that, while the total number of permeants N_t remains constant during the simulation, the number of particles in the water and membrane, N_w and N_m respectively, will fluctuate over time. Their averages are given as

$$\begin{aligned} \langle N_w \rangle &= c_w \sigma (L - h_m)\,, & (3.8)\\ \langle N_m \rangle &= c_m \sigma h_m = K c_w \sigma h_m\,. & (3.9) \end{aligned}$$

Using the equality $N_t = N_w + N_m = \langle N_w \rangle + \langle N_m \rangle$, the reference concentration becomes

$$c_{\text{ref}} = c_w = \frac{N_t}{\sigma(h_m K + L - h_m)} \tag{3.10}$$

and we find J as a function of the key parameters

$$J = \frac{2N_tD}{\sigma} \frac{1}{h_mK + L - h_m} \frac{1}{2d + \dfrac{h_m}{K}} . \tag{3.11}$$

This is the equation that will be used for the discussion. The number of crossings follows immediately by multiplying J with $T_{\mathrm{sim}}\sigma$ (Eq. 3.5).

In a final step, we leave the case of the compartmental model and return to the case of general $F(z)$ and $D(z)$ profiles that can take any shape. It is still assumed that the transport kinetics can be described by the Smoluchowski equation, i.e. the kinetics are Markovian. In the general case, the reference concentration is given by

$$c_{\mathrm{ref}} = \frac{e^{-\beta F_{\mathrm{ref}}} N_t}{\sigma \displaystyle\int_L e^{-\beta F(z)} dz} . \tag{3.12}$$

P is given by Eq. 3.1. Using the $\langle \ldots \rangle$ notation for spatial averages in the z-direction, over h or L, these are rewritten as

$$P = \frac{e^{\beta F_{\mathrm{ref}}}}{h \left\langle \dfrac{e^{\beta F(z)}}{D(z)} \right\rangle_h} \tag{3.13}$$

and

$$c_{\mathrm{ref}} = \frac{e^{-\beta F_{\mathrm{ref}}} N_t}{\sigma L \left\langle e^{-\beta F(z)} \right\rangle_L} . \tag{3.14}$$

The flux in Eq. 3.7 now becomes

$$J = \frac{2N_t}{hL\sigma \left\langle \dfrac{e^{\beta F(z)}}{D(z)} \right\rangle_h \left\langle e^{-\beta F(z)} \right\rangle_L} . \tag{3.15}$$

The above equation is the generalization of the compartmental model in Eq. 3.11 to arbitrary free energy and diffusivity profiles. It gives the flux J as a function of the key parameters in the general case.

The flux in the compartmental model (Eq. 3.11) is first discussed for the two limiting cases where the layer does not comprise any water ($d = 0$ so $h = h_m$) and where all water is included in the layer ($h = L$), and next it is illustrated for the intermediate cases ($h_m < h < L$).

For $d = 0$, only the membrane of thickness h_m is considered, and the flux simplifies. For large K (free energy well) and small K (free energy barrier), the dependence on K is constant or linear in K, respectively,

$$J(h_m) = \begin{cases} \dfrac{N_t D}{\sigma h_m^2}, & K \gg 1 \\ \dfrac{N_t D}{\sigma h (L - h_m)} K, & K \ll 1 \end{cases} \tag{3.16}$$

When the membrane is highly soluble for the permeants ($\Delta F > 0$), the number of crossings is independent of K, and thus ΔF. However, when the permeants' solubility in the membrane is lower than in the water phase ($\Delta F < 0$), the number of crossings will drop exponentially with ΔF. A very high free energy of transfer will give very few membrane transitions, with poor statistics for the counting method as a consequence.

For $2d = L - h_m$, the whole water layer in the simulation box is included in the counting of membrane transitions. The considered thickness is $h = L$, so $J(L)$ represents the flux of complete crossings of the simulation box,

$$J(L) = \frac{N_t D}{\sigma (L - h_m)^2} \frac{1}{1 + \dfrac{h_m}{L - h_m} \dfrac{1}{K}} \frac{1}{1 + \dfrac{h_m}{L - h_m} K}. \tag{3.17}$$

Here, $J(L)$ can be interpreted as a measure of the sampling efficiency of permeants over the whole z-direction of the simulation box. It is interesting to see that this equation is symmetric for the replacement of K by $1/K$. Replacing ΔF by $-\Delta F$ does not alter the sampling efficiency $J(L)$. In other words, $J(L)$ is an even function of ΔF through the appearance of K in this expression. This is an important realization: the flux in a simulation can be low because either a high barrier makes it difficult for the permeants to pass the membrane, or a deep well makes it difficult to leave the membrane once they are trapped. In summary, the larger the difference between the free energy minima and maxima across the membrane normal, given by $|\Delta F|$, the lower is the sampling efficiency, because J drops with both K and $1/K$. A high variety in solubility hence leads to lower sampling efficiency.

We now approximate $J(L)$ to allow comparison with the previous approximations of $J(h_m)$ in Eq. 3.16. For large K (free energy well) and small K (free energy barrier), $J(L)$ is inversely proportional to K, or linear in K, respectively,

$$J(L) = \begin{cases} \dfrac{N_t D}{\sigma h(L - h_m)} \dfrac{1}{K}, & K \gg 1 \\ \dfrac{N_t D}{\sigma h(L - h_m)} K, & K \ll 1 \end{cases} \tag{3.18}$$

When K is small, $J(h_m) \approx J(L)$. This can be understood because the exact location of the boundaries, be it at $h = h_m$ or $h = L$, is relatively unimportant when the barrier is high. When K is large, however, we find that $J(h) \gg J(L)$. When the membrane is highly soluble and only few particles are in the water phase, the exact boundary location does matter. Omitting the water phase, or including a small or larger part, has a large effect on the number of crossings. The reason is that the permeability of the water phase is in this case the limiting resistance for the overall permeability of the considered layer, hence the sensitivity to the included water layer thickness.

For d between 0 and $(L - h_m)/2$, the number of crossings lies between $J(h_m)$ and $J(L)$. Fig. 3.2 visualizes the trends for the toy system (Fig. 3.1) with numerical values that are typical for MD settings, for instance for a bilayer consisting of 72 phospholipid molecules [30]. The simulation box had sizes $L = 70\,\text{Å}$ and $\sigma = (50\,\text{Å})^2$, the membrane thickness was set to $h_m = 55\,\text{Å}$, the box contained $N_t = 10$ permeating particles with diffusivity $D = 0.5\,\text{Å}^2/\text{ps}$, and the total simulation time was set to $T_{\text{sim}} = 1\,\mu\text{s}$.

According to Eq. 3.7, the permeability and the reference concentration are the main contributing factors, which are plotted in Fig. 3.2b-c for several values of d. The semi-log plots clearly show the constant (zero slope), linear (positive slope), and inversely linear (negative slope) dependence on K in the limiting cases $K \gg 0$ and $K \ll 0$. The number of crossings is mainly the product of these two graphs, and the semi-log plot in Fig. 3.2a is indeed the sum of the curves except for a vertical shift. The widespread curves for small K (i.e. $\Delta F \ll 0$) in Fig. 3.2a-b are a signature of the sensitivity to the chosen layer thickness when the membrane is a permeant trap. Let us focus on the number of complete crossings of the simulation box (black line), which refers to the sampling efficiency. The vertical dashed line in Fig. 3.2a indicates 100 crossings, corresponding with a standard error of about 10%. This corresponds to a free energy difference of about $|\Delta F| = 5k_BT$, indicated with vertical lines in the other plots. This means that the sampling of the complete simulation

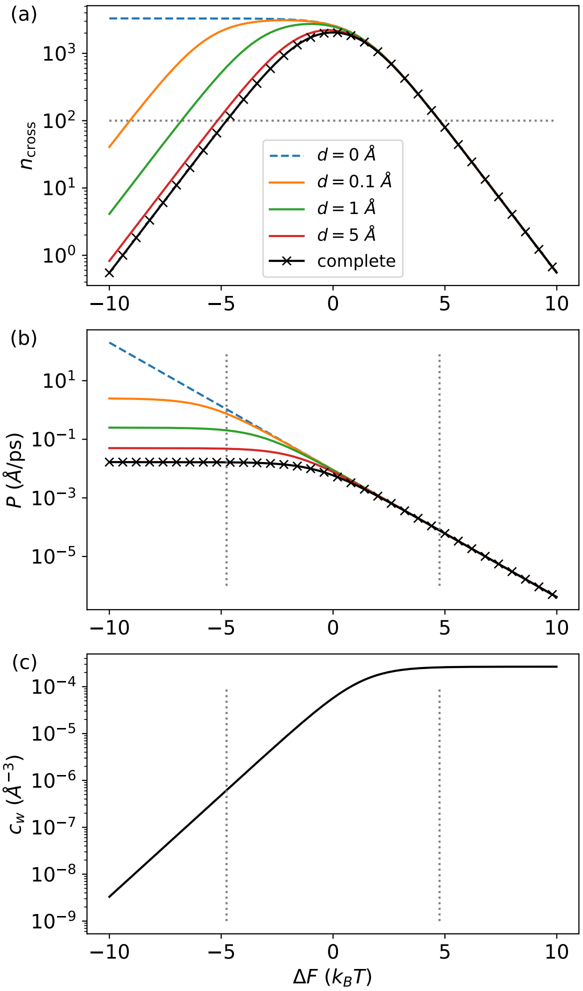

Figure 3.2: Number of crossings n_{cross} (a), permeability P (b) and reference concentration c_w (c) in the model system of Fig. 3.1 as a function of the free energy difference $\Delta F = -k_B T \ln K$, where $\Delta F > 0$ is a barrier and $\Delta F < 0$ a well. Various water layers d are considered. Blue dashed line: water slab not taken into account. Black line crosses: complete simulation box considered; this is indicative of overall sampling. The horizontal dashed line in (a) is at 100 crossings, vertical dashed lines in (b) and (c) indicate the corresponding free energy difference.

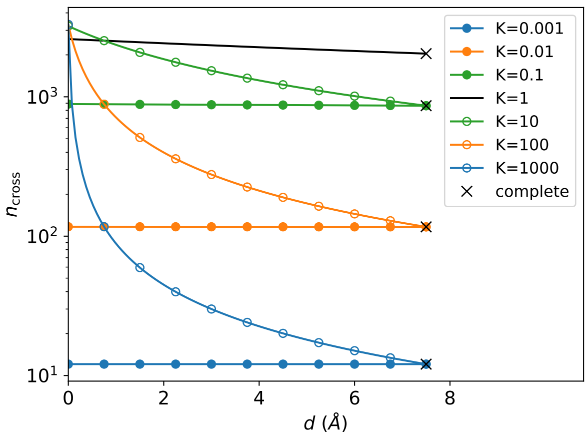

Figure 3.3: Number of crossings n_{cross} as a function of the water layer d in the model system of Fig. 3.1, for various free energy barriers ($K < 0$) and free energy wells ($K > 1$). Black crosses: complete simulation box considered.

box becomes poor when $|\Delta F|$ is larger than $5k_BT$ and one should be wary of statistics. When $\Delta F \gg 0$, the statistics are poor because the membrane forms a high barrier, making crossings a rare event. However, when $\Delta F \ll 0$, the poor statistics are caused by the low permeant concentration c_w in the water phase (Fig. 3.2c). When all permeants are trapped in the membrane, meanwhile not contributing to the crossings, there is barely any permeant left in the water phase as a candidate to perform a crossing.

Fig. 3.3 plots the number of crossings as a function of the layer thickness for several values of K. The curves for low K are almost unaffected by considering some water layer. In contrast, the curves for high K indeed decrease much faster than those for low K, as those are more sensitive to the layer thickness. For complete crossings at $h = L$, the curve for a given K coincides with the corresponding curve for $1/K$ (indicated with a black cross in the graph), illustrating the symmetry between ΔF and $-\Delta F$.

For all curves in Fig. 3.3, n_{cross} decreases with increasing thickness h. This is a consequence of the composition rule in Eq. 3.2 for permeability. A higher thickness gives a lower permeability according to Eq. 3.2. Using $J = 2c_{\text{ref}}P$, a similar composition rule holds for the flux,

$$\frac{1}{J} = \sum_i \frac{1}{J_i} \tag{3.19}$$

where J_i is the bidirectional flux through a layer i (see Eq. 3.5). An equivalent composition rule holds for $n_{\mathrm{cross}} = T_{\mathrm{sim}}\,\sigma\,J$. Hence, J and n_{cross} also decrease when the considered thickness is increased. For a symmetric bilayer membrane, it immediately follows from the composition rule that the entrance flux through one leaflet is identical to the escape flux through that leaflet, $J_{\mathrm{entr}} = J_{\mathrm{esc}}$, and the complete crossing flux through the entire membrane is half of that, $J = J_{\mathrm{entr}}/2 = J_{\mathrm{esc}}/2$. Likewise, $P = P_{\mathrm{half}}/2$, where P_{half} is the permeability of one membrane leaflet. It is important to note that these composition rules are based on the compartmentalized inhomogeneous solubility-diffusion model, and are thus only true under the assumption of perfectly diffusive behavior. Non-Markovian kinetics might distort these composition rules,[104] e.g. when memory effects are at play for ethanol crossings through a phospholipid membrane [71].

Finally, the symmetry in ΔF is shown in the general case of arbitrary profiles in Eq. 3.15. When the diffusion profile is taken to be constant, $D(z) = D$, and considering the full simulation box, $h = L$, the flux becomes

$$J(L) = \frac{N_t}{hL\sigma D \left\langle e^{\beta F(z)} \right\rangle_L \left\langle e^{-\beta F(z)} \right\rangle_L} . \tag{3.20}$$

This highlights that the same number of crossings will be encountered when a profile $F(z)$ is replaced by $-F(z)$, even though the permeability changes. While it may be counterintuitive, a profile with a high free energy barrier will therefore give the same sampling efficiency as a profile with a low free energy barrier. Highly soluble membranes are thus not necessarily improving the statistics in the counting method. This realization is important for drug design, where substances with high permeability might actually be trapped by the membrane, thus reducing their efficacy.

3.2 CURVED MEMBRANE PERMEABILITY

In this section, the definition of permeability for curved membranes will be derived in the case of diffusive transport through membranes. The Smoluchowski equation is often referred to as the inhomogeneous diffusion solubility model, and describes the evolution of the concentration $c(\bar{r}, t)$ based on the position-dependent diffusivity tensor $\bar{\bar{D}}$ and free energy F,

$$\frac{\partial c(\bar{r}, t)}{\partial t} = \nabla \left(\bar{\bar{D}}(\bar{r}) e^{-\beta F(\bar{r})} \nabla \left(e^{\beta F(\bar{r})} c(\bar{r}, t) \right) \right) \tag{3.21}$$

where $\beta = 1/(k_B T)$ with k_B Boltzmann constant and T temperature. The Smoluchowski equation has as an advantage that it can be solved analytically under steady-state conditions both for flat membranes and spherically shaped membranes. First, while the solution for flat membranes is well-known, we will revise here the solution for systems with spherical symmetry. Second, the escape and entrance permeability will be defined. Within the diffusive assumption, the new permeability definition will be derived using a special limiting case: a purely homogeneous medium, i.e. the membrane is imaginary. In this case, we will impose that a curved 'membrane' should have the same permeability value as its flat counterpart. Third, we will transfer the permeability definitions to the counting method, which does not assume diffusive transport.

3.2.1 Inhomogeneous solubility-diffusion model under radial symmetry

Consider first the case of a flat membrane with translational symmetry in the membrane plane. The free energy F is position-dependent, and the anisotropic diffusion tensor $\bar{\bar{D}}$ has components parallel to the membrane ($D_{||}$) and orthogonal to the membrane ($D_\perp$). The position-dependent profiles along the normal z to the flat membrane surface are denoted $F(z)$ and $D_\perp(z)$. By assuming translational symmetry in the x and y directions, imposing a concentration gradient Δc over the membrane under steady-state conditions, and solving the Smoluchowski equation, the permeability can be obtained as $P = J/\Delta c$, where J is the net flux of permeants crossing the membrane [30, 31, 66–69],

$$\frac{1}{P} = e^{-\beta F_{\mathrm{ref}}} \int_{-h/2}^{h/2} \frac{1}{D_\perp(z) e^{-\beta F(z)}} dz \tag{3.22}$$

Next, consider the case of a liposome with radial symmetry, for which an update of Eq. 3.22 will be made. The radial symmetry of the medium leads to the profiles $F(r)$ and $D_\perp(r)$, which are the free energy and diffusion profile dependent on the radial distance r from the liposome center. Not only the medium, but also the boundary conditions are assumed to be radially symmetric in steady-state (see below, Fig. 3.4). The anisotropic inhomogeneous Smoluchowski equation [30] under radial symmetry reads, for the one-dimensional transport along r, as

$$\frac{\partial c}{\partial t} = \frac{1}{r^2} \frac{\partial}{\partial r} \left(r^2 D_\perp(r) e^{-\beta F(r)} \frac{\partial}{\partial r} \left(e^{\beta F(r)} c \right) \right) \tag{3.23}$$

Under steady-state conditions ($\partial c/\partial t = 0$), we need to solve

$$\frac{1}{r^2}\frac{\partial}{\partial r}\left(r^2 D_\perp(r) e^{-\beta F(r)} \frac{\partial}{\partial r}\left(e^{\beta F(r)} c\right)\right) = 0 \tag{3.24}$$

The first integration over r gives an integration constant A,

$$r^2 D_\perp(r) e^{-\beta F(r)} \frac{\partial}{\partial r}\left(e^{\beta F(r)} c\right) = A \tag{3.25}$$

The flux vector may be recognized, which is a vector along the radial direction $\bar{e}_r$ with length $J(r)$. This lets us rewrite Eq. 3.25 as,

$$J(r) = -D_\perp(r) e^{-\beta F(r)} \frac{\partial}{\partial r}\left(e^{\beta F(r)} c\right) = -\frac{A}{r^2} \tag{3.26}$$

which gives us insight in the behavior of the flux. As A is constant, the flux $J(r)$ diminishes as $1/r^2$ under radial symmetry.

After rearrangement of Eq. 3.25, integrating once more over $[r_1, r_2]$ gives

$$e^{\beta F(r_2)} c(r_2) - e^{\beta F(r_1)} c(r_1) = A \int_{r_1}^{r_2} \frac{1}{r'^2 D_\perp(r') e^{-\beta F(r')}} dr' \tag{3.27}$$

Next, the steady-state boundary conditions of the two cases in Fig. 3.4 are imposed on Eq. 3.27. In Fig. 3.4a, particles are entering the liposome from the outside, and any particle reaching the inside is assumed to be consumed instantaneously. With $c(r_1) = 0$, $c(r_2) \neq 0$, and $F(r_2) = F_{\text{ref},2}$ the reference free energy, the steady-state simplifies to

$$c(r_2) = -e^{-\beta F_{\text{ref},2}} J(r) r^2 \int_{r_1}^{r_2} \frac{1}{r'^2 D_\perp(r') e^{-\beta F(r')}} dr' \tag{3.28}$$

where r in the product $J(r)r^2$ can be taken at wish, as the product is constant according to Eq. 3.26. With $c(r_2) = \Delta c$, this leads to a liposome permeability definition that is dependent on the chosen r distance,

$$\frac{1}{P_{\text{entr}}(r)} = \frac{\Delta c}{|J(r)|} = r^2 e^{-\beta F_{\text{ref},2}} \int_{r_1}^{r_2} \frac{1}{r'^2 D_\perp(r') e^{-\beta F(r')}} dr' \tag{3.29}$$

The subscript 'entr' refers to the reference concentration being at location r_2, with particles *entering* the liposome.

In Fig. 3.4b, particles are enclosed inside the liposome, and any escaping particle is assumed to be consumed instantaneously. The

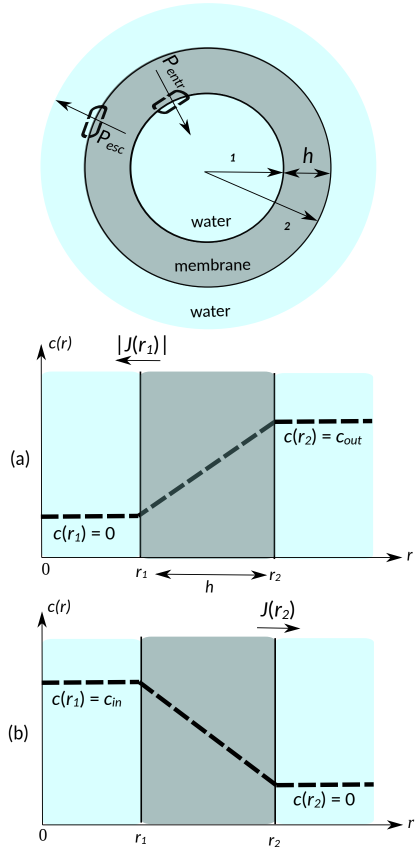

Figure 3.4: Definition of radii r_1 and r_2, and membrane thickness h for a liposome with radial symmetry. (a) Steady-state condition for entrance. The flux $|J(r_1)|$ is the entrance flux. (b) Steady-state condition for escape. The flux $J(r_2)$ is the escape flux.

concentration inside the liposome is nevertheless kept constant in this theoretical situation. With $c(r_1) \neq 0$, $c(r_2) = 0$, and $F(r_1) = F_{\mathrm{ref},1}$ the reference free energy, the steady-state in Eq. 3.27 simplifies to

$$c(r_1) = e^{-\beta F_{\mathrm{ref},1}} J(r) r^2 \int_{r_1}^{r_2} \frac{1}{r'^2 D_\perp(r') e^{-\beta F(r')}} dr' \tag{3.30}$$

where r in the product $J(r)r^2$ is arbitrary. With $c(r_1) = \Delta c$, this again leads to a permeability definition that is dependent on the chosen r distance,

$$\frac{1}{P_{\mathrm{esc}}(r)} = \frac{\Delta c}{|J(r)|} = r^2 e^{-\beta F_{\mathrm{ref},1}} \int_{r_1}^{r_2} \frac{1}{r'^2 D(r') e^{-\beta F(r')}} dr' \tag{3.31}$$

The subscript ‘esc’ refers to the reference concentration being at location r_1, with particles *escaping* from the liposome.

Let us have a closer look at the references $F_{\text{ref},1}$ and $F_{\text{ref},2}$, inside and outside, respectively. When the solubility of the permeants is the same inside and outside the liposome, the permeants have the same free energy inside and outside, F_{ref} in short, and Eqs. 3.29 and 3.31 are equivalent and equal to

$$\frac{1}{P(r)} = r^2 e^{-\beta F_{\text{ref}}} \int_{r_1}^{r_2} \frac{1}{r'^2 D(r') e^{-\beta F(r')}} dr' \tag{3.32}$$

However, it can also occur that the liposome packages a formulation inside that differs from the outside water phase, such that $F_{\text{ref},1} \neq F_{\text{ref},2}$. Micelles are other molecular structures, where often the inside and outside environment differ. The permeability then depends on the chosen reference, i.e. entering from outside (P_{entr}) or escaping from inside (P_{esc}), but either definition is simply related by the permeant’s solubility ratio,

$$\frac{P_{\text{entr}}(r)}{P_{\text{esc}}(r)} = e^{-\beta(F_{\text{ref},1} - F_{\text{ref},2})} \tag{3.33}$$

In thermodynamic equilibrium, this free energy ratio would be equal to the concentration ratio $c(r_2)/c(r_1)$. The dependence of the permeability definition on the reference is not characteristic for liposomes with radial symmetry, but it also appears for flat bilayers where the left and right side of the membrane differ. The latter situation is in practice usually not encountered in a single flat bilayer simulation, as left and right compartments are then indiscernible because of periodic boundary conditions.

The permeability Eqs. 3.29 and 3.31 are dependent on r and thus do not define the liposome’s transport properties uniquely. In the next subsection, we define the liposome permeability by comparing with a flat membrane and discuss the dependence on the curvature.

3.2.2 Defining liposome permeability

While the product $J(r)r^2$ is independent of r in steady-state with spherical symmetry, $P_{\text{entr}}(r)$ or $P_{\text{esc}}(r)$ are not. The question arises which r is most appropriate to represent the permeability. Let us first look at the steady-state conditions of Fig. 3.4a for P_{entr}. Since $c(r_1)$ is kept at zero in this steady-state situation, all flux at $r = r_1$ originates from permeants that started at the other side of the membrane at $r = r_2$. In other words, no recrossings can occur at $r = r_1$ because of the boundary condition. Hence, $|J(r_1)|$ can be regarded as the entrance flux of permeants that effectively crossed the membrane. This makes us define the *entrance permeability* from Eq. 3.29 as

$$P_{\mathrm{entr}} \equiv P_{\mathrm{entr}}(r_1) \tag{3.34}$$

Similarly, for $P_{\mathrm{esc}}(r)$ in Fig. 3.4b, the flux at $r = r_2$ is now equal to the escape flux, which is the flux of particles effectively coming from the liposome's inside and escaping all the way through the membrane, as there are no recrossings possible under the condition $c(r_2) = 0$. This makes us define the *escape permeability* from Eq. 3.31 as

$$P_{\mathrm{esc}} \equiv P_{\mathrm{esc}}(r_2) \tag{3.35}$$

based on the flux $|J(r_2)|$ through r_2 caused by a concentration at the reference location r_1. The escape and entrance permeabilities are related to each other. By filling in their definitions into Eqs. 3.29 and 3.31 and taking the ratio, their relation reads

$$P_{\mathrm{esc}} \frac{e^{-\beta F_{\mathrm{ref},1}}}{r_1^2} = P_{\mathrm{entr}} \frac{e^{-\beta F_{\mathrm{ref},2}}}{r_2^2} \tag{3.36}$$

Whilst P_{entr} and P_{esc} have a clear interpretation, it still leaves the question open whether P_{entr} or P_{esc} is more suitable to describe the liposome's membrane permeation. With $P_{\mathrm{entr}}/P_{\mathrm{esc}} = r_2^2/r_1^2 = (1+h/r_1)^2$, it is clear that P_{entr} is higher than P_{esc}, even by an infinite factor for the most curved membrane. This can have an implication on comparing experimental escape or entrance permeabilities of curved liposomes with simulated data of flat bilayers. Concretely, $P_{\mathrm{entr}}/P_{\mathrm{esc}}$ gives a difference of 2% for a cell-sized vesicle with a diameter of $1\,\mu$m, with $r_1 = 500\,\mathrm{nm}$ and $r_2 = 505\,\mathrm{nm}$. Meanwhile, $P_{\mathrm{entr}}/P_{\mathrm{esc}}$ is a factor 4 for a very small liposome with $r_1 = 5\,\mathrm{nm}$ and $r_2 = 10\,\mathrm{nm}$. Curvature effects are thus significant for smaller liposomes. A wide liposome size distribution in experiment will also negatively influence the quality of the comparison between experiment and flat membrane simulations.

As a strategy to address whether P_{entr} or P_{esc} is more suitable, we keep the final aim in mind, where we would like to assess if a liposome membrane is more, or less, permeable than a flat bilayer. A membrane that is indiscernible between the liposome and the flat setup, except for its curvature, should then have the same permeability value. We will therefore construct a hypothetical homogeneous liposome and flat bilayer, and use this condition of equivalent permeabilities as a guideline.

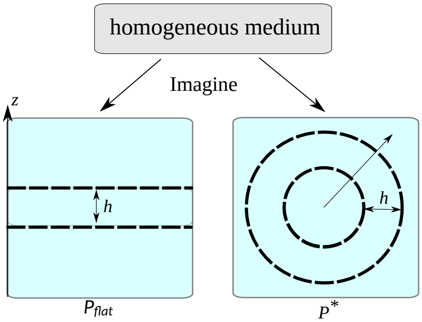

Figure 3.5: Imaginary flat bilayer and imaginary liposome of thickness h in a homogeneous water box. We impose that these have equal permeability as a guideline to define the liposome's permeability P^*.

To create the homogeneous systems, we look at the artificial situation of a pure water box, in which we draw in our mind an imaginary flat bilayer or an imaginary liposome, as shown in Fig. 3.5. The imaginary membranes both have thickness h. Since the membranes are just lines in our imagination and actually consist of just pure water, the permeability through the imaginary flat membrane and imaginary liposome should be exactly the same, i.e. they should be equal to the permeability through a layer h of homogeneous water. The diffusivity D in homogeneous water is independent of z or r, and the free energy is constant everywhere. The permeability through a flat imaginary bilayer of thickness h follows from Eq. 3.22,

$$P_{\text{flat}} = \frac{D}{h} \tag{3.37}$$

whereas Eq. 3.32 gives the permeability for the imaginary liposome,

$$P(r) = \frac{r_1 r_2}{r^2} \frac{D}{h} \tag{3.38}$$

As we are working with imaginary membranes, we aim for the liposome permeability to be equal to the flat bilayer permeability. Comparing the two previous equations, this is possible by defining the liposome permeability as $P^* \equiv P(r^*)$, evaluated at a radial distance $r^* = \sqrt{r_1 r_2}$, which lies intermediate between r_1 and r_2. With this definition, the target $P^* = P_{\text{flat}}$ is achieved.

Moreover, this P^* definition can be linked to the liposome escape and entrance permeability, which are

$$P_{\text{entr}} = \frac{r_2}{r_1} \frac{D}{h} \tag{3.39}$$

$$P_{\text{esc}} = \frac{r_1}{r_2} \frac{D}{h} \tag{3.40}$$

for the homogeneous medium. It is clear that $P_{\text{esc}} < P_{\text{flat}} < P_{\text{entr}}$, and we notice that P^* is the geometric mean of the escape and entrance permeability,

$$P^* \equiv P\left(\sqrt{r_1 r_2}\right) = \sqrt{P_{\text{entr}} P_{\text{esc}}} \tag{3.41}$$

In conclusion, choosing the geometric mean of escape and entrance permeability as the liposome permeability permits a fair comparison with the flat bilayer. For a membrane with position-independent diffusivity and free energy, the flat and curved bilayers will have the same permeability value, as aimed for.

Finally, let us discuss how the P^* definition acts for arbitrary membranes. To elucidate the effects, we will turn again to the purely diffusive assumption, since the Smoluchowski equation provide analytical solutions. Consider a membrane with position-dependent diffusivity or free energy across the membrane, assuming equal permeant solubility on both sides of the membrane. Maintain the liposome permeability definition of Eq. 3.41 also in this general case, Eqs. 3.29, 3.31, 3.34, and 3.35 lead to

$$P^* = r_1 r_2 e^{-\beta F_{\text{ref}}} \int_{r_1}^{r_2} \frac{1}{r'^2 D_\perp(r') e^{-\beta F(r')}} dr' \tag{3.42}$$

This expression allows us to highlight the effect of curvature. Consider a flat membrane with $F(z)$ and $D_\perp(z)$ along the membrane normal and a liposome with $F(r)$ and $D_\perp(r)$ along the radial direction. Assume those two F profiles and D profiles look identical, and the membranes have identical thickness $h = r_2 - r_1$. The permeability through the flat bilayer follows from Eq. 3.22 and has the following shape,

$$\frac{1}{P_{\text{flat}}} = \int_{-h/2}^{h/2} f(z) dz \tag{3.43}$$

with $f(z)$ a specific function of the F and D profiles. Meanwhile, Eq. 3.42 gives the permeability for the liposome, which has this shape

$$\frac{1}{P^*} = \int_{r_1}^{r_2} \frac{r_1 r_2}{r^2} f(r) dr^2 \tag{3.44}$$

figuring the *same* function f. For homogeneous media, the function f is constant, and $P_{\text{flat}} = P^*$ as anticipated. For inhomogeneous media, however, f is not constant. The additional $r_1 r_2 / r^2$ in the integrand is a reweighing factor. The area under the curve $r_1 r_2 / r^2$ over the interval $[r_1, r_2]$ is equal to the area under the curve 1, meaning that the function f is redistributed over the interval. Values closer to the liposome center receive a higher weight in the integral. This reweighing is in fact a consequence of the Jacobian r^2 factor arising from using the spherical coordinate r. The practical consequence of the reweighing is that two identical membranes, yet one is flat and the other is curved, will differ in permeability: $P_{\text{flat}} \neq P^*$. Moreover, the permeability changes with curvature. Inhomogeneity in F or D will therefore make the permeability P^* curvature-dependent, and the effect depends on the liposome size and membrane thickness.

The liposome permeability is the geometric mean of the escape and entrance permeabilities, and it can also be written as the permeability $P(r)$ evaluated at the geometric mean $r^* = \sqrt{r_1 r_2}$ of the radii. While this follows from the reasoning with imaginary membranes, this geometric mean can also be given a physical interpretation. Eq. 3.32 for $1/P(r)$ implies that the function $P(r)$ itself is a $1/r^2$ function multiplied by a factor a that is independent of r; hence $P(r) = a/r^2$. Consequently, the average function value of $P(r)$ over the membrane thickness h is

$$\big\langle P(r) \big\rangle_h = a/h \int_{r_1}^{r_2} \frac{1}{r'^2} dr' \tag{3.45}$$

The integral is here equal to $h/(r_1 r_2)$. Averaging a $1/r^2$ function, where the r^2 originates from the spherical surface areas of liposomes, makes the square of the geometric mean, $r_1 r_2$, appear. For the average of $P(r)$, this leads to

$$\big\langle P(r) \big\rangle_h = a \frac{1}{r_1 r_2} = P(r^*) \equiv P^* \tag{3.46}$$

This effectively gives our definition of the liposome permeability P^* the interpretation of the mean value of $P(r)$, taken over the whole membrane thickness. Moreover, the appearance of the geometric mean allows to formulate an elegant summation rule for the permeabilities of two subsequent layers, $[r_1, r_2]$ and $[r_2, r_3]$,

$$\frac{1}{r_1 r_3 P_{[1,3]}} = \frac{1}{r_1 r_2 P_{[1,2]}} + \frac{1}{r_2 r_3 P_{[2,3]}} \tag{3.47}$$

The summation rule is obtained by slightly rearranging Eq. 3.42 and splitting up the integration interval $[r_1, r_3]$ of the total permeability $P_{[1,3]}$.

We end this subsection by offering another way to look at the additional r^2 factor in the denominator of Eq. 3.44. This Jacobian factor can be absorbed by defining an adapted free energy profile.

The free energy is related to the permeant concentration by $c(r) = c_{\text{ref}}\, e^{-\beta(F(r)-F_{\text{ref}})}$ where the reference concentration and free energy are taken at some reference radial distance r_{ref}. Let us define the radial density profile $\rho(r)dr = c(r)4\pi r^2 dr$, which is the number of particles in a spherical shell with radius r with infinitesimal thickness dr. The corresponding free energy profile, apart from a constant shift $-\ln(4\pi)$, is

$$\begin{aligned} \tilde{F}(r) &= F(r) - 2\ln(r) && (3.48) \\ e^{-\beta\tilde{F}(r)} &= r^2 e^{-\beta F(r)} && (3.49) \\ \rho(r) &= \rho_{\text{ref}}\, e^{-\beta(\tilde{F}(r)-\tilde{F}_{\text{ref}})} && (3.50) \end{aligned}$$

with $\tilde{\rho}_{\text{ref}}$ and $\tilde{F}_{\text{ref}}$ the radial density and the adapted free energy at location r_{ref}, respectively. This means that liposome permeability of Eq. 3.42 may be rewritten as

$$P^* = e^{-\beta\tilde{F}_{\text{ref}}} \int_{r_1}^{r_2} \frac{1}{D_\perp(r')e^{-\beta\tilde{F}(r')}} dr' \qquad (3.51)$$

which has now the same shape as the flat membrane equation (Eq. 3.22), but it figures the adapted free energy $\tilde{F}(r)$ associated to the radial density $\rho(r)$ instead of the permeant concentration $c(r)$. In other words, if the Jacobian factor r^2 is incorporated in the free energy, our liposome definition P^* resorts to the shape of the flat bilayer equation. The Jacobian causes the dependence of the permeability on the curvature. Indeed, the importance of the Jacobian factor depends on the boundaries r_1 and r_2. For highly curved membranes, the Jacobian factor changes $\tilde{F}$ considerably with respect to F. However, for slightly curved membranes in large liposomes, the $-2\ln r$ factor is nearly constant over the integrand.

3.2.3 Liposome permeability from the counting method

As described in the section 3.1 on permeability for flat membranes, permeability can be calculated by counting the crossings through the membrane, as demonstrated in Eq. 3.6. In the flat membranes, the dividing surfaces at $z = \pm h/2$ are flat surfaces with equal area σ. However, these become spherical surfaces for the liposome at $r = r_1$ and $r = r_2$, whose area depends on the radial distance r. Therefore, we will provide an update of the counting method for spherically shaped membranes.

Consider again a long equilibrium MD simulation, this time of a liposome. Count the number of crossings n_{entr} of permeants entering the liposome through the membrane and reaching the inner spherical dividing surface with cross-section $\sigma_1 = 4\pi r_1^2$ at radius r_1. The corresponding inward flux at r_1 is

$$|J_{\text{entr}}| = \frac{n_{\text{entr}}}{T_{\text{sim}}\sigma_1} \tag{3.52}$$

with $J_{\text{entr}} < 0$. Similarly, the flux of escaping particles reaching $\sigma_2 = 4\pi r_2^2$ is

$$J_{\text{esc}} = \frac{n_{\text{esc}}}{T_{\text{sim}}\sigma_2} \tag{3.53}$$

with $J_{\text{esc}} > 0$. In other words, the flat membrane fluxes $J_{\leftarrow}$ and $J_{\rightarrow}$ are the equivalents of the liposome radial fluxes J_{entr} (< 0) and J_{esc} (> 0) of membrane crossings. Since the equilibrium MD can be seen as a superposition of the two steady-states in Fig. 3.4, similarly as in the derivation of Eq. 3.6, these two equilibrium radial fluxes are equal to the two steady-state fluxes of the previous subsection (Fig. 3.4). Using the definitions $P_{\text{entr}} \equiv P_{\text{entr}}(r_1)$ and $P_{\text{esc}} \equiv P_{\text{esc}}(r_2)$ from the previous subsection, the permeability equations become

$$P_{\text{entr}} = \frac{|J_{\text{entr}}|}{c_{\text{ref}}} \tag{3.54}$$

$$P_{\text{esc}} = \frac{J_{\text{esc}}}{c_{\text{ref}}} \tag{3.55}$$

By transferring our liposome permeability definition Eq. 3.41 for P^* to the case of non-diffusive transport, the geometric mean of P_{entr} and P_{esc} is again used,

$$P^* = \frac{\sqrt{|J_{\text{entr}}|\, J_{\text{esc}}}}{c_{\text{ref}}} = \frac{|J_{\text{entr}}|}{c_{\text{ref}}}\frac{r_1}{r_2} = \frac{J_{\text{esc}}}{c_{\text{ref}}}\frac{r_1}{r_2} \tag{3.56}$$

In terms from crossings the total number of (bidirectional) crossings $n_{\text{cross}} = n_{\text{esc}} + n_{\text{entr}}$ through the liposome membrane, the liposome permeability reads

$$P^* = = \frac{n_{\text{cross}}}{8T_{\text{sim}}\pi r_1 r_2\, c_{\text{ref}}} \tag{3.57}$$

Here, $n_{\text{esc}} \approx n_{\text{entr}}$ was used, assuming that in a long equilibrium simulation, there is no accumulation of particles, and the numbers of permeants entering or escaping the liposome are approximately equal.

3.2.4 Illustration with CG MD

The equation defining curved membranes' permeability (P^*) is exemplified through CG MD simulations of systems comprising both flat and curved membranes, enabling a comparative analysis of water permeability in these systems. The reported permeabilities in this section are all based on the counting method, computed with Eq. 3.6 for flat membranes, Eqs. 3.54-3.55 for P_{entr} and P_{esc} of liposomes, and Eq. 3.41 for liposome permeability P^*.

Systems and computational details

Two homogeneous membranes consisting of DPPC and two binary membranes consisting of DPPC and 10% cholesterol were modeled with CG MD simulations. The simulation box (see Fig. 3.6 either contained a flat membrane (label F) or a liposome (label L) with a radius of approximately 50 Å. The composition of each system is given in Table 3.1. The box also contained 0.15 Molar sodium chloride, as well as a very low concentration of 20 neutral N0 beads, which have not been focused on in the present work.

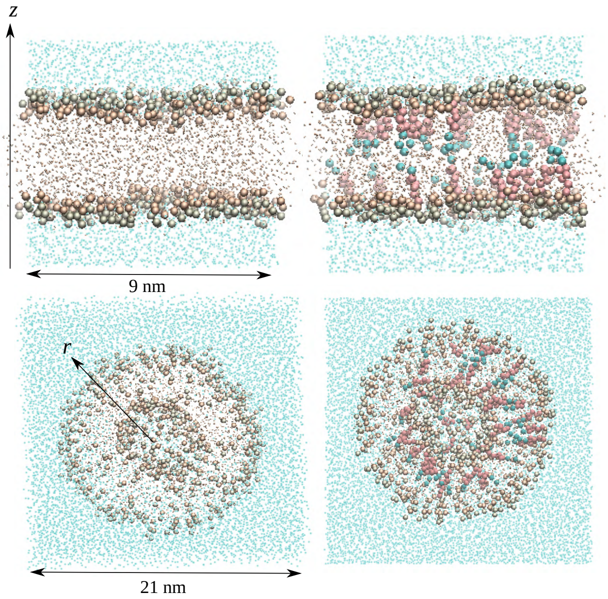

Figure 3.6: Simulation box of flat membranes (top) and liposomes (bottom), modeled with a CG forcefield. Left: pure DPPC; right: DPPC:CHOL composition. Large beads are phosphate head groups (PO4 beads, light green), glycerol groups (GL1 beads, light brown), and cholesterol (pink and blue). Small beads are water (light blue) and DPPC tail beads (light orange).

system	DPPC:chol (%)	# lipids	# in / out	# waters	# ion pairs
F	100:0	256	128 / 128	2504	29
F-Ch	90:10	260	130 / 130	2452	28
L	100:0	518	124 / 394	54507	603
L-Ch	90:10	545	145 / 400	76608	842

Table 3.1: Composition of the simulated flat bilayers (label F) and the liposomes (label L) with number of lipids in each leaflet, number of water molecules, and number of sodium chloride ion pairs. Each system also contained 20 N0 beads. The DPPC versus cholesterol content is given in percentages.

Initial structures of the membranes were prepared with the CHARMM-GUI website [147, 149, 150]. Using the Martini 2 forcefield for the CG beads, the MD simulations were run with the Gromacs-2021.4 [142, 146]. The Coulombic interactions were calculated using the reaction-field approach [141]. Truncation of 11 Å was applied for the Coulombic and the van der Waals interactions, where potentials were shifted to zero at the cutoff with the potential-shift-Verlet modifiers. The neighbor list length was 11 Å, updated using the Verlet neighbor search algorithm. The equations of motion were integrated with a time step of 20 fs using the leap-frog integrator, and coordinates were stored every 20 ps. The velocity rescale thermostat was used with the coupling constant of 1 ps to set the temperature at 323 K, which lies above the melting temperature of DPPC, thus ensuring that the membrane is in the liquid disordered phase [151]. The Parrinello-Rahman barostat at 1 bar was employed with a coupling constant of 12 ps, and semi-isotropic and isotropic isothermal compressibility of 3×10^{-4} and 4.5×10^{-5} bar^{-1} for systems with a flat bilayer and a liposome, respectively. At every 100 time steps, the center of mass motion of the system was removed. First, systems were energy minimized and equilibrated in the NPT ensemble for 100 ns, up to 600 ns for liposomes to allow for water exchange between interior and exterior, followed by a 1000 ns NPT production run.

Membranes' structure

The membrane thickness and area per lipid in Table 3.2 are measures of the membrane's geometry and compactness. To determine the membrane thickness h from the MD trajectories, the average position of the phosphate Martini beads (PO4) is evaluated, using z or r for the flat or curved membranes, respectively. For a flat membrane, the bilayer is centered around $z = 0$ and then the average $|z|$ over all PO4 beads is computed, which is equal to $h/2$.

For a liposome, the membrane is centered around $r = 0$ and the two average radial distances of the PO4 beads in the inner and outer layer are used as the two radii r_1 and r_2, which determine the thickness $h = r_2 - r_1$. It has been verified that no PO4 beads flip-flopped between leaflets during the simulation.

To determine the area per lipid A_l, the number of lipids per leaflet is counted and is reported in Table 3.2. For a liposome, the average areas per lipid $A_{l,1}$ and $A_{l,2}$ are computed as the area $4\pi r_1^2$ and $4\pi r_2^2$, divided by the number of lipids in the inner and outer leaflet, respectively.

Comparing the flat and curved membranes in Table 3.2, the curvature makes the membrane appear to be thinner, with a reduction in h from about 40.2 Å to about 35.6 Å. The curvature makes the area per lipid lower in the inner liposome leaflet compared to the flat membrane, meaning that the phosphate groups are more densely packed in the inner leaflet, while the inverse effect is seen for the outer leaflet. Inspired by the permeability definition in Eq. 3.41, we compute the geometric mean of the areas, $A_l^* = \sqrt{A_{l,1} A_{l,2}}$. This value indicates that overall, the liposome's lipids are less densely packed than in the flat membrane. This is also confirmed by estimating the volume per lipid (values not shown).

The incorporation of cholesterol introduces a clear reduction in the area per lipid, in accordance with other works reporting on the effect of cholesterol. Alwarawrah et al. reported that the area per DOPC lipid at 323 K decreases from 67.1 Å^2 to 59.6 Å^2 by including 10% cholesterol in the membrane [155]. A similar trend was observed by another research group, analytically investigating the effect of cholesterol on the area per lipid at 323 K, with a 15% reduction in the area being occupied by lipid molecules in the membrane containing 10% cholesterol [156]. In our simulation, this fall in the area per DPPC lipid is about 9% (from 63.6 Å^2 to 58.1 Å^2) for the flat membranes and 7% (from 66.4 Å^2 to 61.6 Å^2) for the curved membranes. Cholesterol in the membrane is also known to increase the membrane thickness. MD simulation was performed at 323 K by Leeb et al. to assess the changes in the membrane thickness composing cholesterol. They resulted that 10% cholesterol can increase the DPPC bilayer thickness from 40.5 Å to 43.7 Å (8%) [157]. A smaller increase of about 6% for the thickness was reported at 323 K for the DPPC-chol (10% chol) membrane by Alwarawrah [155]. However, this effect on the membrane's thickness is less noticeable in our systems with a flat (2%) or curved (0.7%) bilayer, suggesting here a stronger effect of the curvature than of the cholesterol content.

system	h	A_l				
F	40.2	63.6				
F-Ch	41.2	58.1				
system	h	r_1	r_2	$A_{l,1}$	$A_{l,2}$	A_l^*
L	35.6	20.7	56.3	43.6	101.1	66.4
L-Ch	35.3	21.0	56.3	38.1	99.5	61.6

Table 3.2: Structural characteristics of simulated flat and curved membranes: membrane thickness h (in Å); radii r_1 and r_2 (in Å); area per lipid A_l, $A_{l,1}$, $A_{l,2}$, and A_l^* (in Å^2).

Water permeability

To compute the permeability of water molecules through the membrane, the number of crossings and water concentrations need to be evaluated. For flat membranes, the dividing surfaces are set to $|z| = h/2$, and membrane crossings are detected with the Rickflow package [71]. The water concentration is evaluated in the flat region of the water histogram. For the liposomes, we implemented an extension of the Rickflow package to detect membrane crossings through the spherical dividing surfaces with radii r_1 and r_2. The reference water concentration inside (outside) the liposome is determined by counting the average number of water beads with $r < 12\,\text{Å}$ ($r > 70\,\text{Å}$) where the water histograms visually flatten out, and dividing by the appropriate volume. In our simulations, the number of crossings of water beads varies between 41 and 179, and the water concentration varies between 0.94 and 0.98 g/cm^3.

Fig. 3.7 provides detail on the permeability of water molecules through the flat and curved membranes. Cholesterol seems to reduce the permeability, in accordance with the tighter packing (volume per lipid) in cholesterol containing membranes. A drop of 24% is seen in both the flat (P) and curved (P^*) bilayer (though not statistically significant).

Finally, let us focus on the effect of curvature. For the liposomes, the entrance permeability is about a factor 6.4 (7.0) times higher than the escape permeability for the membrane without (with) cholesterol. This very large range in permeabilities illustrates the ambiguity in the numerical evaluation of liposome permeability. Fortunately, our definition P^* gives a single value, which may be directly compared to the flat membranes. As shown in Fig. 3.7, the curvature increases the permeability roughly by a factor 1.7 in the membranes without/with cholesterol. In our simulations, the curvature decreased the membrane thickness and increased the area per lipid. The elevation seen

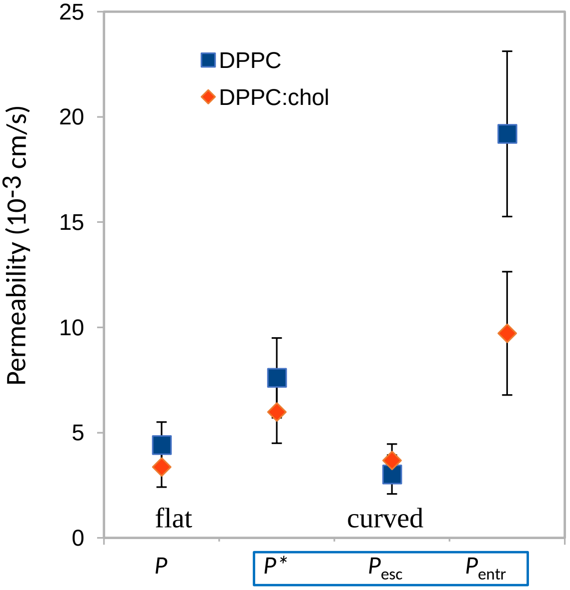

Figure 3.7: Water permeability of flat membranes (P) and liposomes (P^*, P_{esc}, P_{entr}). Error bars refer to standard error assuming that crossings are independent observations of a Poisson process [32]. Composition without (squares) or with (diamonds) cholesterol.

in the water permeability for the curved membranes can be due to these changes in the thickness and the area per lipid, as these changes can facilitate the water permeation through the bilayer. The liposome permeability definition P^* thus enabled a fair assessment of the curvature effect on the permeability of DPPC and DPPC:chol membranes.

Chapter 4

COUNTING CROSSINGS LIMITATIONS

In this chapter, we focus on the limitations of the counting crossings method using CG MD simulations. Our discussion on the simulation results revolves around how the free energy profile of the permeant affects the accuracy of the counting crossing method in permeability calculations.

As outlined in Section 2.2, we conducted simulations involving 16 CG beads, each characterized by distinct free energy profile. This approach allowed us to assess the influence of the permeant's free energy profile on the efficiency of the counting crossings method. In the subsequent sections, we will demonstrate that all permeants' free energy profiles can be classified into three distinct types. Furthermore, we will elucidate the relationship between the permeant's free energy profile and its permeability through the membrane.

4.1 THREE TYPES OF FREE ENERGY PROFILES

The free energy profile was determined from the histogram $p(z)$ of the position of the CG beads as $F(z) = -k_B T \ln p(z)$. Fig. 4.1 presents $F(z)$ for three exemplary bead types. Bead AC2 has a deep free energy well, hence it is highly soluble in the membrane ($K \gg 1$). Bead P1 has a high free energy barrier and is insoluble in the membrane

($K \ll 1$). Bead SN0 shows a mix of free energy well and barrier, where the solubility depends on the exact location in the membrane. The other bead types had similar profiles with different elevations.

4.2 NUMBER OF CROSSINGS: EFFECT OF FREE ENERGY

Fig. 4.2 shows the number of detected crossings versus ΔF for the 16 beads (full symbols), where ΔF is computed as the free energy difference between the membrane center and the membrane border. The graph clearly follows the shape of the curves in Fig. 3.2a, where n_{cross} generally drops with $|\Delta F|$. These MD values are compared to the model values of n_{cross} (open symbols), based on the flux in the compartmental model (Eq. 3.11) or the more general formulation of the Smoluchwoski model (Eq. 3.15). The model parameters were inferred from the MD simulations.

For Eq. 3.11, K is computed as $\exp(-\beta\Delta F)$, $h_m = 4.6\,\text{nm}$ corresponding to the membrane, the average box length $L = 10\,\text{nm}$, and $T_{\text{sim}} = 270\,\text{ns}$. The normal diffusivity D_{zz} describes diffusion normal to the membrane surface, but the measured D_{zz} already incorporates the effects of the barrier or well. Therefore, the lateral diffusivity $D_{||} = (D_{xx} + D_{yy})/2$ was taken as the diffusivity D in the model, since diffusion parallel to the membrane is not hindered by free energy barriers/wells. The water thickness d was varied from

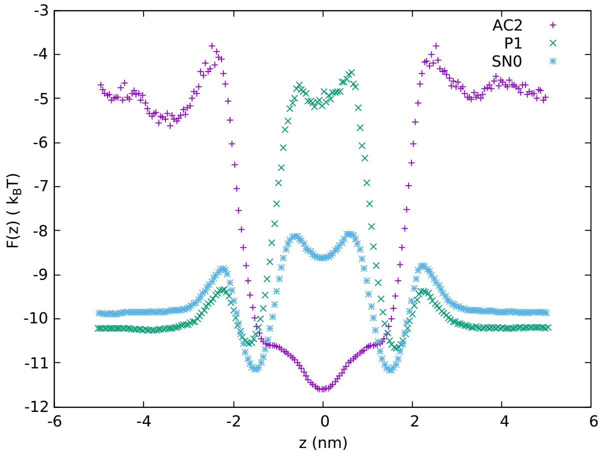

Figure 4.1: Free energy of three selected bead types that are representative of a free energy barrier (P1), a free energy well (AC2) and a mix of both (SN0). The profile $F(z) = -k_B T \ln p(z)$ is plotted with $p(z)$ the histogram of the 20 permeants' z-coordinates over all 90 000 snapshots.

0 to $(L - h_m)/2$, giving a range of crossings that is indicated as a dashed vertical line on the graph. The lower end of the line corresponds to the number of crossings through the whole simulation box ($h = L$), while the higher end corresponds to the number of crossings through the membrane only. For $\Delta F \ll 0$, the number of crossings clearly is highly sensitive to the considered membrane thickness. For $\Delta F \gg 0$, the number of crossings is no longer sensitive to the water layer thickness (lines mostly hidden by symbols), in accordance with Fig. 3.2a. It was found that a decent correspondence with the MD data could be obtained for a small water layer thickness $d = 0.1\,\mathrm{nm}$, which was added to the plot with a gray open symbol. The spread of the vertical lines however indicate that almost any value can be the outcome by tuning the parameter d. This indicates again that the number of crossings, and hence the permeability, is very sensitive to the considered thickness. One should therefore be cautious when interpreting and citing experimental or computational results for highly permeable membranes.

For Eq. 3.15, the integral is evaluated using the measured free energy profile $F(z)$, the same constant diffusivity, and $d \approx 0$ (not

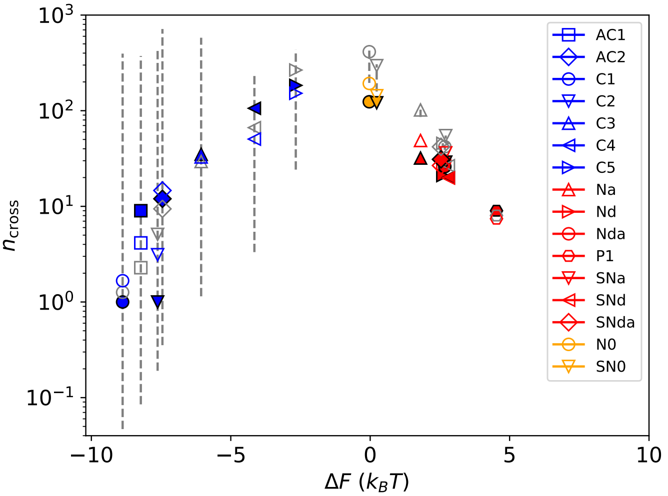

Figure 4.2: Number of crossings n_{cross} as a function of ΔF for the 16 permeant types. Filled symbols: value as measured in the MD simulations with color according to bead type, i.e. well (blue), barrier (red), and mix (orange). Grey open symbols: value based on compartmental model (Eq. 3.11) with $d = 0.1\,\mathrm{nm}$. Vertical dashed lines show the range between setting $d = 0$ (top of line) and $d = (L - h_m)/2$ (bottom of line). Colored open symbols: value based on general Smoluchowski model (Eq. 3.15).

exact because of binning in $p(z)$), giving the values indicated with a colored open symbol. Compared to the compartmental model, this more general model uses a position-dependent solubility, which allows describing more details of the membrane. Despite the crudeness in the parameter estimations, a good agreement is found between these model values and the numerical MD data in Fig. 4.2. The permeants in the present simulations are of course only a single bead without internal degrees of freedom, and the membrane contains only one phospholipid type. For more realistic membranes and realistic permeants, the compartmental model or the more general formulation (Eqs. 3.11, 3.15) might not have a sufficient level of detail to match the MD results. An extension of the model in Fig. 3.1 could for instance be a model that has both a free energy well and barrier. However, the complexity of more realistic simulations not only comes from the inhomogeneity in F and D, but there might also be memory effects that make the kinetics non-Markovian, while the Smoluchowski equation is based on the Markovian assumption. Another challenging situation is when the permeation is accompanied by hysteresis, which is caused by not observing energy barriers in some orthogonal degree(s) of freedom (orthogonal to the permeation direction z). This is for instance the case when the permeant has an internal degree of freedom that is changed during the permeation, e.g. a dihedral angle in an oligopeptide, or an orientational degree of freedom, e.g. the ring plane in ibuprofen. A two-dimensional or higher-dimensional diffusive equation should then be constructed, which captures all reaction coordinates that are relevant for the permeation.

In these more advanced approaches, based on more elaborate multidimensional models with kernels, the free energy would still be one of the main parameters. The present analysis based on a Smoluchowski equation can therefore be seen as a decent first approximation to gain insight in the sampling efficiency. The presented curves clearly illustrate that a higher variation in the free energy profile results in lower sampling efficiency. Both deep wells and high barriers cause a dramatic drop in crossings, and the counting method for permeability will perform inaccurately in those cases.

Concluding remarks. In both the cases of a high free energy barrier and a deep free energy well, it can be concluded that the permeability calculation by counting crossings will face failure because of the insufficient number of crossing during the simulation. To overcome this problem, one should resort either to running longer MD simulations to observe more crossings, using larger simulation boxes with more permeants, or implementing other simulation methods that are applicable for rare events, such as replica exchange transition interface sampling (RETIS) or milestoning [102, 103, 158, 159]. In recent work, the connection between RETIS and the permeability was derived, and this method can be a valid alternative for the counting method [104, 160]. Another train of thought is the use of biased simulations, where large variety in the free energy is canceled out artificially by adding a bias potential [161–163].

CHAPTER 5

INVESTIGATING pH-SENSITIVE LIPOSOME: CURVATURE AND COMPOSITION EFFECT

The derived equation for curved membrane permeability will be applied to a pH-sensitive liposome system in this chapter, and the resulting permeability values will be reported. The discussion will explore the influence of membrane curvature and composition on membrane properties, including membrane permeability in this system.

In this chapter, we conduct simulations on 62 systems consisting of flat and curved membranes to evaluate the impact of membrane curvature and composition on pH-sensitive liposomes permeability. Specifics on the simulated systems and settings are given in Section 2.3.

5.1 AREA PER LIPID

Membrane composition effect

In this section, we will assess the impact of membrane curvature and composition on the membrane area per lipid. Fig. 5.1 illustrates how FAs and cholesterol affect the APL of the flat membrane. A pure DPPC flat membrane has an APL of 63.6 Å^2, which agrees well with experimental values at a temperature of 323 K [164]. Flat bilayers containing neutral FAs exhibit a smaller APL, for instance, with F-10C10 and F-10C14 showing decreases of 6% each. This is in agreement with an experimental study reporting that the APL decreases in the presence of saturated long-chain FAs, such as stearic acid, in a DPPC monolayer [165]. They attributed this to the impact of neutral FAs, which cause the DPPC molecules to separate and 'dilute', thus reducing the electrostatic repulsion between their head groups.

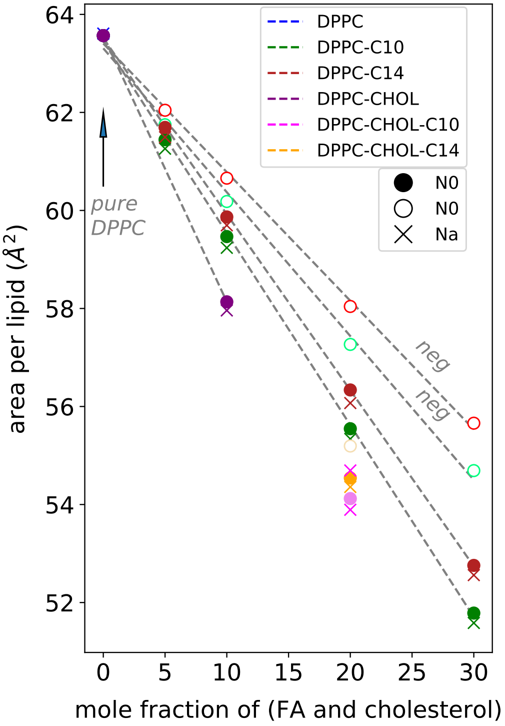

Figure 5.1: APL of flat bilayers as a function of the molar fraction of FAs and cholesterol combined. Symbols are circles for systems containing N0, crosses for systems containing Na. Full (dark) and empty (lighter) circles show systems with neutral and deprotonated FAs, respectively. Gray dashed lines are linear regression fits.

The incorporation of cholesterol into the membrane also results in the strongest reduction of APL, from 63.6 $Å^2$ to 58.1 $Å^2$ (a decrease of about 9% for F-10Ch). Similar trends were reported in simulation studies for different phospholipid molecules, with a 13 to 21% decrease in APL by incorporating 10 to 30% cholesterol in a lipid membrane [166, 167]. In all our systems, the type of the permeants (N0 or Na) does not significantly affect the membrane's APL (Tables in SI of Paper 4 in Part 7.2), indicating that the low concentration of permeants does not disturb the membrane structure. Moreover, in systems containing both FAs and cholesterol, the drop in APL is even more substantial compared to systems containing cholesterol alone.

A similar trend of APL reduction is noticeable in systems with deprotonated FAs, but less pronounced (a decrease of 5% for both F-10C10-n and F-10C14-n, and stronger with higher FA concentration) than with the neutral FAs. The deprotonated FA charges can cause repulsive forces, increasing the distance between FAs and counteracting the 'diluting' effect of FAs which was mentioned earlier in this section. Interestingly, a recent study by Larsson et al. investigated the effect of C10-n on the APL of a POPC membrane, using an all-atom forcefield at 310.15 K [130]. The APL was also computed differently, dividing the simulation box by the number of phospholipid molecules without counting the number of C10-n, so the trends in APL cannot be compared directly with our results. They found a modest increase of about 3% in the area per POPC molecule caused by incorporating 10% C10-n. The authors attributed this rise to the repulsion between the negative charges of C10-n.

The APL reduction caused by FAs or cholesterol can be also be understood by looking at the small size of the FAs molecules, which have just one tail, compared to the DPPC molecules with two tails. Moreover, the shorter chain FA, C10 consisting of three CG beads, has also a larger impact on reducing APL than the longer chain FA, C14 with four beads. The dependence of the APL on the FA concentration is approximately linear in Fig. 5.1. By fitting the slope of the graphs, an estimate of the area per molecule type could be estimated (values in SI), similarly to the ideal mixing fitting in monolayers (see e.g., [165]). In terms of molecule size, this gives the ordering DPPC > C14-n > C10-n > C14 > C10 > Chol, indicating that neutral FAs and cholesterol can indeed modify the membrane's structure more strongly than the deprotonated FAs.

Membrane curvature effect

Next, the curved membranes are discussed, based on the APL of the inner (A_{in}) and the outer (A_{out}) leaflet of the liposome bilayer, as shown in Fig. 5.2. A decrease in the liposome curvature leads to a reduction in the APL of the outer layer, while the inner layer's APL increases (Fig. 5.2a). This effect has also been observed by Risselada and Marrink, and it can be explained by the spherical shape of liposomes, which causes contradictory effects on their inner (concave) and outer (convex) layers [132]. In liposomes, the lipid head groups in the outer layer move further apart, while those in the inner layer move closer together [168]. Consequently, the outer leaflet features a less tightly packed arrangement of lipids, while the inner leaflet is characterized by a denser packing of lipids compared to a flat membrane [92, 93, 132]. In the pure DPPC bilayers (Fig. 5.2a), the APL in both leaflets gradually approaches that of a flat bilayer with zero curvature (63.6 Å, system F). Nevertheless, the A_{in} and A_{out} values for the largest simulated liposome, L_{130}, are still noticeably different from the flat bilayer's APL. As seen from the geometric mean of A_{in} and A_{out}, denoted A^* , curvature causes an increase of at most 4% for the pure DPPC bilayers, from the flat bilayer value (63.6 Å, system F) to the curved membrane ($A^* = 66.3$ Å, system L_{50}).

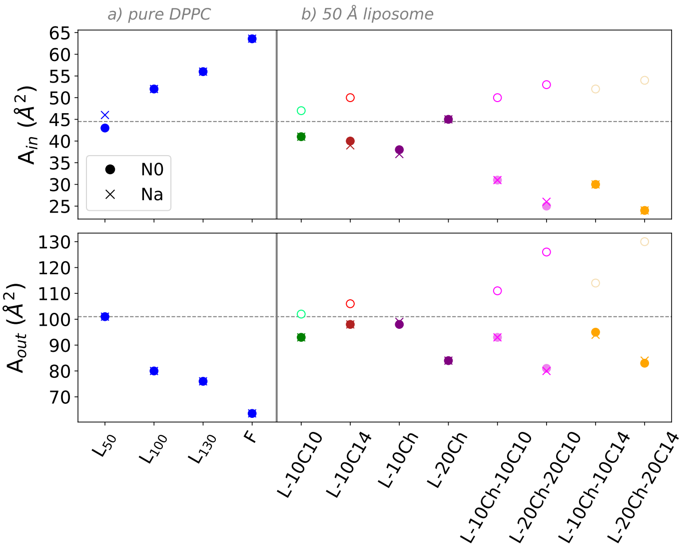

Figure 5.2: APL of liposomes. A_{in} and A_{out} represent APL of the inner and the outer layers of the liposomes, respectively. Symbols are circles for systems containing N0, crosses for systems containing Na. Symbol color according to legend of Fig. 5.1. Full and open circles are used for systems with neutral and deprotonated FAs, respectively. The same colors as in Fig. 4 are used. (a) Comparison of pure DPPC membranes with varying curvature. (b) Comparison of liposomes with radius 50 Å with varying composition. The dashed horizontal line shows APL for the pure DPPC liposome L_{50}, averaged over the systems containing N0 and Na.

The membrane composition (Fig. 5.2b) is varied in the highly curved liposomes with radius 50 Å. Similar to flat bilayers, both A_{in} and A_{out} tend to decrease in the presence of neutral FAs or cholesterol, and particularly in systems containing both (e.g., a drop of 48%

in A_{in} and 18% in A_{out} for L-20Ch-20C14 compared to L_{50}). The impact of neutral FAs on the APL of highly curved liposomes is here comparable to that of flat bilayers of equivalent composition, resulting in a decrease of 5% and 7% in A_{in} and 8% and 3% in A_{out} for L-10C10 and L-10C14, respectively.

In contrast, deprotonated FAs have the opposite effect, causing a significant increase of almost 16% and 5% in A_{in} and A_{out}, respectively, for L-10C14-n, compared to the pure DPPC composition. The results suggest that the repulsive forces of deprotonated FAs have a stronger effect on curved membranes than on flat membranes: the deprotonated FAs not only fail to decrease the APL, but actually increase it. Our findings illustrate that the APL is modified both by composition and curvature, but APL changes induced by composition can be much stronger than the curvature effect, when considering A^*, especially for high concentrations of cholesterol or in small liposomes.

5.2 MEMBRANE DISTRIBUTION AND THICKNESS

Membrane curvature effect

Fig. 5.3a shows the probability distribution of membranes composed of pure DPPC with varying curvature. Among these membranes, L_{50}, with the highest curvature, displays the least symmetric distribution, with a higher probability in the outer layer. The observed asymmetry can be explained by the densely-packed and disordered inner layer of L_{50}. In addition to having the least symmetric probability profile, L_{50} also has the smallest thickness (35.6 Å) compared to other pure DPPC membranes (Tables 2.1, 2.2). The phenomenon of decreasing membrane thickness with increasing curvature was also observed by Risselada and Marrink, who studied the impact of curvature on lipid packing and dynamics of DPPC liposomes using CG MD [132].

Membrane composition effect

Fig. 5.3b shows the impact of FAs on the membrane structure of flat bilayers. The presence of FAs results in a more compact membrane structure, with increasing DPPC probability near the center of the membrane (Fig. 5.3b). Simultaneously, the thickness is reduced (Table 2.1). This compactness and reduced thickness stem from a decrease in the space between the tails of the upper and lower leaflets in the central region of the membrane. For instance, the inclusion of 30% neutral C10 and C14 to the flat membrane leads to a decrease in thickness from 40.2 Å to 38.7 Å and 39.3 Å, respectively. The reduced

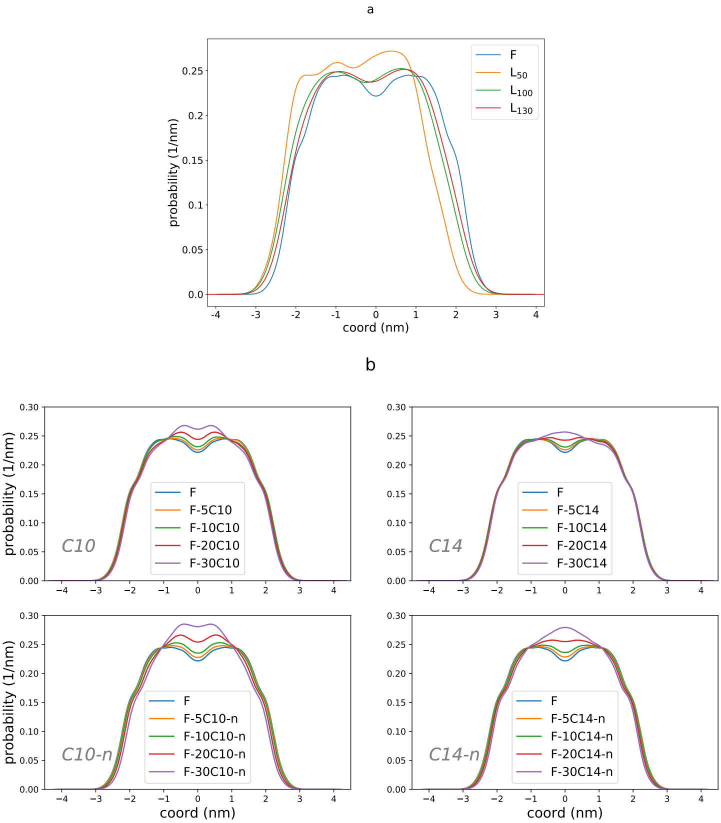

Figure 5.3: Probability distribution of the DPPC lipid in different systems. (a) Effect of curvature on pure DPPC bilayers. Profiles have been shifted to center the span of the histograms around 0 to facilitate comparison. (b) Effect of composition on flat bilayers. The upper and lower plots show the probability distribution of the DPPC in the membrane including neutral and deprotonated FAs, respectively.

thickness is particularly evident in systems with deprotonated FAs, with the smallest thickness of 37.5 Å observed for F-30C10-n (see SI). This reduction was also seen for C10-n's effect on a flat POPC membrane in a combined all-atom and coarse-grained computational study by Larsson and co-authors [130], where it was reported that by including 10% C10-n in the membrane, the membrane thickness decreased by about 1%. They associated this reduction to the C10-n tendency to stay near the head group region, pushing the POPC molecules apart and disrupting the lipid tail packing. They also showed that neutral C10 slightly increases the thickness of the POPC membrane. This increase was attributed to the acyl chain order parameter and the neutral C10 tendency to stay deeper in the POPC membrane. In contrast, in our simulations of DPPC membranes, C10 and C10-n are embedded at similar depths. This means that the specific modifying effect of a FA not only depends on the chosen FA, but also on its interaction with the specific phospholipid type.

5.3 FREE ENERGY OF PERMEANTS

In this section, we will discuss the effect of membrane curvature and composition on permeants' free energy profile along the z direction.

Membrane composition effect

The effect of FAs on the N0 permeants is illustrated in Fig. 5.4 for flat bilayers.

The lowest point in the free energy well is situated between 1 and 2 nm from the center of the membrane. Conversely, the highest point in the free energy barrier is positioned in the middle of the membrane, with a distance of less than 1 nm from the center. Neutral FAs (upper plots) primarily affect the head group region, resulting in a smaller free energy well, which facilitates the escape of N0 permeants from the membrane. In contrast, deprotonated FAs (lower plots) reduce the free energy barrier in the bilayer center significantly, and they may slightly reduce the barrier in the head group region. As suggested and investigated by another group, these differences could arise from the distinct preferences of neutral and deprotonated FAs to stay near the tail and head group regions, respectively [129]. Consequently, incorporating FAs in the system can modify the solubility of permeants N0 in the head group or tail regions of the membrane. The general effect could be framed as a 'smoothing' of the free energy profile with less deep wells and/or lower barriers. These observations suggest that including FAs in the system could facilitate permeation.

Membrane curvature effect

Fig. 5.5 depicts how the membrane curvature impacts the free energy profile of three different permeants through the membrane. Every permeant encounters a free energy barrier positioned in the center of the membrane. As expected, water does not exhibit any distinct free energy well, whereas N0 and Na experience a free energy well around 1.7 nm from the membrane center. Moreover, these two permeants must surmount an additional free energy barrier situated at a distance of approximately 2.5 nm from the membrane center. For N0 and Na (Fig. 5.5b-c), the curvature reduces the free energy barriers

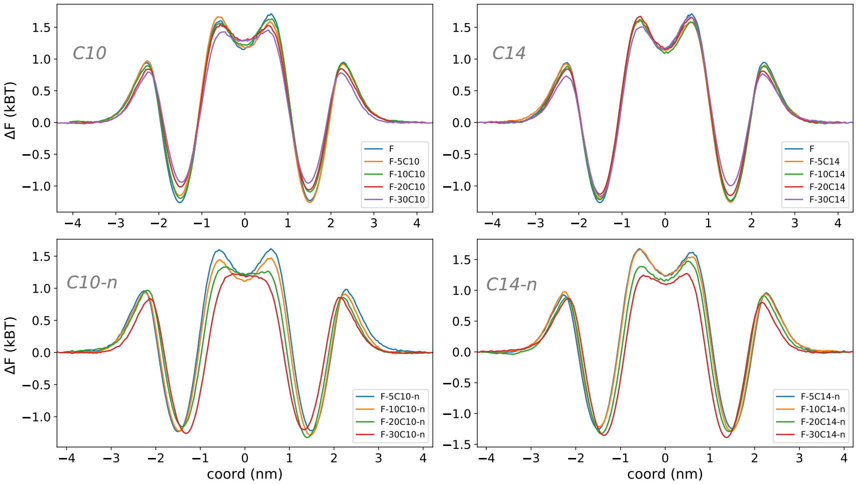

Figure 5.4: Effect of composition on the free energy profile of N0 permeants in flat bilayers, in comparison to the pure DPPC membrane (F). The membranes include C10 (left) or C14 (right) FAs, either in neutral (top) or deprotonated (bottom, label '-n') state. The legend specifies the mole fraction of FAs, e.g. F-5C10 contains 5% of C10.

near the head group region for L_{100} and L_{130} compared to the flat bilayer. However, L_{50} exhibits an opposite trend, with deeper free energy wells and larger free energy barrier in the inner leaflet (left part of the axis) due to the confinement of the interior region. For water (Fig. 5.5a), the permeation barrier is situated in the hydrophobic part of the bilayer, as expected [71]. Although the curvature does not significantly alter the height of the free energy barrier, the extensiveness of the barrier decreases with curvature. The reduced barrier width is in accordance with the smaller membrane thickness h of curved membranes (Table 2.2) compared to flat membranes (Table 2.1). Another cause for an apparent reduction in thickness could be undulations of the large membrane patches in the liposome systems [29]. Some analysis packages have been developed recently to measure APL and membrane thickness despite fluctuations, e.g., SuaVE [169, 170] and LipidDyn [171]. We computed a set of parameters with the SuaVE package (results in SI of Paper 4 in Part 7.2) and found that this more advanced tool confirms that the thickness does decrease with curvature. Moreover, the free energy profiles for L_{100} and L_{130} reveal a good agreement with the published results of an all-atom simulation study on the impact of curvature on water permeability by Yesylevskyy et al. [93]. This study found that curvature decreases the energy barrier of water permeation through dioleoylphosphatidylcholine (DOPC) membranes, a result which is consistent with our observations for L_{100} and L_{130}. However, the barrier for L_{50} is not reduced in our simulations. This may be due to the highly decreased membrane thickness and more densely packed membrane in this system (see previous subsections). Regardless, we found that the width of the free energy profile was reduced by curvature in the liposomes, which may facilitate water permeation through the membrane. The permeability values will be computed explicitly in the next subsection to verify this hypothesis.

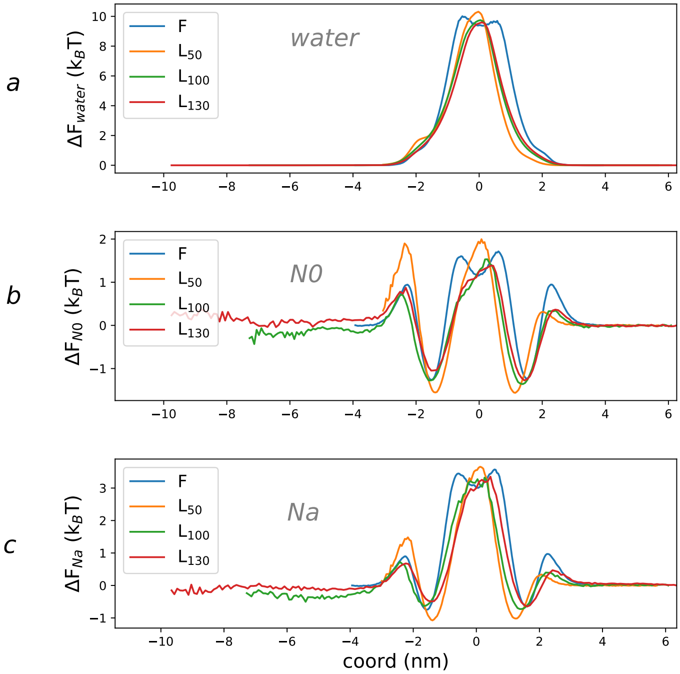

Figure 5.5: Free energy profile of permeants (water, N0, and Na) as a function of membrane coordinate (z-coordinate or shifted radial coordinate) in systems with pure DPPC to see the curvature effect. The top figure plots are based on the same membrane systems as in the middle figure. Profiles have been shifted to center the span of the DPPC histograms around 0 to facilitate comparison (similar to Fig. 5.3a).

5.4 PERMEABILITY

After a thorough analysis of the structural membrane characteristics in the previous section, this section will investigate the dynamics and kinetics of membrane permeation. We will examine how the curvature and composition of the membrane affect the permeability of water, N0, and Na. To compare the 62 systems, this is done step by step: first focusing on flat membranes, next on simple pure DPPC membranes, and in the last two steps the various curvatures and compositions are combined.

5.4.1 Composition effect in flat membranes

First, the composition effect on permeability is studied for flat membranes (Fig. 5.6). Overall, changes in the membrane composition have a greater impact on the permeability of N0 than of water. For Na, changes in permeability are less clear due to the large error bars, which are attributed to the high energy barrier for Na (Fig. 5.4) and poor statistics resulting from low number of crossings. Similarly, for water, the permeabilities have large error bars because the number of water crossings in the counting method was low, which is expected for a highly hydrophilic compound. As a result, comparing the water permeability values in all systems with these high error bars is not applicable. Instead, we will compare these values with experimental values. Generally, water permeability values in this figure are distributed in the range of 28×10^{-4} cm/s to 59×10^{-4} cm/s, with a value of almost 44×10^{-4} cm/s for the permeability through the pure DPPC flat bilayer (system F). This value is in good agreement with other experimental and simulation works. The water permeability of pure DPPC was reported as 17×10^{-4} at 323 K by Winter et al., and Yesylevskyy et al. presented a permeability range of 2.5×10^{-4} to 3.6×10^{-4} for pure DPPC at the same temperature. Additionally, Carruthers and Melchior reported a value of 2.04×10^{-4} for water permeability through egg PC at 283 K. [93, 111, 133, 172, 173]

For N0, the addition of FAs C10 and C14 in the membrane gradually increases the permeability of N0, with the highest value observed for the system with 30% C14-n, resulting in an almost 36% increase in permeability. This effect of fatty acids on the permeability was also seen in Fig 5.4, with neutral and deprotonated FAs lowering the free energy barrier for the permeant N0 in different regions of the membrane.

Arouri et al. (2013) suggested that the increased permeability may be due to the non-cylindrical shape of FAs, which imposes a curvature stress in the membrane and alters the lateral pressure profile [174]. As a result, defects and pores created by these molecules can destabilize the membrane and increase its permeability. Another study conducted a CG MD simulation to investigate the permeation of cell-penetrating peptide cargo complexes through a DOPC lipid membrane [175]. Their results show that the presence of deprotonated palmitic acid (C16), a longer FA, enhances the permeability of

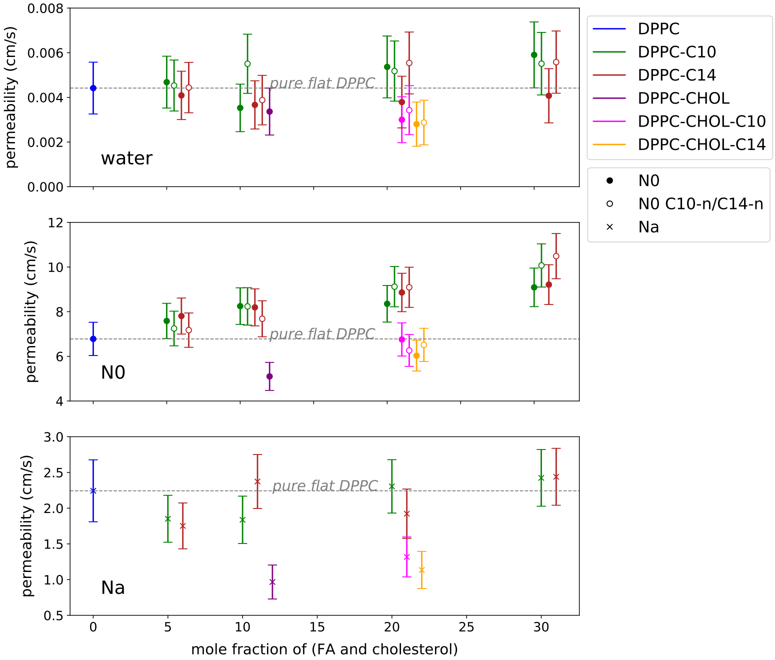

Figure 5.6: Effect of composition on the permeability of permeants through flat membranes. The permeants are water, N0, and Na. For better visibility, data points have been shifted. Full and empty circles show the systems including neutral and deprotonated FAs, respectively.

these cargos, likely due to its size, shape, and high packing freedom. The results by Arouri et al. and Via et al. are consistent with our findings, as they also suggest that FAs can increase permeability.

The presence of cholesterol has the most significant impact on the permeability, as the inclusion of only 10% cholesterol can already reduce permeability by approximately 25% and 57% for N0 and Na, respectively (dark purple in Fig. 5.6). This result is in agreement with work by Pias and co-workers, who observed a reduction of almost 10% in oxygen permeability through a POPC membrane when 12.5% cholesterol was included [77]. It attributed this reduction to cholesterol's effect on decreasing oxygen solubility in the membrane and possibly diminishing the volume of oxygen that can be transmitted laterally within the membrane. This decrease in the solubility of the permeants was also observed in our systems containing cholesterol, with an increase in the free energy barrier of the permeant in the center of the bilayer (see SI).

Investigating the potential for cholesterol-induced phase separation in flat membranes at 323 K, both F and F-10Chol exhibit the

Lα (liquid disordered) phase, in accordance with experiments by Chiang et al. [176]. This same phase was reported by Cournia and co-workers using CGMD simulations with the same Martini forcefield [177]. The findings are further supported by the APL measurements of pure DPPC and DPPC-10Chol flat membranes (F and F-10Chol), which align with the values reported by Wang et al. For systems involving liposomes containing 20% cholesterol, experimental results at 323 K are inconclusive. Some references suggest the presence of either the Lα phase or a coexistence of Lα and Ld (liquid ordered) phases [176, 178]. The experimental paper by Subczynski et al. also does not provide a definitive determination of the phase at 323 K [179].

Finally, in flat bilayers containing both FAs and cholesterol (pink or yellow in Fig. 5.6), the N0 permeability values still decrease compared to pure DPPC, but not as much as in systems with only cholesterol. The resulting permeability for these DPPC:FA:Chol membranes is a balance between two opposing effects, coming from FAs (enhancing) and cholesterol (reducing). In short, FAs, as N0 permeability enhancers, temper the action of cholesterol.

5.4.2 Effect of curvature on DPPC membranes

The effect of curvature is explored by comparing a series of pure DPPC liposomes with a flat DPPC membrane, which is the limit of an infinitely high radius. As introduced in the Methods section, liposome permeability can be characterized by the three permeabilities P_{esc}, P_{entr} and P^* for the water permeant. Here, P_{esc} describes the escape kinetics of compounds that are initially enclosed inside the liposome,

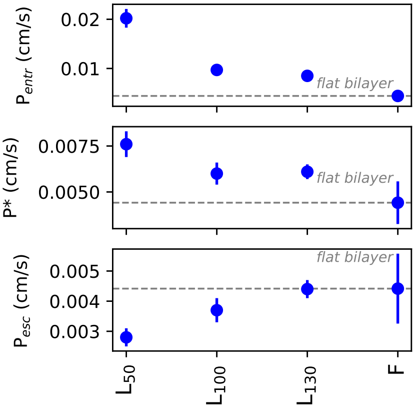

Figure 5.7: Water permeability in pure DPPC systems with varying curvature compared to the flat bilayer. Systems contain permeant N0.

while P_{entr} describe the entrance kinetics when compounds are in the solute and penetrate towards the inside of the liposome. The value P^* serves to compare liposome permeability with that of flat membranes.

In Fig. 5.7, P_{esc} and P_{entr} clearly follow opposite trends: P_{esc} increases and P_{entr} decreases with increasing radius. This can be understood with a simple model. For simplicity, consider a very simple homogeneous membrane of thickness h, as in our previous theoretical paper [136]. The permeant diffusivity is assumed to be a constant D, and the membrane solubility is assumed to be identical to the water phase solubility, so the partitioning coefficient K is equal to 1. Further, it is first assumed that the curvature does not change the permeation kinetics. The permeability of a flat bilayer is then given by $P_{\mathrm{flat}} = D/h$. For a liposome with the membrane spanning between r_1 and r_2 ($r_1 \geq h$), the entrance and escape permeability are given by

$$P_{\mathrm{entr}} = \frac{D}{h}\frac{r_2}{r_1} \tag{5.1}$$

$$P_{\mathrm{esc}} = \frac{D}{h}\frac{r_1}{r_2} \tag{5.2}$$

By substituting the flat membrane permeability, and the identity $r_2 = r_1 + h$, we can recognize the behavior as a function of the factor $x = r_1/h$,

$$P_{\mathrm{entr}} = P_{\mathrm{flat}}\left(1 + \frac{h}{r_1}\right) \tag{5.3}$$

$$P_{\mathrm{esc}} = P_{\mathrm{flat}}\frac{1}{1 + \frac{h}{r_1}} \tag{5.4}$$

These equations show that P_{entr} and P_{esc} have a $1+1/x$ and $x/(1+x)$ dependency, respectively, compared to P_{flat}.

With $x = r_1/h$, this means that P_{esc} is expected to increase while P_{entr} is expected to decrease, with increasing radius, which is indeed clearly the case in Fig. 5.7. (Note that the spacing on the horizontal axis in Fig. 5.7 differs from the variable $x = r_1/h$.) This derivation does not include any change in the permeation kinetics yet. The dominant curvature effect on P_{entr} and P_{esc} is thus a consequence of the geometrical factors involving r_1 and r_2.

Besides the geometrical effect, the curvature might also change the permeation kinetics themselves, e.g., in case curvature loosens the packing and permeants can pass through with lower resistance. This effect is well captured by the liposome permeability P^*, which eliminates the geometrical effect. Indeed, for the theoretical simple membrane, we find that $P^* = \sqrt{P_{\text{entr}} P_{\text{esc}}} = P_{\text{flat}}$. When there are only geometrical effects, P^* is identical to the flat bilayer. When there are both geometrical and permeation kinetics effects, then P^* will differ from the flat bilayer. For water, P^* increases with respect to the flat membrane due to curvature, and we can conclude that curvature enhances the water permeability. For the liposome with the highest curvature, L_{50}, this enhancement amounts even to a factor 1.7 for P^*.

The liposome with the smallest curvature, L_{130}, has a permeability of $P^* = 64 \times 10^{-4}$ cm/s, equivalent to an enhancement factor of 1.4. This indicates that L_{130} is not fully behaving as a flat membrane yet. While this could be numerical coincidence, its P_{esc} value does become indistinguishable from the flat bilayer value (factor 1.04). This gives the impression that this large liposome already behaves similarly to the flat bilayer in terms of the escape kinetics. The curvature effect should indeed diminish with liposome size, and for escape experiments, it should be negligible for liposome sizes that are typically encountered in experimental setups and in nano-sized drug delivery systems. Nevertheless, highly curved membranes may be encountered in exosomes, the caveolae, mitochondrial crystae or membrane pearls, and one should be cautious about possible curvature effects in those systems.

Whilst P^* is most suitable to compare liposome with their flat counterparts, P_{entr} or P_{esc} are usually the relevant kinetic parameters

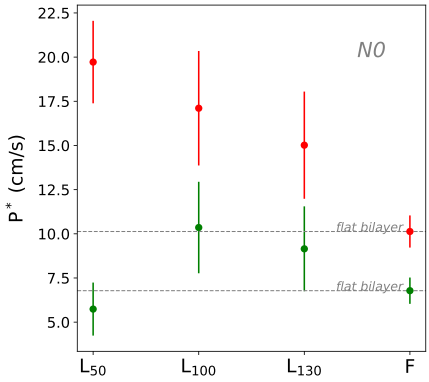

Figure 5.8: N0 permeability in pure DPPC systems with varying curvature compared to the flat bilayer.N0 permeability based on region 1 (green), i.e. extended membrane thickness between r_1' and r_2', or on region 2 (red), i.e. membrane thickness h between r_1 and r_2.

to be compared with experiment [136]. For instance, consider liposomes loaded with a dye that are immersed in a dye-free solution. Over time, samples may be taken from the solution to measure its dye concentration. As the liposomes gradually release their dye load, the solution's dye concentration will gradually increase. The kinetics parameter characterizing the dye release from the liposomes is then given by the escape permeability P_{esc}. In practice, experiments encounter a distribution of liposome sizes, and it is to be anticipated that each of those curved membranes has a different P_{esc} value because of the curvature effect. In experimental literature, the curvature effect has however been neglected. Fortunately, most experimentally available liposomes are fairly large, usually around 100 nm size (radius around 500 Å), and the curvature is likely to become negligible for these larger liposomes. For water, P^*/P_{flat} has already dropped to a factor 1.4 for a 26 nm sized liposome (L_{130} in Fig. 5.7). The trend suggests that experimental literature values of the curved, yet large, liposomes may indeed likely be used for verification of simulation results.

Whereas water has a very large free energy barrier for permeation of about 10 $k_B T$, the N0 free energy profile has a smaller barrier at the membrane center of less than 2 $k_B T$, and a mixture of well and barrier in the head group region. We now investigate how the curvature affects the permeability of this other type of free energy profile. Fig. 5.8 shows the N0 permeability for pure DPPC liposomes and a pure DPPC membrane. Two permeabilities are considered, covering two different regions: region 1 covering the extended membrane thickness (radii r_1' and r_2'), and region 2 focusing on the central barrier for N0 (radii r_1 and r_2 of Table 2.2). Region 2 is thus smaller than region 1 (Fig. 1.5). The results for L_{100} and L_{130} show that the N0 permeability in either region increases with curvature compared to the flat membrane. This increase can be attributed to the curved membrane's reduced thickness and less organized structure. As illustrated in Fig. 5.5, increasing the curvature results in a smaller barrier in the head group region as well as in the center of the membrane for these liposomes. Higher curvature therefore makes permeation easier through both region 1 and region 2 for those liposomes than for a flat membrane.

For L_{50}, however, we observe two opposite impacts on the N0 permeability. Permeation through the central region 2 (red), is higher for L_{50} than that for the flat membrane. Meanwhile, permeation through the entire membrane region 1 (green) is smaller for L_{50}. This is due to the shape of the N0 free energy profile (see Sec. Free energy of permeants). Region 2 only covers the central free energy barrier, which is significantly narrower for L_{50} despite being slightly higher.

Region 1 in addition covers the higher free energy barrier in the head group region of the inner leaflet (Fig. 5.5) in this system, which is caused by the extreme confinement and tight packing of the lipid head groups in that leaflet. This makes the L_{50} permeability over region 1 an outlier in Fig. 5.8.

Our analysis shows that the curvature may enhance the water permeability, while curvature does not affect the N0 permeability (region 1) with statistical significance. Meanwhile, curvature does enhance the N0 permeability of the central permeation barrier (region 2). The diversity in these observations indicates that the curvature effect may be unpredictable for other drug permeants, and new simulations would need to be performed in order to quantify the curvature for each new drug permeant of interest.

5.4.3 Curvature effect on various membrane compositions

Subsequently, the curvature effect was assessed not only for the pure DPPC membranes but also for all other compositions. The water and N0 permeability (through region 2) are compared between liposomes with 50 Å radius and flat membranes in Fig. 5.9. The closer a data point lies to the diagonal, the less this membrane is affected by

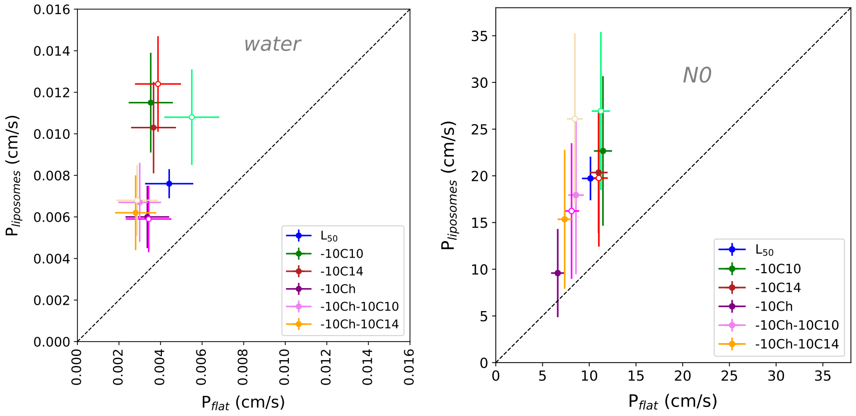

Figure 5.9: Permeability enhancement due to curvature. Comparison of water permeability (left) and N0 permeability (right) in flat bilayers and liposomes with radius 50 Å, various compositions. N0 permeability based on region 2, i.e. membrane thickness h between r_1 and r_2. Systems contain permeant N0. Empty circles show the systems with deprotonated FAs.

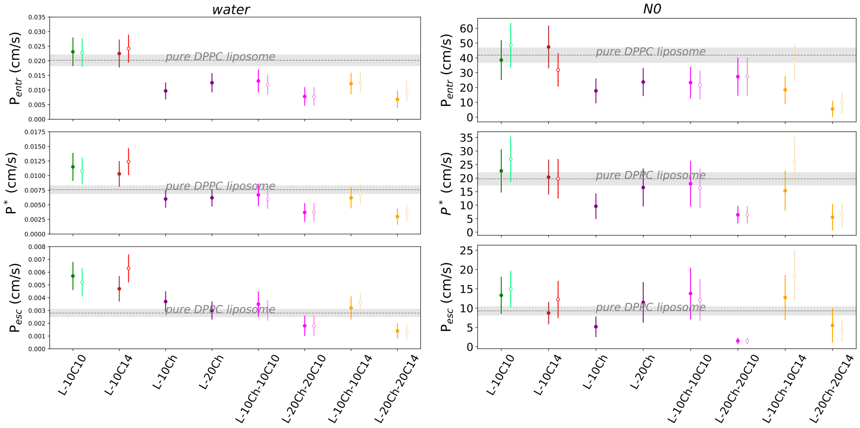

Figure 5.10: Effect of composition on the permeability of water beads (left) and N0 beads (right) through the liposome bilayers. The liposomes have a radius of 50 Å and have various compositions. The permeability of the pure DPPC liposome is indicated with a gray horizontal line. Filled dark and open lighter symbols for systems with neutral or deprotonated FAs, respectively. N0 permeability is computed based on the crossings over the dominant free energy barrier, i.e. region 2 covering the membrane thickness h between r_1 and r_2. Water permeability based on systems that include 20 N0 beads.

curvature. Both water and N0 permeabilities lie consistently above the diagonal. This means that the curvature effect for pure DPPC, which increases the permeability of water and N0 through region 2, is equally present in all systems with cholesterol and/or FAs.

In conclusion, the curvature effect makes the water and N0 (region 2) permeability for these curved multi-lipid membranes higher than for flat multi-lipid membranes with the same composition. The underlying cause of the curvature effect is a change in membrane thickness and solubility, which is reflected by the free energy profile. An additional cause could be the mobility changes of the permeants, which would be reflected by the diffusion profile; the position-dependent diffusivity of the permeants was however not computed in this work.

5.4.4 Composition effect on curved membranes

We now turn to the discussion of the effect of composition for curved membranes, making use of the liposome permeability P^*. The composition effect on the N0 permeability is investigated for small liposomes with radius 50 Å (Fig. 5.10, right). Instead of covering the extended membrane thickness, the permeability is based on the region between the average PO4 positions in the two leaflets, i.e. on region 2. From Fig. 5.4, this means that the focus is put on the highest free energy barrier at the center of the membrane, while the smaller barriers for N0 in the head group region are not considered. Concerning the effect of cholesterol, a similar trend as that of the flat bilayers (Fig. 5.6) is here observed in the plot of the small liposomes (Fig. 5.10). Specifically, inclusion of 10% cholesterol in the membrane (L-10Ch) can decrease P^* by 28% which is less than what was observed for the flat membrane (F-10Ch). Moreover, for curved membranes containing 10% FAs, permeability seem to increase more noticeably compared to the flat membranes with 10% FAs.

Permeability of water molecules through heterogeneous curved membrane of 50 Å radius is provided in Fig. 5.10 (left). Overall, the composition has a similar yet stronger effect on the permeability for water beads than for N0 beads. For all membrane compositions, and for both N0 and water, P_{entr} is considerably larger than P_{esc} in the liposomes with radius 50 Å. This difference between P_{entr} and P_{esc} values is consistent with the definitions of these two permeabilities outlined in Section 3.2.2, where P_{entr} is expected to be larger than P_{esc} due to the smaller inner surface area at r_1 (Eqs. 3.52-3.53). In practice, it means that the timescales in an experiment will depend on whether the compound of interest is initially inside or outside the liposome, as the escape and entrance kinetics can be different.

Concluding remarks. The choice of permeant type (water, N0, Na) is crucial for calculating permeability, reflected by the permeants' free energy profiles and solubility. Variations in membrane composition, influenced by factors like FAs or cholesterol, can lead to significant changes in permeability. FAs generally increase permeability, especially deprotonated FAs due to their charges, while cholesterol reduces it. When both cholesterol and FAs are present, they moderate the permeability-enhancing effect of FAs on N0. Curvature significantly impacts membrane dynamics by reducing thickness and lowering free energy in the head group region, facilitating permeation. Even low curvature increases water permeability, with highly curved membranes showing a more pronounced effect. In experiments, highly curved membranes exhibit a considerable difference between escape and entrance water permeability, with lower curvatures showing a lesser extent of difference. However, realistic liposomes used in drug delivery are often larger and less curved, suggesting less influence from curvature.

Chapter 6

Investigating caveolae: curvature effect

This chapter explores the role of membrane's curvature on the O_2 *buffering by a caveola. The discussion will examine the impact of membrane curvature on the partitioning of* O_2 *between water and the membrane, with the resulting partitioning coefficient of* O_2 *reported from all-atom (AA) simulations. Finally, a coarse-grained (CG) model for* O_2 *will be selected from CG Martini beads, and this new model will be utilized once more to explore the partitioning of* O_2 *between water and the membrane.*

6.1 AA O_2 partitioning

In Section 2.4.1, all-atom (AA) MD was utilized to simulate O_2 permeation through both a flat DPPC membrane and 50 Å-liposome. Section 6.1 will give the results of these simulations. Based on the AA simulations with CHARMM of O_2, its partition coefficient between membrane and water will be evaluated. To have a better understanding of membrane curvature's effect on O_2 partitioning, membrane properties such as thickness and area per lipid will be computed for all systems.

6.1.1 Membrane thickness and area per lipid

The thickness of the membranes was calculated by measuring the distance between two highest peaks in the histogram of phosphate atoms. As can be seen in Table 6.1, the thickness of the flat bilayer at the temperature of 323 K and pressure of 1 bar is 4 nm, consistent with experiments, 3.9 nm [18]. Increasing the membrane's curvature reduces the membrane thickness, to 3 nm. The opposite trend occurs with the area per lipid. To calculate the area per lipid for the flat bilayer, the area of the box in the xy direction was divided by the number of the lipids in one leaflet. For the liposome, two areas per lipids (inside and outside) were computed, dividing the area of each layer by the number of the lipids in that layer. The highest peaks in the phosphate atoms' histogram were chosen as radii to calculate the areas of the leaflets. As it is shown in Table 6.1, the area per lipid in the outer lipid layer of the liposome, 1.02 nm^2, was almost twice the flat bilayer's area per lipid, 0.61 nm^2. The area per lipid for the liposome's inner layer, 0.65 nm^2, was close to that of the flat bilayer and to the experimental value at 323 K and 1 bar, namely 0.63 nm^2 [18].

6.1.2 AA O_2 free energy profile

The O_2 free energy profile in both the flat bilayer and the liposome were plotted in Fig. 6.1 as a function of the membrane depth, also called permeation coordinate. For the flat bilayer, this is the normal to the membrane, i.e. the z-coordinate (Fig. 6.1 right). For the curved membrane, this is the radial distance r from the liposome center (Fig. 6.1 center). The poor statistics in the water phase inside the liposome (Fig. 6.1 right) is because of the small size of the liposome. As can be observed in Fig. 6.2 right, for the liposome, O_2 prefers to stay in the lipid part of the membrane, with two free energy wells, rather than in the middle part of two leaflets compared to the flat bilayer, with one free energy well. This could be a result of the decrease in the membrane thickness. Moreover, the barrier that O_2 needs to overcome to reach the water phase from the membrane's outer leaflet was reduced from 3 k_BT to 2 k_BT (k_B: the Boltzmann constant).

6.1.3 AA O_2 partition coefficient

To calculate the O_2 partition coefficient (K) through the membrane, the free energy was set to zero in the water phase. K was calculated along the permeation direction for both systems using $\Delta F = k_BT \ln K$. As expected, in Fig. 6.1 left, O_2 is more soluble to the mid-membrane than the water phase. This behavior is slightly changed with increasing the curvature, with the highest solubility in the both lipid phases. As the area per lipid is smaller for the inner leaflet, O_2

got stuck more in this layer with the highest K and deepest free energy well shown in the plots. As reported in Table 6.1, the average K ($<K>$) for the flat bilayer, 4.06, is slightly bigger than the liposome, 3.95, which shows that the relative O_2 concentration is smaller in the liposome compared to the flat bilayer. It is assumed that the asymmetricity of the free energy and partition coefficient profiles could be because of the smaller thickness and different area per lipids in each layers in the liposome.

systems	thickness (nm)	area per lipid (nm^2)		$<K>$
		inside layer	outside layer	
flat bilayer	4.0	0.61	0.61	4.06
liposome	3.06	0.65	1.02	3.95

Table 6.1: Thickness (nm), area per lipid (nm^2) and partition coefficient $<K>$ in two systems of flat bilayer and liposome.

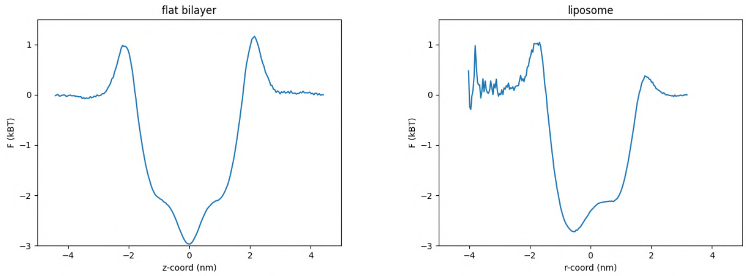

Figure 6.1: The O_2 free energy profile as a function of the permeation coordinate of the flat bilayer (z, left) or the liposome (r, right).

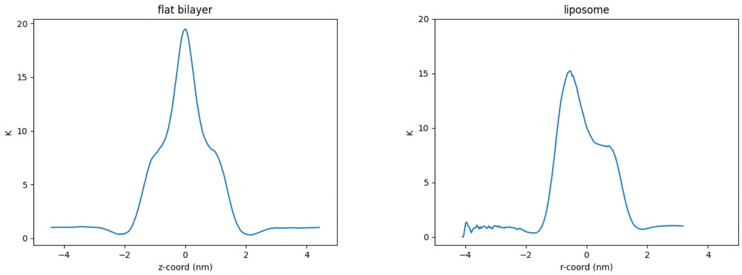

Figure 6.2: The O_2 partition coefficient profile as a function of the permeation coordinate of the flat bilayer (z, left) or the liposome (r, right).

6.2 CG O_2 MODEL

In Section 6.1, simulating large systems such as caveolae in their true size proved to be quite challenging at the AA resolution, thus impeding a thorough investigation of this system. Therefore, in this section, we introduce a CG model of O_2, which allows for the simulation of systems containing O_2 at a CG resolution. This advancement makes the simulation of systems such as caveolae in their true size more feasible and practical.

6.2.1 Selection from existing CG beads

In this study, we selected a CG model for O_2 from existing CG Martini 3 beads. To accomplish this, we investigated the properties of the modeled O_2 in various systems and compared them with the AA O_2.

Size, charge, polarity, and oil-water partitioning

An O_2 molecule has a diameter of approximately 3.4 Å and a molar mass of 32 g/mol [180]. The parametrization of a new CG model for O_2 would entail establishing interactions between the new CG representation and existing beads and a tedious validation. Therefore, it may be more efficient to identify analogous beads among those already established and validated, thereby avoiding a new parametrization process. To identify a bead analogous to O_2 among existing Martini 3 beads, our attention was directed toward the smaller CG beads, particularly those of tiny size (label 'T') with σ (the distance at which the inter-molecular potential between the two particles is zero) value of 3.4 Å and a molar mass of 36 g/mol. Molecular O_2 is a non-charged and non-polar molecule, with its lowest moment being the quadrupolar moment. Within the subset of tiny beads, two bead types meet the conditions of being almost non-charged (a partial charge of up to ± 0.33) and non-polar: the TC and TX bead types are two promising candidates to represent O_2. The Martini 3 forcefield distinguishes six TC beads and four TX beads, each characterized by a polarity index ranging from 1 (minimal polarity) to 6 (maximal polarity) for TC beads and similarly from 1 to 4 for TX beads.

Next, a subset of these ten Martini 3 beads will be excluded through a comparison of the O_2 solubility in water *versus* a non-polar solvent. As noted by Overton more than a century ago [181, 182], the membrane-water partitioning correlates well with oil-water partitioning, such as octane-water (OCO-W) or hexadecane-water (HD-W) partitioning. Therefore, Table 6.2 compares a set of partitioning values of the Martini 3 beads, values from AA simulations of O_2, and experimental values. The partitioning is quantified by the free energy (ΔG) required for the O_2 molecule to transition from one phase to another.

	density	$\Delta G_{\text{transfer}}$ (kJ/mol)				
	(kg/m^3)	HD-W	OCO-W	ETH-W	BENZ-W	CHEX-W
Martini 3 (TC1) [134]		13.2	12.0	10.5	8.2	13.2
Martini 3 (TC2) [134]		11.1	7.8	7.9	4.8	9.6
Martini 3 (TC3) [134]		8.6	6.7	8.2	5.5	8.5
Martini 3 (TC4) [134]		5.6	6.4	8.1	8.0	8.5
Martini 3 (TC5) [134]		3.6	4.5	6.4	6.3.7	5.7
Martini 3 (TC6) [134]		1.3	3.6	6.4	5.0	4.3
Martini 3 (TX1) [134]		8.4	7.6	9.3	9.1	9.6
Martini 3 (TX2) [134]		5.3	5.2	6.4	3.7	5.5
Martini 3 (TX3) [134]		5.4	5.4	7.5	3.6	5.5
Martini 3 (TX4) [134]		1.2	2.7	7.4	2.5	4.3
Martini 3 (TC3) $^{310\text{ K}}$	1.25*					
exp. (O_2) [154] **	1.283 [183]	10.8	9.7	8.0	8.9	9.9
exp. (O_2) [154] $^{310\text{ K} \; **}$	1.241 [183]	11.0	10.5	8.8	9.7	10.8
exp. (O_2) [184]				8.1	9.0	10.1
exp. (O_2) [185]		5.1				
AA CHARMM (O_2) [30] $^{310\text{ K}}$		7.5				

Table 6.2: Comparison of the selected CG beads properties with O_2 molecule in AA MD and experiments. All the reported values are in 300 K and 1 bar unless otherwise specified. '*' indicates the values calculated by new simulations at 310 K and 1 bar by our group. '**' indicates the values at 101.325 kPa.

Let us first introduce the experimental values in Table 6.2. The free energy values for transferring ($\Delta G_{\text{transfer}}$) a permeant from a non-polar solvent (S) to the water (W) phase were calculated based on the difference between a hydration and solvation energy, which both have the gas (G) phase as a starting point [186],

$$\Delta G_{\text{transfer}} = \Delta G^{G \to W}_{\text{hydration}} - \Delta G^{G \to S}_{\text{solvation}} \tag{6.1}$$

Here, $\Delta G^{G \to W}_{\text{hydration}}$ represents the free energy associated with the transition of a permeant from the gas phase to a water environment, while $\Delta G^{G \to S}_{\text{solvation}}$ characterizes the free energy change as the permeant shifts from the gas phase to the solvent phase. Similarly to the Martini 3 paper [134], various solvents were considered: hexadecane (HD), octanol (OCO), ethanol (ETH), benzene (BENZ), and cyclohexane (CHEX). These two free energy values $\Delta G^{G \to W}_{\text{hydration}}$ and $\Delta G^{G \to S}_{\text{hydration}}$ are not directly tabulated for experiments. Instead, they were computed from the relation with the solubility,

$$\Delta G = -RT \ln(x) \tag{6.2}$$

where x represents the mole fraction solubility in the water or the various solvents and R is the universal gas constant. The mole fraction solubility values were sourced from literature at a partial pressure of 101.325 kPa for the gas and at 300 K [154]. Following the calculation of $\Delta G^{G\to W}_{\text{hydration}}$ and $\Delta G^{G\to S}_{\text{solvation}}$, the resulting $\Delta G_{\text{transfer}}$ values (Eq. 6.1) are presented in Table 6.2.

The Martini 3 values are taken from the supporting information of the 2021 reference paper [134], while the additional density calculation was performed for this work. The all-atom (AA) value with the CHARMM forcefield was taken from the O_2 study by Ghysels et al. [73].

Together, the values in Table 6.2 give an overview of the interactions with the water phase and solvents. Specifically for O_2 interacting with a membrane, the HD partitioning is most relevant as it contains the same number of carbon atoms (16 carbons) in the lipid tail as 1-palmitoyl-2-oleoyl-sn-glycero-3-phosphocholine (POPC) [30, 77]. The AA CHARMM simulations give a value of $\Delta G_{\text{transfer}} = 7.5\,\text{kJ/mol}$ for HD-W partitioning. From the ten TC and TX Martini 3 beads, two beads (TC3 and TX1) exhibit the closest resemblance in HD partitioning free energy (8.6 and 8.4 kJ/mol, respectively) compared to the HD partitioning free energy for AA CHARMM O_2. These two beads (TC3 and TX1) are thus good candidates as a CG model for O_2 based on their size, zero charge, non-polar character, and hexadecane-water partitioning.

6.2.2 Solubility of O_2 in the membrane

In this subsection, it will be investigated how the two selected beads (TC3 and TX1) perform in reproducing the free energy plot for molecular O_2 partitioning in a POPC membrane. Given our objective to model O_2 interactions with membranes, the final selection among the remaining beads will be determined by evaluating their solubility in a membrane against their solubility in the water phase. This ensures a sufficiently accurate representation of the water-membrane interactions of the modeled O_2.

The simulated flat membrane composition is a homogeneous POPC bilayer, as phosphocholin is the most abundant phospholipid in all mammalian cell membranes [187]. As a second membrane composition, a molar fraction of 25% cholesterol was considered (see Table 2.4 for an overview). In Figure 6.4 depicts a flat POPC membrane, composing 25% cholesterol, interacting with TC3 beads as a model for O_2."

Permeant	%POPC	% CHOL	$\Delta G_{\text{transfer}}$ (k_BT)
CG TC2	100	0	4.20
CG TC3	100	0	3.26
	75	25	3.06
CG TX1	100	0	3.31
CG TX2	100	0	2.09
AA O_2	100	0	2.78
	75	25	3.14

Table 6.3: The free energy of transfer (in k_BT) of permeants from the membrane to the water phase along the z coordinate.

The free energy associated with the transfer of O_2 from a water environment to a POPC or POPC:CHOL bilayer was calculated. Identical systems (Table 2.4) were compared with an AA CHARMM and CG representation of O_2. The solubility can be visualized by the free energy profile along the membrane normal, since $F(z) = -k_BT\ln\big(hist(z)\big)$, where $hist(z)$ refers to the positional histogram and z to the center of mass position along the membrane normal. The free energy profile $F(z)$ was computed as in Ref. [188] and is given in Fig. 6.3. The $\Delta G_{\text{transfer}}$ of the permeants between water phase and the membrane center is presented in Table 6.3. To confirm the suitability of our selected beads, we included some other CG beads in this part and compared them to O_2 as well.

The TX1, TX2, and TX3 beads lack the barrier of about 1 k_BT to enter the membrane, located around $|z| = 2$ nm, which would lead to an overestimation of the entrance kinetics of O_2 into the membrane (Fig. 6.3a). Among the TC2, TC3, and TC4 beads, the beads TC2 and TC3 exhibit a reasonable entrance barrier (Fig.6.3a). The TC3 bead, however, has a much better agreement with the AA free energy well than TC2, whose well is too deep. This free energy well is important for partitioning in the membrane and the residence time and escape kinetics of O_2 from the membrane. In conclusion, the preselected TC3 bead is indeed a very reasonable choice to mimic the membrane-water partitioning of O_2. The match is not perfect, however. In the CG simulation, the free energy plot displayed a deeper well (0.31 k_BT deeper) and a smaller barrier (0.19 k_BT smaller) compared to the AA simulation, indicating that somewhat higher partitioning in the membrane, slower escape kinetics, and faster entrance kinetics can be expected for TC3 compared to AA simulations.

Apart from a homogeneous POPC membrane, a heterogeneous POPC:CHOL membrane was modeled as well (Fig. 6.3b). The free

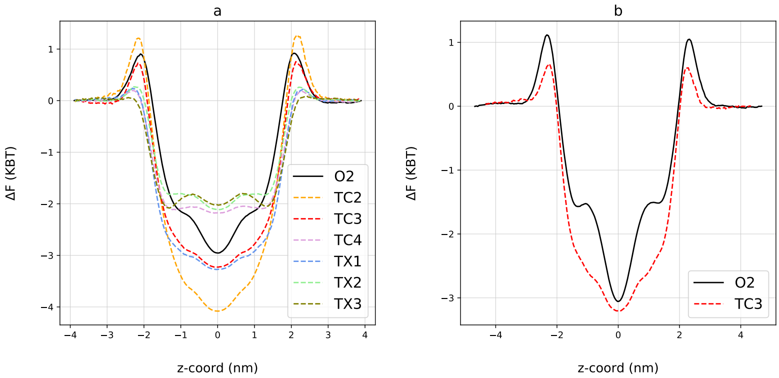

Figure 6.3: Free energy $F(z)$ of transfer through (a) POPC and (b) POPC:CHOL flat bilayers as a function of z coordinate. The coordinate of the mid-bilayer is at $z = 0$. Profiles are shifted to $F = 0$ in the water phase. (a) Comparison for few Martini beads (dashed line) and AA O_2 (solid line) in POPC. (b) Comparison for TC3 bead (red, dashed) and AA O_2 (black, solid) in POPC:CHOL.

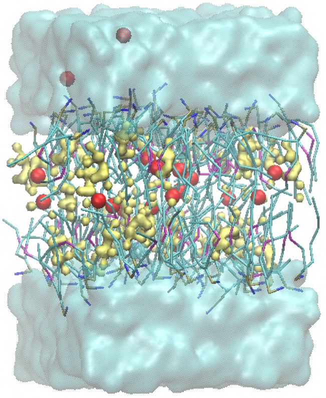

Figure 6.4: Flat membrane model featuring POPC (lines), cholesterol (yellow beads), O_2 (red bead) and water (light blue, surface) in a coarse-grained (CG) representation. A POPC molecule consists of multiple bead types: green for C and D beads, pink for GL beads, brown for PO beads, and blue for CHO beads.

energy of transferring TC3 from water to a POPC:CHOL bilayer with 25% cholesterol was calculated. The free energy profile across the membrane normal is compared with the AA equivalent system with the same composition in Fig. 6.3b. The free energy barrier in the head group region around $|z| = 2.1\,\text{nm}$ for the CG differs from AA simulation (0.52 k_BT smaller). The small shoulders in the tail region of the AA free energy ($|z| \approx 1$ nm) are absent in the CG free energy, but the profiles show a good match in the depth of the free energy well at $z = 0$.

In summary, the membrane-oxygen interactions have led to the decision to select TC3 as the bead to represent molecular O_2. In the next section, the TC3 bead will be evaluated for its other properties, such as diffusivity in a homogeneous phase, hydration free energy, and permeability through a membrane.

6.2.3 Further comparison of AA and CG

Solubility of O_2 in non-polar organic solvents

The free energy associated with the transfer of CG beads between water and six non-polar organic phases (HD, OCO, ETH, BENZ, and CHEX) is presented in Table 6.2 [134]. This data can be compared with experimental values calculated using Eq. 6.1. The experimental values at 300 K align most closely with the values for TC2, TC3 and TX1. This observation was further validated in the previous section by examining the free energy profiles of these beads as they traverse through POPC, revealing plots that closely resemble those observed for O_2. However, for the chosen bead TC3, the difference in $\Delta G_{\mathrm{transfer}}$ between the CG simulation and experiments ranges from approximately 0.2 kJ/mol to 3.4 kJ/mol, with the most notable resemblance observed in ETH-W. The solubility of TC3 in HD at 300 K can also be compared with the AA simulation at 310 K, revealing free energy transfer values of 8.6 and 7.5 kJ/mol in CG and AA, respectively. These values indicate that the transfer from HD to W in both our CG O2 and AA O2 models shows close agreement.

O_2 kinetics: diffusivity

The obtained value of the O_2 diffusivity in water and hexadecane is detailed in Table 6.4. The CG diffusivity value in water, 0.714 $Å^2$/ps, aligns with findings from the AA simulation conducted by Ghysels et al. using the CHARMM forcefield [30]. However, it exhibits a deviation from experimental values (0.252 $Å^2$/ps) [185, 189, 190]. The same trend is observed for diffusivity through HD, with the CG (0.566 $Å^2$/ps) and AA (0.44 $Å^2$/ps) values closely resembling each other but differing from the experimental value (0.249 $Å^2$/ps) [30].

This difference can be due to the fact that simulations cannot accurately calculate kinetic properties. Boundary effects, variations in temperature and pressure, and neglect of quantum effects further contribute to deviations from experimental results.

Systems	in W (Å^2/ps)	in HD (Å^2/ps)
Martini 3 (TC3)	0.714 ±0.06 *	0.566 ±0.02 *
AA CHARMM (O_2)	0.60 [30]	0.44 [30]
exp. (O_2)	0.252 [185, 189]	0.249 [185]
exp. (O_2)	0.19-0.23** [190]	

Table 6.4: Comparison of diffusion coefficient in water and hexadecane for TC3, AA CHARMM O_2 and exp-O_2. Simulations and experiments are done at 310 K and 1 bar. '*' refers to values from new simulations done, and '**' refers to values at 308 K.

O_2 kinetics: permeability through flat bilayer

The permeability P of O_2 through the POPC membrane was determined with the counting method, based on the same simulations as for the O_2 partitioning in a membrane. In the counting method, the permeants are followed during an equilibrium simulation, and the permeability is obtained from counting the number of full membrane crossings [28, 29, 33, 71, 100]. The dividing surface used for determining the crossing was the whole membrane (average position of the phosphate groups plus 0.8 nm), 28 Å and 30 Å from membrane center for permeation through POPC and POPC:CHOL, respectively, for both the CG and AA CHARMM simulations. Given that TC3 exhibited the most analogous free energy profile to O_2, we also calculate the permeability of TC3 through the POPC:CHOL membrane. The resulting values are given in Table 6.5 and were juxtaposed with data obtained from other AA simulations and experimental finding.

The permeability (P) values from Experiment 1, as shown in Table 6.5, were determined by Widomska et al. [191]. They measured induced spin exchanges via bimolecular collisions between O_2 molecules and nitroxide using the saturation-recovery electron paramagnetic resonance (EPR) technique [191]. Similarly, in Experiment 2, the permeability (P) values were also calculated using EPR. It is noteworthy that in Experiment 2, the dividing surfaces were located at 18 Å and 21 Å from the membrane center, significantly deeper within the membrane compared to our chosen dividing surfaces.

Simulation results for the permeability (P) of O_2 have been reported by Pias et al. In both cases, denoted as AA AMBER 1 and AA AMBER 2 in Table 6.5, the General AMBER ForceField (GAFF) model for O_2 was utilized to simulate its permeation through POPC and POPC:CHOL bilayers [192]. Berendsen and Langevin thermostats were employed to regulate the temperature, set at 310 K for AA

AMBER 1 and 308 K for AA AMBER 2, respectively. Notably, the dividing surfaces for P calculations were positioned at 28 Å and 30 Å for both simulations, similar to our simulations.

The P values derived from our CG simulations of modeled O_2 permeation through the membrane, ranging from 70 to 152 cm/s, exhibit a closer resemblance to experimental values, which fall within the range of 49 to 190 cm/s. This contrast with the AA simulation data, which spans from 10 to 26 cm/s. However, it is essential to note that this resemblance does not inherently indicate superior performance of our CG simulation results to AA.

As previously mentioned, experimental P determination relies on EPR, where the accuracy of the dividing surface may be compromised. The broader boundaries in experimental setups do not capture the significance of water–lipid interfacial resistances. Consequently, the resultant P values tend to be notably higher than those from AA simulations.

Moreover, the higher P observed in CG simulations can be attributed to two primary factors. Firstly, the reduced free energy barrier in the head group region of the membrane as can be seen in Fig 6.3, which serves as the maximum point of resistance to O_2 permeation. Secondly, the simplified forcefield of CG beads may introduce inaccuracies in the interactions compared to the atomistic level. This simplification could potentially lead to deviations from the precise atomic-scale dynamics captured in AA simulations.

Across all simulations and experiments reported in Table 6.5, the introduction of CHOL consistently leads to a reduction in O_2 permeability. However, when we introduce CHOL to the membrane, the small free energy shoulder that appear in AA simulation in the middle part of the membrane, does not show in CG simulation. Additionally, the introduction of CHOL reduces the free energy barrier in the head group, as illustrated in Fig. 6.3. These alterations facilitate smoother passage of the modeled TC3 through the membrane, resulting in an increased P.

6.3 CG O_2 PARTITIONING

As described in Section 2.4.3, we conducted simulations of the CG O_2 model in both POPC flat membrane and 50 Å-liposome to investigate the effect of curvature on O_2 partitioning in the membrane. The free energy profile of O_2 used as an indicator of partitioning.

	P_{POPC} (cm/s)	$P_{\text{POPC:CHOL}}$ (cm/s)
CG TC2	70.1 ±10	-
CG TC3	109.1 ±9	126.0 ±9
CG TX1	185.5 ±12	-
CG TX2	151.8 ±7	-
AA CHARMM (O_2)	23.7 ±2	24.3 ±2
AA AMBER 1 (O_2)	26 ±2 [80]	24 ±2 [80]
AA AMBER 2 (O_2)	13 ±1 [193] *	10 ±1 [193]*
Experiment 1	190 [191]	75 [191]
Experiment 2	157 [193]	49 [193]

Table 6.5: Permeability of selected beads through POPC and POPC:CHOL (25% cholesterol) membranes. All the reported values are at 310 K and 1 bar. '*' refers to P values at 308 K.

The free energy profile gives information about the barriers that O_2 must surmount in order to permeate through the membrane. Fig. 6.5 shows the free energy difference with respect to the water phase, i.e. $\Delta F(q) = F(q) - F_{\text{water}}$, where the center of the two membranes was aligned to the value $q = 0$. The flat membrane (blue line) shows that O_2 needs to overcome a barrier of about 0.7 k_BT to enter the POPC membrane based on the CG calculations. More importantly, O_2 experiences a barrier of about 3.7 k_BT to escape from the membrane. These barrier values are in accordance with the more detailed AA calculations [84]. In practice, this means that the POPC membrane will capture O_2 for a while before it can overcome the barrier and escape. This behavior of O_2 storage in membranes has now been well studied in multiple works [71, 73, 76, 87, 194].

Next, we turn to the liposome exhibiting a curved membrane (orange line). The positive and negative q ranges correspond to the outer and inner leaflet, respectively. In the inner leaflet, the liposome shows a heightened barrier compared to the flat bilayer, likely because of the packing structure in the inner leaflet of this fairly small liposome with a diameter of only approximately 10 nm. In the outer leaflet, the barrier is reduced compared to the flat bilayer. The curvature not only alters the head group region but also the membrane center, characterized by a shift of the lowest point of the free energy towards the inner layer. This phenomenon is likely attributed to the compact arrangement of lipids within the inner layer. The symmetry between inner and outer bilayer is thus broken, such that, concretely, the O_2 concentration is higher in the inner leaflet than in the outer leaflet.

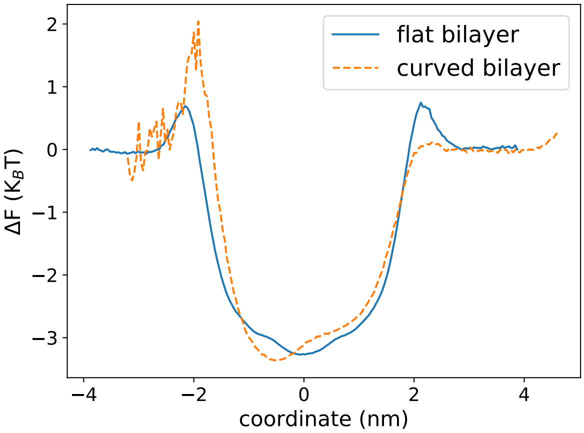

Figure 6.5: The O_2 free energy profile as a function of the permeation coordinate (normal to the membrane).

It is possible that this asymmetry could be mitigated in a liposome with a larger radius.

The changes induced by curvature thus show an opposite trend in the inner and outer leaflets, and it remains unclear how these free energy changes will affect the overall O_2 buffering capacity. To fully understand the effect on the permeation and storage kinetics, the time aspect should also be included. In future work, we aim to investigate the O_2 permeability, O_2 storage capacity, and O_2 residence time.

CHAPTER 7

CONCLUSION AND PERSPECTIVES

7.1 CONCLUSION

The primary aim of this research was to investigate the effect of membrane curvature and composition on membrane permeability. To accomplish this goal, Chapter 3 presents an equation for computing permeability in liposomes, which is independent of the liposome radius. This equation enables us to compare the permeability of flat and curved membranes and thus assess the effect of curvature on the permeability. Additionally, Chapter 4 investigated the efficiency of the counting crossings method for permeability calculations in flat membranes.

The followoing paragraphs provide a summary of the findings concerning the impact of membrane curvature and composition on passive permeability in pH-sensitive liposomes (Chapter 5) and on partitioning of O_2 in curved membranes (Chapter 6).

Passive permeability in pH-sensitive liposomes

In Chapter 5, we employed CG MD simulations to explore the influence of membrane curvature and composition of pH-sensitive liposomes on the permeability of three small permeants with different free energy profiles. This gives us an answer to the question which effect is dominant for the investigated membrane permeabilities: permeant type, composition, or curvature?

First, the permeant type (water, N0, Na), represented by the free energy profile or solubility, is most important. Second, the membrane composition with FAs or cholesterol can cause variations that lie often within a 35% change for water or a 55% change for N0. Introduction of FAs and cholesterol into the membrane exhibits contrasting effects on permeability: while FAs elevate permeability (deprotonated FAs more than neutral FAs because of their charges), cholesterol reduces it. With simultaneous incorporation of cholesterol and FAs, cholesterol tempers the action of FAs as N0 permeability enhancers.

Third, curvature reduces the membrane thickness, and also decreases the free energy in the head group region, except for the highly curved liposomes. Curvature thus facilitates the permeation through the membrane (Fig. 5.9). Concretely, a high curvature (radius 50 Å) increases the water permeability P^* by an enhancement factor of 1.7 for a pure DPPC bilayer. A low curvature (L_{130}) still increases the water permeability P^* by about 1.4, but the escape kinetics seem to have converged to those of a flat bilayer. The escape and entrance water permeability differ considerably, even up to a factor 7 for highly curved membranes, and this persists for the lower curvatures with still a factor 2 difference. Hence, for curved membranes, the type of experiment – escape or entrance – is expected to be dominant in the kinetics. Importantly, realistic liposomes in drug delivery applications are commonly much larger (less curved) than the studied systems, and it is likely that realistic liposomes will have less effect from curvature.

For drug release kinetics, the dominating effect is thus lipid composition for large liposomes and curvature for very small liposomes. The FAs will indeed enhance the passive permeability, but this is still fairly limited, not even a factor 2, for the investigated permeants. Therefore, passive permeation from pH-sensitive liposomes containing FAs may not be a substantial phenomenon, and the undesired occurrence of premature drug release may be less probable. This implies that neither FAs nor curvature can induce premature drug release through pH-sensitive liposomes.

Partitioning of oxygen in curved membranes

In the system consisting of a curved membrane and O_2, the effect of the membrane's curvature on the partitioning of O_2 in the membrane is examined with AA MD simulations. The free energy and partition coefficient profiles demonstrate that O_2's preference to stay in the membrane decreases as the membrane's curvature increases, resulting in the smaller partition coefficient. This leads to lower O_2 concentration in the membrane. In the liposome, O_2 needs to overcome a smaller energy barrier to permeate from the outer leaflet to the water phase, which facilitates the permeation process. This can also be related to the smaller thickness and the larger area per lipid of the outer layer of the curved membrane. These results differ from our initial hypothesis regarding the role of curvature in storing O_2 in caveolae. However, it is worth noting that our simulation did not include cholesterol nor the caveolin protein, which may have a significant impact on the results.

To make the investigation of a whole caveola system (caveolin protein included) computationally feasible in future research, a CG model for O_2 was chosen from Martini 3 beads. This will allow to model O_2 in large simulation boxes encompassing a caveola in its true size, as CG simulations are computationally cheaper than AA simulations. The CG model for O_2 was chosen after assessing a few parameters such as charge, polarity, and partitioning inside the membrane. The CG O_2 model showed a good agreement with AA O_2 for the partitioning between lipids and water. The results showed that the model O_2 can be considered as a good substitute for AA O2.

7.2 PERSPECTIVES

Passive permeability in pH-sensitive liposomes

In our project, we simulated systems comprising 100% charged FAs and 100% neutral FAs due to the unavailability of the dissociation constant for the FAs used in our simulations. For precise membrane modeling involving FAs, it is recommended to calculate the dissociation constant of the FAs using AA MD and compare it with experimental data. Once the dissociation constant would be determined, it could be utilized to simulate large systems in CG resolution, ensuring the incorporation of appropriate proportions of charged and neutral FAs in the lipid composition. This approach would improve accuracy and reliability in modeling complex systems.

Partitioning of oxygen in curved membranes

The results in this thesis indicated that curvature may have a negligible effect in the O_2 partition coefficient, and it is unlikely that membrane curvature is the only mechanism by which a caveola stores O_2. For a comprehensive investigation of the influence of caveolae's structural parameters on O_2 partitioning, it seems imperative to consider all structural aspects, including curvature, cholesterol content, and caveolin protein. Moreover, the timeliness of O_2 transport, specifically its permeability, could be assessed in future studies.

Additionally, we selected our O_2 model from the existing Martini beads since developing a new CG model would have been beyond the scope of this project. However, it would advisable to parameterize a CG Martini model specifically for O_2, as our current model shows proficiency but lacks the complete accuracy.

BIBLIOGRAPHY

[1] F. Ramos-Martín and N. D'Amelio, 'Biomembrane lipids: When physics and chemistry join to shape biological activity', *Biochimie*, vol. 203, pp. 118–138, 2022.

[2] D. Casares, P. V. Escribá and C. A. Rosselló, 'Membrane lipid composition: Effect on membrane and organelle structure, function and compartmentalization and therapeutic avenues', *Int. J. Mol. Sci.*, vol. 20, no. 9, p. 2167, 2019.

[3] K. Renard and B. Byrne, 'Insights into the role of membrane lipids in the structure, function and regulation of integral membrane proteins', *Int. J. Mol. Sci.*, vol. 22, no. 16, p. 9026, 2021.

[4] C. C. De Carvalho and M. J. Caramujo, 'The various roles of fatty acids', *Molecules.*, vol. 23, no. 10, p. 2583, 2018.

[5] G. Maulucci *et al.*, 'Fatty acid-related modulations of membrane fluidity in cells: Detection and implications', *Free Radic. Res.*, vol. 50, no. sup1, S40–S50, 2016.

[6] I. Tabas *et al.*, 'Cholesterol in health and disease', *J. Clin. Invest.*, vol. 110, no. 5, pp. 583–590, 2002.

[7] M. A. Ayee and I. Levitan, 'Paradoxical impact of cholesterol on lipid packing and cell stiffness', *Front. Biosci. (Landmark Ed)*, vol. 21, no. 6, pp. 1245–59, 2016.

[8] N. Filipczak, J. Pan, S. S. K. Yalamarty and V. P. Torchilin, 'Recent advancements in liposome technology', *Adv. Drug Deliv. Rev.*, vol. 156, pp. 4–22, 2020.

[9] E. Beltrán-Gracia, A. López-Camacho, I. Higuera-Ciapara, J. B. Velázquez-Fernández and A. A. Vallejo-Cardona, 'Nanomedicine review: Clinical developments in liposomal applications', *Cancer Nanotechnol.*, vol. 10, no. 1, pp. 1–40, 2019.

[10] A. C. Alves, D. Ribeiro, C. Nunes and S. Reis, 'Biophysics in cancer: The relevance of drug-membrane interaction studies', *Biochim. Biophys. Acta - Biomembr.*, vol. 1858, no. 9, pp. 2231–2244, 2016.

[11] S. Genheden and L. A. Eriksson, 'Estimation of liposome penetration barriers of drug molecules with all-atom and coarse-grained models', *J. Chem. Inf. Model.*, vol. 12, no. 9, pp. 4651–4661, 2016.

[12] D. K. Mishra, R. Shandilya and P. K. Mishra, 'Lipid based nanocarriers: A translational perspective', *Nanomedicine: NBM*, vol. 14, no. 7, pp. 2023–2050, 2018.

[13] A. A. Khan, K. S. Allemailem, S. A. Almatroodi, A. Almatroudi and A. H. Rahmani, 'Recent strategies towards the surface modification of liposomes: An innovative approach for different clinical applications', *3 Biotech*, vol. 10, pp. 1–15, 2020.

[14] M. A. Aghdam *et al.*, 'Recent advances on thermosensitive and ph-sensitive liposomes employed in controlled release', *J. Control. Release*, vol. 315, pp. 1–22, 2019.

[15] M. P. Nikolova, E. M. Kumar and M. S. Chavali, 'Updates on responsive drug delivery based on liposome vehicles for cancer treatment', *Pharmaceutics*, vol. 14, no. 10, p. 2195, 2022.

[16] J. Kurniawan, K. Suga and T. L. Kuhl, 'Interaction forces and membrane charge tunability: Oleic acid containing membranes in different ph conditions', *Biochim. Biophys. Acta - Biomembr.*, vol. 1859, no. 2, pp. 211–217, 2017.

[17] I. Lado-Touriño and A. Cerpa-Naranjo, 'Coarse-grained molecular dynamics of ph-sensitive lipids', *Int. J. Mol. Sci.*, vol. 24, no. 5, p. 4632, 2023.

[18] M.-J. Choi, H.-S. Han and H. Kim, 'Ph-sensitive liposomes containing polymerized phosphatidylethanolamine and fatty acid', *J. Biochem.*, vol. 112, no. 5, pp. 694–699, 1992.

[19] Y. Yang *et al.*, 'Structure–activity relationship of ph-sensitive doxorubicin-fatty acid prodrug albumin nanoparticles', *Nano Lett.*, 2023.

[20] B. Smit and T. L. M. Maesen, 'Molecular Simulations of Zeolites: Adsorption, Diffusion, and Shape Selectivity', *Chem. Rev.*, vol. 108, pp. 4125–4184, 2008.

[21] M. Tagliazucchi, ‘Chemically modified nanopores and nanochannels’, in William Andrew Publishing, 2017, ch. 1, pp. 1–25.

[22] Y. Shen *et al.*, ‘Achieving high permeability and enhanced selectivity for angstrom-scale separations using artificial water channel membranes’, *Nat. Commun.*, vol. 9, p. 2294, 2018.

[23] V. A. Poteryaeva, M. A. Bubenchikov, A. M. Bubenchikov and A. V. Lun-Fu, ‘The interaction of atoms and molecules with nanocapsules and hollow nanowires’, *Sci. Rep.*, vol. 10, p. 15 631, 2020.

[24] A. Mandal, V. Agrahari, V. Khurana, D. Pal and A. Mitra, ‘Transporter effects on cell permeability in drug delivery’, *Expert Opin. Drug Deliv.*, vol. 14, pp. 385–401, 3 2017.

[25] B. J. Bennion *et al.*, ‘Predicting a drug’s membrane permeability: A computational model validated with in vitro permeability assay data’, *J. Phys. Chem. B*, vol. 121, pp. 5228–5237, 20 2017.

[26] L. Galluzzi, I. Vitale and G. Kroemer, ‘Molecular mechanisms of cell death: Recommendations of the nomenclature committee on cell death 2018’, *Cell Death Differ.*, vol. 25, pp. 486–541, 2018.

[27] R. J. Dotson, K. Smith Bueche, G. Angles and S. C. Pias, ‘Influence of cholesterol on the oxygen permeability of membranes: Insight from atomistic simulations’, *Biophys. J.*, vol. 112, no. 11, pp. 2336–2347, 2017.

[28] R. M. Venable, A. Krämer and R. W. Pastor, ‘Molecular Dynamics Simulations of Membrane Permeability’, *Chem. Rev.*, vol. 119, pp. 5954–5997, 9 2019.

[29] O. De Vos, R. M. Venable, T. Van Hecke, G. Hummer, R. W. Pastor and A. Ghysels, ‘Membrane Permeability: Characteristic Times and Lengths for Oxygen and a Simulation-Based Test of the Inhomogeneous Solubility-Diffusion Model’, *J. Chem. Theory Comput.*, vol. 14, no. 7, pp. 3811–3824, 2018.

[30] A. Ghysels, R. M. Venable, R. W. Pastor and G. Hummer, ‘Position-Dependent Diffusion Tensors in Anisotropic Media from Simulation: Oxygen Transport in and through Membranes’, *J. Chem. Theory Comput.*, vol. 13, no. 6, pp. 2962–2976, 2017.

[31] O. De Vos, T. Van Hecke and A. Ghysels, ‘Effect of chain unsaturation and temperature on oxygen diffusion through lipid membranes from simulations’, *Adv. Exp. Med. Biol.*, vol. 1072, pp. 399–404, 2018.

[32] A. Ghysels *et al.*, ‘Permeability of membranes in the liquid ordered and liquid disordered phases’, *Nat. Commun.*, vol. 10, p. 5616, 2019.

[33] R. J. Dotson and S. C. Pias, ‘Reduced oxygen permeability upon protein incorporation within phospholipid bilayers’, *Adv. Exp. Med. Biol.*, vol. 1072, pp. 405–411, 2018.

[34] H.-D. Holtje, W. Sippl, D. Rognan and G. Folkers, ‘Molecular modeling’. Wiley-VCH Weinheim, Germany, 2003, vol. 5.

[35] T. I. Adelusi *et al.*, ‘Molecular modeling in drug discovery’, *Inform. Med. Unlocked*, vol. 29, p. 100 880, 2022.

[36] O. M. Salo-Ahen *et al.*, ‘Molecular dynamics simulations in drug discovery and pharmaceutical development’, *Processes*, vol. 9, no. 1, p. 71, 2020.

[37] A. V. V. Nikezić, A. M. Bondžić and V. M. Vasić, ‘Drug delivery systems based on nanoparticles and related nanostructures’, *Eur. J. Pharm. Sci.*, vol. 151, p. 105 412, 2020.

[38] X. Woodward and C. V. Kelly, ‘Nanoscale membrane curvature sorts lipid phases and alters lipid diffusion’, *bioRxiv*, pp. 2020–09, 2020.

[39] A. Buyan, D. Allender, B. Corry and M. Schick, ‘Lipid redistribution in the highly curved footprint of piezo1’, *Biophys. J.*, vol. 122, no. 11, pp. 1900–1913, 2023.

[40] H. Hashemzadeh, H. Javadi and M. Darvishi, ‘Study of structural stability and formation mechanisms in dspc and dpsm liposomes: A coarse-grained molecular dynamics simulation’, *Sci. Rep.*, vol. 10, no. 1, pp. 1–10, 2020.

[41] S. Yesylevskyy and H. Khandelia, ‘Encurv: Simple technique of maintaining global membrane curvature in molecular dynamics simulations’, *J. Chem. Theory Comput.*, vol. 17, no. 2, pp. 1181–1193, 2021.

[42] A. Arouri, K. E. Lauritsen, H. L. Nielsen and O. G. Mouritsen, ‘Effect of fatty acids on the permeability barrier of model and biological membranes’, *Chem. Phys. Lipids*, vol. 200, pp. 139–146, 2016.

[43] S. Hossain *et al.*, 'Influence of bile composition on membrane incorporation of transient permeability enhancers', *Mol. Pharm.*, vol. 17, no. 11, pp. 4226–4240, 2020.

[44] D. J. Brayden, J. Gleeson and E. G. Walsh, 'A head-to-head multi-parametric high content analysis of a series of medium chain fatty acid intestinal permeation enhancers in Caco-2 cells', *Eur. J. Pharm. Biopharm.*, vol. 88, no. 3, pp. 830–839, 2014.

[45] J. M. Schilling, B. P. Head and H. H. Patel, 'Caveolins as regulators of stress adaptation', *Molecular Pharmacology*, vol. 93, no. 4, pp. 277–285, 2018.

[46] C. R. Woese, O. Kandler and M. L. Wheelis, 'Towards a natural system of organisms: Proposal for the domains archaea, bacteria, and eucarya.' *Proceedings of the National Academy of Sciences*, vol. 87, no. 12, pp. 4576–4579, 1990.

[47] R. Carter, *Book of the month: Oxygen: The molecule that made the world*, 2003.

[48] H. J. Shields, A. Traa and J. M. Van Raamsdonk, 'Beneficial and detrimental effects of reactive oxygen species on lifespan: A comprehensive review of comparative and experimental studies', *Frontiers in Cell and Developmental Biology*, vol. 9, p. 181, 2021.

[49] A. J. Brown and A. M. Galea, 'Cholesterol as an evolutionary response to living with oxygen', *Evolution*, vol. 64, no. 7, pp. 2179–2183, 2010.

[50] J. C. Porta *et al.*, 'Molecular architecture of the human caveolin-1 complex', *Sci. Adv.*, vol. 8, no. 19, eabn7232, 2022.

[51] H. H. Patel *et al.*, 'Mechanisms of cardiac protection from ischemia/reperfusion injury: A role for caveolae and caveolin-1', *The FASEB Journal*, vol. 21, no. 7, pp. 1565–1574, 2007.

[52] B. P. Head *et al.*, 'Loss of caveolin-1 accelerates neurodegeneration and aging', *PloS one*, vol. 5, no. 12, e15697, 2010.

[53] W. K. Subczynski, M. Pasenkiewicz-Gierula, R. N. McElhaney, J. S. Hyde and A. Kusumi, 'Molecular dynamics of 1-palmitoyl-2-oleoylphosphatidylcholine membranes containing transmembrane α-helical peptides with alternating leucine and alanine residues', *Biochemistry*, vol. 42, no. 13, pp. 3939–3948, 2003.

[54] J. Widomska, M. Raguz and W. K. Subczynski, ‘Oxygen permeability of the lipid bilayer membrane made of calf lens lipids’, *BBA - Biomembranes*, vol. 1768, no. 10, pp. 2635–2645, 2007.

[55] M. Möller, J. Lancaster and A. Denicola, ‘The interaction of reactive oxygen and nitrogen species with membranes’, *Curr. Top. Membr.*, vol. 61, pp. 23–42, 2007.

[56] J. Godyń *et al.*, ‘Novel application of capillary electrophoresis with a liposome coated capillary for prediction of blood-brain barrier permeability’, *Talanta*, vol. 217, p. 121 023, 2020.

[57] J. W. Choi, S. H. Bae, M. Kwakc, T. G. Lee, M. B. Heo and D. W. Lee, ‘Extracellular matrix permeability/efficacy assay tip (e-pat) to realize three-dimensional cell-based screening’, *Sens. Actuators B-Chem.*, vol. 321, p. 128 624, 2020.

[58] P. Bacchin, D. Snisarenko, D. Stamatialis, P. Aimar and C. Causserand, ‘Combining fluorescence and permeability measurements in a membrane microfluidic device to study protein sorption mechanisms’, *J. Membr. Sci.*, vol. 614, p. 118 485, 2020.

[59] C. Lin, T.-C. Kuo, J.-C. Lin, Y.-C. Ho and F.-L. Mi, ‘Delivery of polysaccharides from ophiopogon japonicus (ojps) using ojps/chitosan/whey protein co-assembled nanoparticles to treat defective intestinal epithelial tight junction barrier’, *Int. J. Biol. Macromol.*, vol. 160, pp. 558–570, 2020.

[60] E. Awoonor-Williams and C. N. Rowley, ‘Molecular Simulation of Nonfacilitated Membrane Permeation’, *Biochim. Biophys. Acta - Biomembr.*, vol. 1858, no. 7, pp. 1627–1687, 2016.

[61] N. Pokhrel and L. Maibaum, ‘Free Energy Calculations of Membrane Permeation: Challenges Due to Strong Headgroup-Solute Interactions’, *J. Chem. Theory Comput.*, vol. 14, no. 3, pp. 1762–1771, 2018.

[62] C. Hoffmann, A. Centi, R. Menichetti and T. Bereau, ‘Molecular dynamics trajectories for 630 coarse-grained drug membrane permeations’, *Sci. Data*, vol. 7, pp. 1–7, 2020.

[63] C. T. Lee *et al.*, ‘Simulation-based approaches for determining membrane permeability of small compounds’, *J. Chem. Inf. Model*, vol. 56, pp. 721–733, 2016.

[64] W. Shinoda, ‘Permeability across lipid membranes’, *Biochim. Biophys. Acta - Biomembr.*, vol. 1858, no. 10, pp. 2254–2265, 2016.

[65] S. Marrink and H. J. C. Berendsen, 'Simulation of water transport through a lipid membrane', *J. Phys. Chem.*, vol. 98, no. 15, pp. 4155–4168, 1994.

[66] S. J. Marrink and H. J. C. Berendsen, 'Permeation process of small molecules across lipid membranes studied by molecular dynamics simulations', *J. Phys. Chem.*, vol. 100, no. 41, pp. 16 729–16 738, 1996.

[67] K. Gaalswyk, E. Awoonor-Williams and C. N. Rowley, 'Generalized Langevin Methods for Calculating Transmembrane Diffusivity', *J. Chem. Theory Comput.*, vol. 12, no. 11, pp. 5609–5619, 2016.

[68] H. A. L. Filipe *et al.*, 'Quantitative assessment of methods used to obtain rate constants from molecular dynamics simulations—translocation of cholesterol across lipid bilayers', *J. Chem. Theory Comput.*, vol. 14, pp. 3840–3848, 7 2018.

[69] R. J. Ferreira and P. M. Kasson, 'Antibiotic uptake across gram-negative outer membranes: Better predictions towards better antibiotics', *ACS Infect. Dis.*, vol. 5, pp. 2096–2104, 12 2019.

[70] H. Yang *et al.*, 'Effects of low-level lipid peroxidation on the permeability of nitroaromatic molecules across a membrane: A computational study', *ACS Omega*, vol. 5, pp. 4798–4806, 10 2020.

[71] A. Krämer *et al.*, 'Membrane permeability of small molecules from unbiased molecular dynamics simulations', *J. Chem. Phys.*, vol. 153, p. 124 107, 12 2020.

[72] E. Riccardi, A. Krämer, T. S. van Erp and A. Ghysels, 'Permeation rates of oxygen through a lipid bilayer using replica exchange transition interface sampling', *J. Phys. Chem. B*, vol. 125, no. 1, pp. 193–201, 2020.

[73] A. Ghysels, R. M. Venable, R. W. Pastor and G. Hummer, 'Position-dependent diffusion tensors in anisotropic media from simulation: Oxygen transport in and through membranes', *J. Chem. Theory Comput.*, vol. 13, no. 6, pp. 2962–2976, 2017.

[74] E. M. Nemoto, E. M. Harrison, S. C. Pias, D. E. Bragin, D. K. Harrison and J. C. LaManna, 'Oxygen Transport to Tissue XLII'. Springer, 2021.

[75] Q. Wang, R. J. Dotson, G. Angles and S. C. Pias, 'Simulation study of breast cancer lipid changes affecting membrane oxygen permeability: Effects of chain length and cholesterol', in *Oxygen Transport to Tissue XLII*, Springer, 2021, pp. 15–21.

[76] A. Ghysels *et al.*, 'Permeability of membranes in the liquid ordered and liquid disordered phases', *Nat. Commun*, vol. 10, no. 1, p. 5616, 2019.

[77] R. J. Dotson, C. R. Smith, K. Bueche, G. Angles and S. C. Pias, 'Influence of cholesterol on the oxygen permeability of membranes: Insight from atomistic simulations', *Biophys. J.*, vol. 112, no. 11, pp. 2336–2347, 2017.

[78] G. Angles, R. Dotson, K. Bueche and S. C. Pias, 'Predicted decrease in membrane oxygen permeability with addition of cholesterol', *Oxygen Transport to Tissue XXXIX*, pp. 9–14, 2017.

[79] R. Shea, C. Smith and S. C. Pias, 'Magnification of cholesterol-induced membrane resistance on the tissue level: Implications for hypoxia', in *Oxygen Transport to Tissue XXXVIII*, Springer, 2016, pp. 43–50.

[80] R. J. Dotson, E. McClenahan and S. C. Pias, 'Updated evaluation of cholesterol's influence on membrane oxygen permeability', in *Oxygen Transport to Tissue XLII*, Springer, 2021, pp. 23–30.

[81] S. C. Pias, 'How does oxygen diffuse from capillaries to tissue mitochondria? barriers and pathways', *Physiol. J.*, vol. 599, no. 6, pp. 1769–1782, 2021.

[82] S. C. Pias, 'Pathways of oxygen diffusion in cells and tissues: Hydrophobic channeling via networked lipids', *Oxygen Transport to Tissue XLI*, pp. 183–190, 2020.

[83] R. J. Dotson and S. C. Pias, 'Reduced oxygen permeability upon protein incorporation within phospholipid bilayers', *Oxygen Transport to Tissue XL*, pp. 405–411, 2018.

[84] S. Davoudi, Q. Wang, H. H. Patel, S. C. Pias and A. Ghysels, 'Understanding the role of caveolae in oxygen buffering: The effect of membrane curvature', in *International Society on Oxygen Transport to Tissue*, Springer, 2022, pp. 87–91.

[85] S. Davoudi and A. Ghysels, 'Exploring caveolae's role in oxygen" buffering" through coarse-grained molecular dynamics', in *FEARS 2023*, 2023.

[86] O. De Vos, T. Van Hecke and A. Ghysels, ‘Effect of chain unsaturation and temperature on oxygen diffusion through lipid membranes from simulations’, *Oxygen Transport to Tissue Xl*, pp. 399–404, 2018.

[87] O. De Vos, R. M. Venable, T. Van Hecke, G. Hummer, R. W. Pastor and A. Ghysels, ‘Membrane permeability: Characteristic times and lengths for oxygen and a simulation-based test of the inhomogeneous solubility-diffusion model’, *J. Chem. Theory Comput.*, vol. 14, no. 7, pp. 3811–3824, 2018.

[88] S. Wang, T. Ichinomiya, Y. Terada, D. Wang, H. H. Patel and B. P. Head, ‘Synapsin-promoted caveolin-1 overexpression maintains mitochondrial morphology and function in psapp alzheimer’s disease mice’, *Cells*, vol. 10, no. 9, p. 2487, 2021.

[89] H. Alimohamadi, B. Ovryn and P. Rangamani, ‘Modeling membrane nanotube morphology: The role of heterogeneity in composition and material properties’, *Sci. Rep.*, vol. 10, no. 1, pp. 1–15, 2020.

[90] S. Liese and A. Carlson, ‘Membrane shape remodeling by protein crowding’, *Biophys. J.*, vol. 120, no. 12, pp. 2482–2489, 2021.

[91] A. H. Bahrami and G. Hummer, ‘Formation and stability of lipid membrane nanotubes’, *ACS nano*, vol. 11, no. 9, pp. 9558–9565, 2017.

[92] S. O. Yesylevskyy, T. Rivel and C. Ramseyer, ‘The influence of curvature on the properties of the plasma membrane. insights from atomistic molecular dynamics simulations’, *Sci. Rep.*, vol. 7, no. 1, pp. 1–13, 2017.

[93] S. Yesylevskyy, T. Rivel and C. Ramseyer, ‘Curvature increases permeability of the plasma membrane for ions, water and the anti-cancer drugs cisplatin and gemcitabine’, *Sci. Rep.*, vol. 9, no. 1, pp. 1–8, 2019.

[94] K. J. Boyd and E. R. May, ‘Bumpy: A model-independent tool for constructing lipid bilayers of varying curvature and composition’, *J. Chem. Theory Comput.*, vol. 14, no. 12, pp. 6642–6652, 2018.

[95] L. Casalino *et al.*, ‘Ai-driven multiscale simulations illuminate mechanisms of sars-cov-2 spike dynamics’, *Int. J. High Perform. Comput. Appl.*, vol. 35, no. 5, pp. 432–451, 2021.

[96] Z. R. Thornburg *et al.*, ‘Fundamental behaviors emerge from simulations of a living minimal cell’, *Cell*, vol. 185, no. 2, pp. 345–360, 2022.

[97] S. J. Marrink, L. Monticelli, M. N. Melo, R. Alessandri, D. P. Tieleman and P. C. Souza, ‘Two decades of martini: Better beads, broader scope’, *Wiley Interdiscip. Rev. Comput. Mol. Sci.*, e1620, 2022.

[98] I. Patmanidis, P. C. Souza, S. Sami, R. W. Havenith, A. H. de Vries and S. J. Marrink, ‘Modelling structural properties of cyanine dye nanotubes at coarse-grained level’, *Nanoscale advances*, vol. 4, no. 14, pp. 3033–3042, 2022.

[99] W. Pezeshkian, M. König, T. A. Wassenaar and S. J. Marrink, ‘Backmapping triangulated surfaces to coarse-grained membrane models’, *Nat. Commun.*, vol. 11, no. 1, pp. 1–9, 2020.

[100] S. Davoudi and A. Ghysels, ‘Sampling efficiency of the counting method for permeability calculations estimated with the inhomogeneous solubility–diffusion model’, *J. Chem. Phys.*, vol. 154, no. 5, p. 054 106, 2021.

[101] G. Hummer, ‘Position-dependent diffusion coefficients and free energies from Bayesian analysis of equilibrium and replica molecular dynamics simulations’, *New J. Phys.*, vol. 7, no. 1, p. 34, 2005.

[102] L. W. Votapka, C. T. Lee and R. E. Amaro, ‘Two Relations to Estimate Membrane Permeability Using Milestoning’, *J. Phys. Chem. B*, vol. 120, no. 33, pp. 8606–8616, 2016.

[103] E. Riccardi, A. Lervik, S. Roet, O. Aarøen and T. S. van Erp, ‘Pyretis 2: An improbability drive for rare events’, *J. Comput. Chem.*, vol. 41, pp. 370–377, 2020.

[104] A. Ghysels, S. Roet, S. Davoudi and T. S. van Erp, ‘Exact non-markovian permeability from rare event simulations’, *Physical Review Research*, vol. 3, no. 3, p. 033 068, 2021.

[105] E. Riccardi, A. Krämer, T. van Erp and A. Ghysels, ‘Permeation rates of oxygen transport through POPC membrane using replica exchange transition interface sampling’, *J. Phys. Chem. B*, vol. 125, no. 1, pp. 193–201, 2021.

[106] M. Ghorbani, E. Wang, A. Krämer and J. B. Klauda, ‘Molecular dynamics simulations of ethanol permeation through single and double-lipid bilayers’, *J. Chem. Phys.*, vol. 153, p. 125 101, 12 2020.

[107] Q. Al-Awqati, ‘One hundred years of membrane permeability: Does Overton still rule?’, *Nat. Cell Biol.*, vol. 1, E201–E202, 8 1999.

[108] M. N. Möller, Q. Li, C. Chinnaraj, H. C. Cheung, J. R. Lancaster Jr. and A. Denicola, ‘Solubility and diffusion of oxygen in phospholipid membranes’, *Biochim. Biophys. Acta*, vol. 1858, pp. 2923–2930, 2016.

[109] I. Prislan, M. Lokar, M. Zirdum, J. Valant and N. P. Ulrih, ‘Contribution of headgroup and chain length of glycerophospholipids to thermal stability and permeability of liposomes loaded with calcein’, *Chem. Phys. Lipids*, vol. 225, p. 104 807, 2019.

[110] V. Joguparthi, T.-X. Xiang and B. D. Anderson, ‘Liposome transport of hydrophobic drugs: Gel phase lipid bilayer permeability and partitioning of the lactone form of a hydrophobic camptothecin, db-67’, *J. Pharm. Sci.*, vol. 97, no. 1, pp. 400–420, 2008.

[111] N. D. Winter, R. K. Murphy, T. V. O’Halloran and G. C. Schatz, ‘Development and modeling of arsenic-trioxide–loaded thermosensitive liposomes for anticancer drug delivery’, *J. Liposome Res.*, vol. 21, no. 2, pp. 106–115, 2011.

[112] Z. Yue, C. Li, G. A. Voth and J. M. Swanson, ‘Dynamic protonation dramatically affects the membrane permeability of drug-like molecules’, *J. Am. Chem. Soc.*, vol. 141, no. 34, pp. 13 421–13 433, 2019.

[113] M. Palaiokostas, W. Ding, G. Shahane and M. Orsi, ‘Effects of lipid composition on membrane permeation’, *Soft Matter*, vol. 14, no. 42, pp. 8496–8508, 2018.

[114] M. Saeedimasine, A. Montanino, S. Kleiven and A. Villa, ‘Role of lipid composition on the structural and mechanical features of axonal membranes: A molecular simulation study’, *Sci. Rep.*, vol. 9, no. 1, pp. 1–12, 2019.

[115] G. Nasr, H. Greige-Gerges, A. Elaissari and N. Khreich, ‘Liposome permeability to essential oil components: A focus on cholesterol content’, *The Journal of Membrane Biology*, vol. 254, no. 4, pp. 381–395, 2021.

[116] M.-L. Briuglia, C. Rotella, A. McFarlane and D. A. Lamprou, ‘Influence of cholesterol on liposome stability and on in vitro drug release’, *Drug Deliv. Transl. Res.*, vol. 5, no. 3, pp. 231–242, 2015.

[117] E. Sezgin and I. Levental, ‘Membranes in focus’, *Biophys. J.*, vol. 122, no. 11, E1–E4, 2023.

[118] M. Sugita, T. Fujie, K. Yanagisawa, M. Ohue and Y. Akiyama, ‘Lipid composition is critical for accurate membrane permeability prediction of cyclic peptides by molecular dynamics simulations’, *J. Chem. Inf. Model.*, vol. 62, no. 18, pp. 4549–4560, 2022.

[119] N. Ileri Ercan, ‘Understanding interactions of curcumin with lipid bilayers: A coarse-grained molecular dynamics study’, *J. Chem. Inf. Model.*, vol. 59, no. 10, pp. 4413–4426, 2019.

[120] X. Zhang, K. M. Barraza and J. Beauchamp, ‘Cholesterol provides nonsacrificial protection of membrane lipids from chemical damage at air–water interface’, *Proc. Natl. Acad. Sci.*, vol. 115, no. 13, pp. 3255–3260, 2018.

[121] Z. Cao *et al.*, ‘Different effects of cholesterol on membrane permeation of arginine and tryptophan revealed by bias-exchange metadynamics simulations’, *J. Chem. Phys.*, vol. 150, no. 8, p. 084 106, 2019.

[122] E. Falck, M. Patra, M. Karttunen, M. T. Hyvönen and I. Vattulainen, ‘Impact of cholesterol on voids in phospholipid membranes’, *J. Chem. Phys.*, vol. 121, no. 24, pp. 12 676–12 689, 2004.

[123] L. Jin, A. E. Engelhart, K. P. Adamala and J. W. Szostak, ‘Preparation, purification, and use of fatty acid-containing liposomes’, *J. Vis. Exp. (JoVE)*, vol. 132, e57324, 2018.

[124] C. Twarog, S. Fattah, J. Heade, S. Maher, E. Fattal and D. J. Brayden, ‘Intestinal permeation enhancers for oral delivery of macromolecules: A comparison between salcaprozate sodium (SNAC) and sodium caprate (C10)’, *Pharmaceutics*, vol. 11, no. 2, p. 78, 2019.

[125] S. M. Krug, M. Amasheh, I. Dittmann, I. Christoffel, M. Fromm and S. Amasheh, ‘Sodium caprate as an enhancer of macromolecule permeation across tricellular tight junctions of intestinal cells’, *Biomaterials*, vol. 34, no. 1, pp. 275–282, 2013.

[126] F. McCartney, J. P. Gleeson and D. J. Brayden, ‘Safety concerns over the use of intestinal permeation enhancers: A mini-review’, *Tissue barriers*, vol. 4, no. 2, e1176822, 2016.

[127] S. Škulj and M. Vazdar, 'Calculation of apparent p k a values of saturated fatty acids with different lengths in dopc phospholipid bilayers', *Phys. Chem. Chem. Phys.*, vol. 21, no. 19, pp. 10 052–10 060, 2019.

[128] D. Bonhenry, M. Tarek and F. Dehez, 'Effects of phospholipid composition on the transfer of a small cationic peptide across a model biological membrane', *J. Chem. Theory Comput.*, vol. 9, no. 12, pp. 5675–5684, 2013.

[129] A. A. Pashkovskaya, M. Vazdar, L. Zimmermann, O. Jovanovic, P. Pohl and E. E. Pohl, 'Mechanism of long-chain free fatty acid protonation at the membrane-water interface', *Biophys. J.*, vol. 114, no. 9, pp. 2142–2151, 2018.

[130] R. Kneiszl, S. Hossain and P. Larsson, 'In silico-based experiments on mechanistic interactions between several intestinal permeation enhancers with a lipid bilayer model', *Mol. Pharm.*, vol. 19, no. 1, pp. 124–137, 2021.

[131] S. Davoudi, Q. Wang, H. H. Patel, S. C. Pias and A. Ghysels, 'Understanding the role of caveolae in oxygen buffering: The effect of membrane curvature', in *Oxygen Transport to Tissue XLIV*, F. Scholkmann, J. LaManna and U. Wolf, Eds., Springer International Publishing, 2023, pp. 87–91.

[132] H. J. Risselada and S. J. Marrink, 'Curvature effects on lipid packing and dynamics in liposomes revealed by coarse grained molecular dynamics simulations', *Phys. Chem. Chem. Phys.*, vol. 11, no. 12, pp. 2056–2067, 2009.

[133] N. D. Winter and G. C. Schatz, 'Coarse-grained molecular dynamics study of permeability enhancement in dppc bilayers by incorporation of lysolipid', *J. Phys. Chem. B*, vol. 114, no. 15, pp. 5053–5060, 2010.

[134] P. C. Souza *et al.*, 'Martini 3: A general purpose force field for coarse-grained molecular dynamics', *Nat. Methods*, vol. 18, no. 4, pp. 382–388, 2021.

[135] X. Lin, F. Tian and S.-J. Marrink, 'Martini coarse-grained nitrogen gas model for lipid nanobubble simulations', 2021.

[136] S. Davoudi and A. Ghysels, 'Defining permeability of curved membranes in molecular dynamics simulations', *Biophys. J.*, vol. 122, no. 11, pp. 2082–2091, 2023.

[137] M. J. Abraham *et al.*, 'Gromacs: High performance molecular simulations through multi-level parallelism from laptops to supercomputers', *SoftwareX*, vol. 1, pp. 19–25, 2015.

[138] S. J. Marrink, A. H. De Vries and A. E. Mark, 'Coarse grained model for semiquantitative lipid simulations', *J. Phys. Chem. B*, vol. 108, no. 2, pp. 750–760, 2004.

[139] S. J. Marrink, H. J. Risselada, S. Yefimov, D. P. Tieleman and A. H. De Vries, 'The martini force field: Coarse grained model for biomolecular simulations', *J. Phys. Chem. B*, vol. 111, pp. 7812–7824, 27 2007.

[140] P. Mark and L. Nilsson, 'Structure and dynamics of the tip3p, spc, and spc/e water models at 298 k', *J. Phys. Chem. A*, vol. 105, pp. 9954–9960, 43 2001.

[141] I. G. Tironi, R. Sperb, P. E. Smith and W. F. van Gunsteren, 'A generalized reaction field method for molecular dynamics simulations', *J. Chem. Phys.*, vol. 102, no. 13, pp. 5451–5459, 1995.

[142] S. J. Marrink, H. J. Risselada, S. Yefimov, D. P. Tieleman and A. H. De Vries, 'The martini force field: Coarse grained model for biomolecular simulations', *J. Phys. Chem. B*, vol. 111, no. 27, pp. 7812–7824, 2007.

[143] S. Davoudi, S. Amjad-Iranagh and M. Zaeifi Yamchi, 'Molecular dynamic simulation of ca2+-atpase interacting with lipid bilayer membrane', *IET Nanobiotechnol.*, vol. 9, no. 2, pp. 85–94, 2015.

[144] C. I. Nkanga, A. M. Bapolisi, N. I. Okafor and R. W. M. Krause, 'General perception of liposomes: Formation, manufacturing and applications', *Liposomes-advances and perspectives*, 2019.

[145] F. Grünewald, P. C. Souza, H. Abdizadeh, J. Barnoud, A. H. de Vries and S. J. Marrink, 'Titratable martini model for constant ph simulations', *J. Chem. Phys.*, vol. 153, no. 2, 2020.

[146] M. J. Abraham *et al.*, 'Gromacs: High performance molecular simulations through multi-level parallelism from laptops to supercomputers', *SoftwareX*, vol. 1, pp. 19–25, 2015.

[147] S. Jo, T. Kim, V. G. Iyer and W. Im, 'Charmm-gui: A web-based graphical user interface for charmm', *J. Comput. Chem.*, vol. 29, no. 11, pp. 1859–1865, 2008.

[148] B. R. Brooks *et al.*, *J. Comput. Chem.*, vol. 30, no. 10, pp. 1545–1614, 2009.

[149] J. Lee *et al.*, ‘Charmm-gui input generator for namd, gromacs, amber, openmm, and charmm/openmm simulations using the charmm36 additive force field’, *J. Chem. Theory Comput.*, vol. 12, no. 1, pp. 405–413, 2016.

[150] Y. Qi, H. I. Ingólfsson, X. Cheng, J. Lee, S. J. Marrink and W. Im, ‘Charmm-gui martini maker for coarse-grained simulations with the martini force field’, *J. Chem. Theory Comput.*, vol. 11, no. 9, pp. 4486–4494, 2015.

[151] G. Bussi, D. Donadio and M. Parrinello, ‘Canonical sampling through velocity rescaling’, *J. Chem. Phys.*, vol. 126, no. 1, p. 014 101, 2007.

[152] J. Huang and A. D. MacKerell Jr, ‘Charmm36 all-atom additive protein force field: Validation based on comparison to nmr data’, *Journal of computational chemistry*, vol. 34, no. 25, pp. 2135–2145, 2013.

[153] W. L. Jorgensen, J. Chandrasekhar, J. D. Madura, R. W. Impey and M. L. Klein, ‘Comparison of simple potential functions for simulating liquid water’, *The Journal of chemical physics*, vol. 79, no. 2, pp. 926–935, 1983.

[154] R. Battino, ‘Oxygen and Ozone: Solubility Data Series’. Elsevier, 2015, vol. 7.

[155] M. Alwarawrah, J. Dai and J. Huang, ‘A molecular view of the cholesterol condensing effect in dopc lipid bilayers’, *J. Phys. Chem. B*, vol. 114, no. 22, pp. 7516–7523, 2010.

[156] B. Kheyfets and S. Mukhin, ‘Area per lipid in dppc-cholesterol bilayers: Analytical approach’, *arXiv preprint arXiv:1501.02727*, 2015.

[157] F. Leeb and L. Maibaum, ‘Spatially resolving the condensing effect of cholesterol in lipid bilayers’, *Biophys. J.*, vol. 115, no. 11, pp. 2179–2188, 2018.

[158] T. S. van Erp, ‘Reaction rate calculation by parallel path swapping’, *Phys. Rev. Lett.*, vol. 98, p. 268 301, 2007.

[159] A. Lervik, E. Riccardi and T. S. van Erp, ‘PyRETIS: A well-done, medium-sized python library for rare events’, *J. Comput. Chem.*, vol. 38, no. 28, pp. 2439–2451, 2017.

[160] E. Riccardi, A. Krämer, T. S. van Erp and A. Ghysels, ‘Permeation rates of oxygen transport through popc membrane based on replica exchange transition interface sampling’, *In press*, 2020.

[161] E. Darve and A. Pohorille, 'Calculating free energies using average force', *J. Chem. Phys.*, vol. 115, no. 20, pp. 9169–9183, 2001.

[162] J. Comer, K. Schulten and C. Chipot, 'Calculation of lipid-bilayer permeabilities using an average force', *J. Chem. Theory Comput.*, vol. 10, no. 2, pp. 554–564, 2014.

[163] C. T. Lee *et al.*, 'Simulation-Based Approaches for Determining Membrane Permeability of Small Compounds.' eng, *J. Chem. Inf. Model.*, vol. 56, pp. 721–733, 2016.

[164] N. Kučerka, M.-P. Nieh and J. Katsaras, 'Fluid phase lipid areas and bilayer thicknesses of commonly used phosphatidylcholines as a function of temperature', *Biochim. Biophys. Acta - Biomembr.*, vol. 1808, no. 11, pp. 2761–2771, 2011.

[165] K. Hac-Wydro and P. Wydro, 'The influence of fatty acids on model cholesterol/phospholipid membranes', *Chem. Phys. Lipids.*, vol. 150, no. 1, pp. 66–81, 2007.

[166] F. de Meyer and B. Smit, 'Effect of cholesterol on the structure of a phospholipid bilayer', *Proc. Natl. Acad. Sci. U.S.A.*, vol. 106, no. 10, pp. 3654–3658, 2009.

[167] M. Saeedimasine, A. Montanino, S. Kleiven and A. Villa, 'Role of lipid composition on the structural and mechanical features of axonal membranes: A molecular simulation study', *Sci. Rep.*, vol. 9, no. 1, pp. 1–12, 2019.

[168] S. Yesylevskyy, H. Martinez-Seara and P. Jungwirth, 'Curvature matters: Modeling calcium binding to neutral and anionic phospholipid bilayers', *J. Phys. Chem. B*, vol. 127, no. 20, pp. 4523–4531, 2023.

[169] D. E. S. Santos, K. Coutinho and T. A. Soares, 'Surface assessment via grid evaluation (suave) for every surface curvature and cavity shape', *J. Chem. Inf. Model.*, no. 62, pp. 4690–4701, 2022.

[170] D. E. S. Santos, A. De Nicola, V. F. dos Santos, G. Milano and T. A. Soares, 'Exploring the molecular dynamics of a lipid-a vesicle at the atom level: Morphology and permeation mechanism', *J. Chem. Phys. B*, no. 127, pp. 6694–6702, 2023.

[171] S. Scrima *et al.*, 'Unraveling membrane properties at the organelle-level with lipiddyn', *Comput. Struct. Biotechnol. J.*, vol. 30, no. 20, pp. 3604–3614, 2022.

[172] A. Carruthers and D. Melchior, ‘Study of the relationship between bilayer water permeability and bilayer physical state’, *Biochem.*, vol. 22, no. 25, pp. 5797–5807, 1983.

[173] D. Huster, A. J. Jin, K. Arnold and K. Gawrisch, ‘Water permeability of polyunsaturated lipid membranes measured by 17o nmr’, *Biophys. J.*, vol. 73, no. 2, pp. 855–864, 1997.

[174] A. Arouri and O. G. Mouritsen, ‘Membrane-perturbing effect of fatty acids and lysolipids’, *Prog. Lipid Res.*, vol. 52, no. 1, pp. 130–140, 2013.

[175] M. A. Via, N. Wilke, L. S. Mayorga and M. G. Del Pópolo, ‘Surface charge density and fatty acids enhance the membrane permeation rate of cpp–cargo complexes’, *Soft Matter*, vol. 16, no. 43, pp. 9890–9898, 2020.

[176] Y.-W. Chiang, A. J. Costa-Filho and J. H. Freed, ‘Dynamic molecular structure and phase diagram of dppc- cholesterol binary mixtures: A 2d-eldor study’, *J. Phys. Chem. B*, vol. 111, no. 38, pp. 11 260–11 270, 2007.

[177] Y. Wang, P. Gkeka, J. E. Fuchs, K. R. Liedl and Z. Cournia, ‘Dppc-cholesterol phase diagram using coarse-grained molecular dynamics simulations’, *Biochim. Biophys. Acta - Biomembr.*, vol. 1858, no. 11, pp. 2846–2857, 2016.

[178] M. R. Vist and J. H. Davis, ‘Phase equilibria of cholesterol/dipalmitoylphosphatidylcholine mixtures: Deuterium nuclear magnetic resonance and differential scanning calorimetry’, *Biochem.*, vol. 29, no. 2, pp. 451–464, 1990.

[179] W. K. Subczynski, M. Pasenkiewicz-Gierula, J. Widomska, L. Mainali and M. Raguz, ‘High cholesterol/low cholesterol: Effects in biological membranes: A review’, *Cell Biochem. Biophys.*, vol. 75, pp. 369–385, 2017.

[180] N. Mehio, S. Dai and D.-e. Jiang, ‘Quantum mechanical basis for kinetic diameters of small gaseous molecules’, *J. Phys. Chem. A*, vol. 118, no. 6, pp. 1150–1154, 2014.

[181] C. E. Overton, ‘Studien über die Narkose: zugleich ein Beitrag zur allgemeinen Pharmakologie’. G. Fischer, 1901.

[182] A. Missner and P. Pohl, ‘110 years of the meyer–overton rule: Predicting membrane permeability of gases and other small compounds’, *ChemPhysChem*, vol. 10, no. 9-10, pp. 1405–1414, 2009.

[183] 'The engineering toolbox: Oxygen - density and specific weight vs. temperature and pressure'. (2018), [Online]. Available: `https://www.engineeringtoolbox.com/oxygen-O2-density-specific-weight-temperature-pressure-d_2082.html`.

[184] T. Sato, Y. Hamada, M. Sumikawa, S. Araki and H. Yamamoto, 'Solubility of oxygen in organic solvents and calculation of the hansen solubility parameters of oxygen', *Ind. Eng. Chem. Res.*, vol. 53, no. 49, pp. 19 331–19 337, 2014.

[185] L.-K. Ju and C. S. Ho, 'Oxygen diffusion coefficient and solubility in n-hexadecane', *Biotechnol. Bioeng.*, vol. 34, no. 9, pp. 1221–1224, 1989.

[186] C. C. Bannan, G. Calabró, D. Y. Kyu and D. L. Mobley, 'Calculating partition coefficients of small molecules in octanol/water and cyclohexane/water', *J. Chem. Theory Comput.*, vol. 12, no. 8, pp. 4015–4024, 2016.

[187] J. N. van der Veen, J. P. Kennelly, S. Wan, J. E. Vance, D. E. Vance and R. L. Jacobs, 'The critical role of phosphatidylcholine and phosphatidylethanolamine metabolism in health and disease', *Biochim. Biophys. Acta, Biomembr.*, vol. 1859, no. 9, pp. 1558–1572, 2017.

[188] S. Davoudi, K. Raemdonck, K. Braeckmans and A. Ghysels, 'Capric acid and myristic acid permeability enhancers in curved liposome membranes', *J. Chem. Inf. Model.*, vol. 63, no. 21, pp. 6789–6806, 2023.

[189] P. Han and D. M. Bartels, 'Temperature dependence of oxygen diffusion in h_2o and d_2o', *J. Phys. Chem.*, vol. 100, no. 13, pp. 5597–5602, 1996.

[190] W. Xing, M. Yin, Q. Lv, Y. Hu, C. Liu and J. Zhang, 'Oxygen solubility, diffusion coefficient, and solution viscosity', in *Rotating electrode methods and oxygen reduction electrocatalysts*, Elsevier, 2014, pp. 1–31.

[191] J. Widomska, M. Raguz and W. K. Subczynski, 'Oxygen permeability of the lipid bilayer membrane made of calf lens lipids', *Biochim. Biophys. Acta, Biomembr.*, vol. 1768, no. 10, pp. 2635–2645, 2007.

[192] R. Salomon-Ferrer, D. A. Case and R. C. Walker, 'An overview of the amber biomolecular simulation package', *Wiley Interdiscip. Rev. Comput. Mol. Sci.*, vol. 3, no. 2, pp. 198–210, 2013.

[193] G. Angles, A. Hail, R. J. Dotson and S. C. Pias, 'Atomistic simulations modify interpretation of spin-label oximetry data. part 1: Intensified water–lipid interfacial resistances', *Appl. Magn. Reson.*, vol. 52, pp. 1261–1289, 2021.

[194] W. Vervust and A. Ghysels, 'Oxygen storage in stacked phospholipid membranes under an oxygen gradient as a model for myelin sheaths', in *Oxygen Transport to Tissue XLIII*, Springer, 2022, pp. 301–307.

Papers

Paper 1

Sampling efficiency of the counting method for permeability calculations estimated with the inhomogeneous solubility-diffusion model

Samaneh Davoudi and An Ghysels

Journal of Chemical Physics 154(5), 054106 (2021)

The Journal of Chemical Physics ARTICLE scitation.org/journal/jcp

Sampling efficiency of the counting method for permeability calculations estimated with the inhomogeneous solubility–diffusion model

Cite as: J. Chem. Phys. **154**, 054106 (2021); doi: 10.1063/5.0033476
Submitted: 16 October 2020 • Accepted: 8 January 2021 •
Published Online: 2 February 2021

Samaneh Davoudi and An Ghysels[a)]

AFFILIATIONS

IBiTech–BioMMeda Group, Ghent University, Corneel Heymanslaan 10, Block B-entrance 36, 9000 Gent, Belgium

[a)] Author to whom correspondence should be addressed: an.ghysels@ugent.be

ABSTRACT

Permeability is a key property in various fields such as membrane technology for chemical separation and transport of substances through cell membranes. At the molecular scale, the counting method uses the number of membrane crossings in a conventional unbiased molecular dynamics simulation to predict the permeability. This contribution investigates under which conditions the counting method has insufficient statistics. An equation is derived for a compartmental model based on the inhomogeneous solubility–diffusion (Smoluchowski) model, giving insight into how the flux correlates with the solubility of permeants. This equation shows that a membrane crossing is a rare event not only when the membrane forms a large free energy barrier but also when the membrane forms a deep free energy well that traps permeants. Such a permeant trap has a high permeability; yet, the counting method suffers from poor statistics. To illustrate this, coarse-grained MD was run for 16 systems of dipalmitoylphosphatidylcholine bilayer membranes with different permeant types. The composition rule for permeability is shown to also hold for fluxes, and it is highlighted that the considered thickness of the membrane causes uncertainty in the permeability calculation of highly permeable membranes. In conclusion, a high permeability in itself is not an effective indicator of the sampling efficiency of the counting method, and caution should be taken for permeants whose solubility varies greatly over the simulation box. A practical consequence relevant in, e.g., drug design is that a drug with high membrane permeability might get trapped by membranes thus reducing its efficacy.

Published under license by AIP Publishing. https://doi.org/10.1063/5.0033476

I. INTRODUCTION

Permeability is a key property to describe the kinetics of mass transport of a substance through a membrane. It is highly relevant in various research and application fields, such as membrane technology for chemical separation[1–4] and passive permeation of substances through the cell membrane.[5,6] In biology, permeation through the cell membrane is a vital process that is relevant for drug delivery[5,6] and the regulation of cell death and proliferation.[7] A large number of experimental studies have been carried out to provide information on this process during the past decade.[8–14] However, these methods are either expensive or not informative enough, as they are usually unable to provide data on a molecular level.

On the other hand, computational simulations have been proven to give more insight into permeation at the atomic scale.[15–17] Among simulation methods, molecular dynamics (MD) can lay open more details on the kinetics of the process, the property that experiments often cannot provide directly, under the condition that a proper force field for the molecular interactions is available.[18] Different simulation methods have been applied to calculate the permeability, many of which rely on enhanced sampling methods[18–20] and the inhomogeneous solubility–diffusion (ISD) model based on the Smoluchowski equation.[21–28] In the ISD model, the permeability P is expressed in terms of local diffusivity and free energy gradients.[21] A limitation of this approach, however, is that it is generally not clear *a priori* to which degree and in which situation the diffusive hypothesis is valid for the system under study. Moreover, accessing the permeability in this model can be challenging regarding the simulation setup and Bayesian analysis (BA).[29]

Permeability can also be determined by counting crossings through the membrane.[17,30] In the case of rare events, there might be an insufficient number of crossings, and the statistics can be poor. To set the mind, imagine aiming for a 10% error on the number of crossings. When crossings are occurring independently according to a waiting time distribution of a Poisson process, at least 100 events would be needed to achieve the 10% standard error.[25] An example of using the counting method is oxygen and water diffusion through phospholipid membranes.[24,25,31–33]

In this paper, the number of crossings expected in a simulation will be investigated as a function of the simulation properties. Several properties are dictated by the simulation setup, such as the number of permeants and box dimensions. A straightforward way to improve the sampling of the unit cell is to increase the system size. When the cross section doubles and the total number of permeants doubles, the concentration in the solvent phase will remain unaltered, while the number of crossings would double. There are unfortunately limits to this approach because the computational cost increases faster than linearly with the box size, and in comparison, it would be more efficient to double the simulation time T_{sim}. Another approach could be to insert more permeants without altering the simulation box size, meaning that all concentrations—both solvent and membrane—increase. One should be wary of the clustering of the permeants, however, and the permeability might become concentration dependent. For instance, oxygen showed no clustering for oxygen concentrations about ten-fold higher than the oxygen solubility in water,[24] while ethanol permeation through phosphatidylcholine (POPC) membranes differs substantially between low and high concentrations.[29,34]

Other properties are inherent to the chosen membrane, solvent, and permeants. This paper considers the solubility of permeants (or, equivalently, the partitioning coefficient K) and the membrane thickness h_m. It is well known that the membrane forms a high free energy barrier when a permeant is nearly insoluble in the membrane, and the associated low permeability prevents good sampling of the unit cell. It will now be shown that a high permeability, for permeants that are highly soluble in the membrane, is another cause for poor sampling. In contrast to low permeability, a high permeability membrane is often regarded as a membrane where the flux is not rate-limiting, but we will show that high permeability cannot guarantee good sampling of the simulation box either.

The membrane thickness follows from the self-aggregation of phospholipid molecules in the bilayer. It is less discussed in the permeability literature than the partitioning coefficient. Still, using the simplified Overton's model $P = KD/h_m$,[35] where D is the diffusion constant, it is clearly of equal importance as the partitioning coefficient. The membrane thickness is however ill-defined since there is no unique answer as to where an atom ends and another atom begins, and moreover, membranes exhibit thermal undulations with lipid protrusions. In experimental work, a roughly estimated membrane thickness is used to estimate the permeability.[10,36] In simulation work, it is often derived in relation to the plane of the phosphate groups.[29] Hence, another aim of this paper is to showcase the sensitivity of the permeability to the considered thickness. Therefore, in addition to the membrane thickness, the thickness of two additional water layers will be treated as an extra parameter in the discussion. Moreover, this parameter will allow us to discuss the overall sampling efficiency. When the limit of the water layer thickness is taken to cover the whole simulation box, the associated number of crossings represents crossings through the whole simulation box.

Section II will use the ISD model to derive a theoretical expression of how the counting method is affected by the solubility of permeants in the membrane. Section III discusses the dependencies and limiting cases of the derived equation. It is shown under which conditions membrane crossings can be considered as a rare event. A composition rule for the flux is derived as well. Section IV presents the number of crossings of 16 different permeant types through the dipalmitoylphosphatidylcholine (DPPC) bilayer membrane, illustrating the derived equation. Section V summarizes our findings.

II. THEORY

The Smoluchowski equation describes the transport of permeants through an inhomogeneous medium on a free energy profile $F(z)$ with a position-dependent diffusivity $D(z)$, where z is the coordinate along the membrane normal.[21] Assume F_{ref} is the free energy at the reference location, usually taken to be in the water phase on both sides of the membrane. The permeability P of a layer of thickness h follows from solving the Smoluchowski equation under steady-state conditions,[21]

$$\frac{1}{P} = e^{-\beta F_{\mathrm{ref}}} \int_h \frac{e^{\beta F(z)}}{D(z)} dz, \tag{1}$$

where the integration runs over a certain thickness h, and $\beta = 1/(k_B T)$ is the inverse temperature with T being the temperature. In a compartmental model, as illustrated earlier for oxygen transport,[24] F and D are piecewise constant functions, and the integral becomes a sum over the several compartments,

$$\frac{1}{P} = \sum_i \frac{1}{P_i} = \sum_i \frac{h_i}{K_i D_i}, \tag{2}$$

where each layer i is characterized by its thickness h_i, diffusivity D_i, and free energy F_i. The factor $K_i = \exp(-\beta(F_i - F_{\mathrm{ref}}))$ is the partitioning constant in layer i compared to the water phase, and it is equal to the concentration ratio between layer i and the water phase, i.e., $K_i = c_i/c_{\mathrm{ref}}$. The composition rule in Eq. (2) shows that the permeation through a series of layers can be seen as a series of local resistances $1/P_i$, if the same reference F_{ref} is used for each layer.

Let us start with a one-compartmental model for a uniform membrane of thickness h_m, for which the integral in Eq. (1) simplifies to

$$P = \frac{KD}{h_m}. \tag{3}$$

The partitioning coefficient K relates to the free energy difference ΔF between the membrane and the water phase, where ΔF is also

Published under license by AIP Publishing

referred to as the free energy of transfer to bring a permeant from the water phase into the membrane.

This model is extended to the three-compartmental model depicted in Fig. 1, where a water layer of thickness d is added on both sides around the membrane. For simplicity, the diffusivity is assumed to be constant over the whole simulation box. This model will allow for a more complete discussion of the behavior of the counting method. The permeability of this model is obtained by putting the previous permeation resistance $h_m/(KD)$ in series with the permeation resistance of the water phase $2d/D$, where the partitioning coefficient of the water phase is simply 1. This gives the permeability of the membrane plus water layers equal to

$$P = \frac{D}{2d + \frac{h_m}{K}}. \tag{4}$$

Filling in $d = 0$ in Eq. (4) results back in Eq. (3).

Two regimes exist for P, depending on the partitioning coefficient K of the membrane. In the limit of low K, the concentration in the membrane is much lower than in the water phase, and P reduces to the previous equation, $P \approx KD/h_m$, as if the water layer is unimportant. The permeability is then indeed dominated by the height of the barrier and is a linear function of K. This is expected from the integral form in Eq. (1), which is dominated by high F values. In the limit of large K, at least compared to $h_m/(2d)$, the membrane has a high concentration of permeants, and P becomes approximately a constant, $P \approx D/(2d)$, meaning that the permeability of the membrane is not the limiting factor but rather the resistance coming from the water layer.

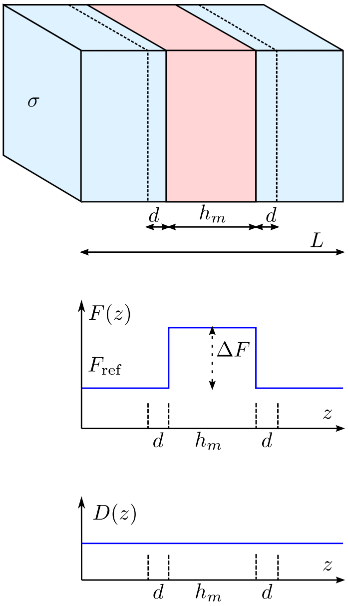

FIG. 1. Simulation box with length L and cross area σ containing the membrane (red) and water (blue). The compartmental model considers the membrane (thickness h_m) and a water layer on both sides (thickness d each). Diffusivity is assumed to be constant, and the free energy profile is piecewise constant.

Given this compartmental model, we will now turn toward the practical situation of a simulation setup. In a simulation, P can be computed using the counting method, by determining the crossing rate J and the reference concentration c_{ref} in the water phase. The number n_{cross} of complete transitions through a membrane with cross section area σ in either direction is counted during a long equilibrium MD simulation of length T_{sim}. Next, the (bidirectional) flux J per unit of time and unit of area in either direction is derived,

$$J = \frac{n_{\mathrm{cross}}}{T_{\mathrm{sim}}\sigma} = |J_{\leftarrow}| + |J_{\rightarrow}|, \tag{5}$$

where $J_{\leftarrow}$ and $J_{\rightarrow}$ are the flux through the membrane in the negative or positive direction, respectively. The well-known formula[17,30] for P from the counting method is

$$P = \frac{|J_{\leftarrow}| + |J_{\rightarrow}|}{2c_{\mathrm{ref}}} = \frac{J}{2c_{\mathrm{ref}}}. \tag{6}$$

The counting method for permeability relies on the number of crossings. The aim is to discuss the number of crossings as a function of the key properties of the membrane and the simulation setup: (1) the free energy of transfer ΔF, (2) considered layer thickness $h = h_m + 2d$, (3) the total number of permeants N_t that are present in the simulation box, and (4) the dimensions of the simulation box, i.e., the height L and cross area σ. For this reason, n_{cross} will be written as a function of these parameters in order to observe their role. Using the first equality in Eq. (5), it is clear that a discussion of J contains similar information as a discussion of n_{cross}, apart from the role of the simulation time T_{sim} and cross area σ, and therefore, the discussion of n_{cross} will be largely based on the discussion of J.

From Eq. (6), it immediately follows

$$J = 2c_{\mathrm{ref}}P, \tag{7}$$

where P is given by Eq. (4). The task at hand is thus to express the reference concentration located in the water phase, as a function of the key parameters K and N_t. The water concentration $c_{\mathrm{ref}} = c_w$ is the average number of permeants $\langle N_w \rangle$ in the water phase divided by the volume of the water phase, which is $\sigma(L - h_m)$ according to Fig. 1. Similarly, the membrane concentration c_m is the average number of permeants $\langle N_m \rangle$ in the membrane divided by the membrane volume σh_m. Note that, while the total number of permeants N_t remains constant during the simulation, the number of particles in the water and membrane, N_w and N_m, respectively, will fluctuate over time. Their averages are given as

$$\langle N_w \rangle = c_w \sigma (L - h_m), \tag{8}$$

$$\langle N_m \rangle = c_m \sigma h_m = K c_w \sigma h_m. \tag{9}$$

Using the equality $N_t = N_w + N_m = \langle N_w \rangle + \langle N_m \rangle$, the reference concentration becomes

$$c_{\text{ref}} = c_w = \frac{N_t}{\sigma (h_m K + L - h_m)}, \tag{10}$$

and we find J as a function of the key parameters

$$J = \frac{2 N_t D}{\sigma} \frac{1}{h_m K + L - h_m} \frac{1}{2d + \dfrac{h_m}{K}}. \tag{11}$$

This is the equation that will be used for the discussion. The number of crossings follows immediately by multiplying J with $T_{\text{sim}}\sigma$ [Eq. (5)].

In a final step, we leave the case of the compartmental model and return to the case of general $F(z)$ and $D(z)$ profiles that can take any shape. It is still assumed that the transport kinetics can be described by the Smoluchowski equation, i.e., the kinetics are Markovian. In the general case, the reference concentration is given by

$$c_{\text{ref}} = \frac{e^{-\beta F_{\text{ref}}} N_t}{\sigma \displaystyle\int_L e^{-\beta F(z)} dz}. \tag{12}$$

P is given by Eq. (1). Using the $\langle \ldots \rangle$ notation for spatial averages in the z-direction, over h or L, these are rewritten as

$$P = \frac{e^{\beta F_{\text{ref}}}}{h \left\langle \dfrac{e^{\beta F(z)}}{D(z)} \right\rangle_h} \tag{13}$$

and

$$c_{\text{ref}} = \frac{e^{-\beta F_{\text{ref}}} N_t}{\sigma L \langle e^{-\beta F(z)} \rangle_L}. \tag{14}$$

The flux in Eq. (7) now becomes

$$J = \frac{2 N_t}{h L \sigma \left\langle \dfrac{e^{\beta F(z)}}{D(z)} \right\rangle_h \langle e^{-\beta F(z)} \rangle_L}. \tag{15}$$

The above equation is the generalization of the compartmental model in Eq. (11) to arbitrary free energy and diffusivity profiles. It gives the flux J as a function of the key parameters in the general case.

III. DISCUSSION

The flux in the compartmental model [Eq. (11)] is first discussed for the two limiting cases where the layer does not comprise any water ($d = 0$, so $h = h_m$) and where all water is included in the layer ($h = L$), and next, it is illustrated for the intermediate cases ($h_m < h < L$).

For $d = 0$, only the membrane of thickness h_m is considered, and the flux simplifies. For large K (free energy well) and small K (free energy barrier), the dependence on K is constant or linear in K, respectively,

$$J(h_m) = \begin{cases} \dfrac{N_t D}{\sigma h_m^2}, & K \gg 1 \\ \dfrac{N_t D}{\sigma h (L - h_m)} K, & K \ll 1. \end{cases} \tag{16}$$

When the membrane is highly soluble for the permeants ($\Delta F > 0$), the number of crossings is independent of K and thus ΔF. However, when the permeants' solubility in the membrane is lower than in the water phase ($\Delta F < 0$), the number of crossings will drop exponentially with ΔF. A very high free energy of transfer will give a very few membrane transitions, with poor statistics for the counting method as a consequence.

For $2d = L - h_m$, the whole water layer in the simulation box is included in the counting of membrane transitions. The considered thickness is $h = L$, so $J(L)$ represents the flux of complete crossings of the simulation box,

$$J(L) = \frac{N_t D}{\sigma (L - h_m)^2} \frac{1}{1 + \dfrac{h_m}{L - h_m} \dfrac{1}{K}} \frac{1}{1 + \dfrac{h_m}{L - h_m} K}. \tag{17}$$

Here, $J(L)$ can be interpreted as a measure of the sampling efficiency of permeants over the whole z-direction of the simulation box. It is interesting to see that this equation is symmetric for the replacement of K by $1/K$. Replacing ΔF by $-\Delta F$ does not alter the sampling efficiency $J(L)$. In other words, $J(L)$ is an even function of ΔF by the appearance of K in this expression. This is an important realization: the flux in a simulation can be low because either a high barrier makes it difficult for the permeants to pass through the membrane or a deep well makes it difficult to leave the membrane once they are trapped. In summary, the larger the difference between the free energy minima and maxima across the membrane normal, given by $|\Delta F|$, the lower is the sampling efficiency because J drops with both K and $1/K$. A high variety in solubility hence leads to lower sampling efficiency.

We now approximate $J(L)$ to allow comparison with the previous approximations of $J(h_m)$ in Eq. (16). For large K (free energy well) and small K (free energy barrier), $J(L)$ is inversely proportional to K or linear in K, respectively,

$$J(L) = \begin{cases} \dfrac{N_t D}{\sigma h (L - h_m)} \dfrac{1}{K}, & K \gg 1 \\ \dfrac{N_t D}{\sigma h (L - h_m)} K, & K \ll 1. \end{cases} \tag{18}$$

When K is small, $J(h_m) \approx J(L)$. This can be understood because the exact location of the boundaries, be it at $h = h_m$ or $h = L$, is relatively unimportant when the barrier is high. When K is large, however, we find that $J(h) \gg J(L)$. When the membrane is highly soluble and only few particles are in the water phase, the exact boundary location does matter. Omitting the water phase or including a small or larger part has a large effect on the number of crossings. The reason is that the permeability of the water phase is in this case the limiting resistance for the overall permeability of the considered layer, hence the sensitivity to the included water layer thickness.

For d between 0 and $(L - h_m)/2$, the number of crossings lies between $J(h_m)$ and $J(L)$. Figure 2 visualizes the trends for the toy system (Fig. 1) with numerical values that are typical for MD settings, for instance for a bilayer consisting of 72 phospholipid molecules.[24] The simulation box had sizes $L = 70$ Å and $\sigma = (50\text{ Å})^2$, the membrane thickness was set to $h_m = 55$ Å, the box contained $N_t = 10$ permeating particles with diffusivity $D = 0.5$ Å^2/ps, and the total simulation time was set to $T_{\text{sim}} = 1\ \mu$s.

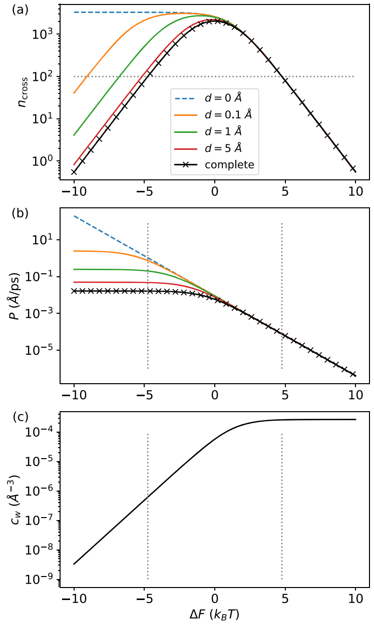

FIG. 2. Number of crossings n_{cross} (a), permeability P (b), and reference concentration c_w (c) in the model system of Fig. 1 as a function of the free energy difference $\Delta F = -k_BT \ln K$, where $\Delta F > 0$ is a barrier and $\Delta F < 0$ is a well. Various water layers d are considered. Blue dashed line: water slab not taken into account. Black line crosses: complete simulation box considered; this is an indicator of overall sampling. The horizontal dashed line in (a) is at 100 crossings, and the vertical dashed lines in (b) and (c) indicate the corresponding free energy difference.

According to Eq. (7), the permeability and the reference concentration are the main contributing factors, which are plotted in Figs. 2(b) and 2(c), for several values of d. The semi-log plots clearly show the constant (zero slope), linear (positive slope), and inversely linear (negative slope) dependence on K in the limiting cases $K \gg 0$ and $K \ll 0$. The number of crossings is mainly the product of these two graphs, and the semi-log plot in Fig. 2(a) is indeed the sum of the curves except for a vertical shift. The widespread curves for small K (i.e., $\Delta F \ll 0$) in Figs. 2(a) and 2(b) are a signature of the sensitivity to the chosen layer thickness when the membrane is a permeant trap. Let us focus on the number of complete crossings of the simulation box (black line), which refers to the sampling efficiency. The vertical dashed line in Fig. 2(a) indicates 100 crossings corresponding with a standard error of about 10%. This corresponds to a free energy difference of about $|\Delta F| = 5k_BT$, indicated with vertical lines in the other plots. This means that the sampling of the complete simulation box becomes poor when $|\Delta F|$ is larger than $5k_BT$ and one should be wary of statistics. When $\Delta F \gg 0$, the statistics are poor because the membrane forms a high barrier making crossings a rare event. However, when $\Delta F \ll 0$, the poor statistics are caused by the low permeant concentration c_w in the water phase [Fig. 2(c)]. When all permeants are trapped in the membrane, meanwhile not contributing to the crossings, there is barely any permeant left in the water phase as a candidate to perform a crossing.

Figure 3 plots the number of crossings as a function of the layer thickness for several values of K. The curves for low K are almost unaffected by considering some water layer. In contrast, the curves for high K indeed decrease much faster than those for low K as those are more sensitive to the layer thickness. For complete crossings at $h = L$, the curve for a given K coincides with the corresponding curve for $1/K$ (indicated with black crosses in the graph), illustrating the symmetry between ΔF and $-\Delta F$.

For all curves in Fig. 3, n_{cross} decreases with increasing thickness h. This is a consequence of the composition rule in Eq. (2) for permeability. A higher thickness gives a lower permeability according to Eq. (2). Using $J = 2c_{\text{ref}}P$, a similar composition rule holds for the flux,

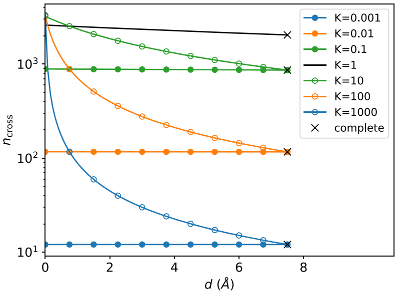

FIG. 3. Number of crossings n_{cross} as a function of the water layer d in the model system of Fig. 1, for various free energy barriers ($K < 0$) and free energy wells ($K > 1$). Black crosses: complete simulation box considered.

Published under license by AIP Publishing

$$\frac{1}{J} = \sum_i \frac{1}{J_i}, \tag{19}$$

where J_i is the bidirectional flux through layer i [see Eq. (5)]. An equivalent composition rule holds for $n_{\mathrm{cross}} = T_{\mathrm{sim}}\ \sigma\ J$. Hence, J and n_{cross} also decrease when the considered thickness is increased. For a symmetric bilayer membrane, it immediately follows from the composition rule that the entrance flux through one leaflet is identical to the escape flux through that leaflet, $J_{\mathrm{entr}} = J_{\mathrm{esc}}$, and the complete crossing flux through the entire membrane is half of that, $J = J_{\mathrm{entr}}/2 = J_{\mathrm{esc}}/2$. Likewise, $P = P_{\mathrm{half}}/2$, where P_{half} is the permeability of one membrane leaflet. It is important to note that these composition rules are based on the compartmentalized inhomogeneous solubility–diffusion model and are thus only true under the assumption of perfectly diffusive behavior. Non-Markovian kinetics might distort these composition rules,[37] e.g., when memory effects are at play for ethanol crossings through a phospholipid membrane.[29]

Finally, the symmetry in ΔF is shown in the general case of arbitrary profiles in Eq. (15). When the diffusion profile is taken to be constant, $D(z) = D$, and considering the full simulation box, $h = L$, the flux becomes

$$J(L) = \frac{N_t}{hL\sigma D\left\langle e^{\beta F(z)}\right\rangle_L \left\langle e^{-\beta F(z)}\right\rangle_L}. \tag{20}$$

This highlights that the same number of crossings will be encountered when a profile $F(z)$ is replaced by $-F(z)$, even though the permeability changes. While it may be counterintuitive, a profile with a high free energy barrier will therefore give the same sampling efficiency as a profile with a low free energy barrier. Highly soluble membranes are thus not necessarily improving the statistics in the counting method. This realization is important for drug design, where substances with high permeability might be trapped by the membrane thus reducing their efficacy.

IV. ILLUSTRATION WITH COARSE GRAINED MOLECULAR DYNAMICS

To illustrate the discussion of Sec. III, a membrane of dipalmitoylphosphatidylcholine (DPPC) was simulated at the molecular scale using a coarse grained (CG) model. A range of different permeants was considered with both positive ΔF (barrier) and negative ΔF (well): 16 bead types of the Martini coarse-grained model were used as the permeating molecule. These beads span a wide range of free energy profiles $F(z)$ across the membrane.

A. Simulation details

Using the Gromacs-2019.3 package,[38] simulations were performed on 16 systems consisting of a phospholipid membrane, CG beads, and water. Each system contained 20 permeant beads of one specific CG type, and it was solvated in 2000 water molecules. The membrane consists of 128 DPPC lipid molecules in each simulation, and its initial coordinates were taken from the MARTINI website.[39] The topology file and initial coordinates of the permeant beads were created manually. The MARTINI force field was used in all systems, mapping atoms of each phospholipid molecule and water molecule into 12 beads and 1 bead, respectively.[40]

Water was modeled by applying the SPC/E model.[41] The particle mesh Ewald approach was employed to calculate the Coulombic interactions. Both the Coulombic and the van der Waals interactions were truncated at 1.1 nm, with the potentials shifted to zero at the cutoff using the potential modifiers. The neighbor list length is 1.4 nm updated using the Verlet neighbor search algorithm. With a time step of 30 fs, the leapfrog integrator was used to integrate the equations of motion. A temperature of 320 K was considered for the simulated systems by the coupling of velocity rescale thermostats, with coupling constant set to 1.0 ps. At every time step, the center of mass motion of the system was removed and periodic boundary conditions were applied in all directions (x, y, z). A Parrinello–Rahman barostat was employed to subject the box vectors to semi-isotropic pressure, using a reference pressure of 1 bar, a coupling parameter of 12 ps, and an isothermal compressibility of 3×10^{-4} bar^{-1}. After adding the permeants, an energy minimization was performed. Next, two equilibrations were performed: NVT simulation of 30 ns and NPT simulation of 30 ns. The production run was 270 ns of NPT simulation for each system. Coordinates were stored every 3 ps resulting in 90 000 snapshots in total for each system.

The number of membrane crossings was determined with the Rickflow package code using dividing surfaces at $|z| = h_m/2 = 2.3$ nm.[29] The diffusion tensor with diagonal elements D_{xx}, D_{yy}, D_{zz} was computed with Gromacs.

B. Numerical results

The free energy profile was determined from the histogram $p(z)$ of the position of the CG beads as $F(z) = -k_B T \ln p(z)$. Figure 4 presents $F(z)$ for three exemplary bead types. Bead AC2 has a deep free energy well; hence, it is highly soluble in the membrane ($K \gg 1$).

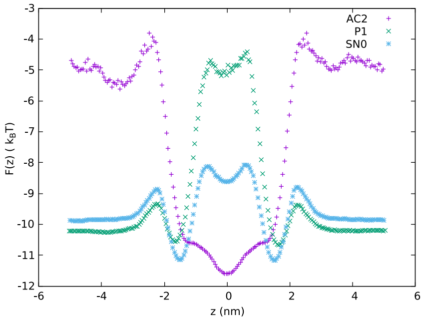

FIG. 4. Free energy of three selected bead types that are representative of a free energy barrier (P1), a free energy well (AC2), and a mix of both (SN0). The profile $F(z) = -k_B T \ln p(z)$ is plotted with $p(z)$, the histogram of the 20 permeants' z-coordinates over all 90 000 snapshots.

Bead P1 has a high free energy barrier and is insoluble in the membrane ($K \ll 1$). Bead SN0 shows a mix of the free energy well and barrier, where the solubility depends on the exact location in the membrane. The other bead types had similar profiles with different elevations.

Figure 5 shows the number of detected crossings vs ΔF for the 16 beads (full symbols), where ΔF is computed as the free energy difference between the membrane center and the membrane border. The graph follows the shape of the curves in Fig. 2(a), where n_{cross} generally drops with $|\Delta F|$. These MD values are compared to the model values of n_{cross} (open symbols) based on the flux in the compartmental model [Eq. (11)] or the more general formulation of the Smoluchwoski model [Eq. (15)]. The model parameters were inferred from the molecular dynamics simulations.

For Eq. (11), K is computed as $\exp(-\beta\Delta F)$, h_m = 4.6 nm corresponding to the membrane thickness, the average box length L = 10 nm, and T_{sim} = 270 ns. The normal diffusivity D_{zz} describes the diffusion normal to the membrane surface, but the measured D_{zz} already incorporates the effects of the barrier or well. Therefore, the lateral diffusivity $D_{\parallel} = (D_{xx} + D_{yy})/2$ was taken as the diffusivity D in the model since diffusion parallel to the membrane is not hindered by free energy barriers/wells. The water thickness d was varied from 0 to $(L - h_m)/2$, giving a range of crossings that is indicated as a dashed vertical line on the graph. The lower end of the line corresponds to the number of crossings through the whole simulation box ($h = L$), while the higher end corresponds to the number of crossings through the membrane only. For $\Delta F \ll 0$, the number of crossings is highly sensitive to the considered membrane thickness. For $\Delta F \gg 0$, the number of crossings is no longer sensitive to the water layer thickness (lines mostly hidden by symbols), in accordance with Fig. 2(a). It was found that a decent correspondence with the MD data could be obtained for a small water layer of thickness d = 0.1 nm, which was added to the plot with a gray open symbol. The spread of the vertical lines however indicates that almost any value can be the outcome by tuning the parameter d. This indicates again that the number of crossings, and hence the permeability, is very sensitive to the considered thickness. One should therefore be cautious when interpreting and citing experimental or computational results for highly permeable membranes.

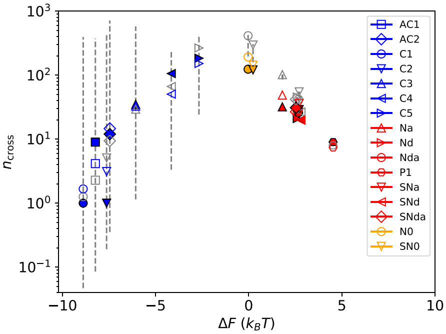

FIG. 5. Number of crossings n_{cross} as a function of ΔF for the 16 permeant types. Filled symbols: value as measured in the MD simulations with color according to the bead type, i.e., well (blue), barrier (red), and mix (orange). Gray open symbols: value based on the compartmental model [Eq. (11)] with d = 0.1 nm. Vertical dashed lines show the range between setting d = 0 (top of the line) and $d = (L - h_m)/2$ (bottom of the line). Colored open symbols: value based on the general Smoluchowski model [Eq. (15)].

For Eq. (15), the integral is evaluated using the measured free energy profile $F(z)$, the same constant diffusivity, and $d \approx 0$ [not exact because of binning in $p(z)$], giving the values indicated with a colored open symbol. Compared to the compartmental model, this more general model uses a position-dependent solubility, which allows us to describe more details of the membrane. Despite the crudeness in the parameter estimations, a good agreement is found between these model values and the numerical MD data in Fig. 5. The permeants in the present simulations are of course only a single bead without internal degrees of freedom, and the membrane contains only one phospholipid type. For more realistic membranes and realistic permeants, the compartmental model or the more general formulation [Eqs. (11) and (15)] might not have a sufficient level of detail to match the MD results. An extension of the model in Fig. 1 could for instance be a model that has both a free energy well and barrier. However, the complexity of more realistic simulations not only comes from the inhomogeneity in F and D but there might also be memory effects that make the kinetics non-Markovian, while the Smoluchowski equation is based on the Markovian assumption. Another challenging situation is when the permeation is accompanied by hysteresis, which is caused by not observing energy barriers in some orthogonal degree(s) of freedom (orthogonal to the permeation direction z). This is for instance the case when the permeant has an internal degree of freedom that is changed during the permeation, e.g., a dihedral angle in an oligopeptide, or an orientational degree of freedom, e.g., the ring plane in ibuprofen. A two-dimensional or higher-dimensional diffusive equation should then be constructed, which captures all reaction coordinates that are relevant for the permeation.

In these more advanced approaches, based on more elaborate multi-dimensional models with kernels, the free energy would still be one of the main parameters. The present analysis based on a Smoluchowski equation can therefore be seen as a decent first approximation to gain insight into the sampling efficiency. The presented curves clearly illustrate that a higher variation in the free energy profile results in lower sampling efficiency. Both deep wells and high barriers cause a dramatic drop in crossings, and the counting method for permeability will perform inaccurately in those cases.

When the counting method suffers from poor statistics and running much longer MD simulations is not expected to be a sufficient measure, a rare event method for rate calculations can be considered, such as replica exchange transition interface sampling (RETIS)[42–44] or milestoning.[45] In recent work, the connection between RETIS and the permeability was derived,[37] and this method can be a valid alternative for the counting method.[46] Another train of thought is the use of biased simulations, where a large variety of free energy is canceled out artificially by adding a bias potential.[20,47,48]

V. CONCLUSION

This paper investigated the efficiency of counting membrane crossings as a method to determine the permeability. A theoretical relation for the flux was derived based on the ISD model using the compartmentalized toy system in Fig. 1. An additional water layer was included in the model to show the sensitivity to the considered thickness, which causes a large uncertainty for high permeability membranes. It was shown that a high permeability in itself is not a qualified indicator of whether the sampling efficiency of the simulation box will be extensive enough for the counting method to be reliable, and caution should be taken for permeants whose solubility varies greatly over the simulation box. A practical effect of this realization in, e.g., drug design is that substances with high permeability might be trapped by the membrane, thus reducing their efficacy.

Moreover, the composition rule for permeabilities was shown to hold for fluxes as well. The limiting behavior of the number of crossings was determined for a high barrier membrane and a permeant trap membrane, and the dependence on the considered water layer was discussed. It was also shown that the sampling efficiency of the complete simulation box remains unaffected when the free energy profile $F(z)$ is inverted to $-F(z)$, if D is a constant. These theoretical considerations were all made under the assumption of purely diffusive kinetics since the ISD model is based on the Smoluchowski equation for Markovian kinetics.

Besides the theoretical assessment of the counting method, 16 systems were simulated by coarse-grained MD to illustrate the theory. The permeants' crossings were detected and the membrane's free energy profile was characterized as a free energy well, a barrier, or a mix of these two. In both the cases of a high free energy barrier and a deep free energy well, it can be concluded that the permeability calculation by counting crossings will face failure because of the insufficient number of crossing during the simulation. To overcome this problem, one should resort either to running longer MD simulations to observe more crossings using larger simulation boxes with more permeants or implementing other simulation methods that are applicable for rare events, e.g., RETIS.

ACKNOWLEDGMENTS

The computational resources (Stevin Supercomputer Infrastructure) and services used in this work were provided by the VSC (Flemish Supercomputer Center), funded by Ghent University, FWO, and the Flemish Government—department EWI.

DATA AVAILABILITY

The data that support the findings of this study are available from the corresponding author upon reasonable request.

REFERENCES

[1] B. Smit and T. L. M. Maesen, Chem. Rev. **108**, 4125 (2008).

[2] M. Tagliazucchi, *Chemically Modified Nanopores and Nanochannels* (William Andrew Publishing, 2017), Chap. 1, pp. 1–25.

[3] Y.-x. Shen, W. Song, D. R. Barden, T. Ren, C. Lang, H. Feroz, C. B. Henderson, P. O. Saboe, D. Tsai, H. Yan, P. J. Butler, G. C. Bazan, W. A. Phillip, R. J. Hickey, P. S. Cremer, H. Vashisth, and M. Kumar, Nat. Commun. **9**, 3304 (2018).

[4] V. A. Poteryaeva, M. A. Bubenchikov, A. M. Bubenchikov, and A. V. Lun-Fu, Sci. Rep. **10**, 15631 (2020).

[5] A. Mandal, V. Agrahari, V. Khurana, D. Pal, and A. K. Mitra, Expert Opin. Drug Delivery **14**, 385 (2017).

[6] B. J. Bennion, N. A. Be, M. W. McNerney, V. Lao, E. M. Carlson, C. A. Valdez, M. A. Malfatti, H. A. Enright, T. H. Nguyen, F. C. Lightstone, and T. S. Carpenter, J. Phys. Chem. B **121**, 5228 (2017).

[7] L. Galluzzi, I. Vitale, S. A. Aaronson, J. M. Abrams, D. Adam, P. Agostinis, E. S. Alnemri, L. Altucci, I. Amelio, D. W. Andrews, and M. Annicchiarico-Petruzzelli, Cell Death Differ. **25**, 486 (2018).

[8] W. K. Subczynski, M. Pasenkiewicz-Gierula, R. N. McElhaney, J. S. Hyde, and A. Kusumi, Biochemistry **42**, 3939 (2003).

[9] J. Widomska, M. Raguz, and W. K. Subczynski, Biochim. Biophys. Acta, Biomembr. **1768**, 2635 (2007).

[10] M. Möller, J. Lancaster, and A. Denicola, Curr. Top. Membr. **61**, 23 (2007).

[11] J. Godyń, D. Gucwa, T. Kobrlova, M. Novak, O. Soukup, B. Malawska, and M. Bajda, Talanta **217**, 121023 (2020).

[12] J. W. Choi, S. H. Bae, M. Kwak, T. G. Lee, M. B. Heo, and D. W. Lee, Sens. Actuators, B **321**, 128624 (2020).

[13] P. Bacchin, D. Snisarenko, D. Stamatialis, P. Aimar, and C. Causserand, J. Membr. Sci. **614**, 118485 (2020).

[14] C. Lin, T.-C. Kuo, J.-C. Lin, Y.-C. Ho, and F.-L. Mi, Int. J. Biol. Macromol. **160**, 558 (2020).

[15] E. Awoonor-Williams and C. N. Rowley, Biochim. Biophys. Acta, Biomembr. **1858**, 1627 (2016).

[16] N. Pokhrel and L. Maibaum, J. Chem. Theory Comput. **14**, 1762 (2018).

[17] R. M. Venable, A. Krämer, and R. W. Pastor, Chem. Rev. **119**, 5954 (2019).

[18] W. Shinoda, Biochim. Biophys. Acta, Biomembr. **1858**, 2254 (2016).

[19] C. Hoffmann, A. Centi, R. Menichetti, and T. Bereau, Sci. Data **7**, 1–7 (2020).

[20] C. T. Lee, J. Comer, C. Herndon, N. Leung, A. Pavlova, R. V. Swift, C. Tung, C. N. Rowley, R. E. Amaro, C. Chipot, Y. Wang, and J. C. Gumbart, J. Chem. Inf. Model. **56**, 721 (2016).

[21] S.-J. Marrink and H. J. C. Berendsen, J. Phys. Chem. **98**, 4155 (1994).

[22] S. J. Marrink and H. J. C. Berendsen, J. Phys. Chem. **100**, 16729 (1996).

[23] K. Gaalswyk, E. Awoonor-Williams, and C. N. Rowley, J. Chem. Theory Comput. **12**, 5609 (2016).

[24] A. Ghysels, R. M. Venable, R. W. Pastor, and G. Hummer, J. Chem. Theory Comput. **13**, 2962 (2017).

[25] O. De Vos, R. M. Venable, T. Van Hecke, G. Hummer, R. W. Pastor, and A. Ghysels, J. Chem. Theory Comput. **14**, 3811 (2018).

[26] H. A. L. Filipe, M. Javanainen, A. Salvador, A. M. Galvão, I. Vattulainen, L. M. S. Loura, and M. J. Moreno, J. Chem. Theory Comput. **14**, 3840 (2018).

[27] R. J. Ferreira and P. M. Kasson, ACS Infect. Dis. **5**, 2096 (2019).

[28] H. Yang, M. Zhou, H. Li, T. Wei, C. Tang, Y. Zhou, and X. Long, ACS Omega **5**, 4798 (2020).

[29] A. Krämer, A. Ghysels, E. Wang, R. M. Venable, J. B. Klauda, B. R. Brooks, and R. W. Pastor, J. Chem. Phys. **153**, 124107 (2020).

[30] R. J. Dotson, C. R. Smith, K. Bueche, G. Angles, and S. C. Pias, Biophys. J. **112**, 2336 (2017).

[31] O. De Vos, T. Van Hecke, and A. Ghysels, Adv. Exp. Med. Biol. **1072**, 399 (2018).

[32] A. Ghysels, A. Krämer, R. M. Venable, W. E. Teague, E. Lyman, K. Gawrisch, and R. W. Pastor, Nat. Commun. **10**, 5616 (2019).

[33] R. J. Dotson and S. C. Pias, Adv. Exp. Med. Biol. **1072**, 405 (2018).

[34] M. Ghorbani, E. Wang, A. Krämer, and J. B. Klauda, J. Chem. Phys. **153**, 125101 (2020).

[35] Q. Al-Awqati, Nat. Cell Biol. **1**, E201 (1999).

[36] M. N. Möller, Q. Li, M. Chinnaraj, H. C. Cheung, J. R. Lancaster, Jr., and A. Denicola, Biochim. Biophys. Acta, Biomembr. **1858**, 2923 (2016).

Published under license by AIP Publishing

Paper 2

Defining permeability of curved membranes in molecular dynamics

Samaneh Davoudi and An Ghysels

Biophysical Journal 122, 2082–2091 (2023)

Biophysical Journal
Article

Biophysical Society

Defining permeability of curved membranes in molecular dynamics simulations

Samaneh Davoudi[1] and An Ghysels[1,*]
[1]IBiTech - Biommeda Group, Faculty of Engineering and Architecture, Ghent University, Gent, Belgium

ABSTRACT Many phospholipid membranes in the cell have a high curvature; for instance, in caveolae, mitochondrial crystae, nanotubes, membrane pearls, small liposomes, or exosomes. Molecular dynamics (MD) simulations are a computational tool to gain insight in the transport behavior at the atomic scale. Membrane permeability is a key kinetic property that might be affected in these highly curved membranes. Unfortunately, the geometry of highly curved membranes creates ambiguity in the permeability value, even with an arbitrarily large factor purely based on geometry, caused by the radial flux not being a constant value in steady state. In this contribution, the ambiguity in permeability for liposomes is countered by providing a new permeability definition. First, the inhomogeneous solubility diffusion model based on the Smoluchowski equation is solved analytically under radial symmetry, from which the entrance and escape permeabilities are defined. Next, the liposome permeability is defined guided by the criterion that a flat and curved membrane should have equal permeability, in case these were to be carved out from an imaginary homogeneous medium. With this criterion, our new definition allows for a fair comparison of flat and curved membranes. The definition is then transferred to the counting method, which is a practical computational approach to derive permeability by counting complete membrane crossings. Finally, the usability of the approach is illustrated with MD simulations of diphosphatidylcholine (DPPC) bilayers, without or with some cholesterol content. Our new liposome permeability definition allows us to compare a spherically shaped membrane with its flat counterpart, thus showcasing how the curvature effect on membrane transport may be assessed.

SIGNIFICANCE Molecular dynamics simulations of highly curved membranes have nowadays become computationally feasible. The permeability calculation of such curved membranes is, however, ambiguous, because the radial flux is not a constant quantity in steady state. This paper therefore offers a new permeability definition for liposomes. This definition allows the consistent comparison between flat and curved membranes, hence facilitating the fair assessment of curvature effects on membrane transport properties.

INTRODUCTION

In the past decade, the role of curved membranes has received increased attention given their fascinating presence in the cell. Biologically, membranes occur in highly curved shapes; for instance, in the crystae of the inner mitochondrial membrane, or the caveolae, which are membrane invaginations in healthy, young cells (1,2). Other membrane structures with high curvature are the rod-like membrane nanotubes (radius 10–100 nm) (3,4), and the spherically shaped membrane pearls (5), exosomes (radius 15–50 nm), or small liposomes.

Modeling membrane structures at the molecular scale allows a level of detail and understanding that is often very challenging to observe experimentally, and hence computational modeling has gained its place as a complementary research tool. Traditionally, flat membranes have been simulated, as they present a decent approximation of membranes with low curvature. Consider, for instance, a larger liposome or extracellular particle with diameter 1 μm. When the simulation box encompasses a patch of membrane of about 5 nm by 5 nm in area and the membrane thickness is roughly ± 5 nm, then the membrane curvature would be barely noticeable. Simulating flat membranes is, moreover, straightforward to implement with standard periodic boundary conditions, allowing the unit cell dimensions to be limited to reasonably small values. In contrast, the cell dimensions, and hence the computational load, are challenged for curved membranes, as the unit cell has to

---

Submitted August 31, 2022, and accepted for publication November 17, 2022.

*Correspondence: an.ghysels@ugent.be

Editor: Siewert Jan Marrink.

https://doi.org/10.1016/j.bpj.2022.11.028

© 2022 Biophysical Society.

encompass the whole curved structure. Nevertheless, in recent years, a lot of progress has been made in computational tools. Yesylevskyy et al. designed simulations of curved membrane patches (6,7). Boyd et al. created the BumPy code to generate curved membrane simulation boxes of various shapes, such as cylinders and half-spheres (8). Code implementations, computational resources, and coarse-grained approaches have evolved to the point of studying systems with tens of thousands to even millions of particles for multiple microseconds; for instance, whole spherical virus particles (9,10). Marrink and coworkers have gradually worked on computational tools to simulate realistic membrane compositions in realistic geometries (11–13). With all of these developments, studying curved membranes has now become feasible.

A key function of membranes is compartmentalization, and, accordingly, membrane permeability is a key property. The membrane permeability affects the transport of oxygen or nutrients, whereas it dictates the retention time of drug molecules when liposomes are used as nanocarriers for drug delivery. Permeability is defined as the ratio of the steady-state net permeant flux J through the membrane, per time per area, and the concentration gradient Δc that is set over the membrane,

$$P = \frac{J}{\Delta c} \tag{1}$$

At the atomic scale, permeability can be measured with several methodologies using molecular dynamics (MD) simulations. In the counting method, the number of membrane crossings observed in an equilibrium simulation is converted to the permeability (14–17). In the inhomogeneous diffusion solubility methodology (18), free energy and diffusion profiles in the Smoluchowski equation are fitted on short MD trajectories, using Bayesian analysis or a minimum likelihood estimate (15,19–23). In the path sampling methodology, rare events are sampled by sampling path ensembles that focus on the more successful permeating trajectories. The permeability calculation was first derived for milestoning (24,25) with some diffusive approximations, and, more recently, it was included in an exact way in the replica exchange transition interface sampling (RETIS) method (26–28). These methods have been developed and are used for flat membranes. However, for a curved membrane simulation of, e.g., a liposome, the permeability definition needs to be revisited. The flux J is a quantity that is expressed *per area*, and, for a spherical liposome, this area $4\pi r^2$ clearly depends on the radial distance r from the liposome center. As we will show, this makes the radial flux J inherently r dependent, and the permeability is ill-defined. This paper will therefore provide a definition of the permeability of spherically curved membranes. The criterion for our definition is that it should be possible to compare permeability among flat and curved membranes. Hence, the definition will allow us to assess the curvature effect on permeability.

The section "theory" starts with the revision of the Smoluchowski equation, which assumes that transport is fully diffusive (without memory), and which can be solved analytically. Based on the analytical derivations, the new permeability definition for curved membranes is presented, which is no longer r dependent. Using this definition, the counting method is also revised for curved membranes. In the section "illustration," a flat and spherically shaped dipalmitoylphosphatidylcholine (DPPC) membrane with or without cholesterol is simulated with coarse-grained (GC) MD, and their water permeability is effectively compared using the new permeability definition.

THEORY

In this section, the definition of permeability for curved membranes will be derived in the case of diffusive transport through membranes. The Smoluchowski equation is often referred to as the inhomogeneous diffusion solubility model, and describes the evolution of the concentration $c(\overline{r}, t)$ based on the position-dependent diffusivity tensor $\overline{\overline{D}}$ and free energy F,

$$\frac{\partial c(\overline{r}, t)}{\partial t} = \nabla\left(\overline{\overline{D}}(\overline{r}) e^{-\beta F(\overline{r})} \nabla\left(e^{\beta F(\overline{r})} c(\overline{r}, t)\right)\right) \tag{2}$$

where $\beta = 1/(k_B T)$ with k_B Boltzmann constant and T temperature. The Smoluchowski equation has as an advantage that it can be solved analytically under steady-state conditions both for flat membranes and spherically shaped membranes. First, although the solution for flat membranes is well known, we will revise here the solution for systems with spherical symmetry. Second, the escape and entrance permeability will be defined. Within the diffusive assumption, the new permeability definition will be derived using a special limiting case: a purely homogeneous medium (i.e., the membrane is imaginary). In this case, we will impose that a curved "membrane" should have the same permeability value as its flat counterpart. Third, we will transfer the permeability definitions to the counting method, which does not assume diffusive transport.

Inhomogeneous solubility-diffusion model under radial symmetry

Consider first the case of a flat membrane with translational symmetry in the membrane plane. The free energy F is position dependent, and the anisotropic diffusion tensor $\overline{\overline{D}}$ has components parallel to the membrane $(D_{\parallel})$ and orthogonal to the membrane $(D_{\perp})$. The position-dependent profiles along the normal z to the flat membrane surface are denoted

$F(z)$ and $D_\perp(z)$. By assuming translational symmetry in the x and y directions, imposing a concentration gradient Δc over the membrane under steady-state conditions, and solving the Smoluchowski equation, the permeability can be obtained as $P = J/\Delta c$, where J is the net flux of permeants crossing the membrane (18,20,22,29–31),

$$\frac{1}{P} = e^{-\beta F_{\mathrm{ref}}} \int_{-h/2}^{h/2} \frac{1}{D_\perp(z) e^{-\beta F(z)}} dz \tag{3}$$

Next, consider the case of a liposome with radial symmetry, for which an update of Eq. 3 will be made. The radial symmetry of the medium leads to the profiles $F(r)$ and $D_\perp(r)$, which are the free-energy and diffusion profile dependent on the radial distance r from the liposome center. Not only the medium but also the boundary conditions are assumed to be radially symmetric in steady state (see below; Fig. 1). The anisotropic inhomogeneous Smoluchowski equation (20) under radial symmetry reads, for the one-dimensional transport along r, as

$$\frac{\partial c}{\partial t} = \frac{1}{r^2} \frac{\partial}{\partial r} \left(r^2 D_\perp(r) e^{-\beta F(r)} \frac{\partial}{\partial r} \left(e^{\beta F(r)} c \right) \right) \tag{4}$$

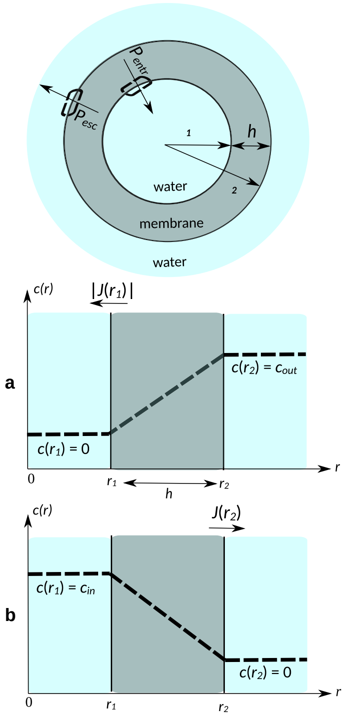

FIGURE 1 Definition of radii r_1 and r_2, and membrane thickness h for a liposome with radial symmetry. (*a*) Steady-state condition for entrance. The flux $|J(r_1)|$ is the entrance flux. (*b*) Steady-state condition for escape. The flux $J(r_2)$ is the escape flux. To see this figure in color, go online.

Under steady-state conditions ($\partial c/\partial t = 0$), we need to solve

$$\frac{1}{r^2} \frac{\partial}{\partial r} \left(r^2 D_\perp(r) e^{-\beta F(r)} \frac{\partial}{\partial r} \left(e^{\beta F(r)} c \right) \right) = 0 \tag{5}$$

The first integration over r gives an integration constant A,

$$r^2 D_\perp(r) e^{-\beta F(r)} \frac{\partial}{\partial r} \left(e^{\beta F(r)} c \right) = A \tag{6}$$

The flux vector may be recognized, which is a vector along the radial direction $\overline{e}_r$ with length $J(r)$. This lets us rewrite Eq. 6 as

$$J(r) = -D_\perp(r) e^{-\beta F(r)} \frac{\partial}{\partial r} \left(e^{\beta F(r)} c \right) = -\frac{A}{r^2} \tag{7}$$

which gives us insight in the behavior of the flux. As A is constant, the flux $J(r)$ diminishes as $1/r^2$ under radial symmetry. After rearrangement of Eq. 6, integrating once more over $[r_1, r_2]$ gives

$$e^{\beta F(r_2)} c(r_2) - e^{\beta F(r_1)} c(r_1) = A \int_{r_1}^{r_2} \frac{1}{r'^2 D_\perp(r') e^{-\beta F(r')}} dr' \tag{8}$$

Next, the steady-state boundary conditions of the two cases in Fig. 1 are imposed on Eq. 8. In Fig. 1 *a*, particles are entering the liposome from the outside, and any particle reaching the inside is assumed to be consumed instantaneously. With $c(r_1) = 0$, $c(r_2) \neq 0$, and $F(r_2) = F_{\mathrm{ref},2}$ the reference free energy, the steady state simplifies to

$$c(r_2) = -e^{-\beta F_{\mathrm{ref},2}} J(r) r^2 \int_{r_1}^{r_2} \frac{1}{r'^2 D_\perp(r') e^{-\beta F(r')}} dr' \tag{9}$$

where r in the product $J(r)r^2$ can be taken at choice, as the product is constant according to Eq. 7. With $c(r_2) = \Delta c$, this leads to a liposome permeability definition that is dependent on the chosen r distance,

$$\frac{1}{P_{\mathrm{entr}}(r)} = \frac{\Delta c}{|J(r)|} = r^2 e^{-\beta F_{\mathrm{ref},2}} \int_{r_1}^{r_2} \frac{1}{r'^2 D_\perp(r') e^{-\beta F(r')}} dr' \tag{10}$$

The subscript “entr” refers to the reference concentration being at location r_2, with particles *entering* the liposome.

In Fig. 1 *b*, particles are enclosed inside the liposome, and any escaping particle is assumed to be consumed instantaneously. The concentration inside the liposome is nevertheless kept constant in this theoretical situation. With $c(r_1) \neq 0$, $c(r_2) = 0$, and $F(r_1) = F_{\mathrm{ref},1}$ the reference free energy, the steady state in Eq. 8 simplifies to

$$c(r_1) = e^{-\beta F_{\mathrm{ref},1}} J(r) r^2 \int_{r_1}^{r_2} \frac{1}{r'^2 D_{\perp}(r') e^{-\beta F(r')}} dr' \quad (11)$$

where r in the product $J(r)r^2$ is arbitrary. With $c(r_1) = \Delta c$, this again leads to a permeability definition that is dependent on the chosen r distance,

$$\frac{1}{P_{\mathrm{esc}}(r)} = \frac{\Delta c}{|J(r)|} = r^2 e^{-\beta F_{\mathrm{ref},1}} \int_{r_1}^{r_2} \frac{1}{r'^2 D(r') e^{-\beta F(r')}} dr' \quad (12)$$

The subscript "esc" refers to the reference concentration being at location r_1, with particles *escaping* from the liposome.

Let us have a closer look at the references $F_{\mathrm{ref},1}$ and $F_{\mathrm{ref},2}$, inside and outside, respectively. When the solubility of the permeants is the same inside and outside the liposome, the permeants have the same free energy inside and outside, F_{ref} in short, and Eqs. 10 and 12 are equivalent and equal to

$$\frac{1}{P(r)} = r^2 e^{-\beta F_{\mathrm{ref}}} \int_{r_1}^{r_2} \frac{1}{r'^2 D(r') e^{-\beta F(r')}} dr' \quad (13)$$

However, it can also occur that the liposome packages a formulation inside that differs from the outside water phase, such that $F_{\mathrm{ref},1} \neq F_{\mathrm{ref},2}$. Micelles are other molecular structures where often the inside and outside environment differ. The permeability then depends on the chosen reference (i.e., entering from outside (P_{entr}) or escaping from inside (P_{esc})), but either definition is simply related by the permeant's solubility ratio,

$$\frac{P_{\mathrm{entr}}(r)}{P_{\mathrm{esc}}(r)} = e^{-\beta\left(F_{\mathrm{ref},1} - F_{\mathrm{ref},2}\right)} \quad (14)$$

In thermodynamic equilibrium, this free-energy ratio would be equal to the concentration ratio $c(r_2)/c(r_1)$. The dependence of the permeability definition on the reference is not characteristic for liposomes with radial symmetry, but it also appears for flat bilayers where the left and right side of the membrane differ. The latter situation is, in practice, usually not encountered in a single flat bilayer simulation, as left and right compartments are then indiscernible because of periodic boundary conditions.

The permeability Eqs. 10 and 12 are dependent on r and thus do not define the liposome's transport properties uniquely. In the next subsection, we define the liposome permeability by comparing with a flat membrane and discuss the dependence on the curvature.

Defining liposome permeability

While the product $J(r)r^2$ is independent of r in steady state with spherical symmetry, $P_{\mathrm{entr}}(r)$ or $P_{\mathrm{esc}}(r)$ are not. The question arises of which r is most appropriate to represent the permeability. Let us first look at the steady-state conditions of Fig. 1 *a* for P_{entr}. Since $c(r_1)$ is kept at zero in this steady-state situation, all flux at $r = r_1$ originates from permeants that started at the other side of the membrane at $r = r_2$. In other words, no recrossings can occur at $r = r_1$ because of the boundary condition. Hence, $|J(r_1)|$ can be regarded as the entrance flux of permeants that effectively crossed the membrane. This makes us define the entrance permeability from Eq. 10 as

$$P_{\mathrm{entr}} \equiv P_{\mathrm{entr}}(r_1) \quad (15)$$

Similarly, for $P_{\mathrm{esc}}(r)$ in Fig. 1 *b*, the flux at $r = r_2$ is now equal to the escape flux, which is the flux of particles effectively coming from the liposome's inside and escaping all the way through the membrane, as there are no recrossings possible under the condition $c(r_2) = 0$. This makes us define the escape permeability from Eq. 12 as

$$P_{\mathrm{esc}} \equiv P_{\mathrm{esc}}(r_2) \quad (16)$$

based on the flux $|J(r_2)|$ through r_2 caused by a concentration at the reference location r_1. The escape and entrance permeabilities are related to each other. By filling in their definitions into Eqs. 10 and 12 and taking the ratio, their relation reads

$$P_{\mathrm{esc}} \frac{e^{-\beta F_{\mathrm{ref},1}}}{r_1^2} = P_{\mathrm{entr}} \frac{e^{-\beta F_{\mathrm{ref},2}}}{r_2^2} \quad (17)$$

Although P_{entr} and P_{esc} have a clear interpretation, it still leaves the question open whether P_{entr} or P_{esc} is more suitable to describe the liposome's membrane permeation. With $P_{\mathrm{entr}}/P_{\mathrm{esc}} = r_2^2/r_1^2 = (1 + h/r_1)^2$, it is clear that P_{entr} is higher than P_{esc}, even by an infinite factor for the most curved membrane. This can have an implication on comparing experimental escape or entrance permeabilities of curved liposomes with simulated data of flat bilayers. Concretely, $P_{\mathrm{entr}}/P_{\mathrm{esc}}$ gives a difference of 2% for a cell-sized vesicle with a diameter of 1 μm, with $r_1 = 500$ nm and $r_2 = 505$ nm. Meanwhile, $P_{\mathrm{entr}}/P_{\mathrm{esc}}$ is a factor 4 for a very small liposome with $r_1 = 5$ nm and $r_2 = 10$ nm. Curvature effects are thus significant for smaller liposomes. A wide liposome size distribution in experiment will also negatively influence the quality of the comparison between experiment and flat membrane simulations.

As a strategy to address the question of whether P_{entr} or P_{esc} is more suitable, we keep the final aim in mind, where we would like to assess whether a liposome membrane is more, or less, permeable than a flat bilayer. A membrane that is indiscernible between the liposome and the flat setup, except for its curvature, should then have the same permeability value. We will therefore construct a hypothetical homogeneous liposome and flat bilayer, and use this condition of equivalent permeabilities as a guideline.

To create the homogeneous systems, we look at the artificial situation of a pure water box, in which we draw in our mind an imaginary flat bilayer or an imaginary liposome, as shown in Fig. 2. The imaginary membranes both have thickness h. Since the membranes are just lines in our imagination and actually consist of just pure water, the permeability through the imaginary flat membrane and imaginary liposome should be exactly the same; i.e., they should be equal to the permeability through a layer h of homogeneous water. The diffusivity D in homogeneous water is independent of z or r, and the free energy is constant everywhere. The permeability through a flat imaginary bilayer of thickness h follows from Eq. 3,

$$P_{\mathrm{flat}} = \frac{D}{h} \tag{18}$$

whereas Eq. 13 gives the permeability for the imaginary liposome,

$$P(r) = \frac{r_1 r_2}{r^2}\frac{D}{h} \tag{19}$$

As we are working with imaginary membranes, we aim for the liposome permeability to be equal to the flat bilayer permeability. Comparing the two previous equations, this is possible by defining the liposome permeability as $P^* \equiv P(r^*)$, evaluated at a radial distance $r^* = \sqrt{r_1 r_2}$, which lies intermediate between r_1 and r_2. With this definition, the target $P^* = P_{\mathrm{flat}}$ is achieved.

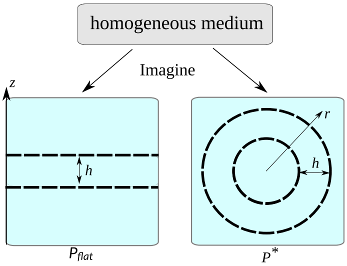

FIGURE 2 Imaginary flat bilayer and imaginary liposome of thickness h in a homogeneous water box. We impose that these have equal permeability as a guideline to define the liposome's permeability P^*. To see this figure in color, go online.

Moreover, this P^* definition can be linked to the liposome escape and entrance permeability, which are

$$P_{\mathrm{entr}} = \frac{r_2}{r_1}\frac{D}{h} \tag{20}$$

$$P_{\mathrm{esc}} = \frac{r_1}{r_2}\frac{D}{h} \tag{21}$$

for the homogeneous medium. It is clear that $P_{\mathrm{esc}} < P_{\mathrm{flat}} < P_{\mathrm{entr}}$, and we notice that P^* is the geometric mean of the escape and entrance permeability,

$$P^* \equiv P(\sqrt{r_1 r_2}) = \sqrt{P_{\mathrm{entr}} P_{\mathrm{esc}}} \tag{22}$$

In conclusion, choosing the geometric mean of escape and entrance permeability as the liposome permeability permits a fair comparison with the flat bilayer. For a membrane with position-independent diffusivity and free energy, the flat and curved bilayers will have the same permeability value, as aimed for.

Finally, let us discuss how the P^* definition acts for arbitrary membranes. To elucidate the effects, we will turn again to the purely diffusive assumption, since the Smoluchowski equation provide analytical solutions. Consider a membrane with position-dependent diffusivity or free energy across the membrane, assuming equal permeant solubility on both sides of the membrane. Maintain the liposome permeability definition of Eq. 22 also in this general case, and Eqs. 10, 12, 15, and 16 lead to

$$P^* = r_1 r_2 e^{-\beta F_{\mathrm{ref}}} \int_{r_1}^{r_2} \frac{1}{r'^2 D_\perp(r') e^{-\beta F(r')}} dr' \tag{23}$$

This expression allows us to highlight the effect of curvature. Consider a flat membrane with $F(z)$ and $D_\perp(z)$ along the membrane normal and a liposome with $F(r)$ and $D_\perp(r)$ along the radial direction. Assume those two F profiles and D profiles look identical, and the membranes have identical thickness $h = r_2 - r_1$. The permeability through the flat bilayer follows from Eq. 3 and has the following shape,

$$\frac{1}{P_{\mathrm{flat}}} = \int_{-h/2}^{h/2} f(z) dz \tag{24}$$

with $f(z)$ a specific function of the F and D profiles. Meanwhile, Eq. 23 gives the permeability for the liposome, which has this shape

$$\frac{1}{P^*} = \int_{r_1}^{r_2} \frac{r_1 r_2}{r^2} f(r) dr^2 \tag{25}$$

figuring the same function f. For homogeneous media, the function f is constant, and $P_{\mathrm{flat}} = P^*$ as anticipated. For inhomogeneous media, however, f is not constant. The additional $r_1 r_2 / r^2$ in the integrand is a reweighing factor. The area under the curve $r_1 r_2 / r^2$ over the interval $[r_1, r_2]$ is equal to the area under the curve 1, meaning that the function f is redistributed over the interval. Values closer to the liposome center receive a higher weight in the integral. This reweighing is in fact a consequence of the Jacobian r^2 factor arising from using the spherical coordinate r. The practical consequence of the reweighing is that two identical membranes, except for one being flat and the other curved, will differ in permeability: $P_{\mathrm{flat}} \neq P^*$. Moreover, the permeability changes with curvature. Inhomogeneity in F or D will therefore make the permeability P^* curvature dependent, and the effect depends on the liposome size and membrane thickness.

The liposome permeability is the geometric mean of the escape and entrance permeabilities, and it can also be written as the permeability $P(r)$ evaluated at the geometric mean $r^* = \sqrt{r_1 r_2}$ of the radii. While this follows from the reasoning with imaginary membranes, this geometric mean can also be given a physical interpretation. Eq. 13 for $1/P(r)$ implies that the function $P(r)$ itself is a $1/\,r^2$ function multiplied by a factor a that is independent of r; hence, $P(r) = a/r^2$. Consequently, the average function value of $P(r)$ over the membrane thickness h is

$$\langle P(r) \rangle_h = \frac{a}{h} \int_{r_1}^{r_2} \frac{1}{r'^2} dr' \tag{26}$$

The integral here is equal to $h/(r_1 r_2)$. Averaging a $1/\,r^2$ function, where the r^2 originates from the spherical surface areas of liposomes, makes the square of the geometric mean, $r_1 r_2$, appear. For the average of $P(r)$, this leads to

$$\langle P(r) \rangle_h = a \frac{1}{r_1 r_2} = P(r^*) \equiv P^* \tag{27}$$

This effectively gives our definition of the liposome permeability P^* the interpretation of the mean value of $P(r)$, taken over the whole membrane thickness. Moreover, the appearance of the geometric mean allows us to formulate an elegant summation rule for the permeabilities of two subsequent layers, $[r_1, r_2]$ and $[r_2, r_3]$,

$$\frac{1}{r_1 r_3 P_{[1,3]}} = \frac{1}{r_1 r_2 P_{[1,2]}} + \frac{1}{r_2 r_3 P_{[2,3]}} \tag{28}$$

The summation rule is obtained by slightly rearranging Eq. 23 and splitting up the integration interval $[r_1, r_3]$ of the total permeability $P_{[1,3]}$.

We end this subsection by offering another way to look at the additional r^2 factor in the denominator of Eq. 25. This Jacobian factor can be absorbed by defining an adapted free energy profile. The free energy is related to the permeant concentration by $c(r) = c_{ref} e^{-\beta(F(r) - F_{\mathrm{ref}})}$ where the reference concentration and free energy are taken at some reference radial distance r_{ref}. Let us define the radial density profile $\rho(r)dr = c(r) 4\pi r^2 dr$, which is the number of particles in a spherical shell with radius r with infinitesimal thickness dr. The corresponding free energy profile, apart from a constant shift $-\ln(4\pi)$, is

$$\tilde{F}(r) = F(r) - 2\ln(r) \tag{29}$$

$$e^{-\beta \tilde{F}(r)} = r^2 e^{-\beta F(r)} \tag{30}$$

$$\rho(r) = \rho_{\mathrm{ref}} e^{-\beta\left(\tilde{F}(r) - \tilde{F}_{ref}\right)} \tag{31}$$

with $\tilde{\rho}_{\mathrm{ref}}$ and $\tilde{F}_{\mathrm{ref}}$ the radial density and the adapted free energy at location r_{ref}, respectively. This means that liposome permeability of Eq. 23 may be rewritten as

$$P^* = e^{-\beta \tilde{F}_{\mathrm{ref}}} \int_{r_1}^{r_2} \frac{1}{D_\perp(r') e^{-\beta \tilde{F}(r')}} dr' \tag{32}$$

which has now the same shape as the flat membrane equation (Eq. 3), but it figures the adapted free energy $\tilde{F}(r)$ associated to the radial density $\rho(r)$ instead of the permeant concentration $c(r)$. In other words, if the Jacobian factor r^2 is incorporated in the free energy, our liposome definition P^* resorts to the shape of the flat bilayer equation. The Jacobian causes the dependence of the permeability on the curvature. Indeed, the importance of the Jacobian factor - depends on the boundaries r_1 and r_2. For highly curved membranes, the Jacobian factor changes $\tilde{F}$ considerably with respect to F. However, for slightly curved membranes in large liposomes, the $-2\ln r$ factor is nearly constant over the integrand, and the curvature effect is minimal.

Liposome permeability from the counting method

In the counting method, the permeability is measured in a long equilibrium MD simulation, which can be seen as the superposition of two steady states, one steady state with only permeants on one side of the membrane, the other steady state with only permeants at the opposite side (similar to Fig. 1). For a flat bilayer, the number of complete transitions n_{cross} through a membrane with cross-sectional area σ in either direction are counted during a long equilibrium MD simulation of length T_{sim} (14). This gives the (bidirectional) flux $|J_{\leftarrow}| + J_{\rightarrow}$ of complete crossings per unit of time and unit of area in either direction, where $J_{\leftarrow}$ (<0) and $J_{\rightarrow}$ (>0) are the flux through the membrane in the negative or positive direction, respectively (15,17). We would like to stress that these fluxes refer to crossings and thus differ from the concept of a local flux at a certain location. In an equilibrium simulation, the two fluxes are equal in size, $|J_{\leftarrow}| = J_{\rightarrow}$. Then the well-known formula for P from the counting method in an equilibrium simulation is, assuming equal free energy to the left and right of the membrane,

$$P = \frac{|J_{\leftarrow}|}{c_{\mathrm{ref}}} = \frac{J_{\rightarrow}}{c_{\mathrm{ref}}} = \frac{|J_{\leftarrow}| + J_{\rightarrow}}{2c_{\mathrm{ref}}} = \frac{n_{\mathrm{cross}}}{2\sigma \quad T_{\mathrm{sim}} c_{\mathrm{ref}}} \tag{33}$$

The dividing surfaces for the flat bilayer at $z = \pm h/2$ are flat surfaces with equal area σ. However, these become spherical surfaces for the liposome at $r = r_1$ and $r = r_2$, whose area depends on the radial distance r. Therefore, we will provide an update of the counting method for spherically shaped membranes.

Consider again a long equilibrium MD simulation, this time of a liposome. Count the number of crossings n_{entr} of permeants entering the liposome through the membrane and reaching the inner spherical dividing surface with cross section $\sigma_1 = 4\pi r_1^2$ at radius r_1. The corresponding inward flux at r_1 is

$$|J_{\mathrm{entr}}| = \frac{n_{\mathrm{entr}}}{T_{\mathrm{sim}} \sigma_1} \tag{34}$$

with $J_{\mathrm{entr}} < 0$. Similarly, the flux of escaping particles reaching $\sigma_2 = 4\pi r_2^2$ is

$$J_{\mathrm{esc}} = \frac{n_{\mathrm{esc}}}{T_{\mathrm{sim}} \sigma_2} \tag{35}$$

with $J_{\mathrm{esc}} > 0$. In other words, the flat membrane fluxes $J_{\leftarrow}$ and $J_{\rightarrow}$ are the equivalents of the liposome radial fluxes J_{entr} (<0) and J_{esc} (>0) of membrane crossings. Since the equilibrium MD can be seen as a superposition of the two steady states in Fig. 1, as in the derivation of Eq. 33, these two equilibrium radial fluxes are equal to the two steady-state fluxes of the previous subsection (Fig. 1). Using the definitions $P_{\mathrm{entr}} \equiv P_{\mathrm{entr}}(r_1)$ and $P_{\mathrm{esc}} \equiv P_{\mathrm{esc}}(r_2)$ from the previous subsection, the permeability equations become

$$P_{\mathrm{entr}} = \frac{|J_{\mathrm{entr}}|}{c_{\mathrm{ref}}} \tag{36}$$

$$P_{\mathrm{esc}} = \frac{J_{\mathrm{esc}}}{c_{\mathrm{ref}}} \tag{37}$$

By transferring our liposome permeability definition Eq. 22 for P^* to the case of non-diffusive transport, the geometric mean of P_{entr} and P_{esc} is again used,

$$P^* = \frac{\sqrt{|J_{\mathrm{entr}}| \quad J_{\mathrm{esc}}}}{c_{\mathrm{ref}}} = \frac{|J_{\mathrm{entr}}|}{c_{\mathrm{ref}}} \frac{r_1}{r_2} = \frac{J_{\mathrm{esc}}}{c_{\mathrm{ref}}} \frac{r_1}{r_2} \tag{38}$$

In terms of the total number of (bidirectional) crossings $n_{\mathrm{cross}} = n_{\mathrm{esc}} + n_{\mathrm{entr}}$ through the liposome membrane, the liposome permeability reads

$$P^* = \quad = \frac{n_{\mathrm{cross}}}{8 T_{\mathrm{sim}} \pi r_1 r_2 c_{\mathrm{ref}}} \tag{39}$$

Here, $n_{\mathrm{esc}} \approx n_{\mathrm{entr}}$ was used, assuming that, in a long equilibrium simulation, there is no accumulation of particles, and the numbers of permeants entering or escaping the liposome are approximately equal.

ILLUSTRATION: PERMEABILITY OF FLAT AND CURVED DPPC MEMBRANES

Systems and computational details

Two homogeneous membranes consisting of DPPC and two binary membranes consisting of DPPC and 10% cholesterol were modeled with coarse-grained MD simulations. The simulation box (see Fig. 3) either contained a flat membrane (label F) or a liposome (label L) with a radius of approximately 50 Å. The composition of each system is given in Table 1. The box also contained 0.15 M sodium chloride, as well as a very low concentration of 20 neutral N0 beads, which have not been focused on in the present paper.

Initial structures of the membranes were prepared with the CHARMM-GUI Web site (32–34). Using the Martini 2 forcefield for the CG beads (35), the MD simulations were run with the Gromacs-2021.4 (36). The Coulombic interactions were calculated using the reaction-field approach (37). Truncation of 11 Å was applied for the Coulombic and

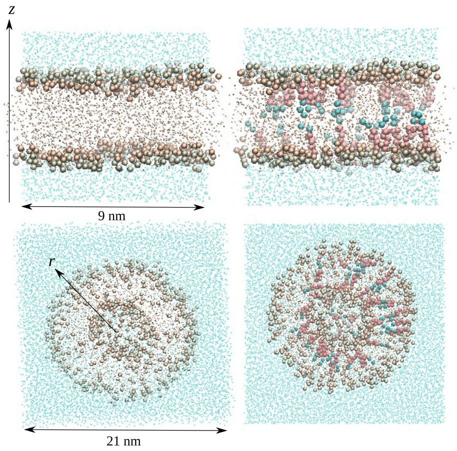

FIGURE 3 Simulation box of flat membranes (*top*) and liposomes (*bottom*), modeled with a CG forcefield. (*Left*) Pure DPPC; (*right*) DPPC:chol composition. Large beads are phosphate head groups (PO4 beads, *light green*), glycerol groups (GL1 beads, *light brown*), and cholesterol (*pink and blue*). Small beads are water (*light blue*) and DPPC tail beads (*light orange*). To see this figure in color, go online.

TABLE 1 Composition of the Simulated Flat Bilayers and the Liposomes with Number of Lipids in Each Leaflet, Number of Water Molecules, and Number of Sodium Chloride Ion Pairs

system	DPPC:chol (%)	# lipids	# in/out	# waters	# ion pairs
F	100:0	256	128/128	2504	29
F-Ch	90:10	260	130/130	2452	28
L	100:0	518	124/394	54,507	603
L-Ch	90:10	545	145/400	76,608	842

Each system also contained 20 N0 beads. F: simulated flat bilayers; L: liposomes; Ch: cholesterol.

the van der Waals interactions, where potentials were shifted to zero at the cutoff with the potential-shift-Verlet modifiers. The neighbor list length was 11 Å, updated using the Verlet neighbor search algorithm. The equations of motion were integrated with a time step of 20 fs using the leap-frog integrator, and coordinates were stored every 20 ps. The velocity rescale thermostat was used with the coupling constant of 1 ps (38) to set the temperature at 323 K, which lies above the melting temperature of DPPC, thus ensuring that the membrane is in the liquid disordered phase. The Parrinello-Rahman barostat at 1 bar was employed with a coupling constant of 12 ps, and semi-isotropic and isotropic isothermal compressibility of 3×10^{-3} and 4.5×10^{-5} bar^{-1} for systems with a flat bilayer and a liposome, respectively. At every 100 time steps, the center of mass motion of the system was removed. First, systems were energy minimized and equilibrated in the NPT ensemble for 100 ns, up to 600 ns for liposomes to allow for water exchange between interior and exterior, followed by a 1000 ns NPT production run.

Membrane structure

The membrane thickness and area per lipid in Table 2 are measures for the membrane's geometry and compactness. To determine the membrane thickness h from the MD trajectories, the average position of the phosphate Martini beads (PO4) is evaluated, using z or r for the flat or curved membranes, respectively. For a flat membrane, the bilayer is centered on $z = 0$ and then the average $|z|$ over all PO4 beads is computed, which is equal to $h/2$. For a liposome, the membrane is centered on $r = 0$ and the two average radial distances of the PO4 beads in the inner and outer layer are used as the two radii r_1 and r_2, which determine the thickness $h = r_2 - r_1$. It has been verified that no PO4 beads flipflopped between leaflets during the simulation.

TABLE 2 Structural Characteristics of Simulated Flat and Curved Membranes: Membrane Thickness h; Radii r_1 and r_2 (in Å); Area per Lipid A_l, $A_{l,1}$, $A_{l,2}$, and A_l^* (in $Å^2$)

system	h	A_l
F	40.2	63.6
F-Ch	41.2	58.1

system	h	r_1	r_2	$A_{l,1}$	$A_{l,2}$	A_l^*
L	35.6	20.7	56.3	43.6	101.1	66.4
L-Ch	35.3	21.0	56.3	38.1	99.5	61.6

To determine the area per lipid A_l, the number of lipids per leaflet is counted and is reported in Table 2. For a liposome, the average areas per lipid $A_{l,1}$ and $A_{l,2}$ are computed as the area $4\pi r_1^2$ and $4\pi r_2^2$, divided by the number of lipids in the inner and outer leaflet, respectively.

Comparing the flat and curved membranes in Table 2, the curvature makes the membrane appear to be thinner, with a reduction in h from about 40.2 Å to about 35.6 Å. The curvature makes the area per lipid lower in the inner liposome leaflet compared with the flat membrane, meaning that the phosphate groups are more densely packed in the inner leaflet, whereas the inverse effect is seen for the outer leaflet. Inspired by the permeability definition in Eq. 22, we compute the geometric mean of the areas, $A_l^* = \sqrt{A_{l,1} A_{l,2}}$. This value indicates that, overall, the liposome's lipids are less densely packed than in the flat membrane. This is also confirmed by estimating the volume per lipid (values not shown).

The incorporation of cholesterol introduces a clear reduction in the area per lipid, in accordance with other works reporting on the effect of cholesterol. Alwarawrah et al. reported that the area per DOPC lipid at 323 K decreases from 67.1 to 59.6 $Å^2$ by including 10% cholesterol in the membrane (39). A similar trend was observed by another research group, analytically investigating the effect of cholesterol on the area per lipid at 323 K, with a 15% reduction in the area being occupied by lipid molecules in the membrane containing 10% cholesterol (40). In our simulation, this fall in the area per DPPC lipid is about 9% (from 63.6 to 58.1 $Å^2$) for the flat membranes and 7% (from 66.4 to 61.6 $Å^2$) for the curved membranes. Cholesterol in the membrane is also known to increase the membrane thickness. MD simulation was performed at 323 K by Leeb et al. to assess the changes in the membrane thickness composing cholesterol. They found that 10% cholesterol can increase the DPPC bilayer thickness from 40.5 to 43.7 Å (8%) (41). A smaller increase of about 6% for the thickness was reported at 323 K for the DPPC:chol membrane (10% cholesterol) by Alwarawrah et al. (39). However, this effect on the membrane's thickness is less noticeable in our systems with a flat (2%) or curved (0.7%) bilayer, suggesting here a stronger effect of the curvature than of the cholesterol content.

Water permeability

To compute the permeability of water molecules through the membrane, the number of crossings and water concentrations need be evaluated. For flat membranes, the dividing surfaces are set to $|z| = h/2$, and membrane crossings are detected with the Rickflow package (23). The water

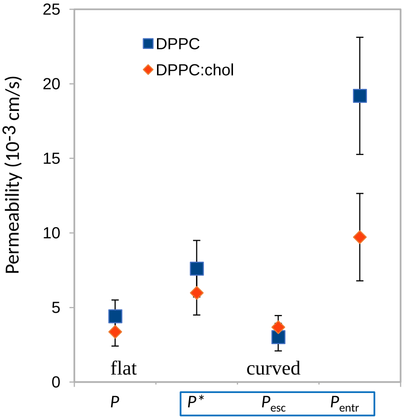

FIGURE 4 Water permeability of flat membranes (P) and liposomes (P^*, P_{esc}, P_{entr}). Error bars refer to standard error assuming that crossings are independent observations of a Poisson process (16). Composition without (*squares*) or with (*diamonds*) cholesterol. To see this figure in color, go online.

concentration is evaluated in the flat region of the water histogram. For the liposomes, we implemented an extension of the Rickflow package detect membrane crossings through the spherical dividing surfaces with radii r_1 and r_2. The reference water concentration inside (outside) the liposome is determined by counting the average number of water beads with $r < 12$ Å ($r > 70$ Å) where the water histograms visually flatten out, and dividing by the appropriate volume. In our simulations, the number of crossings of water beads varies between 41 and 179, and the water concentration varies between 0.94 and 0.98 g/cm^3.

Fig. 4 provides detail on the permeability of water molecules through the flat and curved membranes. Cholesterol seems to reduce the permeability, in accordance with the tighter packing (volume per lipid) in cholesterol-containing membranes. A drop of 24% is seen in both the flat (P) and curved (P^*) bilayer (although not statistically significant).

Finally, let us focus on the effect of curvature. For the liposomes, the entrance permeability is about a factor 6.4 (7.0) times higher than the escape permeability for the membrane without (with) cholesterol. This very large range in permeabilities illustrates the ambiguity in the numerical evaluation of liposome permeability. Fortunately, our definition P^* gives a single value, which may be directly compared with the flat membranes. As shown in Fig. 4, the curvature increases the permeability roughly by a factor 1.7 in the membranes without/with cholesterol. In other words, the liposome permeability definition in this paper allowed for assessing the curvature effect for DPPC (DPPC:chol) membranes.

CONCLUSIONS

The geometry of highly curved membranes, such as liposomes, creates ambiguity in the permeability value, as a large range of values can be found between the entrance and escape permeabilities (Eqs. 15 and 16). This is caused by the flux being dependent on the radial distance, which appears in the area of the spherical dividing surface. Unfortunately, the large range of values for a liposome prevents a straightforward comparison between flat and curved membrane permeability. The ambiguity for liposomes, of an arbitrarily large factor purely based on geometry, was countered in this contribution by providing a new permeability definition. The criterion that was used as a guideline was that a flat and curved membrane should have the same permeability value when the medium is completely homogeneous. This resulted in defining the liposome permeability P^* as the geometric mean of the entrance and escape permeabilities (Eq. 22). The Smoluchowski equation, implying diffusive transport, was heavily used to elucidate the effects of curvature with analytical expressions, but the liposome permeability definition was also transferred to the counting method (Eq. 39), which has no diffusive assumption.

As an illustrative example, MD simulations of a DPPC and DPPC:chol membrane were run. For a small liposome with radius of about 5 nm, the entrance permeability was a factor 6.4 to 7.0 higher than the escape permeability, clearly showing the ambiguity in permeability values. Using the liposome permeability P^*, the permeability could be compared effectively between the flat and curved membrane. In our simulations, the curvature decreased the membrane thickness and increased the area per lipid. The elevation seen in the water permeability for the curved membranes can be due to these changes in the thickness and the area per lipid, as these changes can facilitate the water permeation through the bilayer. The liposome permeability definition P^* thus enabled a fair assessment of the curvature effect on the permeability of DPPC and DPPC:chol membranes.

AUTHOR CONTRIBUTIONS

A.G. designed the research. S.D. carried out all simulations. A.G. and S.D. analyzed the data and wrote the article.

ACKNOWLEDGMENTS

The computational resources (Stevin Supercomputer Infrastructure) and services used in this work were provided by the VSC (Flemish Supercomputer Center), funded by Ghent University, FWO and the Flemish Government, department EWI.

DECLARATION OF INTERESTS

The authors declare no competing interests.

REFERENCES

1. Wang, S., T. Ichinomiya, …, B. P. Head. 2021. Synapsin-promoted caveolin-1 overexpression maintains mitochondrial morphology and function in PSAPP Alzheimer's disease mice. *Cells.* 10:2487.
2. Porta, J. C., B. Han, …, M. D. Ohi. 2022. Molecular architecture of the human caveolin-1 complex. *Sci. Adv.* 8, eabn7232.
3. Alimohamadi, H., B. Ovryn, and P. Rangamani. 2020. Modeling membrane nanotube morphology: the role of heterogeneity in composition and material properties. *Sci. Rep.* 10:2527.
4. Liese, S., and A. Carlson. 2021. Membrane shape remodeling by protein crowding. *Biophys. J.* 120:2482–2489.
5. Bahrami, A. H., and G. Hummer. 2017. Formation and stability of lipid membrane nanotubes. *ACS Nano.* 11:9558–9565.
6. Yesylevskyy, S. O., T. Rivel, and C. Ramseyer. 2017. The influence of curvature on the properties of the plasma membrane. Insights from atomistic molecular dynamics simulations. *Sci. Rep.* 7:16078.
7. Yesylevskyy, S., T. Rivel, and C. Ramseyer. 2019. Curvature increases permeability of the plasma membrane for ions, water and the anti-cancer drugs cisplatin and gemcitabine. *Sci. Rep.* 9:17214–17218.
8. Boyd, K. J., and E. R. May. 2018. BUMPy: a model-independent tool for constructing lipid bilayers of varying curvature and composition. *J. Chem. Theory Comput.* 14:6642–6652.
9. Casalino, L., A. C. Dommer, …, R. E. Amaro. 2021. AI-driven multiscale simulations illuminate mechanisms of SARS-CoV-2 spike dynamics. *Int. J. High Perform. Comput. Appl.* 35:432–451.
10. Thornburg, Z. R., D. M. Bianchi, …, Z. Luthey-Schulten. 2022. Fundamental behaviors emerge from simulations of a living minimal cell. *Cell.* 185:345–360.e28.
11. Marrink, S. J., L. Monticelli, …, P. C. Souza. 2022. Two decades of Martini: better beads, broader scope. *Wiley Interdiscip. Rev. Comput. Mol. Sci.* e1620.
12. Patmanidis, I., P. C. T. Souza, …, S. J. Marrink. 2022. Modelling structural properties of cyanine dye nanotubes at coarse-grained level. *Nanoscale Adv.* 4:3033–3042.
13. Pezeshkian, W., M. König, …, S. J. Marrink. 2020. Backmapping triangulated surfaces to coarse-grained membrane models. *Nat. Commun.* 11:2296–2299.
14. Dotson, R. J., C. R. Smith, …, S. C. Pias. 2017. Influence of cholesterol on the oxygen permeability of membranes: insight from atomistic simulations. *Biophys. J.* 112:2336–2347.
15. Venable, R. M., A. Krämer, and R. W. Pastor. 2019. Molecular dynamics simulations of membrane permeability. *Chem. Rev.* 119: 5954–5997.
16. Ghysels, A., A. Krämer, …, R. W. Pastor. 2019. Permeability of membranes in the liquid ordered and liquid disordered phases. *Nat. Commun.* 10:5616.
17. Davoudi, S., and A. Ghysels. 2021. Sampling efficiency of the counting method for permeability calculations estimated with the inhomogeneous solubility–diffusion model. *J. Chem. Phys.* 154, 054106.
18. Marrink, S. J., and H. J. C. Berendsen. 1996. Permeation process of small molecules across lipid membranes studied by molecular dynamics simulations. *J. Phys. Chem.* 100:16729–16738.
19. Hummer, G. 2005. Position-dependent diffusion coefficients and free energies from Bayesian analysis of equilibrium and replica molecular dynamics simulations. *New J. Phys.* 7:34.
20. Ghysels, A., R. M. Venable, …, G. Hummer. 2017. Position-dependent diffusion tensors in anisotropic media from simulation: oxygen transport in and through Membranes. *J. Chem. Theory Comput.* 13: 2962–2976.
21. De Vos, O., R. M. Venable, …, A. Ghysels. 2018. Membrane permeability: characteristic times and lengths for oxygen and a simulation-based test of the inhomogeneous solubility-diffusion model. *J. Chem. Theory Comput.* 14:3811–3824.
22. De Vos, O., T. Van Hecke, and A. Ghysels. 2018. Effect of chain unsaturation and temperature on oxygen diffusion through lipid membranes from simulations. *Adv. Exp. Med. Biol.* 1072:399–404.
23. Krämer, A., A. Ghysels, …, R. W. Pastor. 2020. Membrane permeability of small molecules from unbiased molecular dynamics simulations. *J. Chem. Phys.* 153, 124107.
24. Votapka, L. W., C. T. Lee, and R. E. Amaro. 2016. Two relations to estimate membrane permeability using milestoning. *J. Phys. Chem. B.* 120:8606–8616.
25. Lee, C. T., J. Comer, …, J. C. Gumbart. 2016. Simulation-based approaches for determining membrane permeability of small compounds. *J. Chem. Inf. Model.* 56:721–733.
26. Riccardi, E., A. Lervik, …, O. Aarøen, T. S. van Erp. 2020. PyRETIS 2: an improbability drive for rare events. *J. Comput. Chem.* 41:370–377.
27. Ghysels, A., S. Roet, …, T. S. van Erp. 2021. Exact non-Markovian permeability from rare event simulations. *Phys. Rev. Res.* 3, 033068.
28. Riccardi, E., A. Krämer, …, A. Ghysels. 2021. Permeation rates of oxygen transport through POPC membrane using replica exchange transition interface sampling. *J. Phys. Chem. B.* 125:193–201.
29. Gaalswyk, K., E. Awoonor-Williams, and C. N. Rowley. 2016. Generalized Langevin methods for calculating transmembrane diffusivity. *J. Chem. Theory Comput.* 12:5609–5619.
30. Filipe, H. A. L., M. Javanainen, …, M. J. Moreno. 2018. Quantitative assessment of methods used to obtain rate constants from molecular dynamics simulations—translocation of cholesterol across lipid bilayers. *J. Chem. Theory Comput.* 14:3840–3848.
31. Ferreira, R. J., and P. M. Kasson. 2019. Antibiotic uptake across gram-negative outer membranes: better predictions towards better antibiotics. *ACS Infect. Dis.* 5:2096–2104.
32. Jo, S., T. Kim, …, W. Im. 2008. CHARMM-GUI: a web-based graphical user interface for CHARMM. *J. Comput. Chem.* 29:1859–1865.
33. Lee, J., X. Cheng, …, W. Im. 2016. CHARMM-GUI input generator for NAMD, GROMACS, AMBER, OpenMM, and CHARMM/OpenMM simulations using the CHARMM36 additive force field. *J. Chem. Theory Comput.* 12:405–413.
34. Qi, Y., H. I. Ingólfsson, …, W. Im. 2015. CHARMM-GUI martini maker for coarse-grained simulations with the martini force field. *J. Chem. Theory Comput.* 11:4486–4494.
35. Marrink, S. J., H. J. Risselada, …, A. H. De Vries. 2007. The MARTINI force field: coarse grained model for biomolecular simulations. *J. Phys. Chem. B.* 111:7812–7824.
36. Abraham, M. J., T. Murtola, …, E. Lindahl. 2015. GROMACS: high performance molecular simulations through multi-level parallelism from laptops to supercomputers. *SoftwareX.* 1-2:19–25.
37. Tironi, I. G., R. Sperb, …, W. F. van Gunsteren. 1995. A generalized reaction field method for molecular dynamics simulations. *J. Chem. Phys.* 102:5451–5459.
38. Bussi, G., D. Donadio, and M. Parrinello. 2007. Canonical sampling through velocity rescaling. *J. Chem. Phys.* 126, 014101.
39. Alwarawrah, M., J. Dai, and J. Huang. 2010. A molecular view of the cholesterol condensing effect in DOPC lipid bilayers. *J. Phys. Chem. B.* 114:7516–7523.
40. Kheyfets, B., and S. Mukhin. 2015. Area per lipid in DPPC-cholesterol bilayers: analytical approach. Preprint at arXiv.1501.02727.
41. Leeb, F., and L. Maibaum. 2018. Spatially resolving the condensing effect of cholesterol in lipid bilayers. *Biophys. J.* 115:2179–2188.

Paper 3

Understanding the Role of Caveolae in Oxygen Buffering: The Effect of Membrane Curvature

Samaneh Davoudi, Qi Wang, Hemal H. Patel and An Ghysels

International Society on Oxygen Transport to Tissue, 58-91 (2023)

15

Understanding the Role of Caveolae in Oxygen Buffering: The Effect of Membrane Curvature

Samaneh Davoudi, Qi Wang, Hemal H. Patel,
Sally C. Pias, and An Ghysels

Abstract

The "oxygen paradox" can be explained as two opposing biological processes with oxygen (O_2) as a reactant. On the one hand, oxygen is essential to aerobic metabolism, powering oxidative phosphorylation in mitochondria. On the other hand, an excess supply of oxygen will generate reactive species which are harmful for the cell. In healthy tissues, the first process must be maximized relative to the second one. We have hypothesized that curved and cholesterol-enriched membrane invaginations called caveolae help maintain the proper oxygen level by taking up oxygen and attenuating its release to the mitochondria. The mechanism by which caveolae may help to buffer the oxygen level in cells is still unclear. Here, we aim to assess how structural aspects of caveolae, the curvature of the membrane, influence the local oxygen abundance and the membrane partitioning. We have modelled a flat bilayer and a liposome composed of dipalmitoylphosphatidylcholine (DPPC), using molecular dynamics simulation. Associated changes in the membrane-level oxygen partition coefficient and free energy profiles will be presented.

Keywords

Caveolae · Oxygen buffering · Molecular dynamics simulation · Oxygen supply

15.1 Introduction

Oxygen is a vital for life, yet it can be toxic at the same time, known as the "oxygen paradox" [1, 2]. This molecule is necessary to the metabolic machinery of a living cell by fueling oxidative phosphorylation in the process of cellular energy generation [1, 2]. However, in a high concentration, it can generate reactive species which leads to the cellular damage [3]. It is suggested that during evolution, the response to this paradox was creating cholesterol inside the membrane to control the concentration of oxygen which are inside the cell and minimize its toxicity [4]. Caveolin, a scaffold protein, plays an important role in controlling the oxygen concentration by regulating caveolae, cholesterol enriched microdomains in the plasma membrane [5, 6]. Caveolae

---

S. Davoudi (✉) · A. Ghysels
IBiTech – Biommeda Research Group, Ghent University, Ghent, Belgium
e-mail: samaneh.davoudi@ugent.be

Q. Wang · S. C. Pias
Department of Chemistry, New Mexico Institute of Mining and Technology (New Mexico Tech), Socorro, NM, USA

H. H. Patel
Department of Anesthesiology, University of California, San Diego, CA, USA

© The Author(s), under exclusive license to Springer Nature Switzerland AG 2023
F. Scholkmann et al. (eds.), *Oxygen Transport to Tissue XLIV*, Advances in Experimental Medicine and Biology 1438, https://doi.org/10.1007/978-3-031-42003-0_15

have been proposed to function as "oxygen capacitors", or storage sites, to optimize cellular metabolic function and promote stress adaptation [7]. With aging, the expression of the caveolin protein decreases in some organs, and it may be associated with increased oxygen toxicity and related disease [8]. Manipulating caveolin protein levels within cells has therapeutic potential for treating oxygen related disorders such as cardiovascular diseases, cancer, and aging.

However, the role of caveolin in the plasma membrane and the mechanism by which it regulates oxygen levels in cells are not yet clear. Simulations, especially molecular dynamics (MD), have made it more feasible to examine oxygen transport at the molecular scale, such as the permeation through the phospholipid bilayers [9–12]. In this paper, we use MD simulations to investigate how a key structural aspect of caveolae, i.e., membrane curvature, may affect oxygen partitioning into the membrane. Two DPPC bilayers with different curvature are simulated at the atomic scale: a flat bilayer with zero curvature and a curved bilayer forming a spherical particle (liposome) with very high curvature. The results feature partition coefficient and free energy profiles for oxygen, spanning the membrane.

15.2 Methods

Two systems with DPPC lipids were simulated using the Gromacs-2021.4 [13]: a flat bilayer consisting of 128 lipids (Fig. 15.1 right) and a 50 Å-radius liposome consisting of 518 lipids (Fig. 15.1 middle). A detailed description of the systems can be found in Table 15.1. Both systems were simulated using all-atom MD. For the system with a liposome, we first generated the model as a coarse-grained structure with CHARMM-GUI [14]. Then, the Martini backmapping tool was used to convert the coarse-grained model to an all-atom one [15]. The two systems were simulated at 323 K, coupled to velocity rescale thermostats with a coupling constant of 1.0 ps [16]. The Parrinello–Rahman barostat was employed to couple the pressure in the system with the flat bilayer, while the system with the liposome was coupled with the Berendsen barostat. Periodic

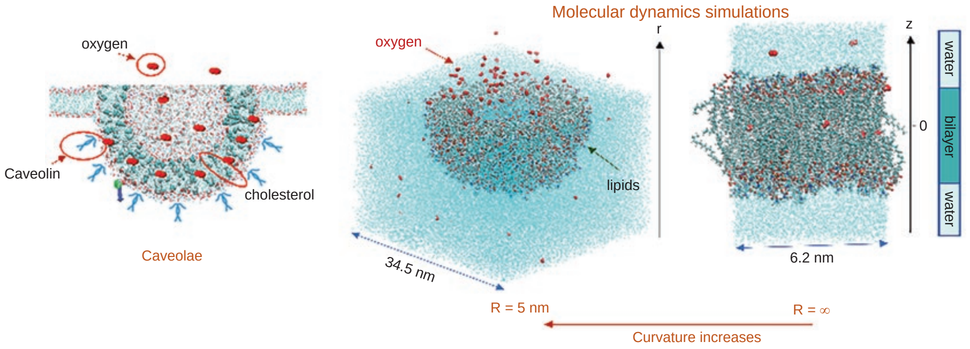

Fig. 15.1 Left: the schematic picture of caveolae. Middle: the system with a liposome, only the lower part is shown. Right: the system with the flat bilayer

Table 15.1 The detailed description of the two systems: flat bilayer and liposome

Systems	# Lipid	# Water	# O_2	Thickness (nm)	Area per lipid (nm^2)		<K>
					Inside layer	Outside layer	
Flat bilayer	128	6341	18	4.02	0.61		4.06
Liposome	518	78,804	164	3.06	0.65	1.02	3.95

boundary conditions were applied in all three dimensions and the box vectors were subjected to semi-isotropic pressure coupling (flat bilayer) or isotropic pressure coupling (liposome), using a reference pressure of 1 bar, a coupling parameter of 5 ps, and an isothermal compressibility of 3×10^{-4} bar^{-1} and 4.5×10^{-4} bar^{-1}. The coordinates were saved every 2 ps. The particle mesh Ewald approach was employed to calculate the Coulombic interactions. At the cutoff of 1.2 nm, the Coulombic and the van der Waals potentials were shifted to zero using force-switch modifiers. CHARMM36 forcefield was implemented to model the lipid and oxygen molecules [17]. Water was modeled by applying the TIP3P model [18]. Using the Verlet neighbor search algorithm, the neighbor list length was updated at 1.2 nm. The equation of motion was integrated with a time step of 2 fs, using the leapfrog integrator. At every time step, the center of mass motion of the system was removed. After adding oxygen molecules at a concentration of 86 μM, an energy minimization was performed, followed by a 50 ns equilibration and 200 ns production run with constant pressure and constant temperature (NPT ensemble).

15.3 Results

15.3.1 Effect of Curvature on Membrane Thickness and Area per Lipid

The thickness of the membranes was determined by measuring the distance between the two highest peaks in the histogram of the phosphates *z*-coordinates. The results (Table 15.1) indicate that the thickness of the flat bilayer at a temperature of 323 K and at a pressure of 1 bar is 4.02 nm, which is consistent with the experimental value of 3.9 nm [19]. Increasing the membrane's curvature reduces the membrane thickness, to 3.06 nm. The opposite trend occurs with the area per lipid. To calculate the area per lipid for the flat bilayer, the area of the box in the *xy* direction was divided by the number of the lipids in one leaflet. For the liposome, two areas per lipid (inside and outside) were computed, dividing the area of each layer by the number of the lipids in that layer. The highest peaks in the phosphate atoms' histogram were chosen as radii to calculate the areas of the leaflets. As shown in Table 15.1, the area per lipid in the outer lipid layer of the liposome, 1.02 nm^2, was almost twice the flat bilayer's area per lipid, 0.61 nm^2. The area per lipid for the liposome's inner layer, 0.65 nm^2, was close to that of the flat bilayer and to the experimental value at 323 K and 1 bar, namely 0.63 nm^2 [19].

15.3.2 Effect of Curvature on Oxygen Free Energy Profile

The oxygen free energy profile in both the flat bilayer and the liposome were plotted in Fig. 15.2 as a function of the membrane depth, also called permeation coordinate. For the flat bilayer, this is the normal to the membrane, i.e., the *z*-coordinate (Fig. 15.1 right). For the curved membrane, this is the radial distance *r* from the liposome center (Fig. 15.1 center). The relatively small size of the liposome results in poor statistics in the water phase inside the liposome (as seen in Fig. 15.2, right). As can be observed in Fig. 15.2, for the liposome, oxygen prefers to stay in the lipid part of the membrane, with two free energy wells, rather than in the middle part of two leaflets compared to the flat bilayer, with one free energy well. This preference may be a consequence of the decrease in the membrane thickness. Additionally, the barrier that oxygen needs to overcome to reach the water phase from the membrane's outer leaflet was reduced from 3 k_BT to 2 k_BT, where k_B represents Boltzmann constant.

15.3.3 Effect of Curvature on Oxygen Partition Coefficient

To calculate the oxygen partition coefficient (*K*) through the membrane, the free energy was set to zero in the water phase. *K* was calculated along the permeation direction for both systems using $\Delta F = k_BT \ln K$. As depicted in Fig. 15.3 left, oxy-

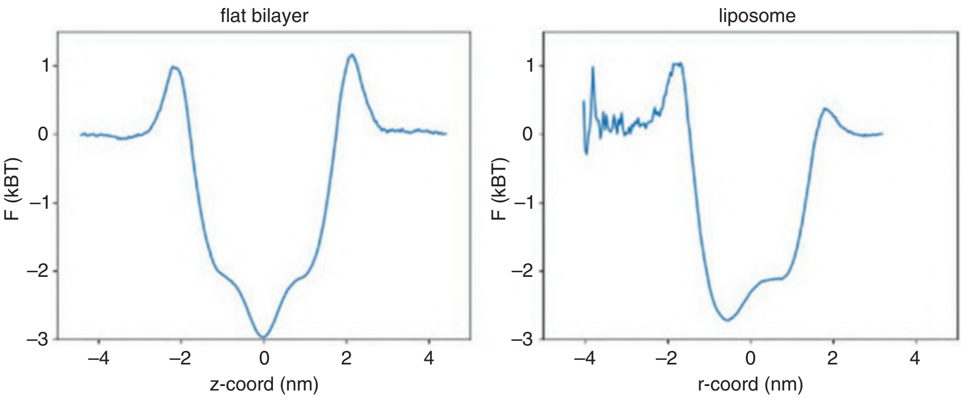

Fig. 15.2 The oxygen free energy profile as a function of the permeation coordinate of the flat bilayer (z, left) or the liposome (r, right)

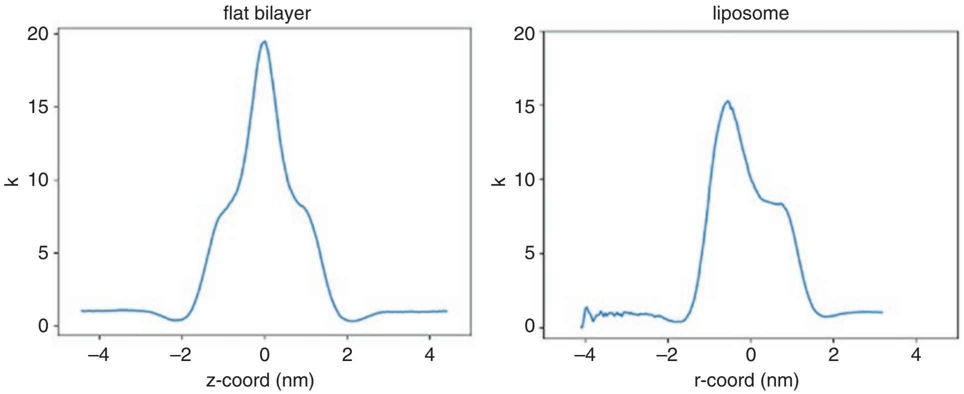

Fig. 15.3 The oxygen partition coefficient profile as a function of the permeation coordinate of the flat bilayer (z, left) or the liposome (r, right)

gen is more soluble in the mid-membrane than the water phase, which is expected. This behavior is slightly altered with an increase in the curvature, with the highest solubility observed in both lipid phases. As the area per lipid is smaller for the inner leaflet, oxygen tends to get trapped more in this layer, resulting in the highest *K* and deepest free energy well, as shown in the plots. As reported in Table 15.1, the average *K* (<*K*>) for the flat bilayer, 4.06, is only slightly larger than for the liposome, 3.95, indicating that the relative oxygen concentration is smaller in the liposome compared to the flat bilayer. It is assumed that the asymmetricity of the free energy and partition coefficient profiles is likely due to the smaller thickness and different area per lipid in each layer in the liposome.

15.4 Conclusion

The free energy and partition coefficient profiles demonstrate that the oxygen preference to stay in the membrane decreases as the membrane's curvature increases, resulting in the smaller partition coefficient. This leads to lower oxygen concentration in the membrane. In the liposome, oxygen needs to overcome a smaller energy barrier to permeate from the outer leaflet to the water phase, which facilitates the permeation process. This can be also related to the smaller thickness and the larger area per lipid of the outer layer of the curved membrane. These results differ from our initial hypothesis regarding the role of curvature in storing oxygen in caveolae. However, it is worth noting that our simulation did not include cholesterol or the caveolin protein, which may have a significant impact on the results. In summary, curvature may have a negligible effect in the oxygen partition coefficient, and it is unlikely that membrane curvature is the only mechanism by which caveolae store oxygen. In future work, also the timeliness of oxygen transport, i.e., oxygen permeability, should be investigated. Based on previous work on water permeability through curved membranes [20, 21], we plan to consider all structural aspects of caveolae and to examine the combined effect of curvature and cholesterol on oxygen permeability through the membrane.

References

1. Woese CR, Kandler O, Wheelis ML (1990) Towards a natural system of organisms: proposal for the domains archaea, bacteria, and eucarya. Proc Natl Acad Sci U S A 87(12):4576–4579
2. Carter R (2003) Oxygen: the molecule that made the world. J R Soc Med 96(1):46–47
3. Shields HJ, Traa A, Van Raamsdonk JM (2021) Beneficial and detrimental effects of reactive oxygen species on lifespan: a comprehensive review of comparative and experimental studies. Front Cell Dev Biol 9:628157
4. Brown AJ, Galea AM (2010) Cholesterol as an evolutionary response to living with oxygen. Evolution 64(7):2179–2183
5. Porta JC, Han B, Gulsevin A et al (2022) Molecular architecture of the human caveolin-1 complex. Sci Adv 8(19):eabn7232
6. Patel HH, Tsutsumi YM, Head BP et al (2007) Mechanisms of cardiac protection from ischemia/reperfusion injury: a role for caveolae and caveolin-1. FASEB J 21(7):1565–1574
7. Schilling JM, Head BP, Patel HH (2018) Caveolins as regulators of stress adaptation. Mol Pharmacol 93(4):277–285
8. Head BP, Peart JN, Panneerselvam M et al (2010) Loss of caveolin-1 accelerates neurodegeneration and aging. PLoS One 5:e15697
9. Riccardi E, Krämer A, van Erp TS et al (2020) Permeation rates of oxygen through a lipid bilayer using replica exchange transition interface sampling. J Phys Chem B 125(1):193–201
10. Ghysels A, Venable RM, Pastor RW et al (2017) Position-dependent diffusion tensors in anisotropic media from simulation: oxygen transport in and through membranes. J Chem Theory Comput 13(6):2962–2976
11. Nemoto EM, Harrison EM, Pias SC et al (2021) Oxygen transport to tissue XLII. Springer, Cham
12. Wang Q, Dotson RJ, Angles G et al (2021) Simulation study of breast cancer lipid changes affecting membrane oxygen permeability: effects of chain length and cholesterol. Adv Exp Med Biol 1269:15–21
13. Abraham MJ, Murtola T, Schulz R et al (2015) GROMACS: high performance molecular simulations through multi-level parallelism from laptops to supercomputers. SoftwareX 1:19–25
14. Qi Y, Ingólfsson HI, Cheng X et al (2015) CHARMM-GUI martini maker for coarse-grained simulations with the martini force field. J Chem Theory Comput 11(9):4486–4494
15. Wassenaar TA, Pluhackova K, Böckmann RA (2014) Going backward: a flexible geometric approach to reverse transformation from coarse grained to atomistic models. J Chem Theory Comput 10(2):676–690
16. Bussi G, Donadio D, Parrinello M (2007) Canonical sampling through velocity rescaling. J Chem Phys 126(1):014101
17. Huang J, MacKerell AD Jr (2013) CHARMM36 all-atom additive protein force field: validation based on comparison to NMR data. J Comput Chem 34(25):2135–2145
18. Jorgensen WL, Chandrasekhar J, Madura JD et al (1983) Comparison of simple potential functions for simulating liquid water. J Chem Phys 79(2):926–935
19. Kučerka N, Nieh MP, Katsaras J (2011) Fluid phase lipid areas and bilayer thicknesses of commonly used phosphatidylcholines as a function of temperature. Biochim Biophys Acta Biomembr 1808(11):2761–2771
20. Davoudi S, Ghysels A (2021) Sampling efficiency of the counting method for permeability calculations estimated with the inhomogeneous solubility–diffusion model. J Chem Phys 154(5):054106
21. Davoudi S, Ghysels A (2023) Defining permeability of curved membranes in molecular dynamics simulations. Biophys J 122:1–10. https://doi.org/10.1016/j.bpj.2022.11.028

Paper 4

Capric acid and myristic acid permeability enhancers in curved liposome membranes

Samaneh Davoudi, Koen Raemdonck, Kevin Braeckmans
and An Ghysels

Journal of Chemical Information and Modeling 63, 6789-6806 (2023)

JCIM JOURNAL OF CHEMICAL INFORMATION AND MODELING

pubs.acs.org/jcim Article

Capric Acid and Myristic Acid Permeability Enhancers in Curved Liposome Membranes

Samaneh Davoudi, Koen Raemdonck, Kevin Braeckmans, and An Ghysels*

Cite This: *J. Chem. Inf. Model.* 2023, 63, 6789−6806 Read Online

ACCESS | Metrics & More | Article Recommendations | Supporting Information

Downloaded via UNIV GHENT on January 8, 2024 at 10:07:29 (UTC).
See https://pubs.acs.org/sharingguidelines for options on how to legitimately share published articles.

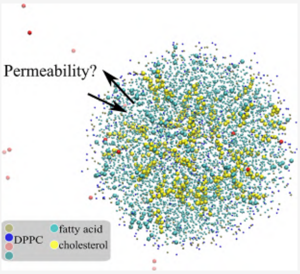

ABSTRACT: Liposomes are considered as advanced drug delivery systems for cancer treatment. A generation of pH-sensitive liposomes is being developed that use fatty acids (FAs) as a trigger for drug release in tumor tissues. However, FAs are also known to enhance permeability, and it is unclear whether FAs in liposomes may cause drug leakage or premature drug release. The passive permeability of the drug through the membrane of the liposome is thus a crucial factor for timely drug delivery. To investigate how the curvature and lipid composition of liposomes affect their passive permeability, coarse-grained molecular dynamics were performed. The permeability was determined with a counting method. Flat bilayers and three liposomes with varying diameters were studied, which had varying lipid compositions of dipalmitoylphosphatidylcholine, cholesterol, and deprotonated or neutral saturated FAs. The investigated permeants were water and two other small permeants, which have different free energy profiles (solubility) across the membrane. First, for the curvature effect, our results showed that curvature increases the water permeability by reducing the membrane thickness. The permeability increase for water is about a factor of 1.7 for the most curved membranes. However, a high curvature decreases permeability for permeants with free energy profiles that are a mix of wells and barriers in the headgroup region of the membrane. Importantly, the type of experimental setup is expected to play a dominant role in the permeability value, i.e., whether permeants are escaping or entering the liposomes. Second, for the composition effect, FAs decrease both the area per lipid (APL) and the membrane thickness, resulting in permeability increases of up to 55%. Cholesterol has a similar effect on the APL but has the opposite impact on membrane thickness and permeability. Therefore, FAs and cholesterol have opposing effects on permeability, with cholesterol's effect being slightly stronger in our simulated bilayers. As all permeability values were well within a factor of 2, and with liposomes usually being larger and less curved in experimental applications, it can be concluded that the passive drug release from a pH-sensitive liposome does not seem to be significantly affected by the presence of FAs.

INTRODUCTION

Nanosized drug delivery systems have been used to facilitate the delivery of drugs to the therapeutic targets in the body and to improve their therapeutic efficiency.[1] Liposomes are spherical lipid-based carriers which may encapsulate drugs and reduce the drugs' unwanted side effects.[2−5] Physical parameters such as bilayer composition and membrane curvature can significantly affect the liposome stability.[6−9]

pH-sensitive liposomes are one type of liposome with a specific composition, and they are currently investigated as potential drug delivery carriers in vitro and in vivo but not yet clinically.[10] pH-sensitive liposomes typically contain a phosphatidylethanolamine derivative and a weakly acidic amphiphile such as a fatty acid (FA). These carriers are designed to respond to the acidic environment of cancerous tissue by utilizing the destabilization of negatively charged groups of FAs (protonation of FAs), triggering the release of their payload.[11−15] However, FAs are also known as so-called permeability enhancers as they increase the permeability by disrupting the membrane structure.[16−18] An important question is whether the FAs can cause drug leakage and premature drug release from these FA-containing liposomes. Such an untimely drug delivery would make pH-sensitive liposomes less efficient. Therefore, the rate at which drugs permeate through the curved bilayers is a crucial parameter in the design of pH-sensitive liposomes as targeted drug delivery systems.

Several groups have applied different methods and models to calculate drug permeability through liposomes.[19−22] For instance, Winter et al. simulated arsenic trioxide permeation in a thermosensitive liposome using coarse-grained (CG) molecular dynamics (MD) simulations and calculated the permeability of a dipalmitoyl-phosphatidylcholine (DPPC) membrane containing a permeation-enhancing lysolipid.[21]

Received: June 20, 2023
Revised: October 18, 2023
Accepted: October 19, 2023
Published: November 2, 2023

ACS Publications © 2023 American Chemical Society

https://doi.org/10.1021/acs.jcim.3c00936

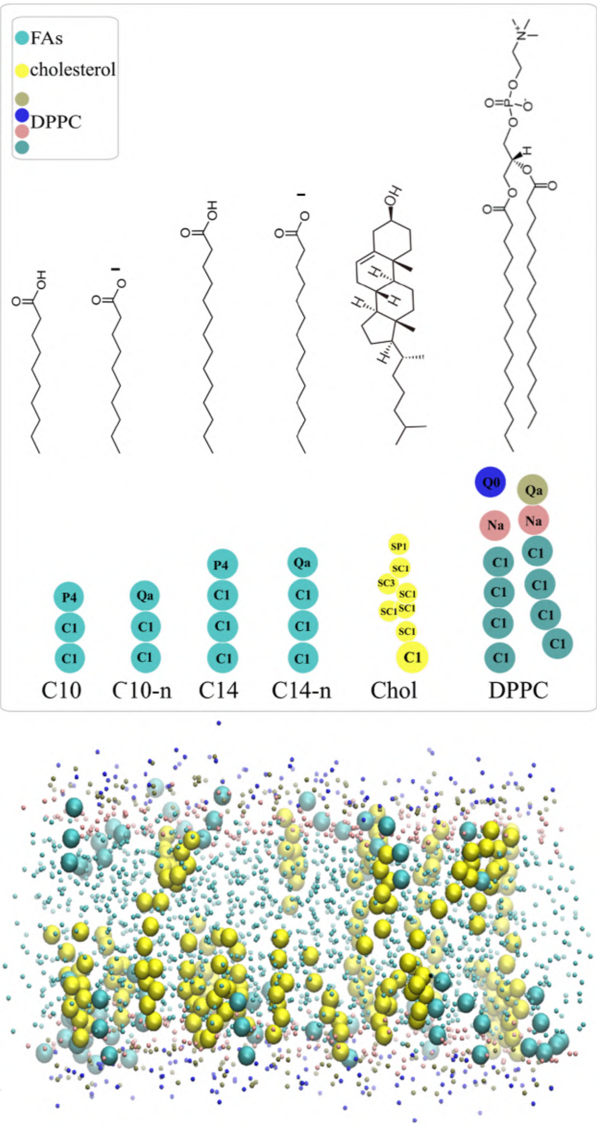

Figure 1. Top: structural formula and corresponding CG structure of the various lipid types (FAs, cholesterol, and phospholipids) in the simulations. Suffix n refers to deprotonated FAs. Bottom: example of a flat membrane containing DPPC, FAs, and cholesterol. Light green beads are FAs and yellow beads are cholesterol. DPPC is presented by points colored by bead type: green for hydrocarbons, pink for glycerol, brown for phosphate, and blue for choline bead type. Water and ions are not shown.

This paper uses MD simulations to estimate the permeability rate through liposome membranes containing FAs as these are relevant for the pH-sensitive liposomes. The membranes will have varying composition and curvature, and the possible dissociation of the FAs will also be taken into account.

To assess the effect of membrane composition on the permeation rate, a wide range of studies have been done.[23−30] Among them, cholesterol has been proven to decrease the permeability of the permeants by decreasing the membrane fluidity caused by an unsaturated tail.[30] Using MD simulations, other groups have concluded that the alteration in the

https://doi.org/10.1021/acs.jcim.3c00936
J. Chem. Inf. Model. 2023, 63, 6789−6806

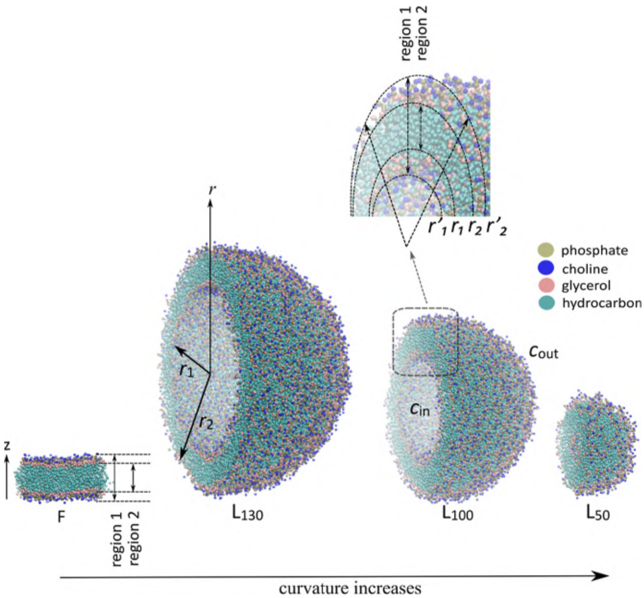

Figure 2. Systems with pure DPPC. From left to right, the curvature of the membrane increases. DPPC is presented by points, colored by bead type: green for hydrocarbons, pink for glycerol, brown for phosphate, and blue for choline bead type. Water and ions are not shown. Region 1 and region 2 are depicted in both a flat bilayer and a liposome. To enhance the clarity of the distinct radius definitions, a segment of the central liposome was excised and magnified, positioned at the upper portion of the figure.

permeability in the presence of cholesterol is due to the gradual reduction in the permeant's solubility in the lipid section of the membrane and enhancement in its center.[31,32] Falck et al. also found that the reduction in the membrane permeability by the presence of cholesterol is due to the decrease in the membrane's free volume.[33]

The effect of FAs in the lipid mix has also been investigated. In contrast to cholesterol, saturated FAs like capric acid (C10) have been shown experimentally to increase the permeability of the 1-palmitoyl-2-oleoyl-phosphatidylcholine (POPC) membrane by measuring the liposome leakage of a fluorescent dye upon exposure to C10 or the permeability of [^{14}C]-mannitol through Caco-2 monolayers.[17,18] Another study, using experimental methods, found that the FA-induced calcein leakage through DPPC liposomes increases with the length of incorporated saturated FAs, C8 to C20, except for C8.[16] They also reported that the effect of C10 on calcein's release rate from liposomes is almost negligible compared to that of myristic acid (C14). Moreover, liposomes containing oleic acid (C18) were evaluated for drug delivery and their ability to encapsulate and release the model drugs,[34] and the permeability increase of the FA was attributed to the presence of the relatively highly soluble single-chain amphiphiles (FAs) rather than the two chains of the POPC phospholipids. In other studies, FAs were confirmed for their effect as permeability enhancers in the intestine,[17,18,35,36] where it is also seen that C10 acts differently in vivo on the intestine permeability at low and high concentrations.[35] The most reported mechanism by different groups is that these FAs fluidize and perturb the membrane, and as a result, intracellular signaling changes and leads to the alteration in intestinal tight junction expression.[35,37]

A particular aspect of a fatty acid is its possible dissociation. A FA molecule can dissociate from its protonated (neutral) state into its deprotonated (negatively charged) state (Figure 1), depending on the dissociation constant of the FA, which differs between the membrane and the water phase. Consequently, when the pH changes, the partitioning of the FA between the water phase, membrane phase, and its neutral or deprotonated form can shift.[38] Different research groups estimated FA dissociation constants in different lipid membranes using MD simulations,[38−40] and a detailed MD study showed the change in FA mobility depending on the charge and chain length.[41] However, previous simulation studies do not explicitly evaluate the permeability at the molecular level for both neutral and deprotonated FAs, thus disregarding the effect of pH and the dissociation constants altogether. Therefore, in this paper, we measure the effect on the permeability for both neutral and deprotonated FAs in liposomes.

Curvature is another parameter that can affect the membrane's permeability.[42] Risselada and Marrink measured the structural properties such as the lipid packing and the lipid order parameter, and their findings suggest that curvature causes the membrane to become thinner and disrupts the packing of the leaflets.[43] Yesylevskyy et al. simulated a series of curved membrane patches and showed that the curvature decreases the order parameter and increases the area per lipid (APL) as computed with a Voronoi technique.[44] As for the permeability of curved membranes, Winter and Schatz

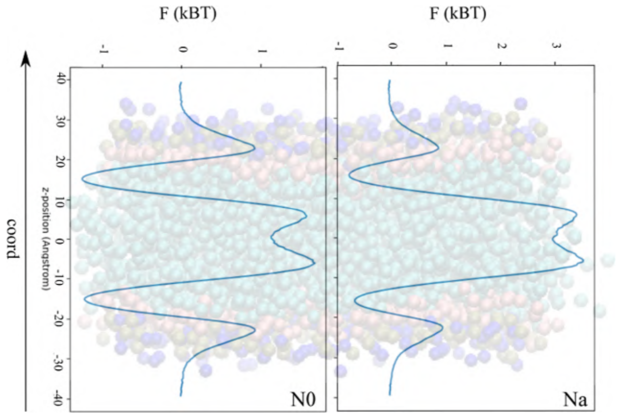

Figure 3. Free energy of permeants N0 and Na through a flat membrane in the z-direction. Na and N0 are CG beads with an intermediate polar character. DPPC is presented by beads, colored by bead type: green for hydrocarbons, pink for glycerol, brown for phosphate, and blue for choline bead type. Water and ions are not shown.

simulated a whole liposome consisting of a phospholipid bilayer containing a lysolipid, as mentioned above. The permeability was calculated to assess the effect of temperature on the dynamical properties, and they found that the permeability is the highest when the membrane goes through a phase transition from gel to liquid in the presence of lysolipid.[45] Yesylevskyy et al. also measured the permeability in the curved membrane patches and studied the liposome's interaction with a loaded drug, where the curvature was found to increase the permeability for small solute-like ions, water, and also bigger ones such as anticancer drugs.[46] However, the mixed effect of the curvature and the FAs on the membrane's permeation rate is still unknown at the molecular scale despite its importance for the understanding and design of drug delivery systems.

In this paper, we will use CG MD to simulate different systems consisting of liposomes and flat bilayers. To assess the effect of composition and the curvature, permeability through liposomes with different lipid types (Figure 1) and sizes (Figure 2) will be compared to the permeability of flat bilayers with similar composition. Both neutral and deprotonated FAs were simulated to have a comprehensive view of their effect. To quantify the permeability, the counting crossings method was applied, which involves tallying the number of crossings that the permeants make through the membrane. Besides the permeability, the structural properties of the flat bilayers and liposomes will also be measured such as APL and membrane thickness.

METHODS

Membrane Permeability from the Counting Crossings Method. To calculate the permeability P for a flat membrane, the same method will be used as in ref 47. The permeability is defined as the ratio of the steady-state net permeant flux J through the membrane, in units of number per time per area and the concentration gradient Δc that is set over the membrane[47]

$$P = \frac{J}{\Delta c} \tag{1}$$

Rather than imposing a steady-state condition in the simulation, the counting crossings method can be used to compute P from a standard equilibrium simulation.[47−50] The bidirectional flux $|J_{\leftarrow}| + |J_{\rightarrow}|$ and the reference concentration c_{ref} in the water phase on either side of the membrane should be determined. Here, the bidirectional flux can be calculated by counting the number of complete crossings n_{cross} through the membrane with cross section area σ in a simulation time T_{sim} of an equilibrium MD simulation, in the absence of a concentration gradient. The permeability of a flat membrane then follows from[51]

$$P = \frac{|J_{\longleftarrow}| + |J_{\longrightarrow}|}{2c_{\text{ref}}} = \frac{n_{\text{cross}}}{2c_{\text{ref}}T_{\text{sim}}\sigma} \tag{2}$$

For curved membranes, the counting crossing method needs to be adapted. The cross-sectional areas on both sides of a flat membrane are equal, while for a liposome, these areas depend on the radial distance r from the liposome's center. Therefore, in a recent paper, we proposed a new definition for the permeability of spherically shaped membranes.[52]

In a long equilibrium MD simulation with a time of T_{sim}, the number of full crossings of the permeants to the inside n_{entr} and to the outside n_{esc} of the liposome should be the same, so $n_{\text{entr}} \approx n_{\text{esc}}$. However, with the cross-sectional areas being dependent on r, the corresponding fluxes are different. The flux of entering permeants ($J_{\text{entr}} < 0$) is measured at the liposome's inner radius r_1 with the cross-section area $\sigma_1 = 4\pi r1^2$

$$|J_{\text{entr}}| = \frac{n_{\text{entr}}}{T_{\text{sim}}\sigma_1} \tag{3}$$

Similarly, the flux of escaping permeants ($J_{\text{esc}} > 0$) reaching the liposome's outer surface at r_2 with area $\sigma_2 = 4\pi r2^2$ is given by

$$J_{\text{esc}} = \frac{n_{\text{esc}}}{T_{\text{sim}}\sigma_2} \tag{4}$$

The associated entrance and escape permeabilities (eq 1) also differ from one another

Table 1. Detailed Description of Simulated Systems Containing a Flat Bilayer (F)[a]

name	system types	lipid composition (%)	lipid lipids	# of CG beads	# of water ions	# of (Å)	h
1	F	DPPC	100	256	2504	29	40.2
2	F-5C10	DPPC/C10	95:5	280	2753	32	40.1
3	F-10C10		90:10	260	2575	30	39.9
4	F-20C10		80:20	250	2491	30	39.3
5	F-30C10		70:30	260	2640	32	38.7
6	F-5C14	DPPC/C14	95:5	280	2753	32	40.1
7	F-10C14		90:10	260	2575	30	40.1
8	F-20C14		80:20	250	2491	30	39.8
9	F-30C14		70:30	260	2640	32	39.3
10	F-10Ch	DPPC/Chol	90:10	260	2452	28	41.2
11	F-10Ch-10C10	DPPC/Chol/C10	80:10:10	260	2498	29	41.0
12	F-10Ch-10C14	DPPC/Chol/C14	80:10:10	260	2498	29	40.9

[a] Each system contained 20 N0 permeants. FAs are neutral. h is the membrane thickness between PO4 beads (region 2, see section Analysis of MD Trajectories). The number of ions column refers to both the number of Na^+ ions and the number of Cl^- ions. Details of other flat bilayer systems can be found in Supporting Information.

$$P_{\mathrm{entr}} = \frac{|J_{\mathrm{entr}}|}{c_{\mathrm{out}}} \tag{5}$$

$$P_{\mathrm{esc}} = \frac{J_{\mathrm{esc}}}{c_{\mathrm{in}}} \tag{6}$$

where c_{in} and c_{out} are the reference concentrations inside and outside the liposome, as indicated in Figure 2.

To define a single value for the liposome permeability, the Smoluchowski equation, often referred to as the inhomogeneous diffusion solubility model,[53] was first solved for the one-dimensional transport along the radial direction r under steady-state conditions for the permeant concentration c ($\partial c/\partial t = 0$).[52] This gave us a permeability $P(r)$ in the radial direction

$$\frac{1}{P(r)} = r^2 e^{-\beta F_{\mathrm{ref}}} \int_{r_1}^{r_2} \frac{1}{r'^2 D(r') e^{-\beta F(r')}} \mathrm{d}r' \tag{7}$$

where $F(r)$ is the free energy profile, $D(r)$ is the diffusivity in the radial direction, and F_{ref} is the free energy in the reference region, which is located in the water phase inside or outside the liposome. Two examples of free energy profiles are shown in Figure 3. By comparing P of an imaginary flat membrane with P_{entr} and P_{esc} of an imaginary liposome in a completely homogeneous simulation box, we could define the liposome permeability as

$$P^* \equiv \sqrt{P_{\mathrm{entr}} P_{\mathrm{esc}}} \tag{8}$$

which is the geometric mean of the escape and entrance permeabilities. This geometric mean can also be given a physical interpretation, as P^* is the average value of $P(r)$ (eq 7) over the membrane thickness h.[52]

The reported permeabilities in this article are all based on the counting method, computed with eq 2 for flat membranes, eqs 3–6 for P_{entr} and P_{esc} of liposomes, and eq 8 for liposome permeability P^*.

Selection of Systems. MD simulations were run for 34 systems containing a flat bilayer (label F in the name) and 28 systems containing a liposome (label L in the name) with various lipid compositions. The sizes of the liposomes (Figure 2) were chosen to be approximately 50, 100, and 130 Å to be able to assess the curvature effect on the permeability while avoiding a very large system with a limit for the simulation time. Liposomes in drug delivery experiments are often larger and will exhibit hence less curvature effects. We chose to investigate highly curved membranes to make the curvature effect as prominent as possible. Coarse graining was applied to reduce the computational cost of the simulations by mapping every few atoms of every molecule to one bead.[54,55] All simulated systems were composed of a membrane, 20 CG beads as permeants, water, and 0.15 M sodium chloride. Various compositions of six lipid types (Figure 1) were included to examine their effect on the permeability: DPPC, cholesterol (Ch, Chol), C10, C14, deprotonated capric acid (C10-n), and deprotonated myristic acid (C14-n). DPPC was chosen as phosphatidylcholines are the most frequently used phospholipids in liposome preparation.[56] The deprotonated FAs (suffix "-n" refers to negative charge) were simulated to investigate the effect of the FAs' dissociation. While recently a titratable Martini force field was developed,[57] which would allow the simulation to run at constant pH, the accuracy of the pK_a for the FAs is still uncertain for these CG beads. Therefore, the FAs in a system are either neutral or all deprotonated.

Based on a study of the sampling efficiency of the counting crossings method,[47] we selected two CG beads: N0 with more outspoken free energy wells in the headgroup region and Na with a higher barrier at the membrane center (Figure 3). They were chosen to assess the effect of different free energy profiles on the permeability. N0 and Na are CG beads of the Martini force field, with intermediate polar character, a radius of 0.23 nm, zero charge, and a mass of 72 amu. The beads do not correspond to a specific molecular structure but can match several chemical compounds. Na is more polar and a hydrogen acceptor, and in combination with the free energy well and higher barrier barrier, it bears a resemblance to molecules such as ester, ether, and ethyl methyl ether. N is less polar and not a strong hydrogen acceptor nor hydrogen donor, and it shares similarities with, e.g., trimethylamine. The first series of simulations were 12 flat bilayers (Table 1) with the 20 N0 permeants and neutral FAs. Similarly, the second series of 12 flat bilayers was performed with the 20 Na permeants. The third series of 10 flat bilayers was again done with the N0 permeants, but all FAs were deprotonated. The detailed description of the last two series is provided in the Supporting Information.

Table 2. Detailed Description of Simulated Systems Containing a Liposome (L)[a]

	system name	lipid types	lipid comp. (%)	# of lipids in	# of lipids out	# of water CG beads	# of ions	r_1 (Å)	r_2 (Å)	h (Å)	A^* (Å^2)
1	L_{50}	DPPC	100	124	394	54,507	603	20.7	56.3	35.6	66.3
2	L_{100}	DPPC	100	1097	1784	185,289	2064	67.7	106.4	38.7	64.6
3	L_{130}	DPPC	100	2092	2992	317,684	3555	96.1	135.0	38.9	65.0
4	L-10C10	DPPC/C10	90:10	113	398	76,779	842	19.3	54.6	35.3	62.0
5	L-10C14	DPPC/C14	90:10	124	387	76,779	842	19.6	54.8	35.2	62.2
6	L-10Ch	DPPC/Chol	90:10	145	400	76,608	842	21.0	56.3	35.3	60.8
7	L-20Ch		80:20	123	451	76,600	842	21.1	55.3	34.2	61.3
8	L-10Ch-10C10	DPPC/Chol/C10	80:10:10	142	396	76,730	842	18.6	54.2	35.6	53.6
9	L-20Ch-20C10		60:20:20	144	418	78,207	842	17.1	52.1	35.0	45.3
10	L-10Ch-10C14	DPPC/Chol/C14	80:10:10	147	391	76,730	842	19.0	54.4	35.4	53.1
11	L-20Ch-20C14		60:20:20	148	414	78,207	842	17.3	52.6	35.3	45.4

[a] L_{50}, L_{100}, and L_{130} are pure DPPC liposomes with a radius of 50, 100, and 130 Å, respectively. Other liposomes have a radius of 50 Å. FAs are neutral. The systems include 20 N0 permeants. h is the membrane thickness between PO4 beads (region 2, see sec. Analysis of MD Trajectories). The number of ions column refers to both the number of Na^+ ions and the number of Cl^- ions. Details of other liposome systems can be found in Supporting Information.

For the liposomes, a first series of 11 systems (Table 2) contained N0 permeants and neutral FAs. All liposomes have a radius of approximately 50 Å, except for the L_{100} system and the L_{130} system. The second series of 11 systems contained Na permeants. The third series of 6 liposomes contained the N0 permeants, but all FAs were deprotonated. The detailed description of the last two series is outlined in Supporting Information. The lipid composition varied from 100% DPPC down to 60% DPPC. The composition and membrane thickness h of all 62 systems can be found in Tables 1 and 2 and the Supporting Information.

An important aspect is whether the membrane is in the liquid-disordered (L_α, L_d) phase or in a gel (L_β) or liquid-ordered phase (L_o). A phase transition can drastically change the APL and other structural and dynamical properties of the membrane, thus likely affecting the permeability as well. This will be discussed when assessing the structural parameters in the Results and Discussion section.

Computational Details. The same protocol as in our recent paper[52] was followed in this work. The systems were simulated using GROMACS-2021.4.[58] Using CHARMM-GUI, the initial structures of the membranes were prepared.[59−62] The Martini 2 force field was used.[63] The reaction-field approach was used to calculate the Coulombic interactions.[64] With the potential-shift-Verlet modifiers, the Coulombic and van der Waals potentials were shifted to zero at a cutoff of 1.1 nm. The neighbor list was updated using the Verlet neighbor search algorithm with the buffer tolerance set to 0.005 kJ mol^{-1} ps^{-1}, which leads to neighbor list cutoffs of about 1.2 nm for various systems. The equation of motion was integrated using the leapfrog integrator with a time step of 20 fs. A temperature of 323 K and a pressure of 1 bar were set for all of the systems. A velocity rescale thermostat coupling was implemented for the entire system as a whole, utilizing a coupling constant of 1.0 ps.[65] The Parrinello−Rahman barostat was used with a coupling constant of 12 ps. For systems with a flat bilayer and a liposome, a semi-isotropic and isotropic isothermal compressibility of 3×10^{-4} and 4.5×10^{-5} bar^{-1} was employed, respectively. At every 100 time steps, the center of mass motion of the system was removed, and periodic boundary conditions were applied in all directions (x, y, and z). Systems were first energy minimized, and next, they were equilibrated by applying the *isothermal−isobaric* (*NPT*) ensemble for 100 ns. Some of the liposome systems required a longer equilibration run to let the water density inside and outside the liposome equilibrate through water membrane crossings. The equilibration times are reported in Supporting Information. The production run was 1 μs of NPT simulation, and the coordinates were stored every 20 ps. For the smallest pure DPPC liposome with N0 or Na beads (L_{50}), as the crossing statistics were not good enough (small water phase inside the liposome), the simulation was extended to 5 μs.

Analysis of MD Trajectories. For flat membranes, the center of the membrane is first computed by averaging the z-coordinate of the DPPC beads, and the trajectories are shifted as a whole along the z-axis to let the center of mass of the membrane coincide with the $z = 0$ plane. Next, periodic boundary conditions are applied to let all coordinates fall in the range of $-L(t)/2$ to $L(t)/2$, where $L(t)$ is the instantaneous box dimension in the z-direction. For liposomes, the center of mass of the DPPC beads is computed as well, and the whole box is shifted to let it coincide with the origin. Periodic boundary conditions are applied in all 3 dimensions, such that all coordinates fall in the range of $-L_\mu(t)/2$ to $L_\mu(t)/2$, where $\mu = x, y$, and z.

The membrane thickness of flat membranes is computed as the distance between the average z-position of the PO4 beads in the upper leaflet and the average z-position of the PO4 beads in the lower leaflet, which is averaged over the trajectory. To compute the properties of systems with liposomes, a few additional settings need to be specified. We considered two radii, the inner radius r_1 and the outer radius r_2 ($r_1 < r_2$, shown in Figure 2). For a liposome, the membrane is centered around $r = 0$, and the two average radial distances of the PO4 beads in the inner and outer layers are used as the two radii r_1 and r_2, which determine the thickness $h = r_2 - r_1$. This is in line with the approach followed by Risselada and Marrink for pure DPPC CG liposomes.[43]

To determine the APL of a liposome, the cross-sectional areas of the inside ($4\pi r_1^2$) or outside ($4\pi r_2^2$) leaflets were divided by the number of molecules (DPPC, FAs, and cholesterol) in that leaflet, giving the values A_{in} and A_{out}, respectively. The number of molecules in the inner or outer leaflet of the liposome was determined by counting all molecules below or above the mid-radius values of r_1 and r_2, respectively. In order to be able to compare the flat and the liposome bilayers, $A^* = \sqrt{A_{\text{in}}A_{\text{out}}}$ was computed, similar to eq 8.[52]

To be more precise in the calculation of the reference permeant concentration c_{ref} inside or outside the liposomes, the r_1 and r_2 radii were not used. Instead, based on the histogram of water bead positions in every system, the radius in which the water phase separated completely from the lipid phase was applied to compute c_{ref}. The number of permeant molecules in these regions was counted and divided by the volume of the relevant region to derive the concentration. The Supporting Information reports the specific cutoff values that define these regions.

For the N0 and Na permeants, the membrane thickness h covers the central membrane part where the highest free energy barrier (see the following) for these two permeants is located. However, besides the free energy barrier at the membrane center, the N0 and Na permeants have additional free energy barriers and wells. A complete membrane crossing means that a permeant is first on one side of the membrane, and next it crosses the membrane and emerges on the other side of the membrane. The dividing surfaces to detect a membrane crossing are a choice in simulations.[66] The thickness h does not encompass the additional free energy barriers and wells at $|z| = 2.5$ nm, so $|z| = h/2$ is a nonideal dividing surface for the N0 and Na permeants. Therefore, another dividing surface is introduced. This extended membrane thickness is defined for the N0 and Na permeants based on visual inspection where the free energy curves of the permeants flatten out: we extend h by 0.8 nm on both sides. The extended membrane thickness is called region 1 (see Figure 2) and is relevant for full membrane crossings. For a flat membrane, region 1 ranges from $-h/2 - 0.8$ nm to $h/2 + 0.8$ nm. For a liposome, region 1 is defined by two new radii, $r_1' = r_1 - 0.8$ nm and $r_2' = r_2 + 0.8$ nm. These radii have also been utilized to calculate the crossing areas σ_1' and σ_2' to be used in eqs 3 and 4 when computing the N0 or Na permeability in the liposome systems.

For water as a permeant, membrane thickness h was used to determine the number of full membrane crossings n_{cross} of water molecules. Given the very high free energy barrier for water permeation through the hydrophobic phase, the water permeability is insensitive to the exact location of the dividing surfaces.[66,67] We refer to this as region 2 (see Figure 2), the region extending over the membrane thickness h. For a flat membrane, the dividing surfaces for water crossings are located at $z = -h/2$ and $z = h/2$, while for a liposome, the dividing surfaces are located at the $r = r_1$ and $r = r_2$ radii. (Note that membrane thickness h in earlier papers by the authors[67,68] refers to region 1.)

In summary, water permeability is based on region 2, N0 permeability on region 1, and Na permeability on region 1, unless specified differently. The error bars or shaded gray areas in the figures of the main document and Supporting Information are computed as two standard errors, assuming the observed crossings follow a Poisson process.[50,66]

Histograms of the permeants (water, N0, and Na beads) and of the DPPC CG beads are generated as follows. For flat membranes, the z-coordinates were normalized with the instantaneous box $L(t)$ dimension in the z-direction, giving values in the -0.5 to 0.5 interval. A histogram of these normalized z-coordinates is computed by using 200 bins. The histogram is then scaled back with the average box length $\langle L \rangle$ in the z-direction, giving values $-\langle L \rangle/2$ to $\langle L \rangle/2$. Free energy profiles of the permeants are computed from this histogram [hist(z)] using $F(z) = -k_{\text{B}}T \ln[\text{hist}(z)]$, and the profiles are shifted as a whole to make $F(z) = 0$ in the water phase. For liposomes, the distance of the relevant beads from the liposome center, which coincides with the origin, is computed at every snapshot. A histogram hist(r) is constructed from these r-distances using 200 bins, and the free energy is constructed using $F(r) = -k_{\text{B}}T\{\ln[\text{hist}(r)] - 2r\}$ and shifting to make $F(r) = 0$ in the water phase. The additional term $-2r$ comes from the Jacobian factor $4\pi r^2$, which lets us interpret $F(r)$ as a measure for solubility. For both flat membranes and liposomes, a density distribution of DPPC beads along z or r is obtained by normalizing a histogram of the DPPC bead positions hist(z) or hist(r)/r^2 by the total count in the histogram.

RESULTS AND DISCUSSION

Area per Lipid. Figure 4 illustrates how FAs and cholesterol affect the APL of the flat membrane. A pure DPPC flat membrane has an APL of 63.6 Å^2, which agrees well with experimental values at a temperature of 323 K.[69] Flat bilayers containing neutral FAs exhibit a smaller APL, for instance, with F-10C10 and F-10C14 showing decreases of 6% each. This is in agreement with an experimental study reporting that the APL decreases in the presence of saturated long-chain FAs, such as stearic acid, in a DPPC monolayer.[70] They attributed this to the impact of neutral FAs, which cause the DPPC molecules to separate and "dilute", thus reducing the electrostatic repulsion between their head groups.

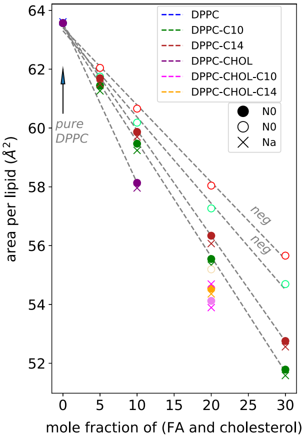

Figure 4. APL of flat bilayers as a function of the molar fraction of FAs and cholesterol combined. Symbols are circles for systems containing N0 and crosses for systems containing Na. Full (dark) and empty (lighter) circles show systems with neutral and deprotonated FAs, respectively. Gray dashed lines are linear regression fits.

The incorporation of cholesterol into the membrane also results in the strongest reduction of APL, from 63.6 to 58.1 Å^2 (a decrease of about 9% for F-10Ch). Similar trends were reported in simulation studies for different phospholipid molecules, with a 13 to 21% decrease in APL by incorporating 10 to 30% cholesterol in a lipid membrane.[24,71] In all of our systems, the type of permeants (N0 or Na) does not significantly affect the membrane's APL (tables in Supporting Information), indicating that the low concentration of permeants does not disturb the membrane structure. Moreover, in systems containing both FAs and cholesterol, the drop in APL is even more substantial compared to systems containing cholesterol alone.

A similar trend of APL reduction is noticeable in systems with deprotonated FAs but less pronounced (a decrease of 5% for both F-10C10-n and F-10C14-n and stronger with higher FA concentration) than that with the neutral FAs. The deprotonated FA charges can cause repulsive forces, increasing the distance between FAs and counteracting the "diluting" effect of FAs which was mentioned earlier in this section. Interestingly, a recent study by Larsson et al. investigated the effect of C10-n on the APL of a POPC membrane using an all-atom force field at 310.15 K.[41] The APL was also computed differently, dividing the simulation box by the number of phospholipid molecules without counting the number of C10-n, so the trends in the APL cannot be compared directly with our results. They found a modest increase of about 3% in the area per POPC molecule caused by the incorporation of 10% C10-n. The authors attributed this rise to the repulsion between the negative charges of C10-n.

The APL reduction caused by FAs or cholesterol can also be understood by looking at the small size of the FAs molecules, which have just one tail, compared to the DPPC molecules with two tails. Moreover, the shorter chain FA, C10 consisting of three CG beads, also has a larger impact on reducing APL than the longer chain FA, C14 with four beads. The dependence of the APL on the FA concentration is approximately linear in Figure 4. By fitting the slope of the graphs, an estimate of the area per molecule type could be estimated (values in Supporting Information), similarly to the ideal mixing fitting in monolayers (see, e.g., ref 70). In terms of molecule size, this gives the ordering DPPC > C14-*n* > C10-*n* > C14 > C10 > Chol, indicating that neutral FAs and cholesterol can indeed modify the membrane's structure more strongly than the deprotonated FAs.

Next, the curved membranes are discussed based on the APL of the inner (A_{in}) and the outer (A_{out}) leaflets of the liposome bilayer, as shown in Figure 5. A decrease in the liposome curvature leads to a reduction in the APL of the outer layer, while the APL of the inner layer increases (Figure 5a). This effect has also been observed by Risselada and Marrink, and it can be explained by the spherical shape of liposomes, which causes contradictory effects on their inner (concave) and outer (convex) layers.[43] In liposomes, the lipid head groups in the outer layer move further apart, while those in the inner layer move closer together.[72] Consequently, the outer leaflet features a less tightly packed arrangement of lipids, while the inner leaflet is characterized by a denser packing of lipids compared to a flat membrane.[43,44,46] In the pure DPPC bilayers (Figure 5a), the APL in both leaflets gradually approaches that of a flat bilayer with zero curvature (63.6 Å, system F). Nevertheless, the A_{in} and A_{out} values for the largest simulated liposome, L_{130}, are still noticeably different from the flat bilayer's APL. As seen from the geometric mean of A_{in} and A_{out}, denoted as A^*, curvature causes an increase of at most 4% for the pure DPPC bilayers, from the flat bilayer value (63.6 Å, system F) to the curved membrane (A^* = 66.3 Å, system L_{50}).

The membrane composition (Figure 5b) is varied in the highly curved liposomes with a radius of 50 Å. Similar to flat bilayers, both A_{in} and A_{out} tend to decrease in the presence of neutral FAs or cholesterol and particularly in systems containing both (e.g., a drop of 48% in A_{in} and 18% in A_{out} for L-20Ch-20C14 compared to L_{50}). The impact of neutral FAs on the APL of highly curved liposomes is here comparable to that of flat bilayers of equivalent composition, resulting in decreases of 5 and 7% in A_{in} and 8 and 3% in A_{out} for L-10C10 and L-10C14, respectively.

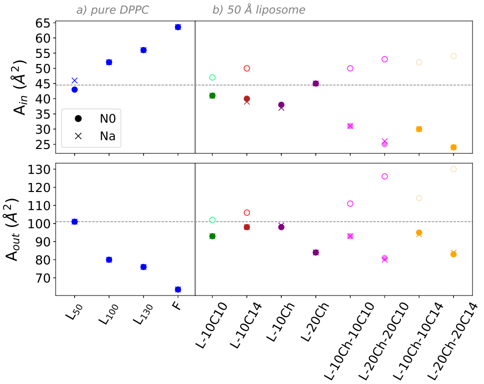

Figure 5. APL of liposomes. A_{in} and A_{out} represent the APL of the inner and outer layers of the liposomes, respectively. Symbols are circles for systems containing N0 and crosses for systems containing Na. The symbol color is according to the legend of Figure 4. Full and open circles are used for systems with neutral and deprotonated FAs, respectively. The same colors as in Figure 4 are used. (a) Comparison of pure DPPC membranes with varying curvature. (b) Comparison of liposomes with a radius of 50 Å with varying composition. The dashed horizontal line shows APL for pure DPPC liposome L_{50}, averaged over the systems containing N0 and Na.

In contrast, deprotonated FAs have the opposite effect, causing significant increases of almost 16 and 5% in A_{in} and A_{out}, respectively, for L-10C14-n, compared to the pure DPPC composition. The results suggest that the repulsive forces of deprotonated FAs have a stronger effect on curved membranes than on flat membranes: the deprotonated FAs not only fail to decrease the APL but actually increase it. Our findings illustrate that the APL is modified by both composition and curvature, but APL changes induced by composition can be much stronger than the curvature effect when considering A^*, especially for high concentrations of cholesterol or in small liposomes.

Membrane DPPC Distribution and Thickness. Figure 6a shows the probability distribution of membranes composed of pure DPPC with varying curvature. Among these membranes, L_{50}, with the highest curvature, displays the least symmetric distribution with a higher probability in the outer layer. The observed asymmetry can be explained by the densely packed and disordered inner layer of L_{50}. In addition to having the least symmetric probability profile, L_{50} also has the smallest thickness (35.6 Å) compared to other pure DPPC membranes (Tables 1 and 2). The phenomenon of decreasing membrane thickness with increasing curvature was also observed by Risselada and Marrink, who studied the impact of curvature on lipid packing and dynamics of DPPC liposomes using CG MD.[43]

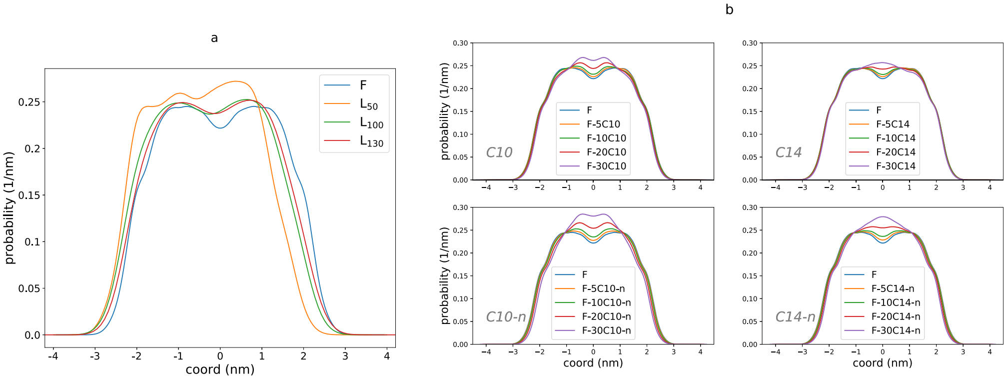

Figure 6. Probability distribution of the DPPC lipid in different systems. (a) Effect of the curvature on pure DPPC bilayers. Profiles have been shifted to center the span of the histograms around 0 to facilitate comparison. (b) Effect of composition on flat bilayers. The upper and lower plots show the probability distribution of the DPPC in the membrane including neutral and deprotonated FAs, respectively.

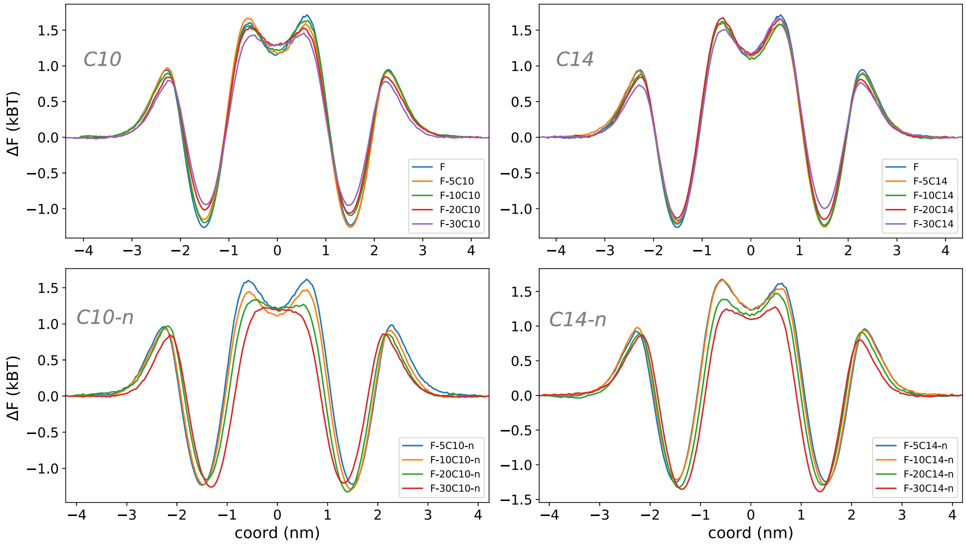

Figure 7. Effect of the composition on the free energy profile of N0 permeants in flat bilayers, in comparison to the pure DPPC membrane (F). The membranes include C10 (left) or C14 (right) FAs, either in neutral (top) or deprotonated (bottom, label "-n") state. The legend specifies the mole fraction of FAs, e.g., F-5C10 contains 5% of C10.

Figure 6b shows the impact of FAs on the membrane structure of the flat bilayers. The presence of FAs results in a more compact membrane structure with an increasing DPPC probability near the center of the membrane (Figure 6b). Simultaneously, the thickness is reduced (Table 1). This compactness and reduced thickness stem from a decrease in the space between the tails of the upper and lower leaflets in the central region of the membrane. For instance, the inclusion of 30% neutral C10 and C14 to the flat membrane leads to a decrease in thickness from 40.2 to 38.7 and 39.3 Å, respectively. The reduced thickness is particularly evident in systems with deprotonated FAs, with the smallest thickness of 37.5 Å observed for F-30C10-n (see Supporting Information). This reduction was also seen for C10-n's effect on a flat POPC membrane in a combined all-atom and CG computational study by Larsson and coauthors,[41] where it was reported that by including 10% C10-n in the membrane, the membrane thickness decreased by about 1%. They associated this reduction to the C10-n tendency to stay near the headgroup region, pushing the POPC molecules apart and disrupting the lipid tail packing. They also showed that neutral C10 slightly increased the thickness of the POPC membrane. This increase was attributed to the acyl chain order parameter and the neutral C10 tendency to stay deeper in the POPC membrane.

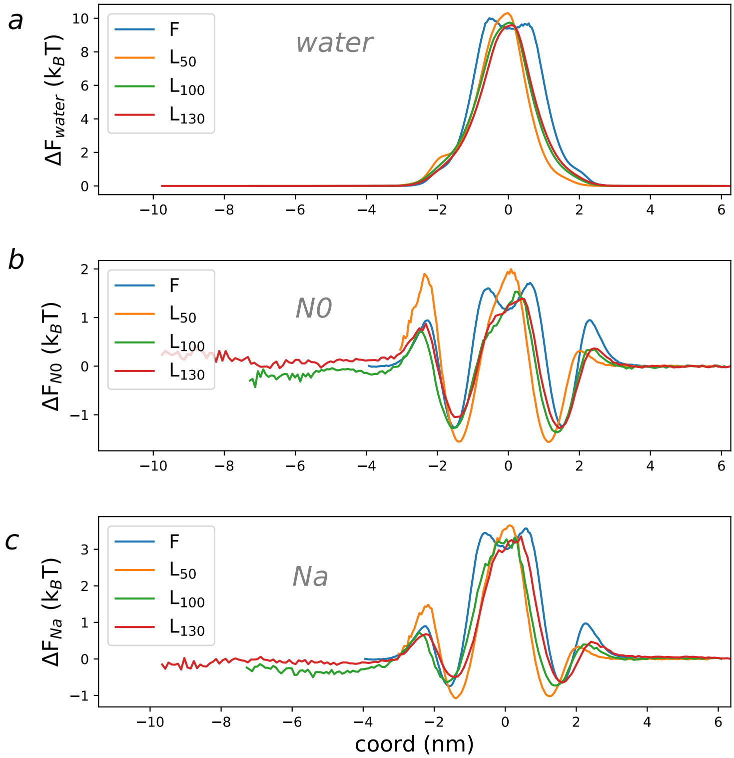

Figure 8. Free energy profile of permeants (water, N0, and Na) as a function of membrane coordinate (z-coordinate or shifted radial coordinate) in systems with pure DPPC to see the curvature effect. The top figure plots are based on the same membrane systems as those in the middle figure. Profiles have been shifted to center the span of the DPPC histograms around 0 to facilitate comparison (similar to Figure 6a).

In contrast, in our simulations of DPPC membranes, C10 and C10-n are embedded at similar depths. This means that the specific modifying effect of a FA depends not only on the chosen FA but also on its interaction with the specific phospholipid type.

Free Energy of Permeants. The effect of FAs on the N0 permeants is illustrated in Figure 7 for flat bilayers. The lowest point in the free energy well is situated between 1 and 2 nm from the center of the membrane. Conversely, the highest point in the free energy barrier is positioned in the middle of the membrane with a distance of less than 1 nm from the center. Neutral FAs (upper plots) primarily affect the headgroup region, resulting in a smaller free energy well, which facilitates the escape of N0 permeants from the membrane. In contrast, deprotonated FAs (lower plots) reduce the free energy barrier in the bilayer center significantly, and they may slightly reduce the barrier in the headgroup region. As suggested and investigated by another group, these differences could arise from the distinct preferences of neutral and deprotonated FAs to stay near the tail and headgroup regions, respectively.[40] Consequently, incorporating FAs in the system can modify the solubility of permeant N0 in the headgroup or tail regions of the membrane. The general effect could be framed as a “smoothing” of the free energy profile with less deep wells and/or lower barriers. These observations suggest that including FAs in the system could facilitate permeation.

Figure 8 depicts how the membrane curvature impacts the free energy profile of three different permeants in the membrane. Every permeant encounters a free energy barrier positioned in the center of the membrane. As expected, water does not exhibit any distinct free energy well, whereas N0 and Na experience a free energy well around 1.7 nm from the membrane center. Moreover, these two permeants must surmount an additional free energy barrier situated at a distance of approximately 2.5 nm from the membrane center. For N0 and Na (Figure 8b,c), the curvature reduces the free energy barriers near the headgroup region for L_{100} and L_{130} compared to the flat bilayer. However, L_{50} exhibits an opposite trend, with deeper free energy wells and a larger free energy barrier in the inner leaflet (left part of the axis) due to the confinement of the interior region. For water (Figure 8a), the permeation barrier is situated in the hydrophobic part of the bilayer, as expected.[66] Although the curvature does not significantly alter the height of the free energy barrier, the extent of the barrier decreases with curvature. The reduced barrier width is in accordance with the smaller membrane thickness h of curved membranes (Table 2) compared to flat

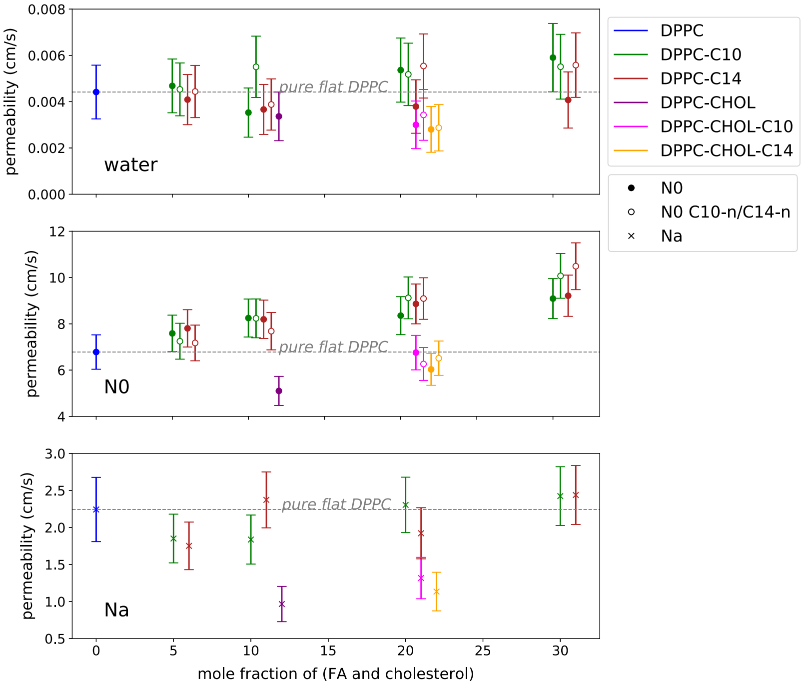

Figure 9. Effect of the composition on the permeability of permeants through flat membranes. The permeants are water, N0, and Na. For better visibility, data points have been shifted. Full and empty circles show the systems including neutral and deprotonated FAs, respectively.

membranes (Table 1). Another cause for an apparent reduction in thickness could be undulations of the large membrane patches in the liposome systems.[67] Some analysis packages have been developed recently to measure APL and membrane thickness despite fluctuations, e.g., SuaVE[73,74] and LipidDyn.[75] We computed a set of parameters with the SuaVE package (results in Supporting Information) and found that this more advanced tool confirms that the thickness does decrease with curvature. Moreover, the free energy profiles for L_{100} and L_{130} reveal a good agreement with the published results of an all-atom simulation study on the impact of curvature on water permeability by Yesylevskyy et al.[46] This study found that curvature decreases the energy barrier of water permeation through dioleoylphosphatidylcholine (DOPC) membranes, a result that is consistent with our observations for L_{100} and L_{130}. However, the barrier for L_{50} is not reduced in our simulations. This may be due to the highly decreased membrane thickness and more densely packed membrane in this system (see previous subsections). Regardless, we found that the width of the free energy profile was reduced by the curvature in the liposomes, which may facilitate water permeation through the membrane. The permeability values will be computed explicitly in the next subsection to verify this hypothesis.

Permeability. After a thorough analysis of the structural membrane characteristics in the previous section, this section investigates the dynamics and kinetics of membrane permeation. We examine how the curvature and composition of the membrane affect the permeability of water, N0, and Na. To compare the 62 systems, this is done step by step: first focusing on flat membranes and next on simple pure DPPC membranes, and in the last two steps, the various curvatures and compositions are combined.

Composition Effect in Flat Membranes. First, the composition effect on permeability is studied for flat membranes (Figure 9). Overall, changes in the membrane composition have a greater impact on the permeability of N0 than that of water. For Na, changes in permeability are less clear due to the large error bars, which are attributed to the high energy barrier for Na (Figure 7) and poor statistics resulting from a low number of crossings. Similarly, for water, the permeabilities have large error bars because the number of water crossings in the counting method was low, which is expected for a highly hydrophilic compound. As a result, comparing the water permeability values in all systems to these high error bars is not applicable. Instead, we compare these values to experimental values. Generally, water permeability values in this figure are distributed in the range of 28×10^{-4} cm/s to 59×10^{-4} cm/s, with a value of almost 44×10^{-4} cm/s for the permeability through the pure DPPC flat bilayer (system F). This value is in good agreement with those of other experimental and simulation works. The water permeability of pure DPPC was reported as 17×10^{-4} at 323 K by Winter et al., and Yesylevskyy et al. presented a permeability range of 2.5×10^{-4} to 3.6×10^{-4} for pure DPPC at the same temperature. Additionally, Carruthers and

Melchior reported a value of 2.04 × 10^{-4} for water permeability through egg PC at 283 K.[21,45,46,76,77]

For N0, the addition of FAs C10 and C14 in the membrane gradually increases the permeability of N0, with the highest value observed for the system with 30% C14-n, resulting in an almost 36% increase in permeability. This effect of fatty acids on the permeability was also seen in Figure 7, with neutral and deprotonated FAs lowering the free energy barrier for the permeant N0 in different regions of the membrane.

Arouri and Mouritsen (2013) suggested that the increased permeability may be due to the noncylindrical shape of FAs, which imposes a curvature stress in the membrane and alters the lateral pressure profile.[78] As a result, defects and pores created by these molecules can destabilize the membrane and increase its permeability. Another study by Via et al. (2020) conducted a CG MD simulation to investigate the permeation of cell-penetrating peptide cargo complexes through a DOPC lipid membrane.[79] Their results show that the presence of deprotonated palmitic acid (C16), a longer FA, enhances the permeability of these cargos, likely due to its size, shape, and high packing freedom. The results by Arouri et al. and Via et al. are consistent with our findings as they also suggest that FAs can increase permeability.

The presence of cholesterol has the most significant impact on the permeability as the inclusion of only 10% cholesterol can already reduce the permeability by approximately 25% and 57% for N0 and Na, respectively (dark purple in Figure 9). This result is in agreement with work by Pias and co-workers, who observed a reduction of almost 10% in oxygen permeability through a POPC membrane when 12.5% cholesterol was included.[32] It attributed to cholesterol's effect on decreasing oxygen solubility in the membrane and possibly diminishing the volume of oxygen that can be transmitted laterally within the membrane. This decrease in the solubility of the permeants was also observed in our systems containing cholesterol, with an increase in the free energy barrier of the permeant in the center of the bilayer (see Supporting Information).

Investigating the potential for cholesterol-induced phase separation in flat membranes at 323 K, both F and F-10Chol exhibit the Lα (liquid-disordered) phase, in accordance with experiments by Chiang et al.[80] This same phase was reported by Cournia and co-workers using CG MD simulations with the same Martini force field.[81] The findings are further supported by the APL measurements of pure DPPC and DPPC-10Chol flat membranes (F and F-10Chol), which align with the values reported by Wang et al. For systems involving liposomes containing 20% cholesterol, experimental results at 323 K are inconclusive. Some references suggest the presence of either the L_α phase or a coexistence of L_α and L_d (liquid-ordered) phases.[80,82] The experimental paper by Subczynski et al. also does not provide a definitive determination of the phase at 323 K.[83]

Finally, in flat bilayers containing both FAs and cholesterol (pink or yellow in Figure 9), the N0 permeability values still decrease compared to pure DPPC but not as much as in systems with only cholesterol. The resulting permeability for these DPPC/FA/Chol membranes is a balance between two opposing effects, which come from FAs (enhancing) and cholesterol (reducing). In short, FAs, as N0 permeability enhancers, temper the action of cholesterol.

Effect of Curvature on DPPC Membranes. The effect of curvature is explored by comparing a series of pure DPPC liposomes with a flat DPPC membrane, which is the limit of an infinitely high radius. As introduced in the Methods section, liposome permeability can be characterized by the three permeabilities P_{esc}, P_{entr}, and P^* for the water permeant. Here, P_{esc} describes the escape kinetics of compounds that are initially enclosed inside the liposome, while P_{entr} describes the entrance kinetics when compounds are in the solute and penetrate toward the inside of the liposome. The value P^* serves to compare the liposome permeability with that of flat membranes.

In Figure 10, P_{esc} and P_{entr} clearly follow opposite trends: P_{esc} increases and P_{entr} decreases with increasing radius. This can be understood with a simple model. For simplicity, consider a very simple homogeneous membrane of thickness h, as in our previous theoretical paper.[52] The permeant diffusivity is assumed to be a constant D, and the membrane solubility is assumed to be identical to the water phase solubility, so the partitioning coefficient K is equal to 1. Further, it is assumed that the curvature does not change the permeation kinetics. The permeability of a flat bilayer is then given by $P_{flat} = D/h$. For a liposome with the membrane spanning between r_1 and r_2 ($r_1 \geq h$), the entrance and escape permeability are given by

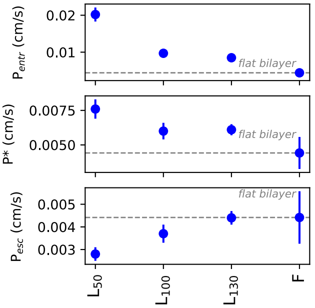

Figure 10. Water permeability in pure DPPC systems with varying curvature compared to the flat bilayer. Systems contain the permeant N0.

$$P_{entr} = \frac{D}{h}\frac{r_2}{r_1} \tag{9}$$

$$P_{esc} = \frac{D}{h}\frac{r_1}{r_2} \tag{10}$$

By substituting the flat membrane permeability and the identity $r_2 = r_1 + h$, we can recognize the behavior as a function of the factor $x = r_1/h$

$$P_{entr} = P_{flat}\left(1 + \frac{h}{r_1}\right) \tag{11}$$

$$P_{esc} = P_{flat}\frac{1}{1 + \frac{h}{r_1}} \tag{12}$$

These equations show that P_{entr} and P_{esc} have $1 + 1/x$ and $x/(1 + x)$ dependency, respectively, compared to P_{flat}.

With $x = r_1/h$, this means that P_{esc} is expected to increase, while P_{entr} is expected to decrease, with increasing radius, which is indeed clearly the case in Figure 10. (Note that the spacing on the horizontal axis in Figure 10 differs from that of the variable $x = r_1/h$.) This derivation does not include any change in the permeation kinetics yet. The dominant curvature effect on P_{entr} and P_{esc} is thus a consequence of geometrical factors involving r_1 and r_2.

Besides the geometrical effect, the curvature might also change the permeation kinetics themselves, e.g., in case the curvature loosens, the packing and permeants can pass through with lower resistance. This effect is well captured by liposome permeability P^*, which eliminates the geometrical effect. Indeed, for the theoretical simple membrane, we find that $P^* = \sqrt{P_{\text{entr}}P_{\text{esc}}} = P_{\text{flat}}$. When there are only geometrical effects, P^* is identical to that of the flat bilayer. When there are both geometrical and permeation kinetic effects, then P^* will differ from the flat bilayer. For water, P^* increases with respect to the flat membrane due to curvature, and we can conclude that curvature enhances the water permeability. For the liposome with the highest curvature, L_{50}, this enhancement amounts even to a factor of 1.7 for P^*.

The liposome with the smallest curvature, L_{130}, has a permeability of $P^* = 64 \times 10^{-4}$ cm/s, equivalent to an enhancement factor of 1.4. This indicates that L_{130} is not fully behaving as a flat membrane yet. While this could be a numerical coincidence, its P_{esc} value does become indistinguishable from the flat bilayer value (factor 1.04). This gives the impression that this large liposome already behaves similarly to the flat bilayer in terms of the escape kinetics. The curvature effect should indeed diminish with liposome size, and for escape experiments, it should be negligible for liposome sizes that are typically encountered in experimental setups and in nanosized drug delivery systems. Nevertheless, highly curved membranes may be encountered in exosomes, the caveolae, mitochondrial cristae, or membrane pearls, and one should be cautious about possible curvature effects in those systems.

While P^* is most suitable to compare liposomes with their flat counterparts, P_{entr} or P_{esc} are usually the relevant kinetic parameters to be compared with experiment.[52] For instance, consider liposomes loaded with a dye that are immersed in a dye-free solution. Over time, samples may be taken from the solution to measure the dye concentration. As the liposomes gradually release their dye load, the solution's dye concentration will gradually increase. The kinetics parameter characterizing the dye release from the liposomes is then given by the escape permeability P_{esc}. In practice, experiments encounter a distribution of liposome sizes, and it is anticipated that each of those curved membranes has a different P_{esc} value because of the curvature effect. In experimental literature, the curvature effect has, however, been neglected. Fortunately, most experimentally available liposomes are fairly large, usually around 100 nm in size (radius around 500 Å), and the curvature is likely to become negligible for these larger liposomes. For water, P^*/P_{flat} has already dropped to a factor of 1.4 for a 26 nm sized liposome (L_{130} in Figure 10). The trend suggests that experimental literature values of the curved, yet large liposomes may indeed likely be used for verification of simulation results.

Whereas water has a very large free energy barrier for permeation of about 10 k_BT, the N0 free energy profile has a smaller barrier at the membrane center of less than 2 k_BT and a mixture of well and barrier in the headgroup region. We now investigate how the curvature affects the permeability of this other type of free energy profile. Figure 11 shows the N0 permeability for pure DPPC liposomes and a pure DPPC membrane. Two permeabilities are considered, covering two different regions: region 1 covering the extended membrane thickness (radii r_1' and r_2'), and region 2 focusing on the central barrier for N0 (radii r_1 and r_2 of Table 2). Region 2 is thus smaller than region 1 (Figure 2). The results for L_{100} and L_{130} show that the N0 permeability in either region increases with curvature compared to that of the flat membrane. This increase can be attributed to the curved membrane's reduced thickness and less organized structure. As illustrated in Figure 8, increasing the curvature results in a smaller barrier in the headgroup region as well as in the center of the membrane for these liposomes. Higher curvature therefore makes permeation easier through both regions 1 and 2 for those liposomes than for a flat membrane.

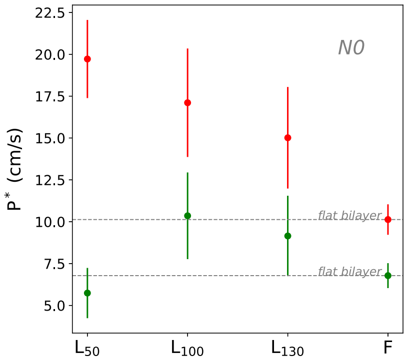

Figure 11. N0 permeability in pure DPPC systems with varying curvature compared with the flat bilayer. N0 permeability based on region 1 (green), i.e., extended membrane thickness between r_1' and r_2' or on region 2 (red), i.e., membrane thickness h between r_1 and r_2.

For L_{50}, however, we observe two opposite impacts on the N0 permeability. Permeation through the central region 2 (red) is higher for L_{50} than that for the flat membrane. Meanwhile, permeation through the entire membrane region 1 (green) is smaller for L_{50}. This is due to the shape of the N0 free energy profile (see section Free Energy of Permeants). Region 2 only covers the central free energy barrier, which is significantly narrower for L_{50} despite being slightly higher. Region 1 in addition covers the higher free energy barrier in the headgroup region of the inner leaflet (Figure 8) in this system, which is caused by the extreme confinement and tight packing of the lipid head groups in that leaflet. This makes the L_{50} permeability over region 1 an outlier in Figure 11.

Our analysis shows that the curvature may enhance the water permeability, while the curvature does not affect the N0 permeability (region 1) with statistical significance. Meanwhile, the curvature does enhance the N0 permeability of the central permeation barrier (region 2). The diversity in these observations indicates that the curvature effect may be unpredictable for other drug permeants, and new simulations would need to be performed in order to quantify the curvature for each new drug permeant of interest.

Curvature Effect on Various Membrane Compositions. Subsequently, the curvature effect was assessed not only for the

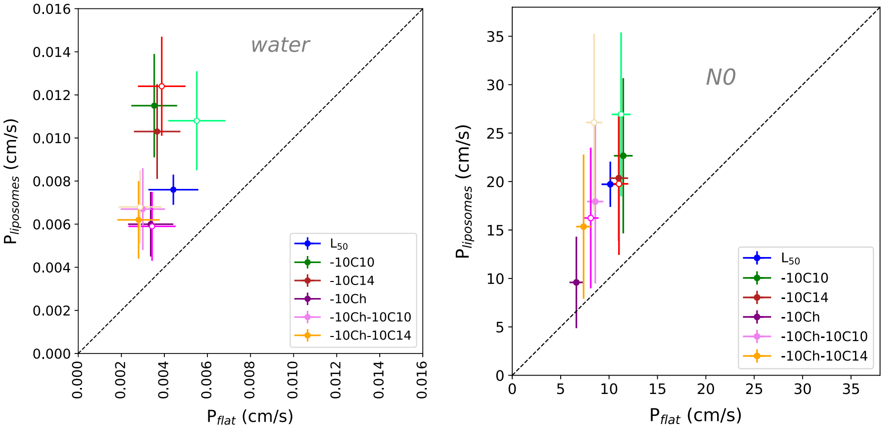

Figure 12. Permeability enhancement due to curvature. Comparison of water permeability (left) and N0 permeability (right) in flat bilayers and liposomes with a radius of 50 Å and various compositions. N0 permeability is based on region 2, i.e., membrane thickness h between r_1 and r_2. Systems contain permeant N0. Empty circles show the systems with deprotonated FAs.

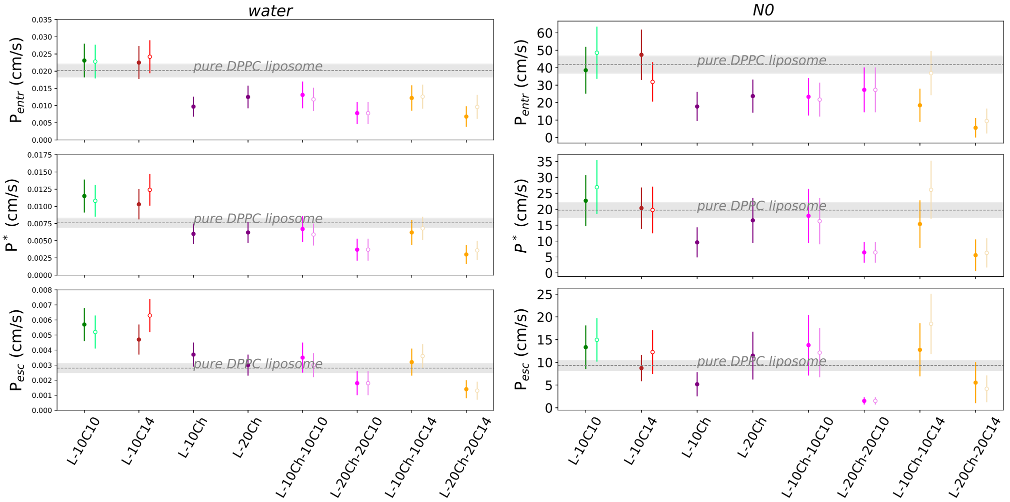

Figure 13. Effect of the composition on the permeability of water beads (left) and N0 beads (right) through the liposome bilayers. The liposomes have a radius of 50 Å and have various compositions. The permeability of the pure DPPC liposome is indicated with a gray horizontal line. Filled (dark) and open (lighter) symbols for systems with neutral or deprotonated FAs, respectively. N0 permeability is computed based on the crossings over the dominant free energy barrier, i.e., region 2 covering the membrane thickness h between r_1 and r_2. Water permeability is based on systems that include 20 N0 beads.

pure DPPC membranes but also for all other compositions. The water and N0 permeability (through region 2) are compared between liposomes with a 50 Å radius and flat membranes in Figure 12. The closer a data point lies to the diagonal, the less this membrane is affected by curvature. Both water and N0 permeabilities lie consistently above the diagonal. This means that the curvature effect for pure DPPC, which increases the permeability of water and N0 through region 2, is equally present in all systems with cholesterol and/or FAs.

In conclusion, the curvature effect makes the water and N0 (region 2) permeability for these curved multilipid membranes higher than for flat multilipid membranes with the same composition. The underlying cause of the curvature effect is a change in the membrane thickness and solubility, which is reflected by the free energy profile. An additional cause could be the mobility changes of the permeants, which would be reflected by the diffusion profile; the position-dependent diffusivity of the permeants was, however, not computed in this work.

Composition Effect on Curved Membranes. We now turn to the discussion of the effect of composition for curved membranes, making use of the liposome permeability P^*. The composition effect on the N0 permeability is investigated for small liposomes with a radius of 50 Å (Figure 13, right). Instead of covering the extended membrane thickness, the permeability is based on the region between the average PO4 positions in the two leaflets, i.e., on region 2. From Figure 7, this means that the focus is put on the highest free energy barrier at the center of the membrane, while the smaller barriers for N0 in the headgroup region are not considered. Concerning the effect of cholesterol, a trend similar to that of the flat bilayers (Figure 9) is observed here in the plot of the small liposomes (Figure 13). Specifically, the inclusion of 10% cholesterol in the membrane (L-10Ch) can decrease P^* by 28%, which is less than what was observed for the flat membrane (F-10Ch). Moreover, for curved membranes containing 10% FAs, permeability seems to increase more noticeably compared to the flat membranes with 10% FAs.

Permeability of water molecules through a heterogeneous curved membrane of 50 Å radius is provided in Figure 13 (left). Overall, the composition has a similar yet stronger effect on the permeability for water beads than for N0 beads. For all membrane compositions and for both N0 and water, P_{entr} is considerably larger than P_{esc} in the liposomes with a radius of 50 Å. This difference between P_{entr} and P_{esc} values is consistent with the definitions of these two permeabilities outlined in section, where P_{entr} is expected to be larger than P_{esc} due to the smaller inner surface area at r_1 (eqs 3 and 4). In practice, it means that the time scales in an experiment will depend on whether the compound of interest is initially inside or outside the liposome as the escape and entrance kinetics can be different.

CONCLUSIONS

This study employed CG MD simulations to explore the influence of membrane curvature and composition on the permeability of three small permeants with different free energy profiles. This leads to the question of which effect is dominant for the investigated membrane permeabilities: permeant type, composition, or curvature? First, the permeant type (water, N0, and Na), represented by the free energy profile or solubility, is most important. Second, the membrane composition with FAs or cholesterol can cause variations that lie often within a 35% change for water or 55% change for N0. Introduction of FAs and cholesterol into the membrane exhibits contrasting effects on permeability: while FAs elevate permeability (deprotonated FAs more than neutral FAs because of their charges), cholesterol reduces it. With the simultaneous incorporation of cholesterol and FAs, cholesterol tempers the action of FAs as N0 permeability enhancers.

Third, curvature reduces the membrane thickness and also decreases the free energy in the headgroup region, except for the highly curved liposomes. Curvature thus facilitates the permeation through the membrane (Figure 12). Concretely, a high curvature (radius of 50 Å) increases the water permeability P^* by an enhancement factor of 1.7 for a pure DPPC bilayer. A low curvature (L_{130}) still increases the water permeability P^* by about 1.4, but the escape kinetics seem to have converged to those of a flat bilayer. The escape and entrance water permeabilities differ considerably, even up to a factor 7 for highly curved membranes, and this persists for the lower curvatures with still a factor 2 difference. Hence, for curved membranes, the type of experiment—escape or entrance—is expected to be dominant in the kinetics. Importantly, realistic liposomes in drug delivery applications are commonly much larger (less curved) than the studied systems, and it is likely that realistic liposomes will have less effect from curvature.

For drug release kinetics, the dominating effect is thus the lipid composition for large liposomes and the curvature for very small liposomes. The FAs will indeed enhance the passive permeability, but this is still fairly limited, not even a factor of 2, for the investigated permeants. Therefore, passive permeation from pH-sensitive liposomes containing FAs may not be a substantial phenomenon, and the undesired occurrence of premature drug release may be less probable.

ASSOCIATED CONTENT

Data Availability Statement

All simulation files were generated using the CHARMM-GUI website (www.charmm-gui.org), while the fatty acid structure files were downloaded from the Martini website (www.cgmartini.nl). GROMACS-2021.4 (www.gromacs.org) was utilized for conducting the molecular dynamics simulations. Simulation settings are described in detail in the Methods section. Inkscape 1.0 (inkscape.org) was employed for creating and editing graphics.

SI Supporting Information

The Supporting Information is available free of charge at https://pubs.acs.org/doi/10.1021/acs.jcim.3c00936.

> Detailed description of the simulated systems including deprotonated FAs or Na permeant, APL for every molecule in the membranes, description of permeant concentration computation in the water phase, and simulation results for the permeant Na (PDF)

AUTHOR INFORMATION

Corresponding Author

An Ghysels − *IBiTech—BioMMedA Group, Ghent University, 9000 Gent, Belgium;* orcid.org/0000-0003-0015-2605; Email: an.ghysels@ugent.be

Authors

Samaneh Davoudi − *IBiTech—BioMMedA Group, Ghent University, 9000 Gent, Belgium;* orcid.org/0000-0002-2473-9999

Koen Raemdonck − *Ghent Research Group on Nanomedicines, Laboratory for General Biochemistry and Physical Pharmacy, Ghent University, 9000 Gent, Belgium*

Kevin Braeckmans − *Bio-Photonic Imaging Group, Laboratory for General Biochemistry and Physical Pharmacy, Ghent University, 9000 Gent, Belgium;* orcid.org/0000-0002-7993-6295

Complete contact information is available at: https://pubs.acs.org/10.1021/acs.jcim.3c00936

Notes

The authors declare no competing financial interest.

ACKNOWLEDGMENTS

The computational resources (Stevin Supercomputer Infrastructure) and services used in this work were provided by the VSC (Flemish Supercomputer Center), funded by Ghent University, FWO, and the Flemish Government—Department

EWI. We acknowledge funding of the FWO (project G002520N and project G094023N), the BOF of Ghent University, and the European Union (ERC, 101086145 PASTIME). The views and opinions expressed are, however, those of the author(s) only and do not necessarily reflect those of the European Union or the European Research Council. Neither the European Union nor the granting authority can be held responsible for them.

■ REFERENCES

(1) Nikezić, A. V. V.; Bondžić, A. M.; Vasić, V. M. Drug delivery systems based on nanoparticles and related nanostructures. *Eur. J. Pharm. Sci.* **2020**, *151*, 105412.

(2) Filipczak, N.; Pan, J.; Yalamarty, S. S. K.; Torchilin, V. P. Recent advancements in liposome technology. *Adv. Drug Delivery Rev.* **2020**, *156*, 4−22.

(3) Beltrán-Gracia, E.; López-Camacho, A.; Higuera-Ciapara, I.; Velázquez-Fernández, J. B.; Vallejo-Cardona, A. A. Nanomedicine review: clinical developments in liposomal applications. *Cancer Nanotechnol.* **2019**, *10*, 11.

(4) Alves, A. C.; Ribeiro, D.; Nunes, C.; Reis, S. Biophysics in cancer: The relevance of drug-membrane interaction studies. *Biochim. Biophys. Acta, Biomembr.* **2016**, *1858*, 2231−2244.

(5) Genheden, S.; Eriksson, L. A. Estimation of liposome penetration barriers of drug molecules with all-atom and coarse-grained models. *J. Chem. Inf. Model.* **2016**, *12*, 4651−4661.

(6) Woodward, X.; Javanainen, M.; Fábián, B.; Kelly, C. V. Nanoscale membrane curvature sorts lipid phases and alters lipid diffusion. *Biophys. J.* **2023**, *122*, 2203−2215.

(7) Buyan, A.; Allender, D.; Corry, B.; Schick, M. Lipid redistribution in the highly curved footprint of Piezo1. *Biophys. J.* **2023**, *122*, 1900−1913.

(8) Hashemzadeh, H.; Javadi, H.; Darvishi, M. Study of Structural stability and formation mechanisms in DSPC and DPSM liposomes: A coarse-grained molecular dynamics simulation. *Sci. Rep.* **2020**, *10*, 1837.

(9) Yesylevskyy, S.; Khandelia, H. Encurv: Simple technique of maintaining global membrane curvature in molecular dynamics simulations. *J. Chem. Theory Comput.* **2021**, *17*, 1181−1193.

(10) Abri Aghdam, M.; Bagheri, R.; Mosafer, J.; Baradaran, B.; Hashemzaei, M.; Baghbanzadeh, A.; de la Guardia, M.; Mokhtarzadeh, A. Recent advances on thermosensitive and pH-sensitive liposomes employed in controlled release. *J. Controlled Release* **2019**, *315*, 1−22.

(11) Nikolova, M. P.; Kumar, E. M.; Chavali, M. S. Updates on Responsive Drug Delivery Based on Liposome Vehicles for Cancer Treatment. *Pharmaceutics* **2022**, *14*, 2195.

(12) Kurniawan, J.; Suga, K.; Kuhl, T. L. Interaction forces and membrane charge tunability: Oleic acid containing membranes in different pH conditions. *Biochim. Biophys. Acta, Biomembr.* **2017**, *1859*, 211−217.

(13) Lado-Touriño, I.; Cerpa-Naranjo, A. Coarse-Grained Molecular Dynamics of pH-Sensitive Lipids. *Int. J. Mol. Sci.* **2023**, *24*, 4632.

(14) Choi, M.-J.; Han, H.-S.; Kim, H. pH-sensitive liposomes containing polymerized phosphatidylethanolamine and fatty acid. *J. Biochem.* **1992**, *112*, 694−699.

(15) Yang, Y.; Li, X.; Song, J.; Li, L.; Ye, Q.; Zuo, S.; Liu, T.; Dong, F.; Liu, X.; He, Z.; et al. Structure−Activity Relationship of pH-Sensitive Doxorubicin-Fatty Acid Prodrug Albumin Nanoparticles. *Nano Lett.* **2023**, *23*, 1530−1538.

(16) Arouri, A.; Lauritsen, K. E.; Nielsen, H. L.; Mouritsen, O. G. Effect of fatty acids on the permeability barrier of model and biological membranes. *Chem. Phys. Lipids* **2016**, *200*, 139−146.

(17) Hossain, S.; Joyce, P.; Parrow, A.; Jõemetsa, S.; Höök, F.; Larsson, P.; Bergström, C. A. S. Influence of bile composition on membrane incorporation of transient permeability enhancers. *Mol. Pharmaceutics* **2020**, *17*, 4226−4240.

(18) Brayden, D. J.; Gleeson, J.; Walsh, E. G. A head-to-head multi-parametric high content analysis of a series of medium chain fatty acid intestinal permeation enhancers in Caco-2 cells. *Eur. J. Pharm. Biopharm.* **2014**, *88*, 830−839.

(19) Prislan, I.; Lokar, M.; Zirdum, M.; Valant, J.; Poklar Ulrih, N. Contribution of headgroup and chain length of glycerophospholipids to thermal stability and permeability of liposomes loaded with calcein. *Chem. Phys. Lipids* **2019**, *225*, 104807.

(20) Joguparthi, V.; Xiang, T.-X.; Anderson, B. D. Liposome transport of hydrophobic drugs: Gel phase lipid bilayer permeability and partitioning of the lactone form of a hydrophobic camptothecin, DB-67. *J. Pharm. Sci.* **2008**, *97*, 400−420.

(21) Winter, N. D.; Murphy, R. K.; O'Halloran, T. V.; Schatz, G. C. Development and modeling of arsenic-trioxide−loaded thermosensitive liposomes for anticancer drug delivery. *J. Liposome Res.* **2011**, *21*, 106−115.

(22) Yue, Z.; Li, C.; Voth, G. A.; Swanson, J. M. Dynamic protonation dramatically affects the membrane permeability of drug-like molecules. *J. Am. Chem. Soc.* **2019**, *141*, 13421−13433.

(23) Palaiokostas, M.; Ding, W.; Shahane, G.; Orsi, M. Effects of lipid composition on membrane permeation. *Soft Matter* **2018**, *14*, 8496−8508.

(24) Saeedimasine, M.; Montanino, A.; Kleiven, S.; Villa, A. Role of lipid composition on the structural and mechanical features of axonal membranes: a molecular simulation study. *Sci. Rep.* **2019**, *9*, 8000.

(25) Nasr, G.; Greige-Gerges, H.; Elaissari, A.; Khreich, N. Liposome Permeability to Essential Oil Components: A Focus on Cholesterol Content. *J. Membr. Biol.* **2021**, *254*, 381−395.

(26) Briuglia, M.-L.; Rotella, C.; McFarlane, A.; Lamprou, D. A. Influence of cholesterol on liposome stability and on in vitro drug release. *Drug Delivery Transl. Res.* **2015**, *5*, 231−242.

(27) Sezgin, E.; Levental, I. Membranes in focus. *Biophys. J.* **2023**, *122*, E1−E4.

(28) Sugita, M.; Fujie, T.; Yanagisawa, K.; Ohue, M.; Akiyama, Y. Lipid Composition Is Critical for Accurate Membrane Permeability Prediction of Cyclic Peptides by Molecular Dynamics Simulations. *J. Chem. Inf. Model.* **2022**, *62*, 4549−4560.

(29) Ileri Ercan, N. Understanding Interactions of Curcumin with Lipid Bilayers: A Coarse-Grained Molecular Dynamics Study. *J. Chem. Inf. Model.* **2019**, *59*, 4413−4426.

(30) Zhang, X.; Barraza, K. M.; Beauchamp, J. Cholesterol provides nonsacrificial protection of membrane lipids from chemical damage at air−water interface. *Proc. Natl. Acad. Sci. U.S.A.* **2018**, *115*, 3255−3260.

(31) Cao, Z.; Zhang, X.; Wang, C.; Liu, L.; Zhao, L.; Wang, J.; Zhou, Y. Different effects of cholesterol on membrane permeation of arginine and tryptophan revealed by bias-exchange metadynamics simulations. *J. Chem. Phys.* **2019**, *150*, 084106.

(32) Dotson, R. J.; Smith, C. R.; Bueche, K.; Angles, G.; Pias, S. C. Influence of cholesterol on the oxygen permeability of membranes: insight from atomistic simulations. *Biophys. J.* **2017**, *112*, 2336−2347.

(33) Falck, E.; Patra, M.; Karttunen, M.; Hyvönen, M. T.; Vattulainen, I. Impact of cholesterol on voids in phospholipid membranes. *J. Chem. Phys.* **2004**, *121*, 12676−12689.

(34) Jin, L.; Engelhart, A. E.; Adamala, K. P.; Szostak, J. W. Preparation, purification, and use of fatty acid-containing liposomes. *J. Visualized Exp.* **2018**, *132*, No. e57324.

(35) Twarog, C.; Fattah, S.; Heade, J.; Maher, S.; Fattal, E.; Brayden, D. J. Intestinal permeation enhancers for oral delivery of macromolecules: a comparison between salcaprozate sodium (SNAC) and sodium caprate (C10). *Pharmaceutics* **2019**, *11*, 78.

(36) Krug, S. M.; Amasheh, M.; Dittmann, I.; Christoffel, I.; Fromm, M.; Amasheh, S. Sodium caprate as an enhancer of macromolecule permeation across tricellular tight junctions of intestinal cells. *Biomaterials* **2013**, *34*, 275−282.

(37) McCartney, F.; Gleeson, J. P.; Brayden, D. J. Safety concerns over the use of intestinal permeation enhancers: A mini-review. *Tissue barriers* **2016**, *4*, No. e1176822.

(38) Škulj, S.; Vazdar, M. Calculation of apparent p K a values of saturated fatty acids with different lengths in DOPC phospholipid bilayers. *Phys. Chem. Chem. Phys.* **2019**, *21*, 10052−10060.

(39) Bonhenry, D.; Tarek, M.; Dehez, F. Effects of phospholipid composition on the transfer of a small cationic peptide across a model biological membrane. *J. Chem. Theory Comput.* **2013**, *9*, 5675−5684.

(40) Pashkovskaya, A. A.; Vazdar, M.; Zimmermann, L.; Jovanovic, O.; Pohl, P.; Pohl, E. E. Mechanism of long-chain free fatty acid protonation at the membrane-water interface. *Biophys. J.* **2018**, *114*, 2142−2151.

(41) Kneiszl, R.; Hossain, S.; Larsson, P. In Silico-Based Experiments on Mechanistic Interactions between Several Intestinal Permeation Enhancers with a Lipid Bilayer Model. *Mol. Pharm.* **2022**, *19*, 124−137.

(42) Davoudi, S., Wang, Q., Patel, H. H., Pias, S. C., Ghysels, A. Understanding the Role of Caveolae in Oxygen Buffering: The Effect of Membrane Curvature. *Oxygen Transport to Tissue XLIV*; Springer, 2023; pp 87−91.

(43) Risselada, H. J.; Marrink, S. J. Curvature effects on lipid packing and dynamics in liposomes revealed by coarse grained molecular dynamics simulations. *Phys. Chem. Chem. Phys.* **2009**, *11*, 2056−2067.

(44) Yesylevskyy, S. O.; Rivel, T.; Ramseyer, C. The influence of curvature on the properties of the plasma membrane. Insights from atomistic molecular dynamics simulations. *Sci. Rep.* **2017**, *7*, 16078.

(45) Winter, N. D.; Schatz, G. C. Coarse-grained molecular dynamics study of permeability enhancement in DPPC bilayers by incorporation of lysolipid. *J. Phys. Chem. B* **2010**, *114*, 5053−5060.

(46) Yesylevskyy, S.; Rivel, T.; Ramseyer, C. Curvature increases permeability of the plasma membrane for ions, water and the anticancer drugs cisplatin and gemcitabine. *Sci. Rep.* **2019**, *9*, 17214.

(47) Davoudi, S.; Ghysels, A. Sampling efficiency of the counting method for permeability calculations estimated with the inhomogeneous solubility−diffusion model. *J. Chem. Phys.* **2021**, *154*, 054106.

(48) Dotson, R. J.; Smith, C. R.; Bueche, K.; Angles, G.; Pias, S. C. Influence of Cholesterol on the Oxygen Permeability of Membranes: Insight from Atomistic Simulations. *Biophys. J.* **2017**, *112*, 2336−2347.

(49) Venable, R. M.; Krämer, A.; Pastor, R. W. Molecular Dynamics Simulations of Membrane Permeability. *Chem. Rev.* **2019**, *119*, 5954−5997.

(50) Ghysels, A.; Krämer, A.; Venable, R.; Teague, W.; Lyman, E.; Gawrisch, K.; Pastor, R. W. Permeability of Membranes in the Liquid Ordered and Liquid Disordered Phases. *Nat. Commun.* **2019**, *10*, 5616.

(51) Ghysels, A.; Roet, S.; Davoudi, S.; van Erp, T. S. Exact non-Markovian permeability from rare event simulations. *Phys. Rev. Res.* **2021**, *3*, 033068.

(52) Davoudi, S.; Ghysels, A. Defining permeability of curved membranes in molecular dynamics simulations. *Biophys. J.* **2023**, *122*, 2082−2091.

(53) Benmameri, M.; Chantemargue, B.; Humeau, A.; Trouillas, P.; Fabre, G. MemCross: Accelerated Weight Histogram method to assess membrane permeability. *Biochim. Biophys. Acta, Biomembr.* **2023**, *1865*, 184120.

(54) Marrink, S. J.; Risselada, H. J.; Yefimov, S.; Tieleman, D. P.; De Vries, A. H. The MARTINI force field: coarse grained model for biomolecular simulations. *J. Phys. Chem. B* **2007**, *111*, 7812−7824.

(55) Davoudi, S.; Amjad-Iranagh, S.; Zaeifi Yamchi, M. Molecular dynamic simulation of Ca2+-ATPase interacting with lipid bilayer membrane. *IET Nanobiotechnol.* **2015**, *9*, 85−94.

(56) Nkanga, C. I.; Bapolisi, A. M.; Okafor, N. I.; Krause, R. W. M. *Liposomes*; Catala, A., Ed.; IntechOpen: Rijeka, 2019; Chapter 3.

(57) Grünewald, F.; Souza, P. C. T.; Abdizadeh, H.; Barnoud, J.; de Vries, A. H.; Marrink, S. J. Titratable Martini model for constant pH simulations. *J. Chem. Phys.* **2020**, *153*, 024118.

(58) Abraham, M. J.; Murtola, T.; Schulz, R.; Páll, S.; Smith, J. C.; Hess, B.; Lindahl, E. GROMACS: High performance molecular simulations through multi-level parallelism from laptops to supercomputers. *SoftwareX* **2015**, *1−2*, 19−25.

(59) Jo, S.; Kim, T.; Iyer, V. G.; Im, W. CHARMM-GUI: a web-based graphical user interface for CHARMM. *J. Comput. Chem.* **2008**, *29*, 1859−1865.

(60) Brooks, B. R.; Brooks, C. L., III; Mackerell, A. D., Jr.; Nilsson, L.; Petrella, R. J.; Roux, B.; Won, Y.; Archontis, G.; Bartels, C.; Boresch, S.; et al. CHARMM: the biomolecular simulation program. *J. Comput. Chem.* **2009**, *30*, 1545−1614.

(61) Lee, J.; Cheng, X.; Swails, J. M.; Yeom, M. S.; Eastman, P. K.; Lemkul, J. A.; Wei, S.; Buckner, J.; Jeong, J. C.; Qi, Y.; et al. CHARMM-GUI input generator for NAMD, GROMACS, AMBER, OpenMM, and CHARMM/OpenMM simulations using the CHARMM36 additive force field. *J. Chem. Theory Comput.* **2016**, *12*, 405−413.

(62) Qi, Y.; Ingólfsson, H. I.; Cheng, X.; Lee, J.; Marrink, S. J.; Im, W. CHARMM-GUI martini maker for coarse-grained simulations with the martini force field. *J. Chem. Theory Comput.* **2015**, *11*, 4486−4494.

(63) Marrink, S. J.; Risselada, H. J.; Yefimov, S.; Tieleman, D. P.; De Vries, A. H. The MARTINI force field: coarse grained model for biomolecular simulations. *J. Phys. Chem. B* **2007**, *111*, 7812−7824.

(64) Tironi, I. G.; Sperb, R.; Smith, P. E.; van Gunsteren, W. F. A generalized reaction field method for molecular dynamics simulations. *J. Chem. Phys.* **1995**, *102*, 5451−5459.

(65) Bussi, G.; Donadio, D.; Parrinello, M. Canonical sampling through velocity rescaling. *J. Chem. Phys.* **2007**, *126*, 014101.

(66) Krämer, A.; Ghysels, A.; Wang, E.; Venable, R. M.; Klauda, J. B.; Brooks, B. R.; Pastor, R. W. Membrane Permeability of Small Molecules from Unbiased Molecular Dynamics Simulations. *J. Chem. Phys.* **2020**, *153*, 124107.

(67) De Vos, O.; Venable, R. M.; Van Hecke, T.; Hummer, G.; Pastor, R. W.; Ghysels, A. Membrane Permeability: Characteristic Times and Lengths for Oxygen and a Simulation-Based Test of the Inhomogeneous Solubility-Diffusion Model. *J. Chem. Theory Comput.* **2018**, *14*, 3811−3824.

(68) Ghysels, A.; Venable, R. M.; Pastor, R. W.; Hummer, G. Position-Dependent Diffusion Tensors in Anisotropic Media from Simulation: Oxygen Transport in and through Membranes. *J. Chem. Theory Comput.* **2017**, *13*, 2962−2976.

(69) Kučerka, N.; Nieh, M.-P.; Katsaras, J. Fluid phase lipid areas and bilayer thicknesses of commonly used phosphatidylcholines as a function of temperature. *Biochim. Biophys. Acta, Biomembr.* **2011**, *1808*, 2761−2771.

(70) Hąc-Wydro, K.; Wydro, P. The influence of fatty acids on model cholesterol/phospholipid membranes. *Chem. Phys. Lipids* **2007**, *150*, 66−81.

(71) de Meyer, F.; Smit, B. Effect of cholesterol on the structure of a phospholipid bilayer. *Proc. Natl. Acad. Sci. U.S.A.* **2009**, *106*, 3654−3658.

(72) Yesylevskyy, S.; Martinez-Seara, H.; Jungwirth, P. Curvature Matters: Modeling Calcium Binding to Neutral and Anionic Phospholipid Bilayers. *J. Phys. Chem. B* **2023**, *127*, 4523−4531.

(73) Santos, D. E. S.; Coutinho, K.; Soares, T. A. Surface Assessment via Grid Evaluation (SuAVE) for Every Surface Curvature and Cavity Shape. *J. Chem. Inf. Model.* **2022**, *62*, 4690−4701.

(74) Santos, D. E. S.; De Nicola, A.; dos Santos, V. F.; Milano, G.; Soares, T. A. Exploring the Molecular Dynamics of a Lipid-A Vesicle at the Atom Level: Morphology and Permeation Mechanism. *J. Phys. Chem. B* **2023**, *127*, 6694−6702.

(75) Scrima, S.; Tiberti, M.; Campo, A.; Corcelle-Termeau, E.; Judith, D.; Foged, M.; Clemmensen, K.; Tooze, S.; Jäättelä, M.; Maeda, K.; Lambrughi, M.; Papaleo, E. Unraveling membrane properties at the organelle-level with LipidDyn. *Comput. Struct. Biotechnol. J.* **2022**, *20*, 3604−3614.

(76) Carruthers, A.; Melchior, D. Study of the relationship between bilayer water permeability and bilayer physical state. *Biochem* **1983**, *22*, 5797−5807.

(77) Huster, D.; Jin, A. J.; Arnold, K.; Gawrisch, K. Water permeability of polyunsaturated lipid membranes measured by 17O NMR. *Biophys. J.* **1997**, *73*, 855−864.

(78) Arouri, A.; Mouritsen, O. G. Membrane-perturbing effect of fatty acids and lysolipids. *Prog. Lipid Res.* **2013**, *52*, 130−140.

(79) Via, M. A.; Wilke, N.; Mayorga, L. S.; Del Pópolo, M. G. Surface charge density and fatty acids enhance the membrane permeation rate of CPP−cargo complexes. *Soft Matter* **2020**, *16*, 9890−9898.

(80) Chiang, Y.-W.; Costa-Filho, A. J.; Freed, J. H. Dynamic molecular structure and phase diagram of DPPC- cholesterol binary mixtures: A 2D-ELDOR study. *J. Phys. Chem. B* **2007**, *111*, 11260−11270.

(81) Wang, Y.; Gkeka, P.; Fuchs, J. E.; Liedl, K. R.; Cournia, Z. DPPC-cholesterol phase diagram using coarse-grained Molecular Dynamics simulations. *Biochim. Biophys. Acta, Biomembr.* **2016**, *1858*, 2846−2857.

(82) Vist, M. R.; Davis, J. H. Phase equilibria of cholesterol/dipalmitoylphosphatidylcholine mixtures: deuterium nuclear magnetic resonance and differential scanning calorimetry. *Biochem* **1990**, *29*, 451−464.

(83) Subczynski, W. K.; Pasenkiewicz-Gierula, M.; Widomska, J.; Mainali, L.; Raguz, M. High cholesterol/low cholesterol: effects in biological membranes: a review. *Cell Biochem. Biophys.* **2017**, *75*, 369−385.

SI for Paper 4

Capric acid and myristic acid permeability enhancers in curved liposome membranes

SUPPORTING INFORMATION

Samaneh Davoudi,[†] Koen Raemdonck,[‡] Kevin Braeckmans,[¶] and An Ghysels[*,§]

†IBiTech - BioMMedA group, Ghent University, Corneel Heymanslaan 10, Block B-entrance 36, 9000 Gent, Belgium

‡Ghent Research Group on Nanomedicines, Laboratory for General Biochemistry and Physical Pharmacy, Ghent University, Ottergemsesteenweg 460, 9000 Gent, Belgium

¶Bio-Photonic Imaging Group, Laboratory for General Biochemistry and Physical Pharmacy, Ghent University, Ottergemsesteenweg 460, 9000 Gent, Belgium

§IBiTech - BioMMedA group, Ghent University, Corneel Heymanslaan 10, Block B - entrance 36, 9000 Gent, Belgium

E-mail: an.ghysels@ugent.be

Contents

1 Simulated systems

The systems with 20 N0 coarse-grained beads as permeants and the neutral FAs are reported in Table 1 and Table 2 of the main document. Below we give the composition of two series containing 20 Na permeants and neutral FAs (Table S1, Table S2), and two series with 20 N0 beads and deprotonated (negatively charged) FAs (Table S3, Table S4).

Some of the liposome simulations containing N0 were required to be given an extended equilibration run (Table S5); this was not considered for the systems containing Na.

Table S1: Detailed description of simulated systems containing a flat bilayer (F). Each system contained 20 Na permeants. Fatty acids are neutral. h is the membrane thickness between PO4 beads (region 2, see Methods Section of main document). Number of Na^+/Cl^- ions refers to the number of each ion.

	system name	lipid types	lipid composition (%)	# of lipids	# of water CG beads	# of Na^+/Cl^-	h
1	F	DPPC	100	256	2504	29	40.2
2	F-5C10	DPPC:C10	95:5	280	2753	32	40.1
3	F-10C10		90:10	260	2575	30	39.9
4	F-20C10		80:20	250	2491	30	39.5
5	F-30C10		70:30	260	2640	32	38.8
6	F-5C14	DPPC:C14	95:5	280	2753	32	40.2
7	F-10C14		90:10	260	2575	30	40.0
8	F-20C14		80:20	250	2491	30	39.8
9	F-30C14		70:30	260	2640	32	39.5
10	F-10Ch	DPPC:Chol	90:10	260	2452	28	41.2
11	F-10Ch-10C10	DPPC:Chol:C10	80:10:10	260	2498	29	41.0
12	F-10Ch-10C14	DPPC:Chol:C14	80:10:10	260	2498	29	41.0

Table S2: Detailed description of simulated systems containing a liposome (L). L_{50}, L_{100}, and L_{130} refer to the liposomes with a radius of 50 Å, 100 Å, and 130 Å, respectively. The other liposomes have a radius of 50 Å. Each system contained 20 Na permeants. Fatty acids are neutral. h is the membrane thickness between PO4 beads (region 2, see Methods Section of main document). Number of Na^+/Cl^- ions refers to the number of each ion.

	system name	lipid types	lipid comp. (%)	# of lipids		# of water CG beads	# of ions	r_1 (Å)	r_2 (Å)	h (Å)	A^* (Å^2)
				in	out		Na^+/Cl^-				
1	L_{50}	DPPC	100	124	394	54507	603	21.1	56.4	35.3	67.9
2	L_{100}	DPPC	100	1097	1784	185289	2064	67.7	106.4	38.7	64.5
3	L_{130}	DPPC	100	2092	2992	317684	3555	96.1	135.0	38.9	65.0
4	L-10C10	DPPC:C10	90:10	113	398	76779	842	19.4	54.6	35.2	62.0
5	L-10C14	DPPC:C14	90:10	124	387	76779	842	19.6	54.8	35.2	61.9
6	L-10Ch	DPPC:Chol	90:10	145	400	76608	842	21.0	56.3	35.3	61.0
7	L-20Ch		80:20	123	451	76600	842	21.0	55.2	34.2	61.3
8	L-10Ch-10C10	DPPC:Chol:C10	80:10:10	142	396	76730	842	18.6	54.2	35.6	53.7
9	L-20Ch-20C10		60:20:20	144	418	78207	842	16.7	52.0	35.3	45.5
10	L-10Ch-10C14	DPPC:Chol:C14	80:10:10	147	391	76730	842	18.5	54.4	35.9	53.1
11	L-20Ch-20C14		60:20:20	148	414	78207	842	17.3	52.6	35.3	45.0

2 Area per lipid

After plotting the APL for various membrane compositions, a linear regression line was fitted. To estimate the APL of a membrane composed solely of one type of lipid molecule, the regression line was extended to the point of 100% lipid composition of that type, giving the APL value of that type. The exception is the APL value for pure DPPC, which was not determined from the regression line, but instead it was directly obtained from the pure DPPC simulation of the flat bilayer.

3 Computation of permeant concentration in the water phase

The reference concentration c_{ref} of the permeants in the water phase needs to be determined for the permeability calculation. For this, the regions were selected where only the water phase was present and the lipid membrane histogram had reached zero. The number of permeants in those regions are counted and divided by the volume of those regions. For flat membranes, c_{ref} is computed based on the region determined by $a < |z| < \langle L_z \rangle/2$, where

Table S3: Detailed description of simulated systems containing a flat bilayer (F). Each system contained 20 N0 permeants. Fatty acids are deprotonated. h is the membrane thickness between PO4 beads (region 2, see Methods Section of main document).

	system name	lipid types	lipid composition (%)	# of lipids	# of water CG beads	# of ions		h (Å)
						Na^+	Cl^-	
1	F-5C10-n	DPPC:C10-n	95:5	280	2747	46	32	40.0
2	F-10C10-n		90:10	260	2577	56	30	39.6
3	F-20C10-n		80:20	250	2495	80	30	38.6
4	F-30C10-n		70:30	260	2649	110	32	37.5
5	F-5C14-n	DPPC:C14-n	95:5	280	2747	46	32	40.1
6	F-10C14-n		90:10	260	2577	56	30	39.8
7	F-20C14-n		80:20	250	2495	80	30	39.1
8	F-30C14-n		70:30	260	2649	110	32	38.2
9	F-10Ch-10C10-n	DPPC:Chol:C10-n	80:10:10	260	2490	55	29	40.6
10	F-10Ch-10C14-n	DPPC:Chol:C14-n	80:10:10	260	2490	55	29	40.7

Table S4: Detailed description of simulated systems containing a liposome (L) with a radius of 50 Å. Each system contained 20 N0 permeants. Fatty acids are deprotonated. h is the membrane thickness between PO4 beads (region 2, see Methods Section of main document).

	system name	lipid types	lipid comp. (%)	# of lipids		# of water CG beads	# of ions		r_1 (Å)	r_2 (Å)	h (Å)	A^* (Å^2)
				in	out		Na^+	Cl^-				
1	L-10C10-n	DPPC:C10-n	90:10	103	408	76753	892	842	19.2	54.5	35.3	63.8
5	L-10C14-n	DPPC:C14-n	90:10	113	398	76753	892	842	20.5	55.1	34.7	65.9
6	L-10Ch-10C10-n	DPPC:Chol:C10-n	80:10:10	134	404	76712	895	842	19.8	54.6	34.8	57.8
4	L-20Ch-20C10-n		60:20:20	133	429	76848	954	842	16.9	52.1	35.1	46.6
5	L-10Ch-10C14-n	DPPC:Chol:C14-n	80:10:10	163	375	76712	895	842	20.1	55.0	34.8	56.5
6	L-20Ch-20C14-n		60:20:20	139	423	76848	954	842	17.7	52.7	35.5	47.8

$\langle L_z \rangle$ is the mean box length. For the liposomes, c_{in} and c_{out} are computed based on the region determined by $0 < r < a$ and $b < r < \langle L_z \rangle/2$, respectively.

4 Free energy profiles of permeants

Similarly to the results in the main document focusing on systems containing N0 beads, we report here additional free energy profiles for systems containing the 20 Na CG beads. We report the effect of composition (Figs. S1) on the Na free energy profile, and the effect of curvature (Fig. S2) on the water free energy profile. In addition, we compare systems with and without cholesterol.

Table S5: Equilibration and production time for systems containing a liposome (L). All systems contain a liposome with a radius of approximately 50 Å. L_{50} refers to the pure DPPC liposome. System names with the suffix '-n ' refer to liposomes containing deprotonated FAs. Each system contains 20 N0 permeants.

system name	equilibration time (ns)	production time (ns)
L_{50}	600	5000
L-10C10	600	1000
L-10Ch	600	1000
L-20Ch	1600	1000
L-20Ch-20C10	1600	1000
L-10C14-n	1100	1000
L-10Ch-10C10-n	1100	1000
L-10Ch-10C14-n	600	1000
L-20Ch-20C14-n	1100	1000
other liposomes	100	1000
flat bilayers	100	1000

Table S6: APL for every component in the membranes. "-n" refers to the systems with deprotonated fatty acids. The area per lipid values for each molecule were determined using the slope of the regression line in the area per lipid plot, which was extrapolated to the hypothetical scenario of a membrane composed of 100% of that molecule.

molecule	APL (Å^2)
DPPC	63.6
Chol	9.25
C10	24.4
C14	27.6
C10-n	33.9
C14-n	37.2

5 Number of permeant crossings

The number of permeant crossings are used to compute the permeability. For water CG beads, only region 2 is considered. For the N0 and Na beads, region 1 and region 2 are considered.

Table S7: Values a and b that determine how the reference concentration c_{ref} is computed in flat membrane simulations and c_{in} and c_{out} in liposome simulations.

molecule	a (Å)	b (Å)
flat membranes	30	-
liposomes with radius 50 Å	12	70
L_{100}	40	120
L_{130}	70	150

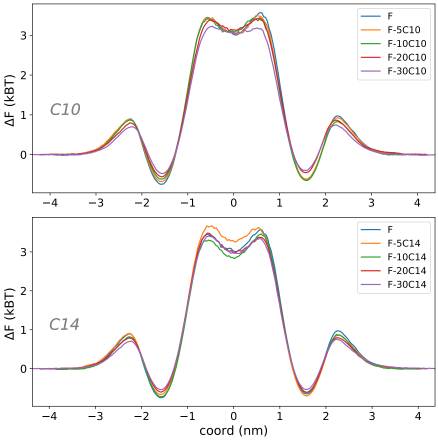

Figure S1: Effect of neutral fatty acids C10 and C14 on the free energy profile of Na permeants in systems with a flat bilayer.

6 Permeability of Na CG bead

The main document focuses mainly on permeabilities of the N0 CG beads, as those had a higher number of membrane crossings, and thus better statistics. In this section, we report extra Na permeabilities. It should be noted some of the N0 systems were simulated with an extended equilibration run (see Methods section main document and Table S5). Meanwhile, the Na systems were not given an extended equilibration run. Some liposome results could therefore still be improved by more extensive equilibration and/or sampling.

Reported errors and grey shaded bands: see Methods section of the main paper (they refer to twice the standard error on the permeability, as expected from a Poisson process.)

7 Water permeability

We have simulated systems with N0 and Na beads. The water behavior is not affected by the presence of these 20 CG beads in our simulations. The main document focuses on water permeabilities in the simulations containing N0 beads rather than Na beads. For

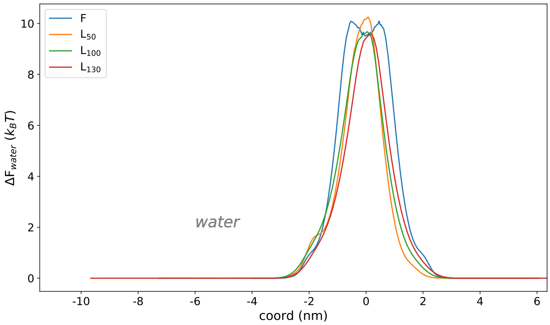

Figure S2: Effect of curvature on the free energy profile of water permeants as a function of membrane coordinate (related to the radial direction) in systems with pure DPPC bilayers.

Table S8: Number of permeant crossings in simulated systems containing a flat bilayer (F). Each system contained 20 permeants. Number of crossings for permeant W is from systems containing N0 permeants.

		neutral FA					deprotonated FA		
	permeant	W	N0		Na		W	N0	
	region	2	1	2	1	2	2	1	2
1	F	58	332	496	107	111	-	-	-
2	F-5C10	65	371	541	127	135	63	349	512
3	F-10C10	44	405	563	123	128	69	386	527
4	F-20C10	60	415	571	152	155	59	408	590
5	F-30C10	64	443	586	149	162	62	433	638
6	F-5C14	57	374	533	119	132	62	347	490
7	F-10C14	46	391	525	158	172	49	363	521
8	F-20C14	43	425	561	124	146	64	409	568
9	F-30C14	45	428	553	150	160	64	430	658
10	F-10Ch	41	264	343	66	69	-	-	-
11	F-10Ch-10C10	34	330	419	89	95	39	309	400
12	F-10Ch-10C14	32	306	374	76	81	33	308	400

completeness, we also report here water permeabilities in the systems containing Na beads. Again, given that the Na liposome systems were not given an extended equilibration run to let the water equilibrate between inside and outside water phases, while some of the N0 systems did get extended, we expect some of Na liposome results to be less accurate than the reported water permeabilities in the N0 liposome systems.

Reported errors and grey shaded bands: see Methods section of the main paper (they refer to twice the standard error on the permeability, as expected from a Poisson process.)

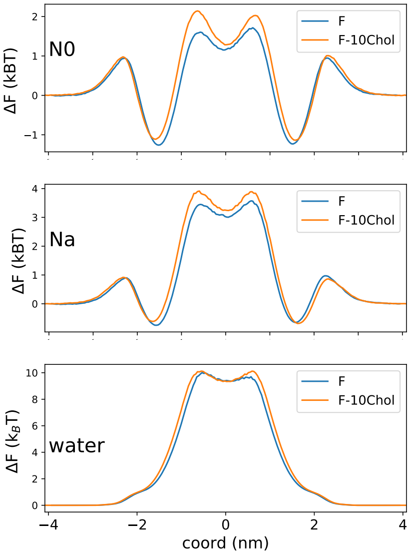

Figure S3: Effect of cholesterol on the free energy profile of all permeants (N0, Na and water) in the flat membranes. The free energy profile of water was calculated in the system containing 20 N0 permeants.

8 SuaVE calculations

In this subsection, the systems are analyzed using the SuaVE package, as published in *J. Chem. Inf. Model. 62, p. 4690-4701 (2023)* by Santos et al. This recently developed open-source software tool puts a grid on the membrane leaflet surfaces, on both sides of the membrane. Such a grid is used to estimate the area per lipid (APL), the membrane thickness h, and the order parameter (see definition in SuaVE paper).

The trajectories have a length of 1μs from which we selected 50 snapshots, separated by 20 ns. The PO4 beads of the bilayers were clustered such that they were not 'cut' by a periodic boundary condition. To apply the SuaVE code, it was also needed to center the bilayer about the origin. The grids were built based on the PO4 beads using the default SuaVE grid settings. For the SuaVE calculation with liposomes, the APL was computed by manually setting the number of PO4 beads to the considered leaflet.

Table S9: Number of permeant crossings in simulated systems containing a liposome (L). Each system contained 20 permeants. The number of crossings for L_{50} is for 5000ns. Number of crossings for permeant W is from systems containing N0 permeants.

		neutral FA					deprotonated FA		
	permeant	W	N0		Na		W	N0	
	region	2	1	2	1	2	2	1	2
1	L_{50}	895	117	571	106	164	-	-	-
2	L_{100}	928	128	223	41	49	-	-	-
3	L_{130}	1698	116	196	51	55	-	-	-
4	L-10C10	197	21	91	4	12	181	18	100
5	L-10C14	205	32	96	14	20	248	12	87
6	L-10Ch	138	7	49	2	6	-	-	-
7	L-20Ch	136	4	32	9	20	-	-	-
8	L-10Ch-10C10	101	6	44	2	6	109	12	47
9	L-20Ch-20C10	47	4	18	4	6	47	8	42
10	L-10Ch-10C14	102	4	48	8	12	139	10	70
11	L-20Ch-20C14	40	2	11	2	5	53	0	28

The average over the 50 snapshots and the standard deviation is given in Table S10 for the flat bilayer and for the larger liposomes.

Table S10: Average APL, h, and order parameter, with standard deviation estimated from 50 snapshots. Data computed with SuaVE.

system	$< A >$ (Å^2)		$\langle h \rangle$ (Å)		$\langle order \rangle$ (-)	
F	63.7	± 0.8	38.7	± 0.3	0.910	± 0.01

system	$< A >$ (Å^2)				$\langle h \rangle$ (Å)		$\langle order \rangle$ (-)			
	inner		outer				inner		outer	
L_{100}	56.9	±0.20	84.8	± 0.20	39.1	± 0.15	0.85	±0.0053	0.79	±0.0089
L_{130}	59.8	±0.14	81.3	± 0.13	39.2	± 0.11	0.86	±0.0040	0.81	±0.0065

In the following figures, the fluctuations of the parameters are visualized for a flat membrane and the L_{100} liposome.

8.1 SuaVE for flat membranes

8.2 SuaVE for larger liposomes

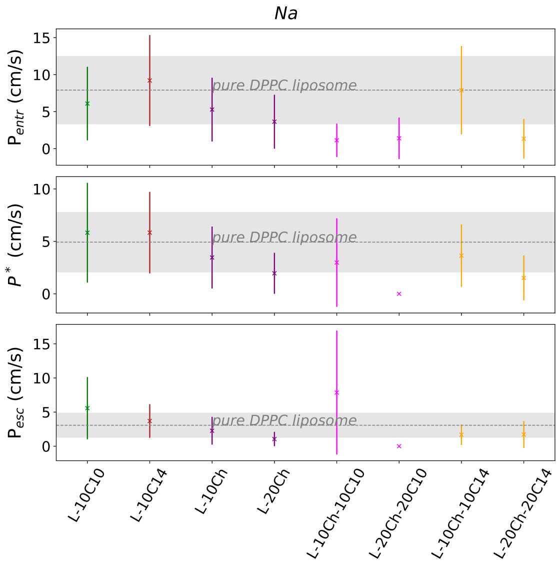

Figure S4: Na permeability in systems with liposomes: effect of composition.

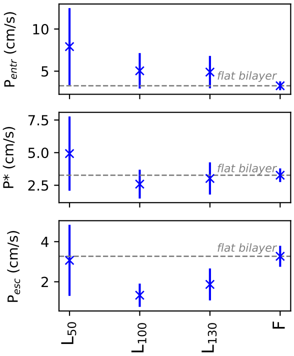

Figure S5: Na permeability in all systems with pure DPPC bilayers with varying curvature compared to the flat bilayer.

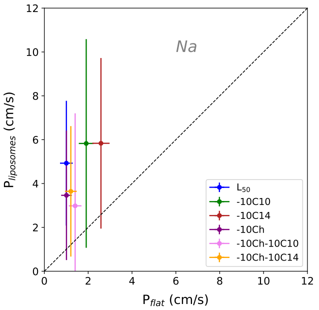

Figure S6: Comparison of the Na permeability in flat and curved membranes.

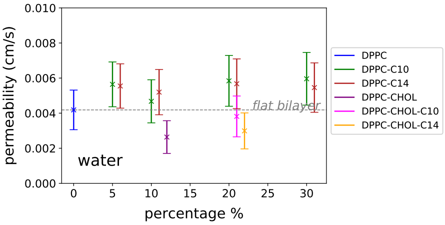

Figure S7: Water permeability of flat bilayers: effect of composition. For better visibility, data points have been shifted. (Systems contain Na permeants.)

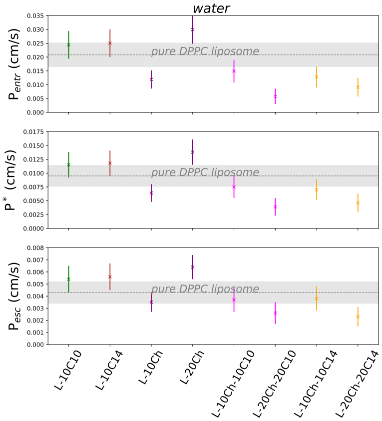

Figure S8: Water permeability in systems with liposomes: effect of composition. (Systems include Na permeants.)

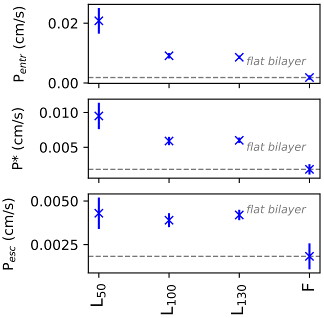

Figure S9: Water permeability in systems with pure DPPC bilayers with varying curvature compared to the flat bilayer. (Systems contain Na permeants.)

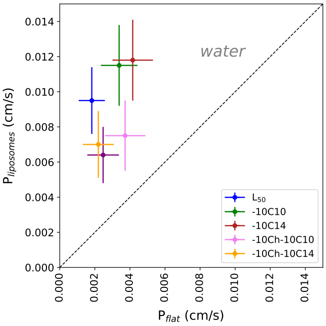

Figure S10: Comparison of the water permeability in flat and curved membranes. (Systems contain Na permeants.)

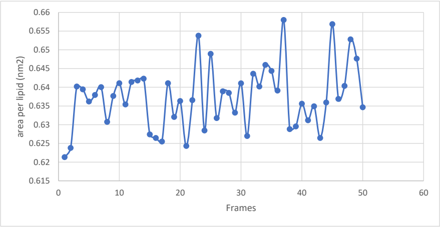

Figure S11: Area per lipid of pure DPPC flat membrane (F). APL computed with SuaVE package.

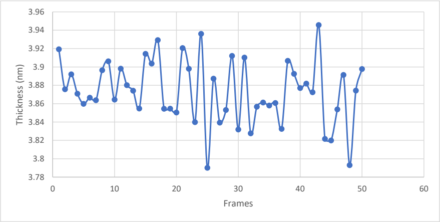

Figure S12: Thickness per lipid of pure DPPC flat membrane (F). Thickness computed with SuaVE package.

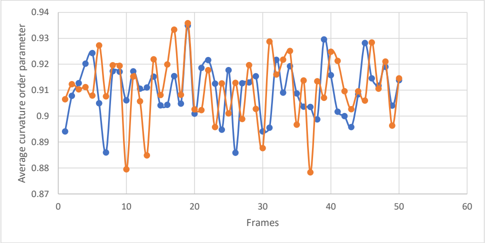

Figure S13: Order parameter of pure DPPC flat membrane (F). Order parameter computed with SuaVE package.

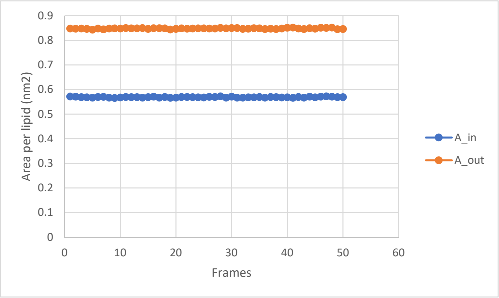

Figure S14: APL of pure DPPC liposome L_{100}. APL computed with SuaVE package.

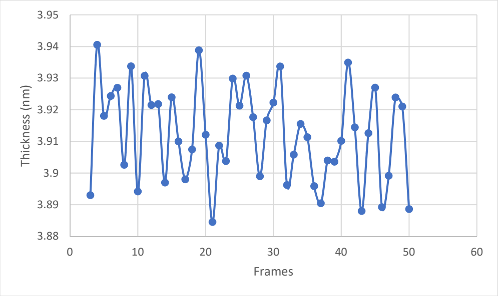

Figure S15: Thickness h of pure DPPC liposome L_{100}. Thickness computed with SuaVE package.

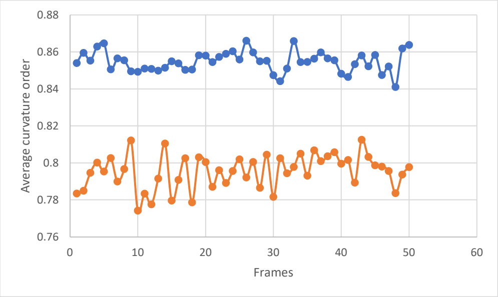

Figure S16: Order parameter of pure DPPC liposome L_{100}. Parameter computed with SuaVE package.

Paper 5

Understanding oxygen “buffering” by caveolae using coarse-grained molecular dynamics simulations

Samaneh Davoudi and An Ghysels

Oxygen Transport to Tissue. ISOTT 2023 (2024)

Understanding oxygen “buffering” by caveolae using coarse-grained molecular dynamics simulations

Samaneh Davoudi, An Ghysels

IBiTech – BioMMedA research group, Ghent University, Ghent, Belgium
Corresponding author: an.ghysels@ugent.be

Abstract The "oxygen paradox" embodies the delicate interplay between two opposing biological processes involving oxygen (O_2). O_2 is indispensable for aerobic metabolism, fuelling oxidative phosphorylation in mitochondria. However, excess O_2 can generate reactive species that harm cells. Thus, maintaining O_2 balance is paramount, requiring the prioritization of its benefits while minimizing potential harm. Previous research hypothesized that caveolae, specialized cholesterol-rich membrane structures with a curved morphology, regulate cellular O_2 levels. Their role in absorbing and controlling O_2 release to mitochondria remains unclear. To address this gap, we aim to explore how caveolae's structural features, particularly membrane curvature, influence local O_2 levels. Using coarse-grained (CG) molecular dynamics simulations (MD), we simulate a caveola-like curved membrane and select a coarse-grained bead as the O_2 model. Comparing a flat bilayer and a liposome of 10 nm diameter, composed of 1-palmitoyl-2-oleoyl-sn-glycero-3-phosphocholine (POPC), allows us to study changes in the O_2 free energy profile. Our findings reveal that curvature has a contrasting effect on the free energy of the outer and inner layer. These findings show the membrane curvature's impact on O_2 partitioning in the membrane and O_2 permeation barriers, paving the way towards our understanding of the role of caveolae curvature in O_2 homeostasis.

Keyword liposome, Martini, oxygen partitioning, free energy profile, membrane curvature

Introduction

The "oxygen paradox" refers to the intricate interplay between two contrasting biological processes involving oxygen (O_2) as a reactant. O_2 is vital for aerobic metabolism, acting as a fuel for oxidative phosphorylation within mitochondria. However, an excessive supply of O_2 can lead to the generation of reactive species that harm cellular health. Therefore, maintaining O_2 homeostasis becomes crucial, requiring a delicate balance that prioritizes the former process while minimizing the latter. In earlier research, a hypothesis was proposed centered around specialized membrane invaginations called caveolae [1]. These unique structures exhibit a curved morphology and are rich in cholesterol. It was postulated that caveolae play a pivotal role in regulating O_2 levels within cells by efficiently absorbing O_2 and attenuating its release to the mitochondria [2]. Caveolae would thus act as dynamic reservoirs for O_2 and aid in its regulation and distribution within cells, hence functioning as O_2 buffers. However, the precise mechanism by which caveolae could facilitate O_2 buffering remains unclear, posing an intriguing research question.

To address this knowledge gap, our primary objective is to investigate how specific structural characteristics of caveolae, such as membrane curvature and cholesterol content, influence the local O_2 abundance and membrane permeability. To accurately simulate a curved membrane resembling caveolae, we employed coarse-grained (CG) molecular dynamics (MD) simulations with interactions described by the well-known Martini force field [3]. The curved membranes require a very large simulation box, and an all-atom (AA) description would make the calculations very computationally demanding, taking up even weeks on a supercomputer. After conducting a comprehensive set of tests, we carefully selected one of the existing CG beads of the Martini force field to serve as the CG O_2 model [4].

In this work, a box containing a flat membrane composed of 1-palmitoyl-2-oleoyl-sn-glycero-3-phosphocholine (POPC) and a number of oxygen molecules is simulated. This membrane with zero curvature serves as the benchmark (Fig. 1). In addition, a liposome with non-zero membrane curvature is modelled to observe the effect of curvature. This approach allows us to examine associated changes in the O_2 concentration across the membrane. With this comparison, we aim to deepen our understanding of the underlying mechanisms governing O_2 homeostasis. Future steps will focus on simulating caveolae at their true size, ranging between 60-80 nm in diameter. Additionally, the caveolin protein will be incorporated into the membrane to bring the simulations closer to realistic caveolae. This deeper understanding has the potential to unlock insights into O_2-related disorders, potentially catalyzing new avenues of research aimed at treating these conditions.

Methods

Simulated systems. To study the effect of curvature, two model systems were simulated in a CG description, i.e. a flat membrane and a liposome with radius of about 50 Å (Fig. 1). Table 1 gives an overview of the components, which shows that ion pairs were added to represent physiological conditions. Each O_2 molecule is represented by one TC3 Martini bead, which was selected based on its size (tiny, “T”), polarity, and charge (non-polar and neutral, “C”), and interaction with phospholipids (“3”) in earlier work [4]. In this study, the oxygen concentration employed is deliberately elevated beyond physiological levels to enhance the sampling of oxygen crossings across the membrane. Importantly, thorough checks have been conducted throughout the simulations, and no instances of aggregation have been observed. Note that one water CG beads represents four water molecules in the Martini force field [3]. The simulations were carried out at a temperature of T=310 K (body temperature) and pressure of 1 bar.

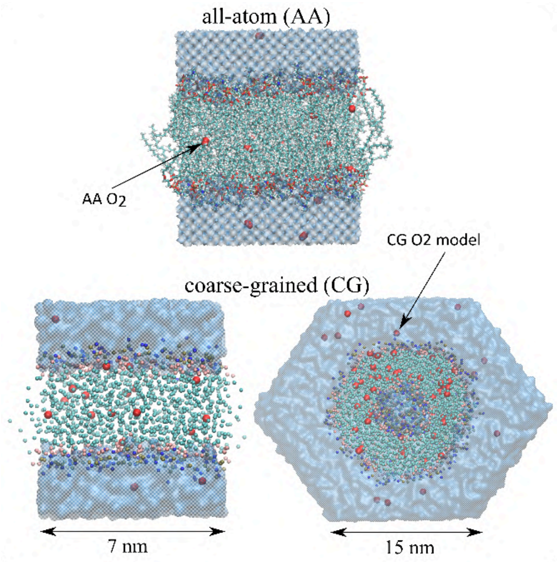

Fig 1. All-atom (AA) description of a flat membrane and coarse-grained (CG) description of flat membrane (left) and liposome (right). Notice the difference in scale for the liposome. Oxygen (red) is indicated with an arrow in both descriptions. For CG systems: POPC is presented by points, color-coded by bead type: green for hydrocarbons, pink for glycerol, brown for phosphate, and blue for choline beads. For AA system: the same color scheme is applied, except the glycerol group is red. Water is depicted as transparent light blue. To maintain clarity, ions are not displayed in the visualization.

systems	**#POPC**	**#W**	**#Na$^+$/Cl$^-$**	**#O2**
POPC-flat	128	1395	14	18

POPC-liposome-50A	394	16618	192	111

Table 1. Detailed description of the two simulated systems: a flat membrane and a liposome with radius of about 50 Å. The number of phospholipid molecules (#POPC), water CG beads (#W), ion pairs (#Na^+/Cl^-), and oxygen CG beads (#O_2) is indicated.

Computational details. The systems were simulated using GROMACS-2021.4 [5]. Using CHARMM-GUI, initial structures of the membranes were prepared [6,7,8,9]. The Martini 3 forcefield was used [3]. The reaction-field approach was used to calculate the Coulombic interactions [10]. With the potential-shift-Verlet modifiers, the Coulombic and the van der Waals potentials were shifted to zero at the cut-off of 1.1 nm. The neighbor list was updated using the Verlet neighbor search algorithm with cutoff length 1.1 nm. The equation of motion was integrated using the leap-frog integrator with a time step of 20 fs. A temperature of 310 K and a pressure of 1 bar were set for all the systems. The velocity rescale thermostats coupling constant was set at 1.0 ps [11]. The Parrinello-Rahman barostat was used with a coupling constant of 12 ps. For systems with a flat membrane and a liposome, semi-isotropic and isotropic isothermal compressibility of $3x10^{-4}$ and 4.5x10-5 bar^{-1} was employed, respectively. A dodecahedron box was used to simulate the liposomes. The center of mass motion of the system was removed every 100 time steps. Systems were first energy minimized and next they were equilibrated applying NPT (isothermal-isobaric) ensemble for 100 ns. The production run was 500 ns of NPT simulation.

Analysis of results. A histogram was made of the position of the O_2 molecules with respect to the center of the membrane. In the case of a flat membrane, position is measured along the membrane's normal axis (z-direction). However, for a liposome, position is determined by measuring the radial distance from the center of the liposome. This center is defined by the average position of the phosphor CG beads (PO4) located in the head group of the POPC molecules. The logarithm of the histogram of the position q along the membrane normal leads to the free energy profile,

$$F(q) = \ - k_B T ln(hist(q))$$

where k_B is Boltzmann's constant and T is the temperature. At 310 K, 1 $k_B T$ is approximately equivalent to $4.28x10^{-21}$ Joules or 2.58 kJ/mol.

Results and discussion

The free energy profile gives information about the barriers that oxygen must surmount in order to permeate through the membrane. Fig. 2 shows the free energy difference Delta F with respect to the water phase, i.e. $\Delta F(q) = F(q) - F_{water}$, where the center of the two membranes was aligned to the value $q=0$. The flat membrane (blue line) shows that O_2 needs to overcome a barrier of about 0.7 k_BT to enter the POPC membrane based on the CG calculations. More importantly, O_2 experiences a barrier of about 3.7 k_BT to escape from the membrane. These barrier values are in accordance with the more detailed AA calculations [3]. In practice, this means that the POPC membrane will capture O_2 for a while before it can overcome the barrier and escape. This behaviour of oxygen storage (partitioning) in membranes has now been well studied in multiple works [12,13,14,15,16].

Next, we turn to the liposome exhibiting a curved membrane (orange line). The positive and negative q ranges correspond to the outer and inner leaflet, respectively. In the inner leaflet, the liposome shows a heightened barrier compared to the flat bilayer, likely because of the packing structure in the inner leaflet of this fairly small liposome with a diameter of only approximately 10 nm. In the outer leaflet, the barrier is reduced compared to the flat bilayer. The curvature not only alters the headgroup region but also the membrane center, characterized by a shift of the lowest point of the free energy towards the inner layer. This phenomenon is likely attributed to the compact arrangement of lipids within the inner layer. The symmetry between inner and outer bilayer is thus broken, such that, concretely, the O_2 concentration is higher in the inner leaflet than in the outer leaflet. It is possible that this asymmetry could be mitigated in a liposome with a larger radius.

The changes induced by curvature thus show an opposite trend in the inner and outer leaflets, and it remains unclear how these free energy changes will affect the overall oxygen buffering capacity behavior. To fully understand the effect on the permeation and storage kinetics, the time aspect should also be included. It should be noted that the diameter of caveolae is significantly larger than the liposomes utilized in our simulations. By focusing on liposomes with the highest curvature, we aimed to explore the limitations of how curvature influences oxygen partitioning within curved membranes. In future work, we aim to investigate the O_2 permeability, O_2 storage capacity, and O_2 residence time.

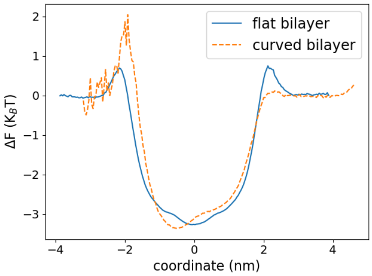

Fig 2. The oxygen free energy profile as a function of the permeation coordinate q (normal to the membrane).

Conclusion

This study employed CG MD simulations to examine the influence of membrane curvature, a structural characteristic of caveolae, on the permeation of oxygen through the membrane. In this investigation, a CG bead was utilized as a representative model for oxygen. By comparing oxygen interaction with a flat membrane and with a liposome membrane, it becomes evident that curvature has a dual effect on oxygen partitioning: it diminishes the free energy barrier in the outer layer while augmenting it in the inner layer. To obtain a more comprehensive understanding of this phenomenon and its impact on oxygen transport, it is essential to compute additional kinetic properties of O_2 in future work.

References

1. Davoudi, Samaneh, et al. "Understanding the Role of Caveolae in Oxygen Buffering: The Effect of Membrane Curvature." International Society on Oxygen Transport to Tissue XLIV. Cham: Springer International Publishing (2022): 87-91.
2. Zuniga-Hertz, Juan Pablo, et al. "The evolution of cholesterol-rich membrane in oxygen adaption: the respiratory system as a model." Frontiers in Physiology 10 (2019): 1340.
3. Souza, Paulo CT, et al. "Martini 3: a general purpose force field for coarse-grained molecular dynamics." Nat. Methods. 18.4 (2021): 382-388.
4. Davoudi, Samaneh, et al. “Validation of coarse-grained model for molecular oxygen.” To be submitted.
5. Abraham, Mark James, et al. "GROMACS: High performance molecular simulations through multi-level parallelism from laptops to supercomputers." SoftwareX 1 (2015): 19-25.
6. Jo, Sunhwan, et al. "CHARMM‐GUI: a web‐based graphical user interface for CHARMM." J. Comput. Chem. 29.11 (2008): 1859-1865.
7. Brooks, Bernard R., et al. "CHARMM: the biomolecular simulation program." J. Comput. Chem. 30.10 (2009): 1545-1614.
8. Lee, Jumin, et al. "CHARMM-GUI input generator for NAMD, GROMACS, AMBER, OpenMM, and CHARMM/OpenMM simulations using the CHARMM36 additive force field." Biophys. J. 110.3 (2016): 641a.
9. Qi, Yifei, et al. "CHARMM-GUI martini maker for coarse-grained simulations with the martini force field." J. Chem. Theory Comput. 11.9 (2015): 4486-4494.
10. Tironi, Ilario G., et al. "A generalized reaction field method for molecular dynamics simulations." J. Chem. Phys. 102.13 (1995): 5451-5459.
11. Bussi, Giovanni, Davide Donadio, and Michele Parrinello. "Canonical sampling through velocity rescaling." J. Chem. Phys. 126.1 (2007).
12. Vervust, Wouter, and An Ghysels. "Oxygen Storage in Stacked Phospholipid Membranes Under an Oxygen Gradient as a Model for Myelin Sheaths." Oxygen

LIST OF PUBLICATIONS

INTERNATIONAL PEER-REVIEWED PUBLICATIONS

Papers discussed in this thesis:

1. **S. Davoudi**, and A. Ghysels, 'Sampling efficiency of the counting method for permeability calculations estimated with the inhomogeneous solubility–diffusion model', *Journal of Chemical Physics* 154, 054106 (2021).
2. **S. Davoudi** and A. Ghysels, 'Defining permeability of curved membranes in molecular dynamics simulations', *Biophysical Journal* 12, 2082-2091 (2023).
3. **S. Davoudi**, Q. Wang, H.H. Patel, SC. Pias and A. Ghysels, 'Understanding the role of caveolae in oxygen buffering: the effect of membrane curvature', *Oxygen Transport to Tissue XLIV. ISOTT 2022. Advances in Experimental Medicine and Biology 1438. Springer*, 87-91 (2023).
4. **S. Davoudi**, K. Raemdonck, K. Braeckmans and A. Ghysels, 'Capric acid and tetradecanoic acid permeability enhancers in curved liposome membranes', *Journal of Chemical Information and Modeling* 63(21), 6789-6806 (2023).
5. **S. Davoudi** and A. Ghysels, 'Understanding oxygen "buffering" by caveolae using coarse-grained molecular dynamics simulations', *Oxygen Transport to Tissue. ISOTT 2023. Advances in Experimental Medicine and Biology*, accepted (2024).
6. **S. Davoudi**, P.A. Vainikka, S.J. Marrink and A. Ghysels, 'Validation of CG model for molecular oxygen', to be submitted (2024), pdf of the paper is not included in the thesis.

Other papers:

7. **S. Davoudi**, S. Amjad-Iranagh, S. and M. Zaeifi Yamchi, 'Molecular dynamic simulation of Ca^{2+}-ATPase interacting with lipid bilayer membrane', *IET Nanobiotechnology* 9(2), 85-94 (2015).

8. A. Ghysels, S. Roet, **S. Davoudi**, and T. S. van Erp, ‘Exact non-Markovian permeability from rare event simulations’, *Physical Review Research* 3, 033068, (2021).

Oral contributions

1. Davoudi, S., Ghysels, A: ‘Assessing counting method efficiency in cell permeability calculation’. 19th National Day on Biomedical Engineering, Brussels, Belgium, 27th of November, 2020.
2. Davoudi, S., Raemdonck, K., Braeckmans, K., and Ghysels, A. ‘Effect of membrane curvature and lipid composition on membrane permeability in liposomal drug delivery’. CRF-ChemCYS 2022 conference, Blankenberge, Belgium, 12th to 14th of October, 2022.
3. Davoudi, S.and Ghysels, A. ‘Exploring caveolae’s role in oxygen "buffering" through coarse-grained molecular dynamics’. FEARS 2023 conference, Ghent, Belgium, 26th of October, 2023.

Poster contributions

Research results were presented as poster presentations on several international conferences.